MEASUREMENT OF THE ^{8}B SOLAR NEUTRINO ENERGY SPECTRUM AT THE SUDBURY NEUTRINO OBSERVATORY

Monica Dunford

A DISSERTATION

in

Physics and Astronomy

Presented to the Faculties of the University of Pennsylvania in Partial Fulfillment of the Requirements for the Degree of Doctor of Philosophy

2006

Eugene W. Beier

Supervisor of Dissertation

Randall D. Kamien

Graduate Group Chairperson

To all my friends, for their unconditional support

Acknowledgments

The completion of this thesis would not have been possible without the excellent guidance of Gene Beier. Gene is the ideal advisor, giving me the intellectual freedom to explore new approaches and ideas but never letting me lose focus of the big picture. His depth of knowledge on all subjects, not just neutrinos and particle physics is awe-inspiring and discussions with him on everything from neodymium to Wagner operas have always been illuminating as well as entertaining.

There is not a single page in this thesis which does not bear the influence of Josh Klein. Working with Josh has been a wonderful pleasure. He is an endless source of creative and innovative ideas and doesn't understand the phrase, 'It can't be done'. Even in the darkest moments, his enthusiasm and optimism for this measurement has never faltered. His experimental creativity and love for experimental physics inspired me throughout grad school and will continue to inspire me throughout my entire career. Outside of work, Josh was also a great friend, patiently teaching me the best defense against strikers on the soccer field to the proper technique of pushing cars out of snow.

At Penn, Vadim Rusu and Chris Kyba have been irreplaceable friends and colleagues. From the beginning, Vadim always kept a big-brother watch on me, teaching me all the necessary survival tools on SNO and later listening to my finishing woes. Without Chris, I would have been committed to an insane asylum long ago. He is a great listening ear, always pulling me away from the precipice of insanity that defines grad school. I owe many thanks to Neil McCauley for the countless hours he invested in the MC processing and the many enjoyable conversations both at work and in the Sudbury bars. Bill Heintzelman, Huaizhang Deng and Jeff Secrest have also been excellent companions, teaching me everything from the fine details of signal extraction,

Fortran and C++ to bird watching in third world countries, the history of communism in China and the liquor laws below the Mason-Dixon line. One could not ask for more well-rounded colleagues. Paul Keener, Rick Van Berg and Godwin Mayers have also been invaluable, always willing to help me with my endless computer and electronic issues and always with a smile.

Within SNO, I am especially grateful to Jeanne Wilson, who writes the best code and documentation, ever. Her help with signal extraction saved me a great amount of time, making the finishing experience much less painful. Working with Aksel Hallin has also been a great experience. His detailed knowledge about all aspects of the detector helped solved many problems in this analysis. I am also grateful to Gabriel Orebi-Gann who did innumerable amounts of grunt work for me and always seemed happy to be doing it as well. Kevin Graham as well as being a wealth of information about energy estimation and contemporary literature has also been a wonderful friend. At site, Noel Gagnon and Fraser Duncan were indispensable, especially during the backplane installation. During the trying days of Crate 16, they were always encouraging and supportive, never giving up. The rest of the SNO site staff and the NCD installation crew was a family away from home, especially Kate Frame, Lina Anselmo and Lee Mayer, who were always great confidants and got me out of the office and onto the soccer field.

Of course nothing in my life would be possible without the unwavering and unconditional support of my family and friends. From the 1500 meter mark in San Diego Crew Classic to sketchy areas in various countries to the descent from Mt. Whitney, they have always there to support, protect or in some cases, drag me to the end. There are no better people in the world and I am infinitely grateful for every moment spent with them. You are the oak from which I can fly.

ABSTRACT

MEASUREMENT OF THE ^{8}B SOLAR NEUTRINO ENERGY SPECTRUM AT THE SUDBURY NEUTRINO OBSERVATORY

Monica Dunford

Eugene W. Beier

The Sudbury Neutrino Observatory, through its measurements of the solar ^{8}B neutrino flux via the charged current (CC) and neutral current (NC) interactions, has successfully demonstrated that solar electron neutrinos undergo flavor transformation enroute to Earth. This work presents a measurement of the ^{8}B neutrino flux combining the pure D_2O (283 days) and the salt phases (391 days) of data using an energy threshold of 4.0 MeV. The measured CC flux, which is sensitive only to electron neutrinos, is $1.67^{+0.04}_{-0.04}(\text{stat.})^{+0.10}_{-0.07}$ (syst.) $\times 10^6 \text{cm}^{-2}\text{s}^{-1}$ and the NC flux, sensitive to all active neutrino flavors, is $4.98^{+0.17}_{-0.16}(\text{stat.})^{+0.20}_{-0.26}$ (syst.) $\times 10^6 \text{cm}^{-2}\text{s}^{-1}$. While the measured NC flux agrees with the flux predicted by the Standard Solar Model, the CC flux is strongly suppressed. These results are consistent with the prediction of matter enhanced neutrino oscillations (MSW) with a large mixing angle (LMA).

The measured fluxes were determined without assumptions about the energy spectrum of the neutrinos interacting via the CC and elastic scattering (ES) interactions. This work presents the extracted CC and ES energy spectra at an energy threshold of 4.0 MeV and finds that both spectra are consistent with an undistorted ^{8}B neutrino energy spectrum.

Contents

List of Figures

List of Tables

Ch. 1

Neutrinos in General, and the Solar ^{8}B Spectrum in Particular

In recent years, numerous experiments using atmospheric [1], solar [2–7], accelerator [8, 9] and reactor [10] neutrinos have concluded that neutrinos are massive. Neutrino mass has been discovered through the phenomenon of neutrino oscillation, where neutrinos of one flavor can transform into another flavor. For flavor transformation to occur at least one of the neutrinos must have a non-zero mass.

The first experimental evidence of neutrino flavor transformation in solar neutrinos was a measurement of the flux of solar electron neutrinos in the 1960s by Ray Davis [4]. More recently, the Sudbury Neutrino Observatory (SNO) studied the flux of all active neutrinos as well as electron neutrinos from the Sun. This sensitivity to all neutrino types allowed for measurement of the total flux of solar neutrinos (which is beneficial for testing solar model theory as well as neutrino properties) and the neutrino mixing parameters, Δm^2 and $\tan^2\theta$.

The aim of this thesis is to make the most precise measurement of ^{8}B solar neu-

trino flux using SNO's data and to test predictions about the shape of the terrestrial electron neutrino energy spectrum that can be distorted by the Sun's matter. These theoretical predictions are discussed in the remainder of this chapter. Experimental sensitivity to matter effects in the Sun using data from SNO requires having high statistics, small systematic uncertainties and a low analysis energy threshold. To increase the statistics of the data set, this thesis combines data taken during SNO's first (283 days[1]) and second (391 days) phases of running. An overview of the SNO detector used to collect this data is given in Chapter 2. Improving systematic uncertainties and lowering the energy threshold of the analysis is a road fraught with difficulties. The limitations to the detector and analysis methods that determine the energy threshold in SNO are discussed in Chapter 3. This thesis has focused on improving the detector hardware, the energy estimation algorithm and other analysis methods to better separate the neutrino signal from the radioactivity backgrounds. These improvements are highlighted in Chapters 4 and 5. Chapters 6-10 detail the analysis techniques used to measure the ^{8}B solar neutrino flux and its energy spectrum.

1.1 Physics of Massive Neutrinos

First postulated in 1930 by Pauli [11] to explain the β decay energy spectrum, the neutrino was thought to be undetectable until 1956 when Reines and Cowan discovered the electron anti-neutrino [12], and it was thought to be massless until the 1990s when evidence of neutrino oscillation was observed. In the Standard Model of

[1]There are in total 306.4 days of neutrino data taken during this phase but periods of high radioactivity have been removed from the total data set for this analysis

particle physics there are three neutrino families (or flavors); electron, muon and tau, all of which have been experimentally observed. The Standard Model [13–16], which describes the properties of all fundamental particles and the electromagnetic, strong and weak interactions, has been an extremely successful theory, withstanding rigorous experimental tests for over 25 years. The neutrino in this theory can interact only through the weak interaction (and gravity which is not included in the model) and carries no color or charge. As a massless particle in the theory, the neutrino exists in a left-handed doublet with its charged lepton partner. The right-handed field is nonexistent. For a particle to obtain mass, it must couple to the Higgs field where the size of this coupling (called the Yukawa coupling) dictates the particle's mass. Coupling to the Higgs requires both a left and right handed field. With the discovery of neutrino mass, the Standard Model had to be expanded to include the existence of a right-hand neutrino field.

1.1.1 Neutrino Mass and Mixing

Neutrinos are produced in weak eigenstates but propagate as mass eigenstates. If the flavor and mass eigenstates are different, there is a possibility of flavor transformation. The relation between the mass and flavor eigenstates is given as follows:

$$\begin{bmatrix} \nu_e \\ \nu_\mu \\ \nu_\tau \end{bmatrix} = \begin{bmatrix} U_{e1} & U_{e2} & U_{e3} \\ U_{\mu 1} & U_{\mu 2} & U_{\mu 3} \\ U_{\tau 1} & U_{\tau 2} & U_{\tau 3} \end{bmatrix} \begin{bmatrix} \nu_1 \\ \nu_2 \\ \nu_3 \end{bmatrix}. \tag{1.1}$$

where U_{ij} is the matrix element used to describe the relation between the i^{th} and j^{th} eigenstates. This mixing matrix, (called the Maki-Nakagawa-Sakata-Pontecorvo

(MNSP) matrix) can be parameterized as

$$U = \begin{pmatrix} 1 & 0 & 0 \\ 0 & c_{23} & s_{23} \\ 0 & -s_{23} & c_{23} \end{pmatrix} \times \begin{pmatrix} c_{13} & 0 & s_{13}e^{i\delta} \\ 0 & 1 & 0 \\ -s_{13}e^{-i\delta} & 0 & c_{13} \end{pmatrix} \times \begin{pmatrix} c_{12} & s_{12} & 0 \\ -s_{12} & c_{12} & 0 \\ 0 & 0 & 1 \end{pmatrix} \tag{1.2}$$

where $c_{ij} = \cos\theta_{ij}$, $s_{ij} = \sin\theta_{ij}$, θ_{ij} is the mixing angle and δ is the CP violating phase. Mixing in the θ_{23} and θ_{12} sectors can be approximated by two flavor oscillation since θ_{13} is small ($\theta_{13} < 13^\circ$) [17] and $\Delta m^2_{23} \gg \Delta m^2_{12}$ (see next section for a discussion of these experimental measurements). For the θ_{12} sector, the matrix reduces to

$$\begin{pmatrix} \nu_e \\ \nu_\mu \end{pmatrix} = \begin{pmatrix} \cos\theta_{12} & \sin\theta_{12} \\ -\sin\theta_{12} & \cos\theta_{12} \end{pmatrix} \begin{pmatrix} \nu_1 \\ \nu_2 \end{pmatrix} \tag{1.3}$$

where θ_{12} is the mixing angle, ν_e and ν_μ are the flavor states and ν_1 and ν_2 are the mass eigenstates. The probability of detecting a ν_e after it has propagated some distance is given by

$$P_{\nu_e \to \nu_e} = 1 - \sin^2 2\theta_{12} \sin^2 \left(\frac{1.27 \Delta m^2 \, L}{E} \right) \tag{1.4}$$

where $\Delta m^2 = {m_2}^2 - {m_1}^2$ in eV^2, L is the distance between the production point and detection point in km and E is the neutrino energy in GeV. If the masses of the neutrinos are zero or the neutrinos have the same mass ($\Delta m^2 = 0$), there is no flavor transformation. The parameters Δm^2 and θ are measured experimentally.

Source	L (m)	E(MeV)	$\overline{m}^2$ (ev^2)
Reactor	$10^2 - 10^5$	1	$10^{-2} - 10^{-5}$
Meson factory	10^2	10	10^{-1}
Accelerators	10^6	10^4	10^{-2}
Atmosphere	10^7	10^4	10^{-3}
Solar core	10^{11}	1	down to 10^{-11}

Table 1.1: Various types of neutrino experiments with their typical Δm^2 sensitivity range.

1.1.2 Evidence for Neutrino Oscillations

To measure the parameters of the MNSP mixing matrix, neutrinos from reactors, accelerators, the atmosphere and the Sun have been used. Experimental sensitivity to measuring the mass squared difference and the mixing angle depends upon the ratio of $\overline{m}^2 = \frac{E}{L}$. Using Equation 1.4, if $\overline{m}^2 \gg \Delta m^2$, then only the average of the oscillation is observed ($P_{\nu_e \to \nu_e} = 1 - \frac{1}{2}\sin^2 2\theta$). If $\overline{m}^2 \ll \Delta m^2$, then the oscillation pattern has not had space to develop ($P_{\nu_e \to \nu_e} = 1$). The sensitivity range of Δm^2 for various types of experiments is listed in Table 1.1. Several experimental results are highlighted below.

Atmospheric and Accelerator Experiments

Cosmic ray interactions in the atmosphere create energetic neutrinos (on the order of many GeV or greater). Super-Kamiokande (Super-K), a water Cherenkov detector, measures the fluxes of both ν_e and ν_μ neutrinos that interact with an H_2O target. Flavor identification of the interacting neutrino is possible by identifying the flavor of the charged lepton produced during the neutrino interaction with the target. Super-K observes a strong zenith angle dependence in the $\Phi(\nu_\mu)$ flux with a deficit of ν_μ

neutrinos that are traveling upward to the detector. No deficit of the ν_e is flux is seen. These results are consistent with the hypothesis that ν_μs produced in the atmosphere are oscillating to ν_τs. The measured mixing parameters at the 90% confidence level [18] are

$$\sin^2 2\theta_{23} > 0.92 \quad \text{and} \quad 1.5 \times 10^{-3} < |\Delta m^2_{23}| < 3.4 \times 10^{-3} eV^2 \tag{1.5}$$

These results have been confirmed by the K2K and MINOS experiments which search for ν_μ disappearance using accelerator produced neutrino beams. These accelerator experiments observe a deficit of ν_μ neutrinos from the beam with mixing parameters that are consistent with Super-K's results [8, 9].

Reactor Experiments

The CHOOZ experiment, which measured the flux of $\overline{\nu}_e$ neutrinos produced from a nuclear reactor about one kilometer from the detector, observed no deficit in the expected $\overline{\nu}_e$ flux [17]. These results indicates that $\overline{\nu}_e$ s is not strongly mixing. This experiment also sets the current limits on θ_{13}.

Solar Experiments

The properties of neutrinos produced in the Sun and experimental measurements of those neutrinos are discussed in detail for the remainder of this chapter. To briefly summarize the results, a deficit in the solar ν_e flux is observed, and implies oscillation into ν_μ and ν_τ flavors. Like the oscillations observed in atmospheric neutrinos, the

observed mixing is large with best fit values [19] of

$$\tan^2\theta_{12} = 0.45 \quad \text{and} \quad \Delta m^2_{12} = 8.0 \times 10^{-5} eV^2. \tag{1.6}$$

1.2 Solar Neutrinos and the ^{8}B Spectrum

Solar neutrinos are produced as a byproduct of nuclear fusion in the core of the Sun. The primary fusion reaction (the pp-chain) is

$$4\mathrm{p} + 2\mathrm{e}^- \longrightarrow {}^4\mathrm{He} + 2\nu_e + \mathrm{E}(26.7\mathrm{MeV}) \tag{1.7}$$

where E represents the kinetic energy of charged particles and the energies of photons and neutrinos. Neutrinos are produced in six reactions in this chain as shown in Figure 1.1. The largest number of neutrinos comes from the $p + p \longrightarrow {}^2\mathrm{H} + \mathrm{e}^+ + \nu_e$ reaction that produces ν_es (referred to as pp neutrinos) ranging from 0.1 to 0.4 MeV. The neutrino energies in the other reactions are larger (the spectra are shown in Figure 1.2) but the fluxes are much reduced in comparison to the main pp reaction. The predicted neutrino fluxes are summarized in Table 1.2. In addition to the pp-chain, neutrinos are produces in the Carbon-Nitrogen-Oxygen (CNO) but the CNO neutrinos are a small part of the total solar neutrino flux.

A Standard Solar Model (SSM, B2005 [20]), which predicts the fluxes of neutrinos, has been very successful in its ability to predict the Sun's behavior, specifically its predictions of the speed of sound that can be measured through helioseismology. Those predictions agree with the measurements to better than 0.1%. The B2005 model also provides the density profile of the Sun which is critical for studying neutrino

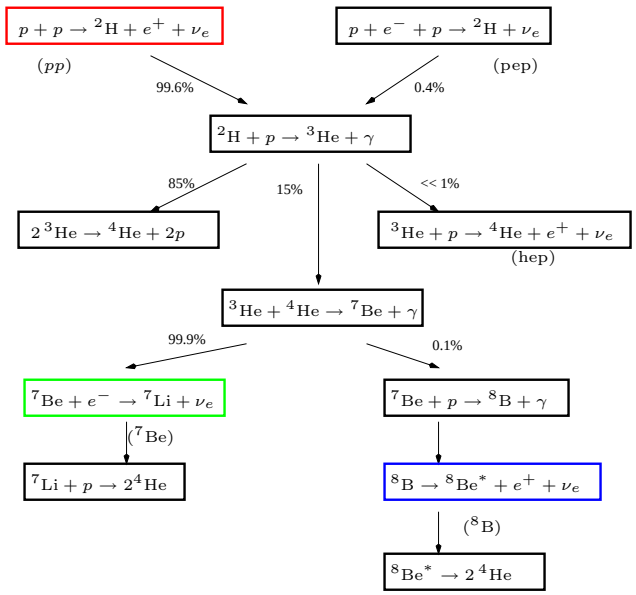

Fig. 1.1: Nuclear reactions involved in the proton-proton (pp) chain from [21].

properties in matter (see Section 1.3).

There are many advantages to using the Sun to study neutrino properties. First, exclusively electron neutrinos are produced in Sun's nuclear fusion reactions. Therefore, any observation of non-electron neutrino types from the Sun must be due to neutrino oscillation or other new physics. Second, although neutrinos interact very weakly, the solar neutrino fluxes are very large, making experimental measurements

Interaction	Predicted Flux ($\times 10^{10}\mathrm{cm}^{-2}\mathrm{s}^{-1}$)
pp	5.99 ($\pm$1%)
pep	1.40×10^{-2} ($\pm$2%)
hep	7.93×10^{-7} ($\pm$16%)
^{7}Be	4.84×10^{-1} ($\pm$12%)
^{8}B	5.69×10^{-4} ($\pm$23%)

Table 1.2: Fluxes of neutrinos from the nuclear fusion reactions in the Sun [20]. The theoretical uncertainty on the flux shown in parenthesis on the right is quoted in terms of percent.

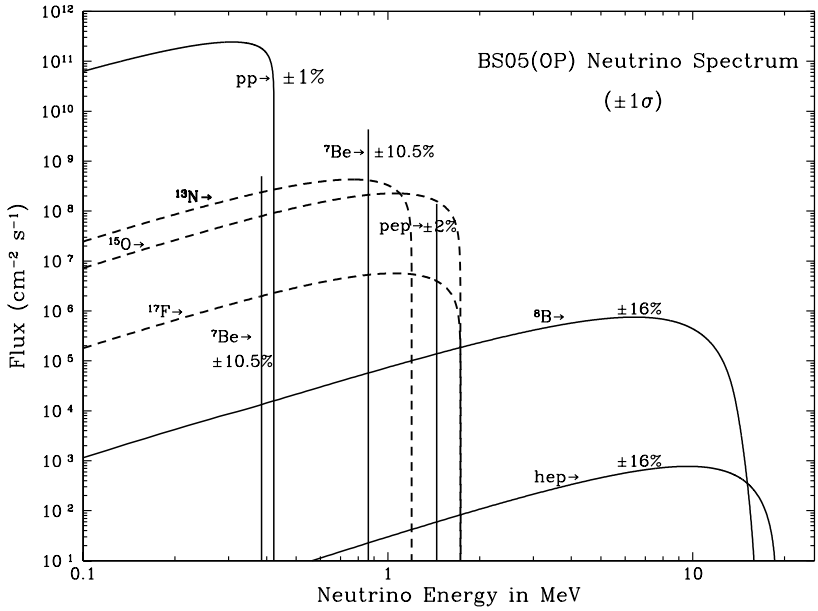

Fig. 1.2: Energy spectra of neutrinos produces by nuclear fusion reactions in the Sun. The dashed lines are neutrino spectra from the CNO cycle neutrinos which are not part of the pp-chain. Taken from [22]

on Earth feasible. Lastly, the energies of solar neutrinos span over two orders of magnitude from 0.1 to 15 MeV, allowing for experimental measurements over a wide range of energies.

Two main experimental techniques have been used to measure solar neutrinos; radiochemical and water Cherenkov. Radiochemical experiments may have a very low energy threshold (below an MeV) but are only sensitive to electron neutrinos and cannot provide information about the energy, direction or time of interaction of the neutrino. Two experiments using a Gallium target were sensitive to all solar electron neutrinos including the pp neutrinos. The Homestake experiment used Chlorine as a target and was sensitive to pep, ^{7}Be, ^{8}B and hep neutrinos. The results of these experiments are summarized in Table 1.3.

Water Cherenkov detectors using an H_2O target volume detect neutrinos by observing Cherenkov light from the recoil electron in a neutrino-electron elastic scattering interaction. This interaction is sensitive mainly to electron neutrinos with some sensitivity to other active neutrino types. Although these detectors can retain information about the initial neutrino direction and its energy, the detector energy threshold is much higher than radiochemical detector thresholds - on the order of 5 MeV. Water Cherenkov detectors measure mainly neutrinos produced in the ^{8}B fusion reaction which has a flux that is four orders of magnitude smaller than the pp neutrino flux. Results from the Kamiokande experiment, a first generation water Cherenkov detector are also listed in Table 1.3. These detectors' ability to measure the energy spectrum of solar neutrinos can be used to test theoretical models about neutrino interactions in matter which predict distortions in the energy spectrum (discussed in more detail in the next section). The initial energy spectrum of the neutrinos produced in the fusion reaction $^8\mathrm{B} \longrightarrow {}^8\mathrm{Be}^* + e^+ + \nu_e$ is independent of the solar model and has been measured very precisely in the laboratory.

Both the radiochemical and water Cherenkov experiments observed fewer solar neutrinos than predicted. Additionally the deficit of electron neutrinos increases with neutrino energy (from the < 1 MeV pp neutrinos to the 15 MeV ^{8}B neutrinos).

1.3 Matter Effects in the Sun

Matter can have a strong effect on the neutrino survival probability, an idea first postulated by Wolfenstein [24] and applied to the Sun by Mikheyev and Smirnov [25]. When propagating through matter, electron neutrinos can interact with the matter via the neutral current and charged current interaction, while muon and tau neu-

Radiochemical Experiments	Medium	Threshold (MeV)	Predicted Flux (SNU)	Measured Flux (SNU)
Homestake	Cl	0.814	8.5 ± 1.8	$2.56 \pm 0.16 \pm 0.16$ [4]
Gallex and GNO	Ga	0.2332	131^{+12}_{-10}	$74.1^{+6.7}_{-6.8}$ [6, 7]
SAGE	Ga	0.2332	131^{+12}_{-10}	$70.9^{+5.3+3.7}_{-5.3-3.2}$ [5]
Water Cherenkov Experiments	Medium	Threshold (MeV)	Predicted Flux ($10^6 \mathrm{cm}^{-2}\mathrm{s}^{-1}$)	Measured Flux ($10^6 \mathrm{cm}^{-2}\mathrm{s}^{-1}$)
Kamiokande	H_2O	7.0	$5.82(1 \pm 0.23)$	$2.82^{+0.25}_{-0.24} \pm 0.27$ [23]

Table 1.3: Summary of the fluxes of solar neutrinos from first generation radiochemical and water Cherenkov detectors. The Solar Neutrino Unit (SNU) is 10^{-36} neutrino reaction per second per target atom. If two uncertainties are quoted the first is statistical and the second is the systematic uncertainty.

trinos can only interact through the neutral current interaction. The addition of the charged current interaction for the electron type neutrino results in a different forward scattering amplitude relative to the other neutrino types. This changes the electron neutrino's relative propagation which in turn changes the neutrino flavor superposition in a phenomenon known as the matter or 'MSW effect'.

For electron neutrinos propagating through the Sun, the inclusion of the charged current interaction with the surrounding matter adds an additional effective potential of $V = 2\sqrt{2}EG_F N_e$ to the ν_e wave equation where E is the neutrino energy, G_F is the Fermi constant and N_e is the electron number density in the medium. The Hamiltonian of the system has a term:

$$H' = \begin{pmatrix} -\Delta m^2 \cos 2\theta + V & \Delta m^2 \sin 2\theta \\ \Delta m^2 \sin 2\theta & \Delta m^2 \cos 2\theta \end{pmatrix} \tag{1.8}$$

When including this potential in the wave function, the instantaneous mixing angle is:

$$\sin^2 2\theta_m = \frac{\Delta m^2 \sin^2 2\theta}{\sqrt{(\Delta m^2 \cos 2\theta - V)^2 + (\Delta m^2 \sin 2\theta)^2}} \tag{1.9}$$

where V is defined above, Δm^2 and θ are the mixing parameters in vacuum and θ_m is the 'matter' mixing angle. At the resonance condition, where $V = \Delta m^2 \cos 2\theta$ the matter mixing angle becomes maximum for νs if $\Delta m^2 > 0$ ($\Delta m^2 \equiv m_2^2 - m_1^2$).

The matter density of the Sun is non-uniform, so that N_e and therefore the Hamiltonian of the system change with time as the neutrinos propagate through the Sun. To understand this potential's effect on the ν_e survival probability, consider a ν_e produced at the center of the Sun with an energy above that required for the resonance condition. At the neutrino's production point, the density is very high and therefore by Equation 1.9, the matter mixing angle is $\theta_m \approx 90^\circ$ ($\sin^2 2\theta_m \approx 0$). The neutrino flavor composition expressed in terms of the mass eigenstates is

$$\nu_1 = \nu_e \cos\theta_m + \nu_\mu \sin\theta_m \tag{1.10}$$

$$\nu_2 = \nu_e \sin\theta_m + \nu_\mu \cos\theta_m \tag{1.11}$$

When $\theta_m \approx 90^\circ$ the neutrino composition will consist largely of the more massive eigenstate, ν_2. Since the Sun's density profile is changing slowly and monotonically decreasing, the matter mixing angle, θ_m decreases (and therefore the mixing increases) with the decreasing density. At some point, the neutrino will encounter a density such that the resonance condition is met and mixing become maximal ($\theta_m = 45^\circ$). As the neutrino continues to propagate to lower densities, the matter density is changing slowly and adiabatically, suppressing any transitions between the ν_1 and ν_2 matter

eigenstates. When the neutrino exits the Sun and $\theta_m = \theta$, the neutrino remains almost entirely in the ν_2 mass eigenstate. As a result the ν_μ component of the solar neutrino flux is enhanced, leading to a measured suppression of the ν_e survival probability compared to the vacuum survival probability. For low energy neutrinos such as the pp neutrinos the resonance condition discussed above is never met, and the behavior of these neutrinos is governed solely by vacuum oscillations (Equation 1.4). Since the ν_e survival probability of higher energy solar neutrinos is suppressed due to MSW effects in the Sun, this results in an energy dependence for the electron component of the neutrino flux.

1.3.1 Signatures of the MSW Effect

Although there is evidence for the matter effect in the Sun by comparison of results from solar neutrino experiments (which include matter effects) and the KamLAND reactor experiment (vacuum oscillations only, see Section 1.4.3), the MSW theory makes two other experimentally testable predictions, neither of which have been explicitly observed. First, the survival probability of the electron neutrino may change as a function of neutrino energy. For the Δm^2 and $\sin^2 2\theta$ allowed by current experiments, this could lead to a distortion of the ^{8}B neutrino energy spectrum especially at energies below 5 MeV. Second, solar neutrinos can also be affected by the Earth's matter. The latter could result in a difference in the measured electron neutrino flux during the day (neutrinos pass through very little of the Earth's matter) versus the night (neutrinos pass through large amounts of the Earth enroute to the detector).

Spectral Distortion

The transition from vacuum oscillations to matter enhanced oscillations occurs between the neutrino energy range of approximately 1 to 5 MeV for solar neutrinos. Therefore, a small distortion of the ^{8}B energy spectrum is expected for neutrino energies in this range. The magnitude of this predicted distortion is very small in the energy range probed by water Cherenkov detectors but it could be measurable if the experiment has small statistical and systematic uncertainties.

Day-Night Asymmetry

A day-night asymmetry occurs when solar neutrinos traveling in the vacuum of space, encounter the Earth's matter. In the reverse process of the Sun's matter effect, electron neutrinos are regenerated. This effect predicts a larger flux of electron type neutrinos from the Sun at night in comparison to the day. The day-night asymmetry is defined as

$$A_{DN} = \frac{2(\Phi_N - \Phi_D)}{\Phi_N + \Phi_D} \tag{1.12}$$

where Φ_N is the night-time flux and Φ_D is the day-time flux.

1.4 Evidence for LMA Oscillations

To study the properties of solar neutrinos more precisely, a variety of second generation experiments were designed. This section details the results for two water Cherenkov detectors and a long baseline reactor experiment, all of which have been used to make detailed measurements of the Δm^2_{12} and $\tan^2\theta_{12}$ mixing parameters.

1.4.1 Super-Kamiokande

Super-Kamiokande (Super-K), the successor to the original Kamiokande experiment, is a water Cherenkov detector with 22.5 kt of H_2O as a fiducial mass. This detector has made very precise measurements of the mixing parameters for both atmospheric and solar neutrinos. Super-K detects solar neutrinos via the elastic scattering interaction, which is sensitive to all active flavors but is over six times more sensitive to electron neutrinos than to ν_μ or ν_τ s. Using 1496 days of data, the measured solar flux assuming only ν_e interactions [26] is

$$\Phi_{\rm ES}^{\rm SK} = 2.35 \pm 0.02(\text{stat.}) \pm 0.08(\text{sys.}) \times 10^6 \text{cm}^{-2}\text{s}^{-1}. \tag{1.13}$$

This flux is 41% of the predicted ^{8}B neutrino flux in Table 1.2. The energy spectrum of the recoil electron is consistent with the energy spectrum predicted by an undistorted ^{8}B neutrino energy spectrum.

Super-K also measures a day-night asymmetry (Equation 1.12) of

$$\text{A}_{\rm DN}^{\rm ES}(\text{Super} - \text{K}) = +0.021 \pm 0.020(\text{stat.})^{+0.013}_{-0.012}(\text{sys.}) \tag{1.14}$$

which is consistent with zero.

1.4.2 SNO

The Sudbury Neutrino Observatory (SNO) uses a water Cherenkov detector that, unlike previous water target experiments, uses 1000 tonnes of D_2O as the target volume (see Chapter 2 for details of the detector). Proposed by Herb Chen [27] in 1984, this experiment aimed to test the hypothesis of neutrino flavor change in

solar neutrinos. With the use of D_2O as a target, solar neutrinos can interact in the detector via elastic scattering (ES)

$$\nu_{e,(\mu,\tau)} + e^- \rightarrow \nu_{e,(\mu,\tau)} + e^-$$

charged current (CC) interactions

$$\nu_e + d \rightarrow p + p + e^-$$

or neutral current (NC) interactions

$$\nu_x + d \rightarrow n + p + \nu_x$$

As in Super-K, the ES interaction is sensitive to all active neutrino flavors but strongly favors electron neutrinos. At solar neutrino energies, the CC interaction is sensitive only to electron neutrinos, while the NC interaction is equally sensitive to all active neutrino flavors. It is through the measurement of the NC interaction that SNO is able to measure the total flux of active neutrino types from the Sun.

SNO has operated in three separate phases: D_2O, salt and NCD. The D_2O phase ran from November 1999 until May 2001 using only pure D_2O in the target volume. Using 306 days of data, the measured CC, ES and NC fluxes [2] (defined as the flux of neutrinos from the Sun measured with the CC, ES or NC interaction) are given below

$$\Phi_{\rm ES}^{\rm SNO,PhaseI} = 2.39^{+0.24}_{-0.23}({\rm stat.})^{+0.12}_{-0.12}\ ({\rm syst.}) \times 10^6 {\rm cm}^{-2}{\rm s}^{-1} \quad (1.15)$$

$$\Phi_{\rm CC}^{\rm SNO,PhaseI} = 1.76^{+0.06}_{-0.05}({\rm stat.})^{+0.09}_{-0.09}\ ({\rm syst.}) \times 10^6 {\rm cm}^{-2}{\rm s}^{-1} \quad (1.16)$$

$$\Phi_{\rm NC}^{\rm SNO,PhaseI} = 5.09^{+0.44}_{-0.43}({\rm stat.})^{+0.46}_{-0.43}\ ({\rm syst.}) \times 10^6 {\rm cm}^{-2}{\rm s}^{-1}. \quad (1.17)$$

The energy threshold of this analysis was 5.0 MeV. The ES flux is consistent with the precision measurement made by Super-K. The CC flux, which measures electron neutrinos only, is lower than the ES flux suggesting that the ES flux must include some fraction of non-electron neutrino type. Furthermore the NC flux is consistent with the predicted ^{8}B flux listed in Table 1.2. The CC, ES and NC fluxes measure the following flavor content

$$CC = \nu_e \tag{1.18}$$

$$ES = \frac{5}{6}\nu_e + \frac{1}{6}(\nu_\mu + \nu_\tau) \tag{1.19}$$

$$NC = \nu_e + \nu_\mu + \nu_\tau. \tag{1.20}$$

As the CC and ES fluxes observe a smaller than predicted flux and NC flux agrees with the SSM, this set of measurements strongly suggests that electron neutrinos produced in the Sun undergo flavor transformation enroute to the Earth.

To enhance the capture efficiency of neutrons produced in the NC interaction, in SNO's second phase 2000 kg of NaCl were added to the D_2O volume. The capture efficiency of neutrons in SNO with NaCl is roughly a factor of three greater than for pure D_2O. Further, neutron capture on chlorine produces multiple γs with a summed energy of 8.6 MeV while neutron capture on pure D_2O produces only a single γ with an energy of 6.25 MeV. Multiple γs in the event produce a more diffuse pattern of Cherenkov light which allows for better separation between CC and NC events (see Chapter 8 for a detailed discussion). SNO's salt phase ran from July 2001 to August 2003 collecting 391 days of data. Using these data at an energy threshold of 5.5 MeV, the measured fluxes [19] (assuming an undistorted CC and ES energy spectra shape) for each of the neutrino interactions in SNO are listed below

$$\Phi_{\rm ES}^{\rm SNO,PhaseII} = 2.34^{+0.23}_{-0.23}({\rm stat.})^{+0.15}_{-0.14}\ ({\rm syst.}) \times 10^6 {\rm cm}^{-2}{\rm s}^{-1} \quad (1.21)$$

$$\Phi_{\rm CC}^{\rm SNO,PhaseII} = 1.72^{+0.05}_{-0.05}({\rm stat.})^{+0.11}_{-0.11}\ ({\rm syst.}) \times 10^6 {\rm cm}^{-2}{\rm s}^{-1} \quad (1.22)$$

$$\Phi_{\rm NC}^{\rm SNO,PhaseII} = 4.81^{+0.19}_{-0.19}({\rm stat.})^{+0.28}_{-0.27}\ ({\rm syst.}) \times 10^6 {\rm cm}^{-2}{\rm s}^{-1}. \quad (1.23)$$

These results yield conclusions similar to the D_2O phase results. Measurement of the CC and ES energy spectrum using the salt phase data is consistent with the undistorted ^{8}B neutrino energy spectrum. Additionally no day-night asymmetry (Equation 1.12) is observed in either the D_2O [28] or salt phase data sets:

$$A_{\rm DN}^{\nu_e}({\rm SNO, PhaseI}) = +0.07 \pm 0.049({\rm stat.})^{+0.013}_{-0.012}({\rm sys.}) \quad (1.24)$$

$$A_{\rm DN}^{\rm CC}({\rm SNO, PhaseII}) = -0.021 \pm 0.063({\rm stat.}) \pm 0.035({\rm sys.}) \quad (1.25)$$

SNO's final phase, the NCD phase[2] which is currently taking data, uses pure D_2O as a target volume with 398 meters of ^{3}He proportional counters in the target volume. The addition of the proportional counters allows for a measurement of neutron capture and hence, the NC flux, that is systematically different from the measurement in the previous two phases.

Using the results from SNO's D_2O and salt phases plus Super-K and all first generation solar results, the allowed mixing parameter space strongly favors the large mixing angle (LMA) region (Figure 1.3, upper plot). Although the mixing is large,

[2]NCD which stands for Neutral Current Detectors is misnomer that has stuck. These detectors detect neutrons not neutral currents.

maximal mixing is ruled out with very high significance (5.3σ).

1.4.3 KamLAND

The KamLAND (Kamioka Liquid-scintillator Anti-Neutrino Detector) experiment detects electron anti-neutrinos neutrinos produced from nuclear reactors in Japan and South Korea. With an average distance between the reactor and detector of roughly 180 km, this experiment probes the θ_{12} neutrino mixing parameters without complications from the MSW effect. Using an energy threshold of 3.4 MeV, the ratio of the measured electron anti-neutrino flux to the expected flux [29] is $0.658 \pm 0.044(\text{stat.}) \pm 0.047(\text{sys.})$.

In the context of two neutrino mixing and assuming CPT is conserved, the KamLAND also measures mixing parameters in the LMA region. Including this measurement with all solar neutrino experiments, yields the best fit parameters of $\Delta^2_{12} = 8.0 \times 10^{-5}\text{eV}^2$ and $\tan^2\theta_{12} = 0.45$ [19]. The 1, 2 and 3σ allowed parameter space is shown in Figure 1.3 (bottom figure). Since matter does not affect the KamLAND results significantly, agreement in the measured mixing parameters between the solar results (which account for the MSW effect when determining the mixing parameters) and these results requires that the survival probability of ^{8}B electron neutrinos is suppressed by the matter effect in the Sun.

1.4.4 Improved Measurement of Mixing Parameters

SNO's measurements of the solar ^{8}B neutrino flux have greatly constrained the allowed Δm^2 and θ_{12} parameter space. This can readily be seen in Figure 1.4 which shows the allowed mixing parameter space from all solar neutrino experiments before SNO's

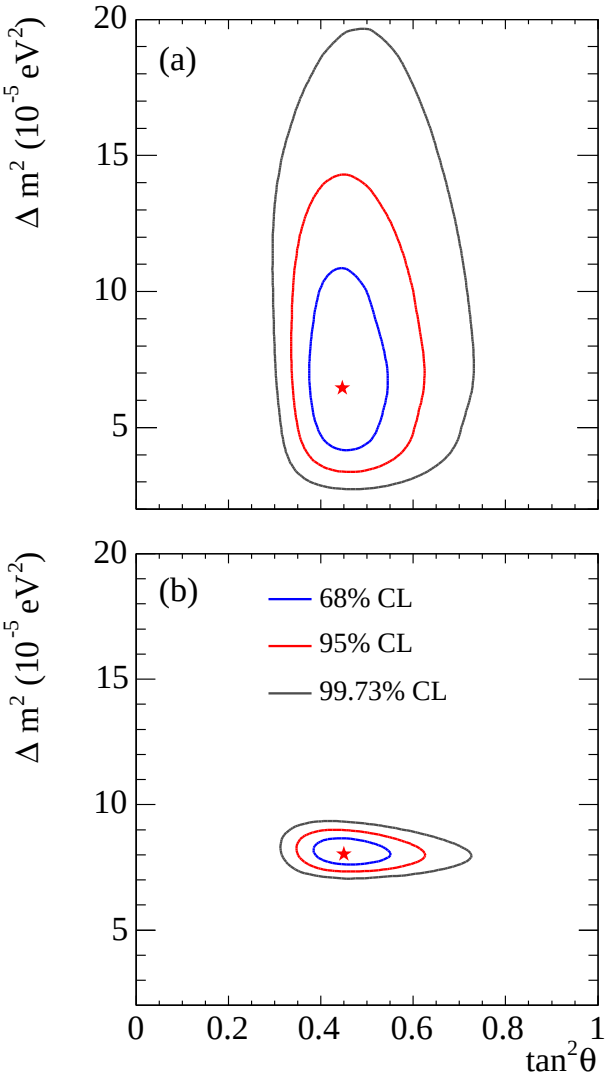

Fig. 1.3: Allowed regions in the Δm^2 -$\tan^2\theta$ plane for different confidence levels. Plot (a) uses results from SNO and other solar neutrino experiments. Plot (b) uses results from the solar experiments plus the KamLAND results. These contour plots were taken from [19].

measurements (compare to Figure 1.3 which is all solar experiments including SNO). A more precise measurement of the CC, ES and NC fluxes would further constrain the allowed parameter space. Additionally the KamLAND and SNO measurements are very complementary. Improvements in the KamLAND measurement constrain Δm^2 whereas SNO's measurements constrain θ_{12}.

To improve the measurement of the ^{8}B neutrino flux, this thesis has focused on lowering the energy threshold to increase the statistics and on improving the detector model to reduce systematic uncertainties. Data taken during the SNO pure D_2O and salt phases have been used jointly to further reduce the statistical uncertainties. Including these two phases and lowering the energy threshold to 4.0 MeV increases the number of NC events by roughly a factor of two over that for the salt phase only data set which used an threshold of 5.5 MeV (as in publication [19]). This low energy measurement of the ^{8}B flux has greater precision than any single phase measurement in SNO including that expected for the final NCD phase data.

1.5 Physics Potential of a Low Energy Spectrum Measurement

Although there is compelling evidence for the MSW effect in the Sun, there are several other possible theories describing the properties of solar neutrinos that are allowed using the current experimental data. The following section highlights the phenomenology and the experimental predictions.

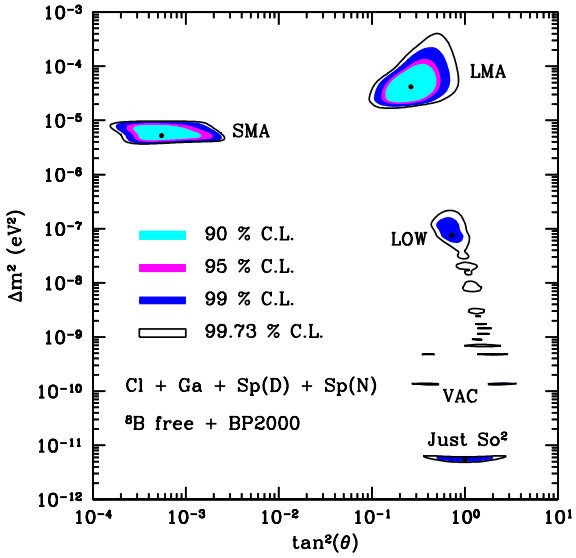

Fig. 1.4: Allowed regions in the Δm^2-$\tan^2\theta$ plane for different confidence levels pre-SNO's measurements. Figure taken from [30]

1.5.1 Non-Standard Interactions

In the Standard Model of particle physics, neutral current interactions are flavor conserving. The existence of flavor changing neutral current interactions could change the MSW resonance condition for solar neutrinos. As a result the energy dependence to the ν_e survival probability is slightly different compared to MSW effect with no non-standard interactions.

The inclusion of non-standard interactions adds to the MSW Hamiltonian of neutrinos in the Sun (Equation 1.8) the additional phenomenological term

$$H_{\mathrm{NSI}} = \sqrt{2} G_F N_f E \begin{pmatrix} 0 & \epsilon \\ \epsilon & \epsilon' \end{pmatrix} \tag{1.26}$$

where G_F is the Fermi constant, N_f is the density of fermions (compared to only electrons for the MSW effect) and E is the neutrino energy. The forward scattering

amplitude for the flavor changing neutral current process ($\nu_e + f \longrightarrow \nu_l + f$) is $\sqrt{2}G_F N_f \epsilon$ and the difference in the elastic forward scattering between $\nu_e + f$ and $\nu_l + f$ is $\sqrt{2}G_F N_f \epsilon'$. With the addition of this term to the Hamiltonian the MSW resonance condition is modified to

$$\Delta m^2 \cos 2\theta - \sqrt{2}G_F N_e E + \sqrt{2}G_F N_f \epsilon' E = 0. \tag{1.27}$$

(The ϵ term contributes to the numerator of of Equation 1.9.) Depending on the magnitude of ϵ', the ν_e survival probability has a different energy dependence relative to that given by the MSW resonance (Figure 1.5). As SNO's sensitivity range (approximately 6 MeV-20 MeV in this figure, which plots neutrino energy) is at the upper end of the survival probability transition, it is not the ideal experiment to measure spectral distortions. Yet, with an electron energy threshold of 4 MeV and with statistical and systematic uncertainties smaller than 15%, SNO can rule out some of the models shown in the figure. For further information on non-standard interactions and their effect on solar neutrinos see [31, 32].

1.5.2 Mass Varying Neutrinos

Mass varying neutrinos (MaVaNs) have been proposed as a means of coupling the density of dark energy to neutrino mass. Both are characterized by similar mass scales (the dark energy mass scale is $\approx (0.002\text{eV})^4$ whereas the neutrino mass-square difference is $\approx (0.01\text{eV})^2$) [33]. This is achieved by introducing a Yukawa coupling between a sterile neutrino and a light scalar field called an acceleron. As a result of this coupling, neutrino mass is dependent upon the local neutrino density and therefore need not be constant as a function of time. MaVaNs theories can be put

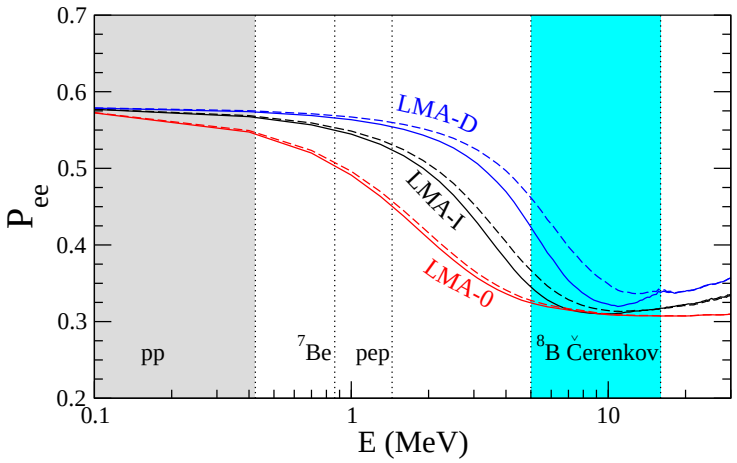

Fig. 1.5: Predicted solar ν_e survival probability for the standard MSW effect (LMA-I) and the MSW effect with non-standard interactions (LMA-D, LMA-0). The energy shown in the neutrino energy. Figure taken from [31].

to the test by studying solar neutrinos which are produced at very high neutrino densities. Effects of MaVaNs on the solar ν_e survival probability have been studied by [34,35] and indicate that the energy dependence of the ν_e survival probability can be radically changed from the MSW prediction (Figure 1.6) and still be consistent with current solar and KamLAND results.

1.5.3 SNO's CC Advantage

To search for spectral distortions in ^{8}B solar neutrinos, SNO's ability to measure the energy spectrum from the CC interaction is an advantage over experiments that only have sensitivity to the ES interaction. Figure 1.7 shows the response of mono-energetic 6 MeV neutrinos. The recoil electron for the ES interaction preserves very little information about the energy of the incident neutrino while for CC interaction, the recoil spectrum of mono-energetic neutrinos is peaked near the kinematic limit.

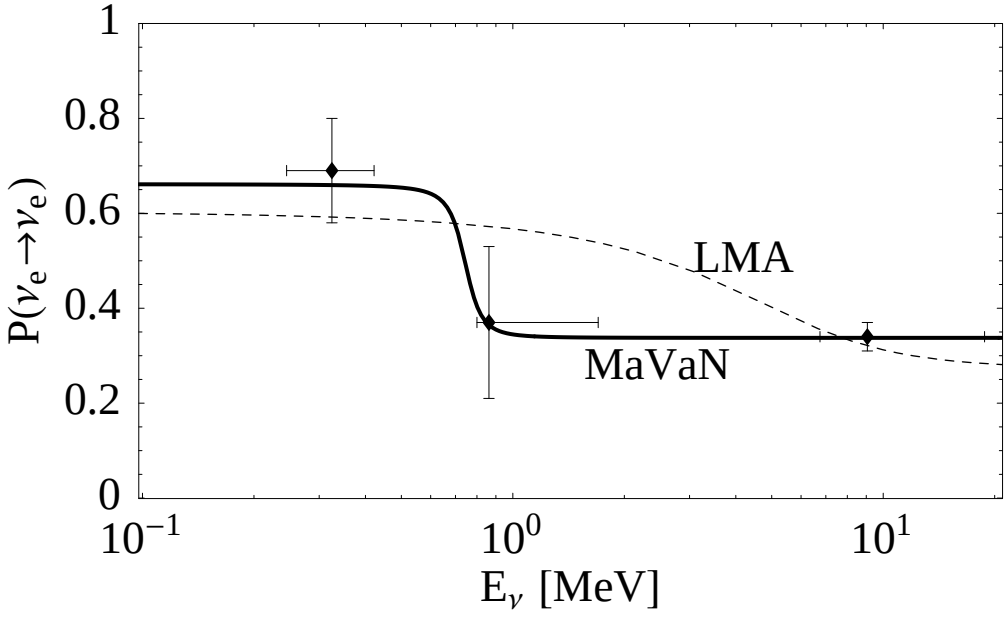

Fig. 1.6: Predicted solar ν_e survival probability for the MSW effect (LMA) and MaVaNs. Figure taken from [35]

As a consequence, the CC spectrum is more sensitive to distortions in the energy spectrum. Figure 1.8 shows the predicted MSW distortion in the ES recoil electron energy spectrum for two values of Δm^2 and $\tan^2\theta$ in the allowed LMA parameter space. Also shown is the ES recoil electron energy for the undistorted ^{8}B neutrino spectrum. Over the energy range of 4 to 20 MeV, a distortion of 10% or less is expected in the ES energy spectrum. In contrast, Figure 1.9 shows the CC energy spectrum for the same mixing parameters. For this interaction, distortions of up to $\pm$15% can be observed in the same electron energy range. Since spectral distortions become more prominent at lower energies, a low detector energy threshold is critical for this measurement.

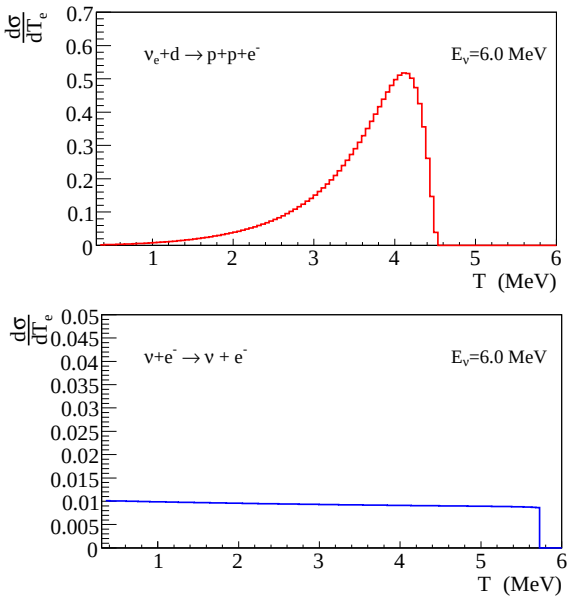

Fig. 1.7: Differential cross section of 6.0 MeV neutrinos for CC and ES interactions. Figure courtesy of J. Klein.

1.6 Summary

In recent years numerous breakthroughs in our understanding of the properties of neutrinos have been made, but an equal number of unanswered questions remain. For solar neutrinos, the MSW effect has shown to be a successful description of neutrino behavior in the Sun. This theory predicts that the survival probability of solar ν_es changes as a function the neutrino energy resulting in a distortion of the ^{8}B neutrino energy spectrum. SNO is in a unique position to search for spectral distortions with its measurement of the neutrino CC interactions. This interaction is more sensitive to energy distortions than to the ES interaction probed by H_2O Cherenkov detectors. Greater sensitivity to energy distortions requires a low detector energy threshold. The remainder of this thesis focuses on achieving that task.

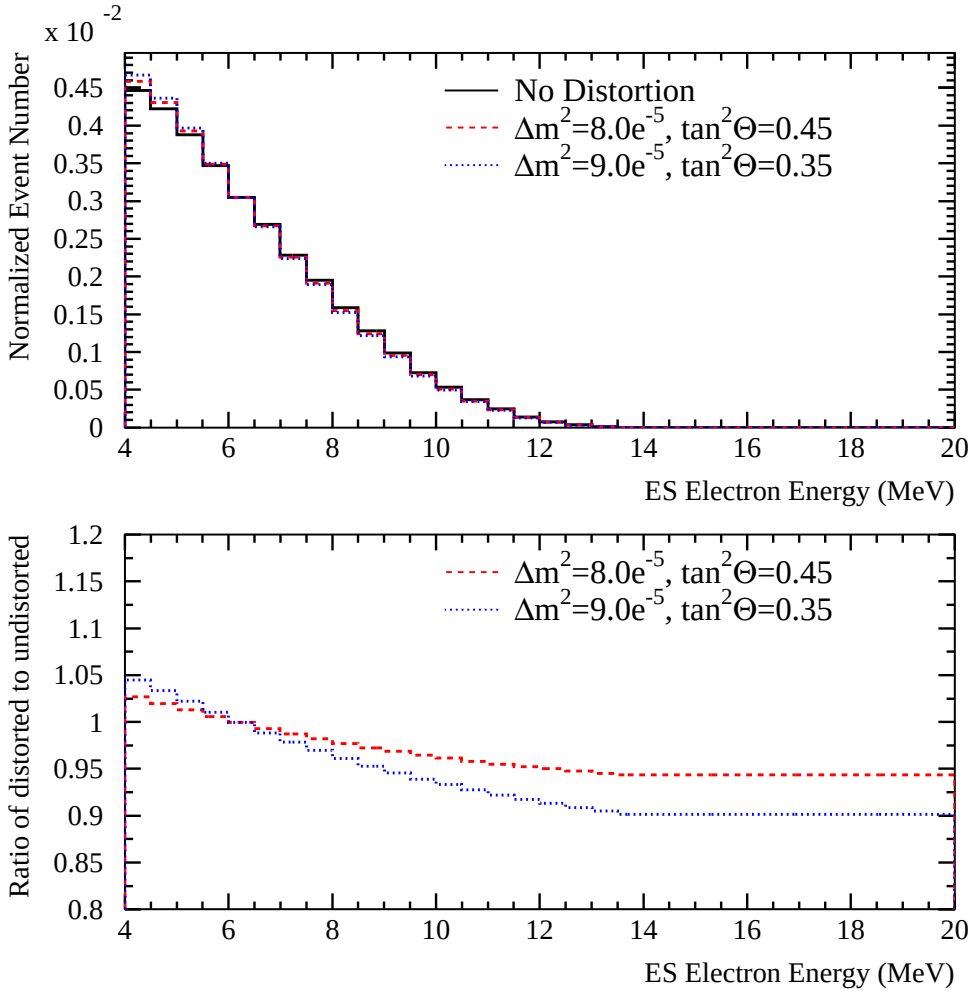

Fig. 1.8: Predicted MSW distortions in ES recoil electron energy spectrum for different values of the mixing parameters. Bottom figure is the ratio of the MSW distorted spectra to the undistorted spectrum. Note that electron energies ranging from 14 to 20 MeV are included as a single bin in this figure.

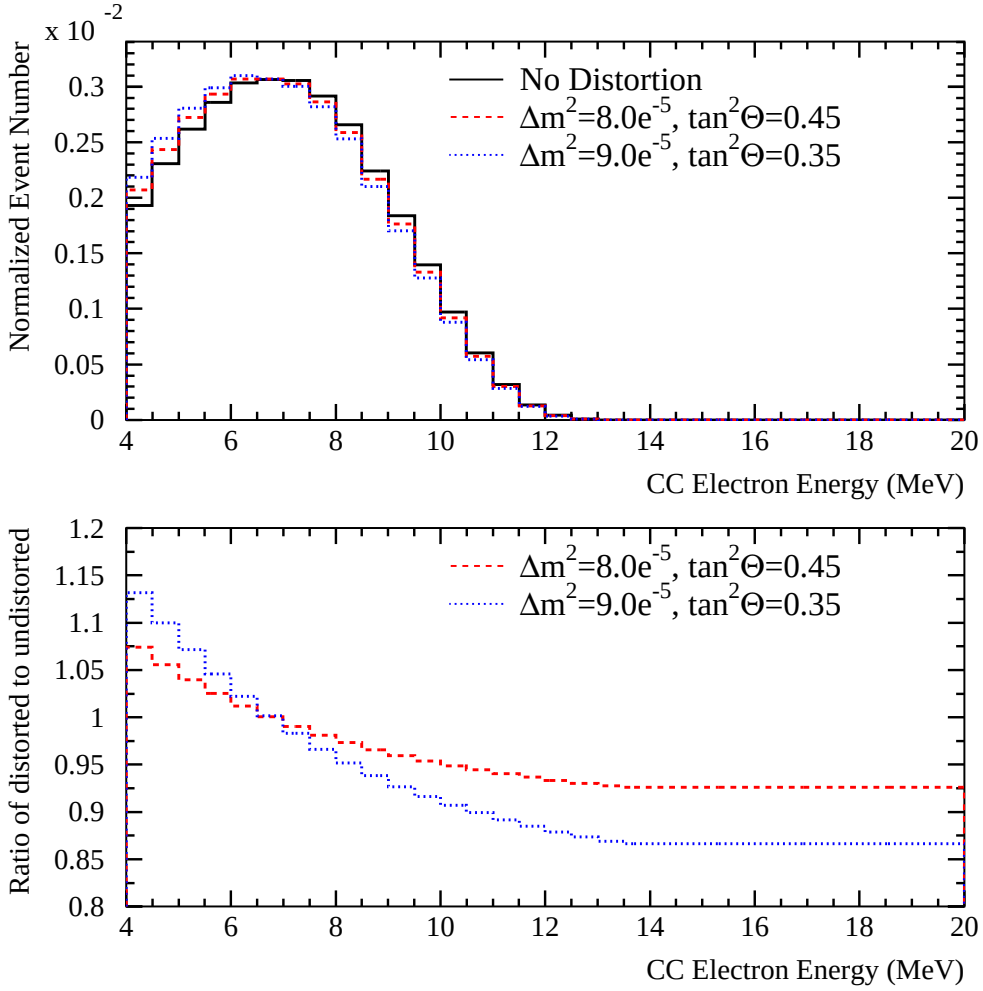

Fig. 1.9: Predicted MSW distortions in CC recoil electron energy spectrum for different values of the mixing parameters. Bottom figure is the ratio of the MSW distorted spectra to the undistorted spectrum. Note that electron energies ranging from 14 to 20 MeV are included as a single bin in this figure.

Ch. 2

The SNO Detector and PMT Electronics

The Sudbury Neutrino Observatory is located near Sudbury, Ontario, a lovely place to spend the winter. Sited on the 6800 ft level of INCO's Creighton mine, the rock overburden is 6010 $\pm$ 20 meters of water equivalent, which results in only 70 cosmic ray muons passing through SNO's volume per day.

As seen in the schematic drawing of the detector (Figure 2.1), the SNO detector consists of two almost concentric spheres. The innermost sphere is a 12 meter diameter acrylic vessel (AV), 5.5 cm in wall thickness, which houses a target mass of 1000 tonnes of D_2O . The 1.5 meter diameter neck at the top of the AV allows us to deploy sources into the D_2O for calibration. The 18 meter diameter outer sphere or PMT Support Structure (PSUP) houses 9438 photo-multiplier tubes (PMTs) that face the D_2O target. With the PMTs alone, the photo-cathode coverage is 31%. Each PMT is surrounded by a 27 cm diameter light concentrator which increases the overall detector light collection to 54%. In addition to the inward facing tubes, there are 91 outward

looking (OWL) tubes. The OWL PMTs point towards the outer H_2O volume and are used as a tag for cosmic ray muons. An inner ultra-pure H_2O volume of 1700 tonnes between the AV and PSUP shields the D_2O target volume from radioactivity in the PSUP and PMTs. Outside the PSUP, 5300 tonnes of H_2O fills the remainder of the cavity and also acts as a shield of radioactivity from the cavity walls. More details of the construction of the SNO detector can be found in [36]. The remainder of this chapter discusses the PMT electronics, calibration systems and simulation software that have the most relevance to lowering the energy threshold for measurement of the ^{8}B neutrino energy spectrum.

The following section is an overview of the general flow of the electronics system followed by an outline detailing the specifics of each type of electronics board in the system. Section 2.2 will focus on the SNO trigger system. Extensive details of the SNO electronics and trigger can be found in [37], [38] and [39]. Section 2.3 is an overview of the calibration hardware used to deploy calibration sources in the detector [36]. Section 2.4 is a brief over of the SNO detector simulation and MC (SNOMAN), see [40] for further information.

2.1 PMT Electronic System

In order to process and record information from roughly 9500 PMTs, an extensive electronics system was designed, primarily by physicists at the University of Pennsylvania. The Cherenkov light from events in SNO is detected by 9438 PMTs. The PMT signals of detected photons travel via 32 meters of 75Ω RG59-like waterproof coaxial cable from the base of the PMT to the front-end electronics. These electronics determine if the PMT signal is above threshold and if so produce multiple trigger signals

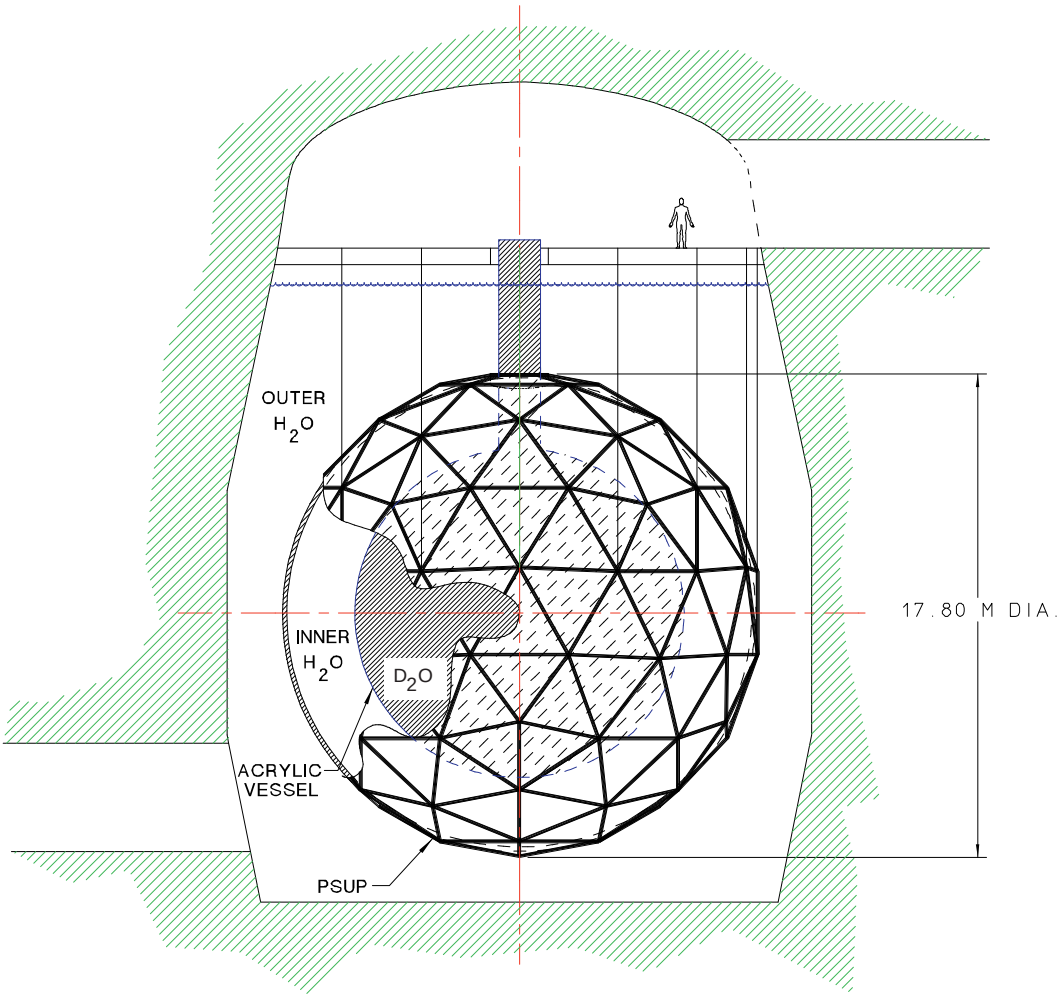

Fig. 2.1: Overview drawing of the SNO detector. Taken from [36]

to be summed over all electronic channels. If enough PMTs have fired in coincidence, a global trigger is initiated which instructs the front-end electronics to digitize the integrated charge and time of firing of all hit PMTs. This digitized PMT information is read out from the front-end electronics by the Data Acquisition System (DAQ) to be stored on disk.

The front-end electronics consist of 19 crates each with 512 channels in 16 boards of 32 channels. The PMT cables are assembled onto a paddle card in groups of eight. Four paddle cards (32 channels) are connected to the Photomultiplier Tube Interface Card (PMTIC), which provides HV to the PMTs. There are 16 PMTICs in a single crate. Once the HV has been subtracted from the PMT signal, the signal is delivered to one of 16 Motherboards, which are directly interfaced with the PMTICs. There are four daughterboards connected to each motherboard. On each daughterboard, custom ASICs determine if the PMT signal is above threshold. When the signal crosses threshold, four main trigger signals are produced: long and short time coincidence trigger pulses and high and low gain charge trigger pulses. These four trigger types are continuously summed for the entire crate at the Crate Trigger Card (CTC). The crate summed trigger signals for all crates are sent to an analog master trigger card (MTC/A), to determine the detector-wide trigger sum. If the detector-wide trigger sum is above the threshold set on the MTC/A by the DAQ, this information is communicated to the digital master trigger card (MTC/D). The MTC/D determines if the trigger that crossed threshold has been masked in by the DAQ and if so initiates the global trigger (GT) which is communicated back to all crates via the CTC.

Once the front-end electronics receives the GT, the integrated charge and time of firing for the hit PMTs, calculated by custom ASICs on the daughterboard, are digitized and stored to on-board memory located on the motherboard. To read out the

PMT information on the motherboard's memory, the DAQ communicates with the front-end electronics via a pair of translator cards (XL1 and XL2). The XL1 interprets DAQ commands sent via a VME board and relays those commands to XL2, located in each crate. The XL2 acquires the PMT information from the motherboards and sends that information to the DAQ via the XL1.

More specifics on the boards discussed here are given below, grouped under the headings PMT electronics for boards providing high voltage to the PMTs, front-end electronics for boards processing the PMT signals, and timing rack electronics for boards involved in the trigger and global control.

- **The PMT Electronics**
  - **PMT Interface Card (PMTIC):** Provides the high voltage power to the PMT and receives the PMT signal (the signal and high voltage are transported on the same cable to the PMT). There are four high voltage relays on the PMTIC, one for each paddle card, each controlling the high voltage to eight PMTs. The PMTs on each paddle card are matched to have the same gain.
  - **PMT Paddle Card:** Provides electrical connection for the PMT cable to the PMTIC. Eight PMT cables are connected to a paddle card and 4 paddle cards are connected to a single PMTIC.
  - **High Voltage Backplane (HVBP):** Provides high voltage power to the PMTIC. It is also used in the transport of the clock signals used to disable and enable the HV relays on the PMTIC.
- **The Front-end Electronics**

– **Daughterboard (DB):** There are four daughterboards per motherboard, each processing signals from eight PMTs. The signal lines from the mother board are sent to fast discriminator chips (SNOD) (four channels per SNOD), which determine whether the PMT signal is above threshold. The PMT signal is also split into high and low gain versions with an approximate ratio of 1:16 between the two gains and sent to an integrator chip (SNOINT). The SNOINT integrates the high and low gain signals using high-quality external capacitors for the integration. There are two integration times, a short integration of about 35 nanoseconds and a long integration of roughly 100 ns. Another custom ASIC, the QUSN7 or 'CMOS' chip calculates the time of firing of the PMT using a time-to-amplitude converter (TAC). When the discriminator fires, the CMOS TAC starts ramping down. It is stopped when a global trigger is received. If no global trigger is received after an internal timeout period, the TAC is reset. The CMOS chip also has internal analog memory that can store up to 16 samples of the low and high gain charge information from the SNOINT. Further, when the discriminator fires, the CMOS chip produces a short coincidence (20 ns) and a long coincidence (100 ns) trigger pulse used in the trigger decision process.

– **FEC32 Motherboard (MB):** Directly connected to the PMTIC, the board receives the signals from the 32 PMTs connected to the PMTIC and sends the signal to the daughterboards to be processed by custom ASICs, which digitize the PMT charge and timing information. The mother board has 4 M-Bytes of RAM to store the digitized information. This memory

capacity is rarely filled during normal data taking but is designed to store up to one million events during a burst of events from a supernova.

  - **Crate Trigger Card (CTC):** Collects and sums the trigger signals from the FECs in a crate and sends the summed trigger signals to the MTC/A. More detail on this board is given in Section 3.1.1.
  - **XL2:** This board is a translator board that communicates with its counterpart the XL1 in the timing rack. The XL2 sends and receives the digital data and address lines to and from the XL1. It converts the signals to GTL (Gunning Transceiver Logic) which is the logic used on the low voltage backplane. The XL2 communicates commands from the DAQ to the MBs and DBs.
  - **Low Voltage Backplane (LVBP):** Provides the low voltage power to the mother board, CTC and XL2. This board transports the digital data and address lines between the mother boards and XL2 as well as the analog trigger lines from the mother boards to the CTC. More detail on this board and recent upgrades can be found in Section 4.1.

- **The Timing Rack Electronics**
  - **Master Trigger Card, Analog (MTC/A):** Collects the trigger signals of a given type from each of the 19 CTCs and sums the signals together. Once the trigger signal is summed, a comparator tests if the summed trigger is above threshold. If threshold has been crossed, the MTC/A sends as 'raw' trigger to the MTC/D. For further details, see the following section.

- **Master Trigger Card, Digital (MTC/D):** Upon receiving a raw trigger from an MTC/A, the MTC/D sends a global trigger (GT) to all crates if the raw trigger from the MTC/A is active. The MTC/D also records which triggers fired during this event and the time that the event occurred. For more information, see the following section.
- **XL1:** The counterpart to the XL2, the XL1 is the communication link between the DAQ and the front-end electronics. The XL1, upon receiving commands from the DAQ via a VME interface, forwards those commands to the crate's XL2. The XL1 also sends and receives the digital data and address lines to and from the XL2 and converts that information into a form appropriate for VME logic to be passed to the DAQ during readout.
- **Analog Measurement Board (AMB):** Digitizes the peak value, the integral and the derivative of the ESumHi trigger for each events. (Explanation of the trigger signals can be found in Section 3.1.1).

2.2 Trigger System

The design goal of any trigger system is straightforward: determine which events in the detector are of interest and inform the DAQ to store those events to disk. The SNO trigger system is an analog system, which has the advantage of being fast, asynchronous, and unlike a digital counterpart, is not governed by a clock time. The disadvantage of an analog system is sensitivity to noise. In this system a synchronous noise of $20\mu V$ on each channel is equivalent to 100 tubes firing. Thus a low noise environment in the trigger electronics is essential to the trigger stability.

The SNO trigger system was designed with several possible types of triggers;

triggers based on the number of PMTs that fire within a given time window, triggers based on the total amount of charge deposited in the PMTs, software triggers and external triggers. A brief summary of each trigger is listed below.

- N_{Hit} **Based Triggers**
  - **N100:** Upon the discriminator firing, each channel produces a square trigger pulse with a width of 93 ns and a rise time of 2.5 ns. All channels in the detector are continuously summed to determine if threshold is crossed. This is SNO's main physics trigger type. For the D_2O and salt phases, 16 hit PMTs within a 100 ns coincidence were required for a detector global trigger.
  - **N20:** Similar to the N100 except that the pulse width is 20 ns. The N20 on each channel can be delayed so that the 'focus' of the N20 can be moved around the detector. The N20 is designed to be a low energy background trigger but due pick-up within the CMOS chip, the threshold for the D_2O and salt phases was the same as the N100 trigger of 16 hits.
  - **OwlN:** Same as the N100 except for the OWL tubes. The OWL triggers are kept separate from the inward channels and serve as a tag for muons.
- **Charge Based Triggers**
  - **ESumHi:** For each PMT, an shaped analog copy of each pulse is produced. The pulses for all tubes are summed together to provide a trigger based on the amount of charge deposited in the detector. Since the shape of the pulse is not sharp in time like the N100, the ESumHi is too slow of a

trigger for physics but is useful for diagnostics of instrumental, non-physics backgrounds.

  - **ESumLo:** A low gain version of the ESumHi
  - **OwlEHi:** Same as the EsumHi but for the OWL tubes. Again, the OWL triggers are kept separate from the inward PMTs triggers.
  - **OwlELo:** A low gain version of the OwlEHi.

- **Fixed Interval, Software and External Triggers**

  - **Pulsed Global Trigger (PGT):** A pulser generated calibration trigger, PGT triggers the detector at a rate of 5 Hz. This trigger is used to measure the PMT noise hits in the detector.
  - **Software Global Trigger:** Software initiated trigger, currently only used to mark the beginning and end of a run.
  - **External Triggers:** The trigger system can handle up to eight external triggers. These triggers are often used to trigger on events from a tagged calibration source for example.
  - **Asynchronous External Trigger:** One of the external triggers, this trigger creates a global trigger without waiting to be latched by the 50 MHz clock (see below for more explanation). Used to trigger on laser events.

When a PMT's discriminator fires, four trigger pulses are produced: the N100 pulse, which is square pulse of 93 ns in width and approximately 30 mV in amplitude, an N20 pulse, which is a square pulse of 20 ns in width and approximately 30 mV in height, an ESumHi pulse which is proportional to the amount of charge in the PMT

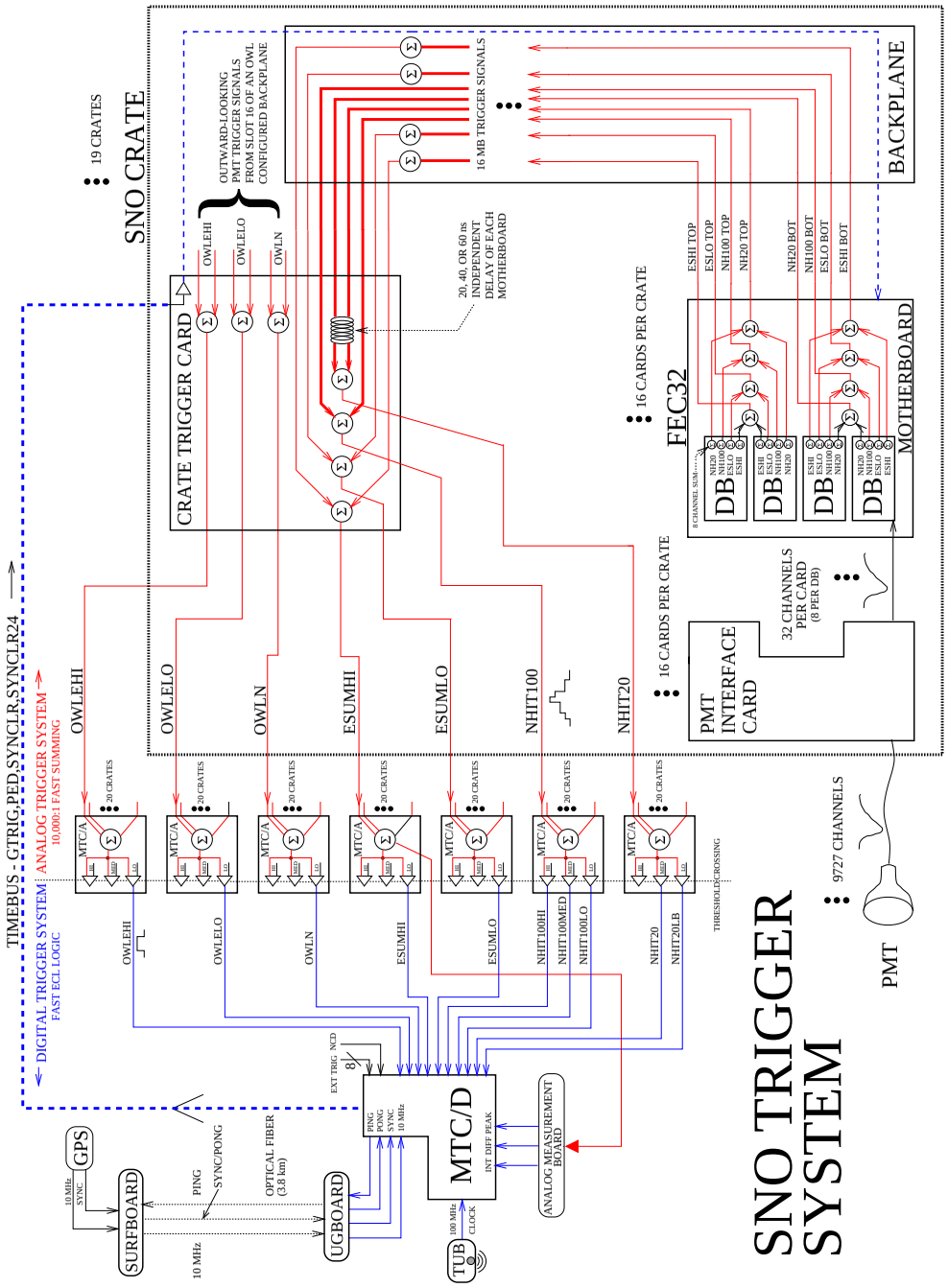

Fig. 2.2: Overview diagram of the SNO trigger system. Taken from [38]

and an ESumLo pulse, which is a low gain version of the ESumHi. As outlined in Figure 2.2, the N100 pulses for the eight channels on the DB are summed together and sent to the MB. On the MB, the DB summed N100 signals are summed again in two groups, the bottom group is a sum of DB 0 and 1 and the top group is a sum of DB 2 and 3. The N100Top and N100Bot sums for each MB are sent along the low voltage backplane to the CTC. Since the trigger system is analog, it is important not to introduce slot dependent path delays to the N100 signals. As slot 15 is directly next to the CTC in physical crate space, the path of its N100Top and N100Bot traces along the LVBP is shorter than the path for slot 0. To compensate for the differences in path length along the backplane, additional delay traces are added on the CTC so that all N100 signals are in time for the final summing. The final crate-wide sum occurs on the CTC, where the N100Top traces for all 16 slots are first summed together (similarly with the N100Bot) and then summed with the N100Bot. The crate summed N100 is sent to the N100 MTC/A located in the timing rack.

The summing of the N20 signals is done in the same fashion as the N100 up until the final CTC summing. Upon the PMT's discriminator firing, the CMOS chip can be programmed to delay the production of the N20 pulse by 0 to 20 ns. Additional delay of the N20Top and N20Bot sums is possible by diverting the summed signals through one of the following delays: no delay length, 20 ns, 40 ns or 60 ns of delay length. If the CMOS and CTC delays are set to zero for all channels, the N20 trigger focuses on the center of the detector, since light produced in the detector's center has an equal distance to travel to the PMTs in all directions. Events that take place off center are closer to one side of the PSUP, therefore light traveling long path lengths across the detector is no longer within a 20 ns coincidence with light that travels a short distance to the PSUP. As the N20 signal for each channel can be delayed, it is

possible to move the focus point of the N20 trigger, so that light from events near the PSUP, for example, are within a 20 ns coincidence. The motivation for this is to give us the ability to focus on background regions of interest and gain low trigger threshold data in these regions. Unfortunately the potential of the N20 trigger in the D_2O and salt phases was never utilized for two main reasons. First, due to an initialization problem with the DAQ, the N20 delays on the CTC were being set to random values, making the N20 'focus' unknown. This problem has been fixed for the NCD phase. Second, due to noise induced onto the N20Top and N20Bot signals on the LVBP it was not possible to set the N20 trigger threshold lower than the N100 trigger threshold making the N20 trigger redundant. In Chapter 4, we discuss improvements that have been made to the LVBP in order to lower the N20 trigger threshold for the NCD phase.

Since the bandwidth of the ESumHi and ESumLo trigger pulses is significantly lower than the N100 and N20 signals, they can be handled with less care. Similar to the N100 and N20 signals, the ESumHi signals from all PMTs on the DB are summed together and on the MB, DBs 0 and 1 are summed (ESumHi Top) and DBs 2 and 3 are summed (ESumHi Bot). The ESumHi Top and ESumHi Bot for each slot are then summed together on the LVBP and sent to the CTC. Since the rise time of the ESumHi pulses are gradual compared to the N100 and N20 pulses, differences in time due to path length along the LVBP are negligible. Once at the CTC, the two ESumHi signals are summed in a final sum and sent to the ESumHi MTC/A. The ESumLo signals are handled in exactly the same fashion and sent to the ESumLo MTC/A.

To save information about the shape of the ESumHi sum that can later be used to tag instrumental events (see Appendix B.2), a copy of the summed ESumHi signal is sent to the analog measurement board (AMB). A straightforward design, the AMB

receives two input signals, the ESumHi analog sum and the raw trigger pulse from the MTC/D. The raw trigger signal from the MTC/D is used to define the time at which the ESumHi trigger signal crossed threshold. The analog ESumHi sum is first inverted and the derivative, integral and peak are determined. To take the derivative of the ESumHi, a differentiating op-amp circuit is used and the output is then sent to a 8-bit flash analog digital converter (ADC). To find the peak and integral, the analog sum is routed through a delay cable so that the gate that commences the integrating and peak finding opens approximately 70 ns before the signal crossed threshold. The integral of the analog sum is taken over a 200 ns period, approximately 70 ns before to 130 ns after threshold crossing. The integration is done with an integrating op-amp circuit and digitized with an 8-bit flash ADC. Using a transistor followed by a diode in an op-amp feedback loop, the peak circuit is designed to follow the signal until it reaches a maximum and hold that voltage until the end of the 200 ns integration period. This signal is then inverted before being sent to an 8-bit flash ADC. The digitization and readout of this ADC is controlled by two 40 ns TTL pulses separated by a few nanoseconds generated from the raw trigger. Modifications made to the original AMB design are listed in Appendix B.2.4. These measurements of the ESumHi signal are a critical component of the analysis cuts used to remove non-physics events from the data set.

The triggers from the OWL tubes are handled separately from the triggers of the inward tubes. The electronics of the OWL tubes is exactly the same as the inward tubes' electronics. This was done so that mother boards and daughterboards could be switched into any slot in a crate. In order to separate the OWL N100, EsumHi and ESumLo trigger from the inward triggers, the LVBP has jumpers that disconnect the triggers from Slot 15 from the normal trigger sums and divert them to an OWL

trigger sum on the CTC. For the OWL crates, the N100, ESumHi and ESumLo top and bottom sums are sent via a separate path on the LVBP to the OwlN, OwlEHi, and OwlELo summing nodes on the CTC. The OWL N20 is not used for a trigger. On the CTC, the top and bottom OwlN, OwlEHi, and OwlELo are summed and sent to their respective MTC/A.

There are seven MTC/As, one for each trigger type outlined above. To sum the individual crate signals into a final detector wide trigger sum, the trigger signal from each crate is terminated and sent to one of four summing nodes, which sums the trigger signals for five crates. As the trigger system is a current based analog system, high occupancy events result in large amounts of current. To protect the summing transistors from large amounts of current a diode clamp limits the current to two crates equivalent. The sums of each node are then summed by a final summing node. The total detector wide sum is offset by 5 Volts in order to maximize the dynamic range of the threshold comparator, which is ± 5 Volts. The final trigger sum is copied into three signals and sent to low, medium and high threshold comparators, the thresholds of which are set by the DAQ. If a trigger sum passes a comparator's threshold a raw trigger pulse is generated and sent to the MTC/D.

The MTC/D receives as input the raw triggers from the low, medium and high comparators of each MTC/A. Upon receiving a raw trigger, the MTC/D determines if the firing trigger is masked in by the DAQ. If it is not masked in, the MTC/D takes no action. If it is masked in, the MTC/D sends a global trigger (GT) to all crates on the next rising edge of the 50 MHz clock. Synchronizing the GT with the clock allows the time of the trigger to be known. In addition to the 50 MHz clock, the time from a commercial GPS 10 MHz clock is also recorded. The MTC/D also records the state of all raw triggers at the time of the GT. After sending a GT, the MTC/D locks

out, forbidding additional global triggers for 440 ns. This allows for light reflecting off the PMTs, which has a long path length, to be included in the event.

The SNO trigger system has performed extremely well. For the main physics trigger, the N100M, the trigger threshold is 16 hits with 100% trigger efficiency at 25 hits or T=4.0 MeV[1].

2.3 Calibration Systems

Calibration of the SNO detector is essential in understanding both signal and background events. Necessary calibrations consist of electronic calibrations which determine the basic charge and timing information of the PMTs and front-end electronics and source calibrations which determine the detector's response to signal and background events. The calibration system designed for SNO is very flexible, allowing for multiple sources spanning an energy range of 20 MeV and multiple positions both inside and outside the D_2O volume. The following section highlights the features of this system.

2.3.1 Electronic Calibrations

For the calibration of the SNO electronics there are two necessary calibrations:

- **Electronic Calibration (ECA):** There are two sets of ECA runs, the pedestal run that calculates the pedestal value of the charge ADCs and the time slope run that calculates the slope of the CMOS TAC. To determine the pedestal values and TAC slopes, the DAQ sends a programmed pulse to the channel

[1]For a further discussion see Section 4.1.1

causing its discriminator to fire. This pulse is followed at a fixed delay by a global trigger. The time slope is measured by varying the delay between the programmed pulse and the global trigger. Since the pedestal values and TAC slope can change over time these calibration runs are done on a bi-weekly basis for the pedestal measurement and a bi-monthly basis for the TAC measurement. Taking solar neutrino data is not possible during these runs although the HV is left on. More on the ECA calibration can be found in [41].

- **PMT Calibration (PCA):** The PMT discriminator fires when the leading edge of the pulse crosses a given voltage threshold. The firing time depends on the rise time of the pulse. To remove timing differences due to this "discriminator walk", an isotropic laserball source is deployed to measure the relationship between charge deposit and discriminator firing time. The PCA laserball run is done on a monthly basis. For more details on this calibration see [42].

2.3.2 Detector Calibrations

To measure the overall PMT collection efficiency, the PMT and concentrator angular response, the optical attenuations, energy response as a function of detector position and detector acceptance of low energy backgrounds, SNO utilizes several different calibration sources. As seen in Figure 2.3, the SNO calibration system has the capability of deploying sources along the central z-axis but also in the x-z and y-z planes with an accuracy of within 2 cm. It is also possible to deploy sources outside of the acrylic vessel using several guide tubes as indicated in the figure.

Several sources are used for calibration of the SNO detector.

- **Laserball** [43] A triggered, isotropic, multi-wavelength laser source used to

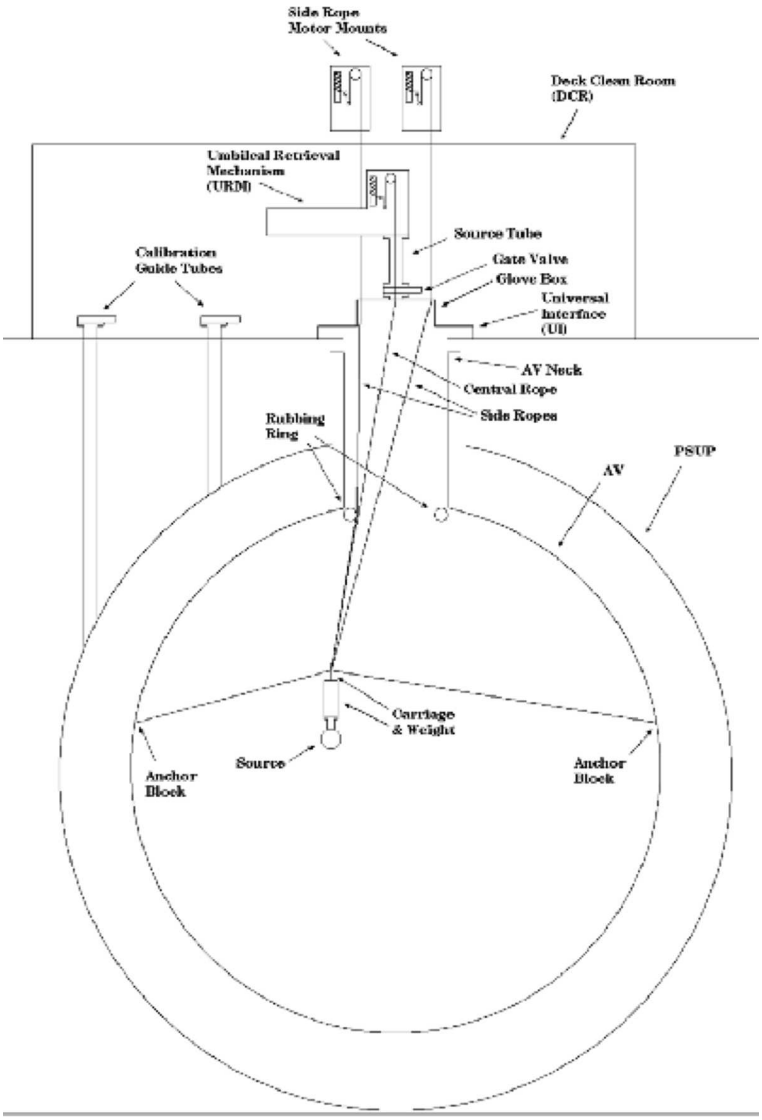

Fig. 2.3: Overview drawing of the SNO calibration system.

measure PMT timing, media attenuations, PMT angular response and PMT-to-PMT efficiency variations.

- ^{16}N [44]: A triggered source and the main calibration source used to measure the overall collection efficiency, energy systematic uncertainties such as position-to-position uncertainties and time variations in energy. It is a 6.13 MeV γ source from the de-excitation of the ^{16}O resulting from the β decay of ^{16}N.

- ^{8}Li [45]: A triggered β source with an endpoint of 14 MeV, from the β decay of ^{8}Li. This source is used to confirm the energy systematics uncertainties derived from ^{16}N as well as to determine energy scale non-linearities.

- **pT** [46]: A non-triggered source which collides protons on a ^{3}H target producing ^{4}He which through de-excitation produces a 19.8 MeV γ. This was not deployed in the salt phase due to copious production of neutrons. This source is used to determine the energy scale non-linearities at very high energies.

- ^{252}Cf**:** A non-triggered neutron source from the fission of ^{252}Cf. This source is used to determine the neutron capture efficiency in SNO.

- **AmBe:** A "triggered" source with a 4.14 MeV γ and neutron in coincidence. The source is triggered by requiring this coincidence and is used for measurements of the neutron capture efficiency. This source was not deployed in the D_2O phase.

- **Acrylic Sources,** ^{238}U **and** ^{232}Th [47]: Source of either ^{238}U or ^{232}Th encapsulated in acrylic, used to measure the detector's acceptance of low energy backgrounds. These sources can either be canned (acrylic is surrounded by plastic

which prevents the β from producing light in the detector) or uncanned. None of the sources are triggered but are made very hot such that they overwhelm the nominal amounts of radioactivity.

- **Radon Spike** [48] A controlled injection of Rn either into the D_2O or H_2O water systems. This source is an excellent isotropic source used to measure the detector's response to low energy backgrounds. The source is untriggered but again very hot as to overwhelm the nominal amount of detector radioactivity.

2.4 Detector Simulation Software

The processing of PMT information from the SNO electronics and the Monte Carlo (MC) simulation are handled using the SNO Monte Carlo and ANalysis software (SNOMAN) [40] which is a package of Fortran routines using a CERNLIB ZEBRA memory management data structure [49]. The SNOMAN code applies the necessary electronics calibrations to the PMT data utilizing the SNO database (SNODB) [50] which is based upon the CERNLIB HEPDB software package [51]. The user can access the data and MC output via PAW ntuples [52] or ROOT trees [53].

For the MC simulation, electron and gamma propagation is handled by the EGS4 (Electron Gamma Shower code) simulation [54] which is called internally in SNOMAN. The number of Cherenkov photons emitted from a charged track is determined from the asymptotic formula for light yield for each track segment in EGS [55], [56]. Neutron propagation up to 20 MeV is modeled using the MCNP code (**M**onte **C**arlo **N-P**article Transport Code System) [57]. SNOMAN is capable of simulating all relevant interactions in SNO including neutrino interactions, electrons, gammas, all the

calibration sources described in 2.3.2, low energy decays from the ^{238}U and ^{232}Th chains and atmospheric and cosmic muons. Additionally the simulation models all significant detector geometries, such as the AV, the acrylic tiles, the acrylic belly plates and grooves, the Kevlar ropes, the neck, the PSUP and the source container if deployed.

The angular response of the PMTs, which is the PMT's efficiency of photon detection as a function of the photon's angle of incidence and wavelength is modeled within SNOMAN in two ways. The first is a detailed simulation of photon propagation in the phototube [55] (called 3d-PMT). This model propagates individual photons through a PMT and concentrator model, simulating reflections from the glass and concentrator, and the photo-cathode response. The 3d-PMT model is the model used by the MC simulation. A second model (called Grey Disk) is a phenomenological model of the PMT angular response. The angular response in this model is derived from laserball measurements. Grey Disk is used by the energy estimators (see Chapter 5) to quickly determine the angular response. The PMT angular response in these two models agrees very well as detailed in [58].

Simulation of the PMT electronics includes modeling of the PMT discriminator, accounting for such effects as the summation of multiple photons to create a single hit and individual channel variations in the discriminator thresholds [59], [60]. A full simulation of the SNO trigger system is modeled, including both the N_{Hit} based and ESum triggers. SNOMAN also contains the position and direction reconstruction and energy reconstruction algorithms used to estimate the location, direction and energy of both data and MC events in SNO.

Ch. 3

Limitations Affecting the Analysis Energy Threshold

There are several major factors that define SNO's analysis energy threshold. First, the PMT channel thresholds place physical limits on the photon collection efficiency of the Cherenkov light and the system trigger threshold cuts low energy events. Second, low energy background events from the ^{238}U and ^{232}Th decay chains can contaminate the solar spectrum at low energies. Above electron kinetic energies of 5.5 MeV, the number of low energy background events that leak into the signal region is small but the number of low energy decays rises steeply with lower energy. As a result the energy resolution directly affects the number of background events in the signal region. This chapter discusses both of these limitations in detail, while Chapter 4 discusses several improvements that were made to the hardware and energy reconstruction that resulted in a lower analysis energy threshold.

3.1 Limitations from Hardware

The SNO electronics limits the acceptance of low energy events by having a defined trigger threshold and by the PMTs' efficiency for detecting photons. To maximize the detector acceptance, SNO's trigger system was designed to be close to 100% efficient even at electron energies of 4.0 MeV. The following section discusses a few shortcomings of the very successful trigger system. Additionally the PMT discriminator thresholds limit the efficiency of detecting photons affecting the detector's acceptance. Also discussed in this section are the contributing factors which set the channel thresholds.

3.1.1 The System Trigger Threshold

While the SNO trigger system discussed in Section 2.2 is 100% efficient at 4.0 MeV, improving the trigger acceptance at lower energies requires lowering the threshold of the main physics trigger, the N100M. The salt phase N100M threshold of 16 hits was necessary to maintain detector stability. When the trigger threshold is lowered, pick-up from the front-end electronics can lead to large increases in event rate, swamping the read-out system. A second source of trigger instability is N100 and N20 drop-out. Due to a design oversight in the CMOS ASIC chip, a runt pulse from the discriminator can cause the CMOS chip to produce a N100 or N20 pulse that stays low for many microseconds. This 'dropped-out' channel will not be reset until the next firing of the channel's discriminator. All channels experience drop-out, although some channels are worse than others. The net effect of individual channel drop-out is that the trigger threshold effectively fluctuates between 14 to 16 hits depending on how many channels are dropped out for a given period of time. As a result, the detector becomes

unstable due to front-end pick-up around 12 hits and the N100 threshold must be set much higher to avoid drop-out pushing the trigger threshold into the unstable region. Section 4.1 discusses hardware improvements that have allowed us to lower our main trigger thresholds.

3.1.2 The PMT Thresholds

In addition to the system trigger thresholds, the individual PMT discriminator thresholds affect the detector's efficiency of photon detection. Ideally, the discriminator is set at a quarter of a photo-electron (p.e.). In practice, the noise environment of the front-end electronics forces the discriminator threshold to be set slightly higher. The PMT discriminators are most sensitive to pick-up during readout by the XL2. This pick-up is especially dangerous since multiple channels can experience readout induced pick-up simultaneously resulting in non-physics event triggers. To avoid setting the channel discriminator thresholds in a pick-up sensitive region, a DAQ algorithm is used to optimize the discriminator threshold for each channel. This algorithm determines the channel thresholds by forcing the channel to fire 1000 times. After these firings, the noise rate on the channel is counted. The channel is then readout and the noise rate counted again. Since readout induces pick-up on the channel, the channel discriminator is raised until the noise rate when the channel is being readout is equal to the noise rate when the channel is not being accessed.

Higher discriminator thresholds results in fewer detected photons. This degrades the detector's response, worsening the energy resolution and the signal and background separation. Section 4.1 discusses electronic improvements designed to reduce this pick-up sensitivity and lower discriminator thresholds.

3.2 Limitations from Low Energy Backgrounds

SNO's analysis energy threshold is set so that the number of β-γ events (low energy decays in the ^{238}U and ^{232}Th chains) in the signal region is small (less than 5% of the total solar neutrino signal). Cherenkov light from β-γ events is difficult to distinguish from that for the neutrino signal as the recoil electrons from low energy signal events tend to multiple scatter more. Although the low energy background energy spectrum falls off very quickly with energy, there can be a significant number of β-γ events in the signal region due to non-zero position and energy reconstruction resolution, as demonstrated in Figure 3.1.

In the ^{238}U chain the dominant background to the CC, ES and NC signals is ^{214}Bi decay. This daughter decays with a branching mode that includes a β^- greater than 99% of decays. One mode (18% of β^- events) has only a single β^- with an endpoint energy of 3.27 MeV. In the ^{232}Th chain the significant background to the signals is ^{208}Tl which decays to several β^- branches all of which cascade through a 2.614 MeV γ to the ^{208}Tl final state. Full decay schemes for both the ^{238}U and ^{232}Th chains are shown in Figures 3.2.

For SNO ^{238}U and ^{232}Th backgrounds are classified into two types: internal backgrounds, which are decays that occur within the D_2O volume, and external backgrounds, which are decays that occur outside the D_2O volume. Because γ rays from ^{214}Bi and ^{208}Tl can also photo-disintegrate the deuteron producing neutrons that are indistinguishable from NC produced neutrons, the D_2O is highly purified and is carefully monitored. With extensive radioassays, the internal levels of ^{238}U and ^{232}Th have been measured to be less than 8.67×10^{-15} g/g D_2O and 1.64×10^{-15} g/g D_2O respectively. For the external backgrounds, there are residual amounts of radioactiv-

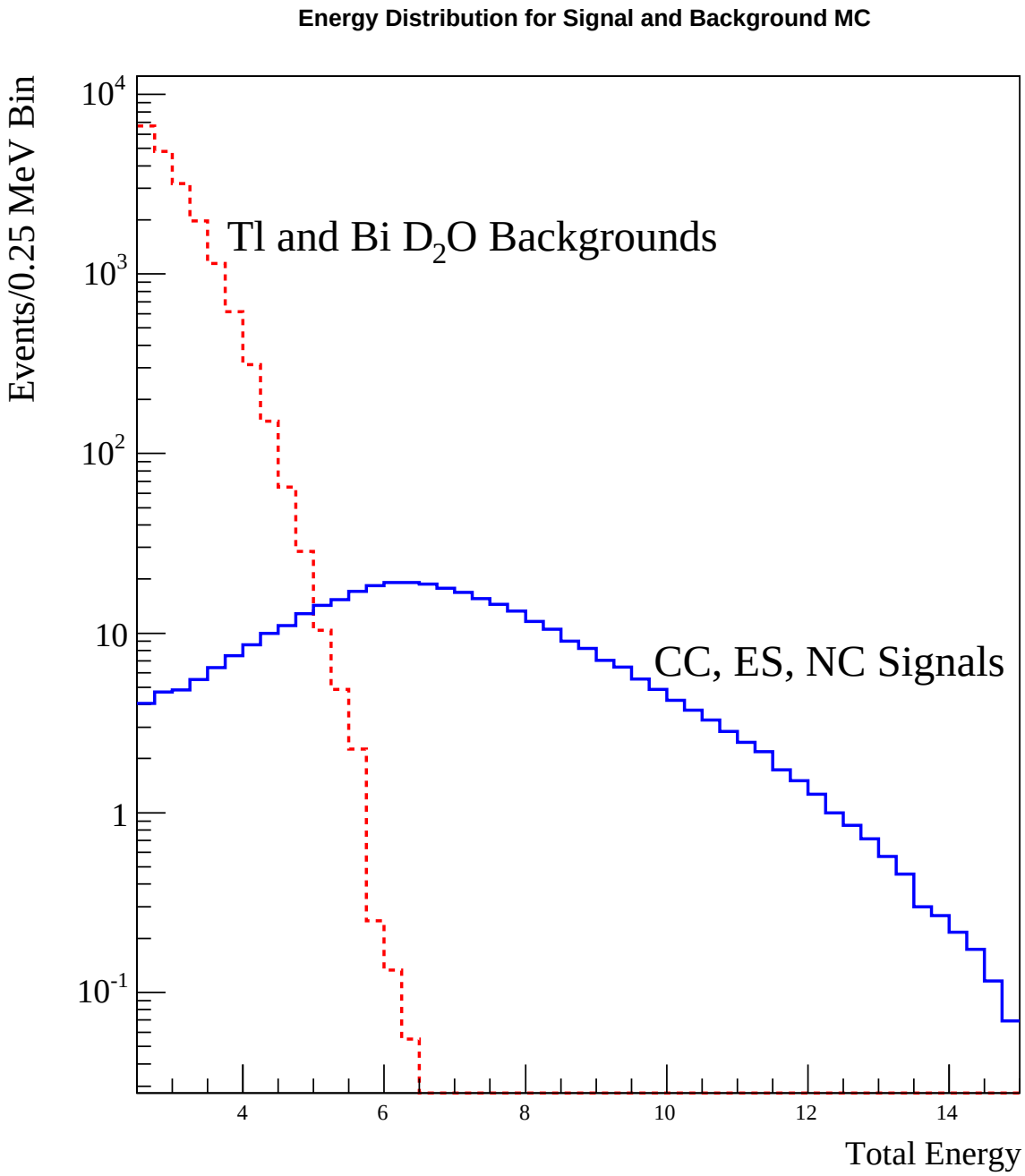

Fig. 3.1: Energy distribution for low energy background from the ^{238}U (parent of ^{214}Bi) and ^{232}Th (parent of ^{208}Tl) decay chains and CC, ES and NC signal MC. Note that the energies shown are in total energy in MeV.

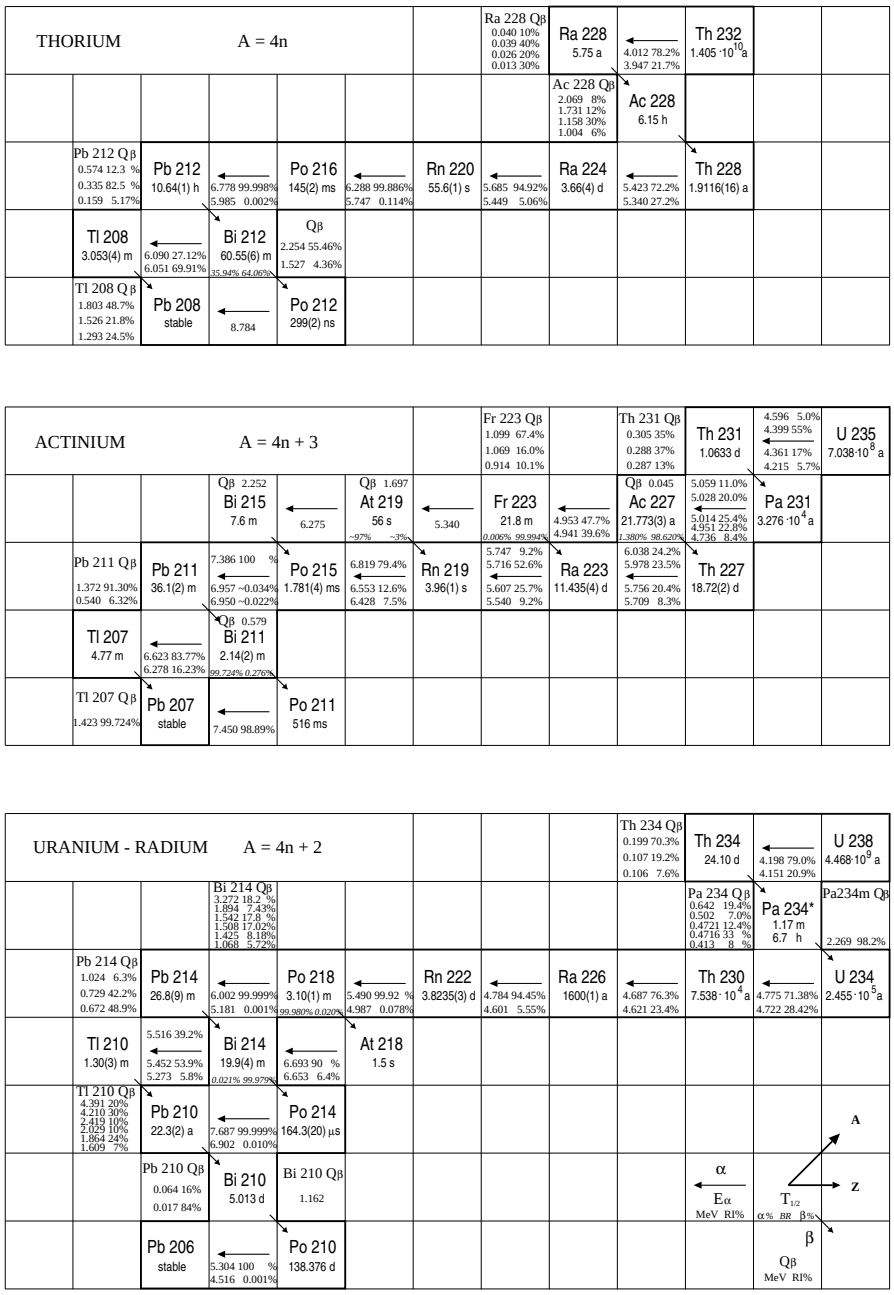

Fig. 3.2: The ^{232}Th and ^{238}U decay chains. The Actinium decay chain is shown in the figure but is not a significant background in SNO. Figure courtesy of J. Farine.

ity in the acrylic of the AV, the H_2O and the glass of the PMTs. Radioassays in the H_2O measure the activity in the water to be $5.2 \pm 1.6 \times 10^{-14}$ g Th/g H_2O and $20.6 \pm 5.0 \times 10^{-14}$ g U/g H_2O [61].

A concentration of 3.8×10^{-15} g Th/g D_2O or 30×10^{-15} g U/g D_2O in the heavy water would contribute one photo-disintegration neutron per day to the NC signal. To protect the heavy water from high levels of radioactivity in the mine's air, the lab has extensive air filtration systems. For further protection, a barrier of nitrogen gas is used as a physical boundary between the D_2O and the lab air. Large volumes of both heavy and light water are circulated over time to measure the U and Th levels using MnO_x, HTiO and radon radioassays. Details on these assay techniques can be found in [62] and [63]. More information on SNO's water systems can be found in [36].

As low energy β-γ backgrounds may mis-reconstruct to higher energies, improving the energy resolution of the energy estimator algorithm improves the signal to background separation. The following section gives an overview of the traditional energy estimator used for previous SNO measurements and highlights several of its limitations. A more sophisticated energy estimator algorithm that greatly enhances the signal to background separation is discussed in Chapter 5.

3.2.1 Energy Resolution

In past SNO publications [64], [2], [28], [65], [19], the method used to determine the energy of events (called RSP) is based on the number of PMT hits caused by prompt photons (photons that did not Rayleigh scatter or reflect). The motivation behind using prompt hits only is that scattered and reflected hits are complicated to model and only account for roughly 12% of all hits in a given event. A prompt hit is defined

by this algorithm as a hit that has a time residual within ±10ns. The time residual for each hit tube is given by $t_{res} = t_{pmt} - \frac{r_{pmt}}{c}$, where t_{pmt} is the pmt time, r_{pmt} is the distance from the event position to the PMT and c is the average speed of light in all three media. The distribution of time residuals with the timing cut overlaid can be seen in Figure 3.3. The number of prompt hits in the in-time window (N_{eff}) is then

$$N_{eff} = N_{win} - N_{dark} \tag{3.1}$$

where N_{win} is the number of tubes in the in-time window and N_{dark} is the number of expected noise hits in the in-time window calculated using PGT data.

The number of prompt hits in the in-time window is proportional to energy but has positional and directional dependence. To account for position and direction dependence in N_{eff} the following optical adjustment is made

$$N_{\text{Corr}} = N_{eff} \times \frac{1}{\epsilon_{optical}} \times \frac{1}{\epsilon_{hardware}} \times \frac{1}{\epsilon_{drift}} \tag{3.2}$$

where $\epsilon_{optical}$ is a optical adjustment for the event position ($\vec{r}$) and direction ($\vec{u}$), $\epsilon_{hardware}$ is a correction for the number of tubes that are online at the time of the event, and ϵ_{drift} is a correction to account for small drifts in the detector's gain over time. The optical correction is more defined as

$$\epsilon_{optical} = \sum_{\theta'} \sum_{\phi'} \sum_{\lambda} \frac{\epsilon_{pmt}(\lambda)}{\lambda^2} g(\theta', \phi') \tag{3.3}$$

$$\times \exp^{-\mu_1 d_1 - \mu_2 d_2 - \mu_3 d_3} P(\vec{r}, \theta, \theta', \phi') M(\vec{r}, \theta', \phi') \tag{3.4}$$

where

θ' and ϕ' are the Cherenkov photon direction relative to $\vec{u}$

θ is the angle between $\vec{r}$ and $\vec{u}$

λ is the photon's wavelength

ϵ_{pmt} is the PMT wavelength response

$g(\theta', \phi')$ is the Cherenkov light distribution

μ_i is the attenuation for medium i

d_i is photon's distance through medium i

$i = 1$ for D_2O , $i = 2$ for Acrylic, $i = 3$ for H_2O

$P(\vec{r}, \theta, \theta', \phi')$ is the PMT angular response

$M(\vec{r}, \theta', \phi')$ is the multi-photon correction

With $\epsilon_{optical}$ applied, N_{Corr} is the number of prompt hits which an event with energy E *would* have had the event occurred at the detector's center. It is only a function of electron energy. To translate N_{Corr} to energy in MeV, MC of electrons is used to create a $N_{\mathrm{Corr}} \rightarrow E(MeV)$ map. The overall PMT efficiency factor needed for the MC simulation is tuned so that the mean N_{Corr} for MC and data agrees for ^{16}N calibration γ rays at the detector's center.

Although the RSP energy estimator has many virtues and has had many successes as detailed in [66], it has several major limitations. First, RSP uses prompt light only. While Rayleigh scattered and reflected light contribute only 12% of the hits in an event, a 12% increase in hit statistics is approximately a 6% improvement in energy

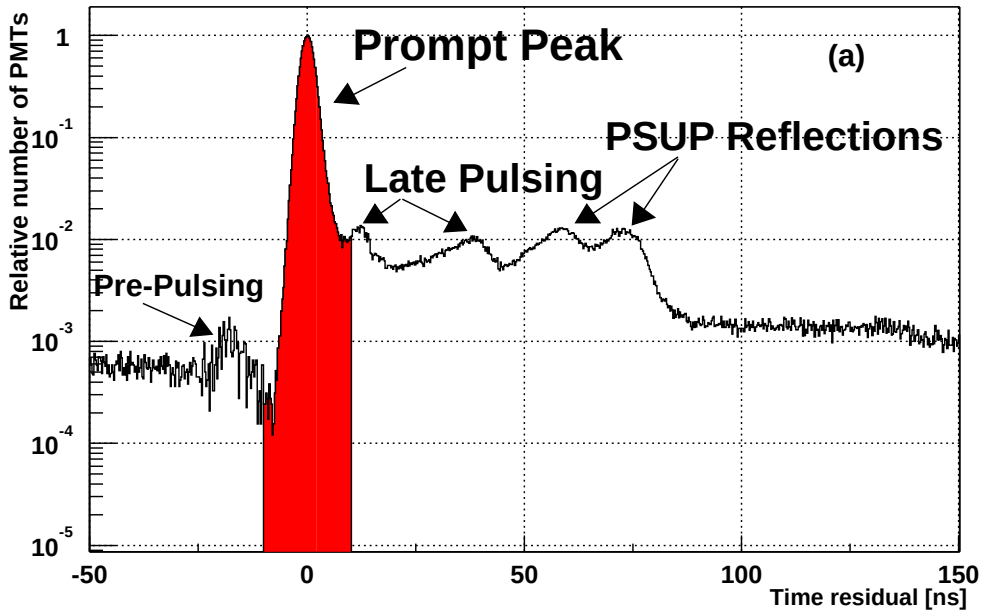

Fig. 3.3: PMT timing distribution for laser data taken at the center of the detector. The shaded area indicates the prompt timing window used by the energy estimator algorithm, RSP. Figure taken from [66]

resolution. This estimated improvement in resolution would be especially critical in reducing the amount of low energy background events that leak into the signal region. Second, RSP does not take into account detector asymmetries such as the neck and the location of offline tubes. Third, a timing cut is sensitive to any shifts in the time residual distribution such as that caused by mis-reconstruction of events. Fourth, the mapping between N_{Corr} and energy in MeV is not a continuous distribution. This makes the measurement of energy sensitive to bin size. Fifth, the RSP estimated energy is a mapping, not a likelihood fit. Without doing a maximum likelihood or χ^2 fit, we can not define figure-of-merit or goodness-of-fit parameters that can test whether or not a given event is a good fit to the Cherenkov electron hypothesis.

Having the ability to test a figure of merit for each event is beneficial to removing low energy background events, since a β-γ event would have a poor figure of merit in the electron hypothesis.

Ch. 4

Improving Upon SNO's Limitations

As detailed in the previous chapter, SNO's ability to measure the low energy spectrum of the solar ^{8}B neutrinos is limited by the hardware efficiency, the amount of low energy radioactivity and the energy resolution of our energy reconstruction algorithms. As this thesis uses existing data from SNO's D_2O and salt phases, it is impossible to improve the hardware efficiency or reduce the amount of radioactivity in the detector. This chapter however details an upgrade to the front-end electronics system that has improved the hardware efficiency during the current NCD phase. More pertinent to the spectrum measurement at hand, this chapter also discusses how improvements to the energy reconstruction algorithm can reduce the number of low energy background events that leak into the signal region. A detailed description of a new energy reconstruction algorithm which has succeeded in significantly reducing background events is given in the following chapter.

4.1 Lowering Hardware Thresholds: Low Voltage Backplane

On the low voltage backplane, the analog trigger signals travel alongside digital signals that produce an adverse noise environment for the analog system and degrade the quality of the trigger signals. On the low voltage backplane used during the D_2O and salt phases (Mark I), the GTL termination voltage plane was physically placed directly underneath the analog trigger lines with no ground plane for shielding. As a result, pick-up on the trigger lines from this voltage plane swamped any real trigger signal. To correct this, the Mark I backplane was modified so that the GTL termination was external to the board, confined to two small surface strips of copper near the CTC and XL2. Although this reduced the amount of noise on the trigger lines, the power plane was too small for the local current requirements of the digital lines, resulting in synchronous noise on the FEC discriminator lines during crate readout. This synchronous noise, named a "slot-of-fire", from its appearance on the event display, created a vicious cycle where many discriminators would fire, the detector would trigger, the crate would be read out again, creating more noise on the discriminator lines, repeating the cycle (as discussed in Section 3.1.2). In extreme cases the detector would fall into a feedback loop, continuously reading out a given slot making collecting good solar neutrino data impossible.

SNO's trigger and PMT thresholds are currently set at a level designed specifically to avoid slots-of-fire. In most cases, no more than 12 tubes fire from GTL pick-up. A N100Med threshold of 16 hits prevents these types of events from triggering the detector. Without slots-of-fire, the N100Med trigger threshold could reasonably be lowered to 14 or, ambitiously, to 12, before being limited by high rates of instrumental

backgrounds. Similarly, the channel discriminator thresholds had to be raised because of noise induced on the lines by the poor GTL termination. Improving the ambient noise environment would allow these thresholds to be lowered, having a significant beneficial impact on SNO's physics potential. Decreasing the average discriminator threshold by 0.5-1.0 counts is equivalent to increasing the number of hits per MeV by roughly 1.5-3.0%, or lowering the system trigger threshold by 3 or 4 hits. Improving the trigger efficiency and lowering channel thresholds is especially critical for the NCD phase as the loss of photons due to absorption and scattering of light from the NCDs will broaden the detector energy resolution (through both statistical and systematic effects) leading to a higher apparent level of background events. Figure 4.1 shows how the trigger efficiency worsens in the NCD phase compared to the salt phase.

To improve the detector's efficiency during the NCD phase, a new Mark II backplane was designed with the goal of eliminating the slots-of-fire problem and reducing the overall ambient noise in the crate. The major changes consisted of distributing the GTL termination voltage plane over a large area of copper, burying that copper plane far from the analog trigger lines, and shielding the GTL plane with several ground layers. Other minor changes were made, such as fixing a slot addressing problem for slot 12 and moving the digital clock lines away from the analog trigger lines. The digital clock lines were also routed differentially, further reducing noise on the trigger lines. After installing a prototype in one crate, it was discovered that an additional ground connection between backplane ground and crate ground was necessary. The Mark IIa backplanes with this additional grounding were installed in all crates during the detector shutdown for the NCD installation in November 2004.

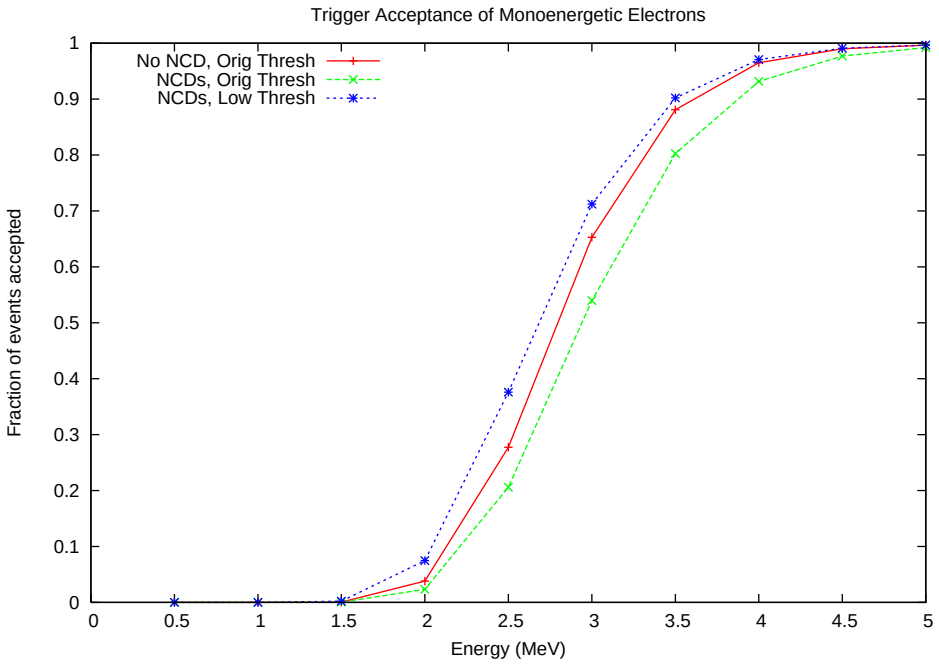

Fig. 4.1: The simulated trigger acceptance for MC isotropic mono-energetic electrons in the volume. The red-solid curve is the trigger acceptance for the D_2O and salt phases, the green-dotted curve represents the acceptance for the NCD phase, and the blue-dashed curve represent the acceptance with the N100M threshold at 14 hits and the N20 threshold at 13 hits. Energy plotted is total electron energy. Figure courtesy of Stan Seibert.

4.1.1 Improving the Trigger Threshold

At a minimum for the NCD phase, we want to lower the trigger thresholds to compensate for the lost light and restore the trigger acceptance to that of the salt phase. Figure 4.2 shows the trigger acceptance as a function of total energy for various settings of the N100M trigger, keeping the N20 trigger fixed at its salt phase threshold of 16 hits. Setting the N100M trigger to 14.5 would approximately restore the trigger acceptance to its pre-NCD state. A non-integer N_{Hit} trigger threshold is a valid threshold albeit unusual since the real trigger threshold value is an analog voltage set by the MTC/A comparator and can be set to intermediate values. With the increased detector stability, the N100M threshold was lowered to 13 hits from 16 hits, the N100H to 17 hits from 20 hits and the N20 threshold to 12.5 hits from 16 hits. Lowering the N20 is especially advantageous for measuring the amount of radioactivity from the NCD surface. For more details on the measurement of the trigger efficiency in the NCD phase see [67].

In addition to pick-up from the GTL voltage plane, the N100 and N20 trigger lines experienced pick-up from the digital clock signals that are bussed on the backplane. In the Mark IIa backplane, these clock signals are buried deep below several ground planes from the trigger lines. Figure 4.3 and Figure 4.4 show before-and-after comparisons of the N_{Hit} 100 and N_{Hit} 20 signals and it can be seen that much of the clock noise has disappeared. Additionally the bandwidth of the trigger pulses has increased, as seen in the sharper rise time and ringing on the pulses. This ringing is removed downstream as the bandwidth narrows due to cables and parasitic capacitances on the MTC/A's.

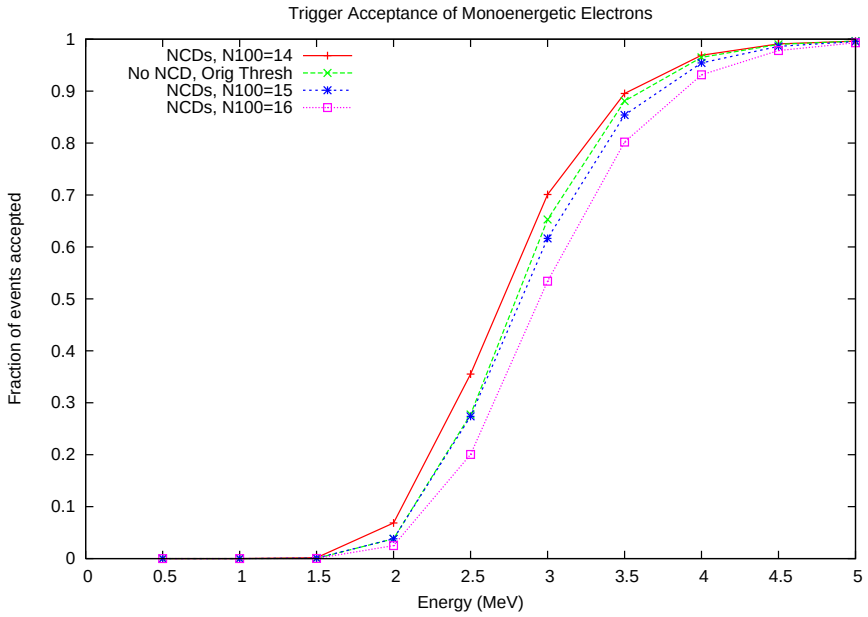

Fig. 4.2: Simulated trigger acceptance for isotropic mono-energetic electrons in the fiducial volume, for several N100M thresholds. The N20 trigger threshold is fixed at 16 in all cases. Energy plotted is total electron energy. Figure courtesy of Stan Seibert.

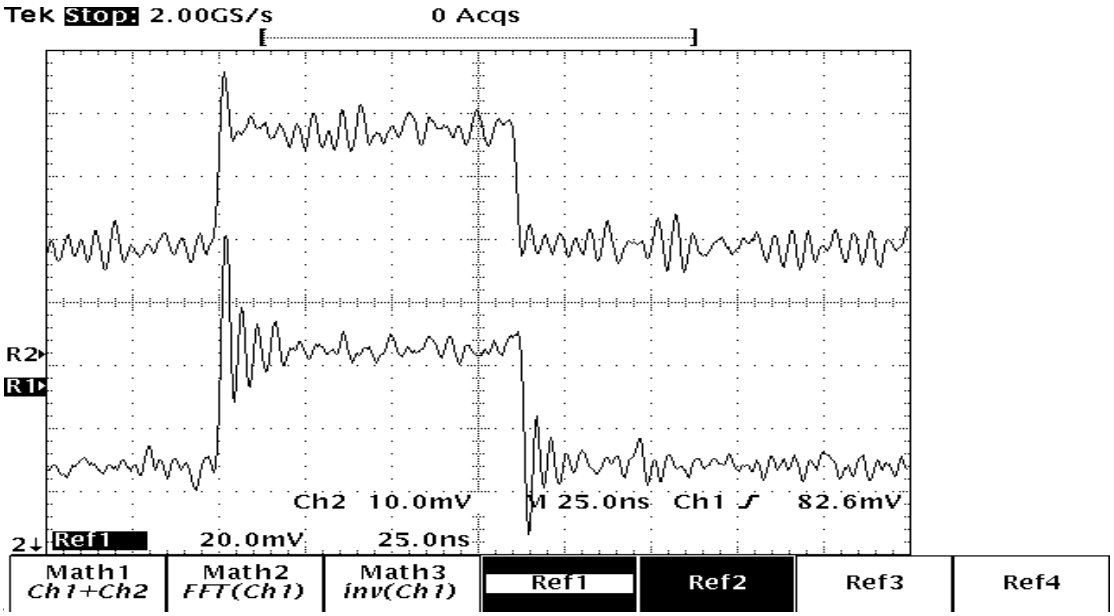

Fig. 4.3: Top trace is the N_{Hit} 100 pulse for the Mark I BP, Bottom is for the Mark II BP. On the Top trace pick-up from the clocks can be seen first and 8th division from the left.

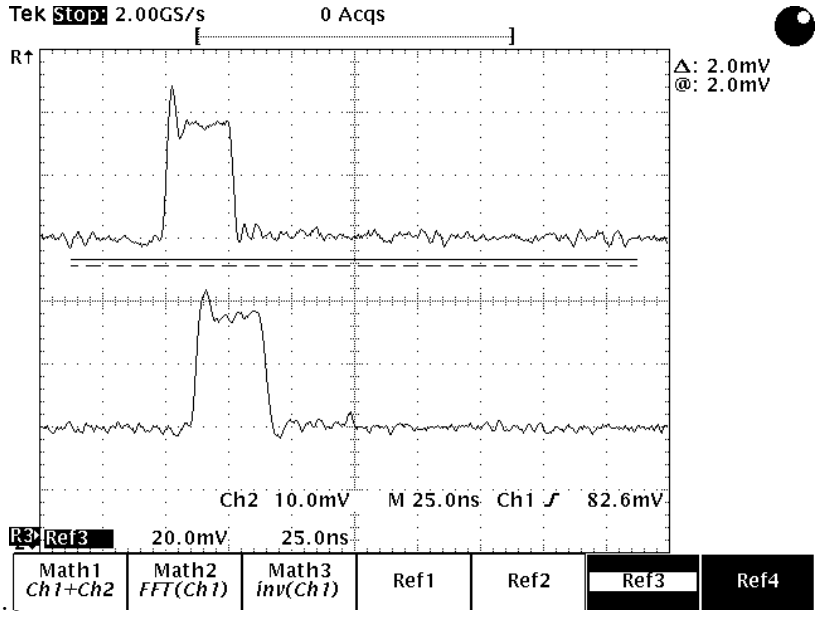

Fig. 4.4: Top trace is the N_{Hit} 20 pulse for the Mark I BP, bottom is for the Mark II BP.

4.1.2 Improving the Channel Threshold

A secondary goal of the Mark IIa backplane design was to lower the channel discriminator thresholds, since the thresholds are affected by noise from readout. As seen in Figure 4.5, the improved noise environment has resulted in lowering the average crate threshold by 0.64 DAC counts, corresponding to a 1.9% increase in hits/MeV. With the Mark IIa backplanes alone, the channel thresholds only decreased by 0.19 counts but with the increased detector stability the criteria of the channel threshold algorithm could be relaxed. The individual channel threshold is set when the channel is quiet during readout (see Section 3.1.2). This criteria was relaxed such that the channel can have no more than three additional firings during readout. Additionally the crate to crate variation in channel threshold is much reduced.

4.1.3 Background Verification

As the Mark IIa backplane was designed to eliminate slot-of-fire events, a check was done to ensure that the backplane is not producing new types of instrumental backgrounds. Since any new backplane-produced instrumental backgrounds would have some pattern in crate address space, the channel-to-channel correlations, which is the correlation function of two tubes that are N adjacent channels apart in crate space both being hit in the same event were compared for the Mark I and Mark IIa backplanes (Figure 4.6). In the figure the channel correlation plots are normalized to the first bin, which is the probability that if channel x is hit then channel x will also be hit. Since the channel is being compared to itself that correlation is 100% and the ordinate represents the percent correlation for each channel bin. A linear function fit to the difference in the correlation functions for the Mark I and Mark IIa backplanes

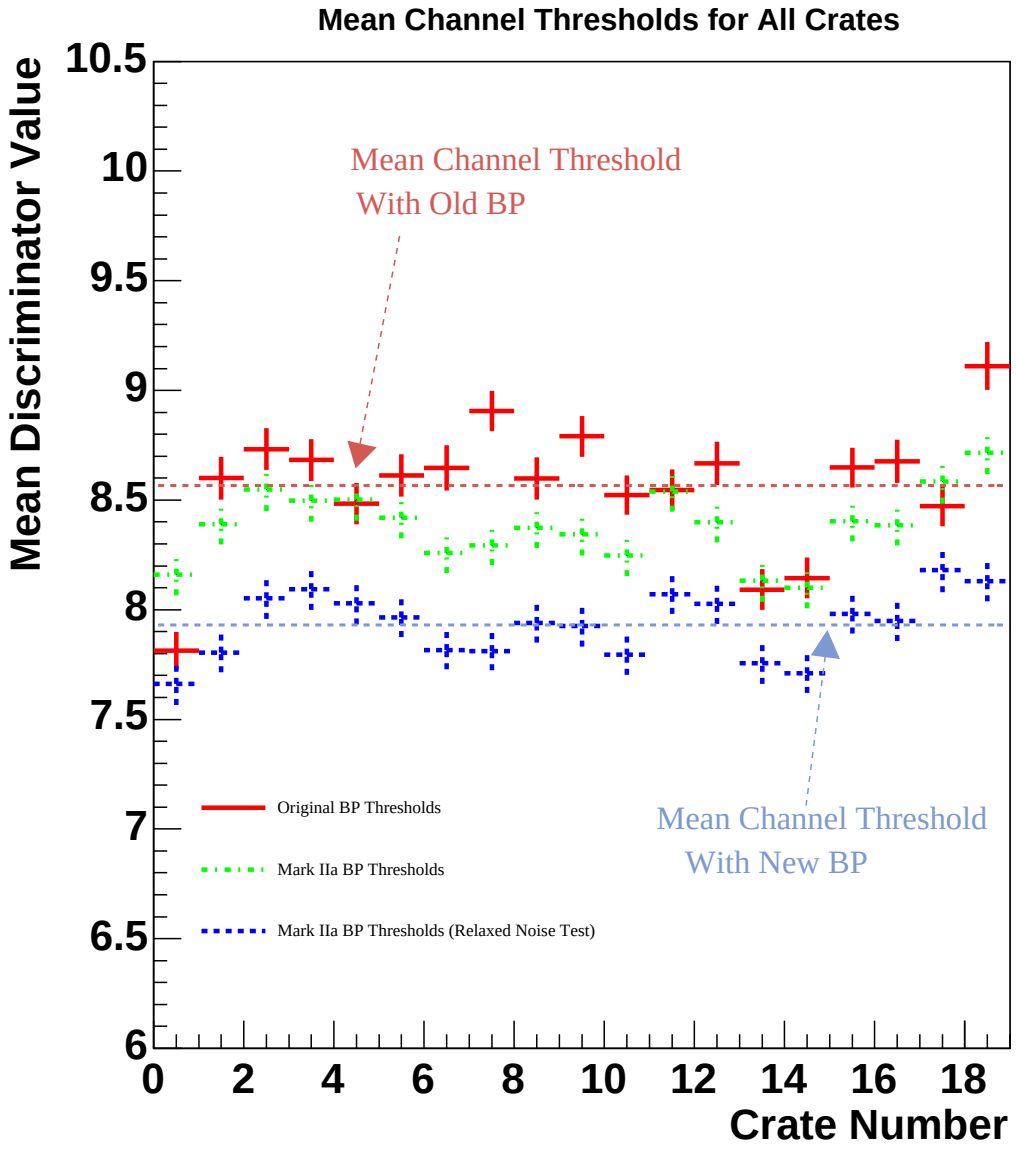

Fig. 4.5: Average crate channel thresholds for the Mark I backplanes, the Mark IIa backplanes and the Mark IIa backplanes with the relaxed channel threshold algorithm discussed in the text. Error bars indicate the spread in threshold values.

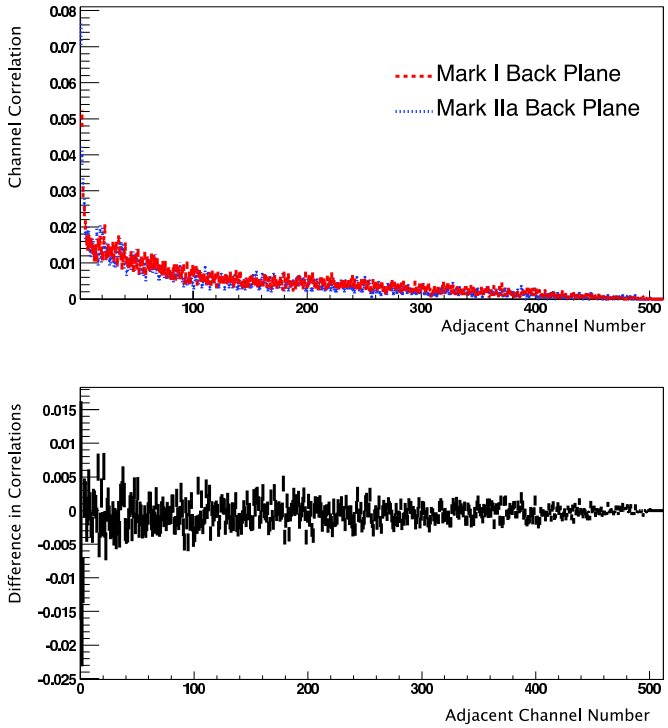

Fig. 4.6: Top: Channel correlations for the Mark I and Mark IIa backplanes. Bottom: Difference in correlation probability between the two backplane versions.

is consistent with flat passing through zero, concluding that the Mark IIa backplanes are not producing new forms of instrumental backgrounds.

4.2 Expected Gains from Improving the Energy Resolution

While the improved trigger thresholds and channel discriminator thresholds gained by the Mark IIa backplanes have reduced the hardware limitations for the NCD phase, the only means of lowering the analysis energy threshold for the D_2O and salt data

sets is to reduce the number of low energy background events in the signal region. As discussed in Section 3.2, the number of low energy ^{238}U and ^{232}Th chain decays that leak into the signal window is dependent upon the energy resolution. This resolution can be improved in two ways. First, the number of hit PMTs for each MeV of energy can be increased. This is possible even with data already taken, by including late (scattered or reflected) light in the energy estimator (roughly 12% of the light in an event). Second, the energy estimator itself can be improved to represent the data better, reducing large tails that fall inside the signal region.

This section highlights an analytic approach used to estimating the signal and background separation in order to test the dependence of energy resolution on the analysis energy threshold[1]. The goal of this analytic study is to determine what results in better signal and background separation; improving the PMT hit statistics or improving the energy estimator's model of the detector.

4.2.1 An Analytic Study of Energy Resolution

To study the signal and background separation, the distribution of the number of Cherenkov photons produced in an event is smeared with a detector response function to mimic SNO's energy response. This detector response function has two parts: a binomial component which reproduces the detector's PMT hit statistics, including loss of photons in the detector from attenuation, photo-cathode coverage, and PMT quantum efficiency and a Gaussian component which accounts for broadening due to misunderstanding of optics and calibration source effects. The response function

[1]Using SNO's MC to study improvements in the energy resolution is not practical since the MC individually propagates each photon to determine if a PMT was hit. Narrowing the energy resolution within this model is difficult.

is fit to the distribution of the number of hits for ^{16}N data to obtain the nominal values of the binomial and Gaussian components. The results of this fit are shown in Figure 4.7, where the inset is the number of Cherenkov photons for ^{16}N and the main figure is the detector response function fit to the ^{16}N N_{Hit} distribution. The number of hits can be converted to energy in MeV using the mapping discussed in Section 3.2.1.

Having obtained the nominal detector response function, this function is applied to the distribution of the number of Cherenkov photons for the neutrino signals and internal ^{214}Bi and ^{208}Tl backgrounds (Figure 4.8) to estimate the ratio of the number of signal to background events in the detector. To study how improvements in energy resolution affects signal and background separation, the PMT hit statistics resolution (binomial component of the response function) and the energy estimator model resolution (Gaussian component of the response function) are narrowed in the response function. As seen in Figure 4.9, improving these resolutions visibly separates the backgrounds from the signal.

To quantify the reduction in the number of backgrounds in the signal region seen in this figure, the PMT hit statistic resolution and energy estimator model resolution are varied independently in the response function. For each variation in the detector response function, the number of background events above 5 MeV is determined, as shown in Figure 4.10. This figure demonstrates that improvements in the energy estimator model resolution has a smaller effect on the number of background events above 5 MeV than the PMT hit statistics resolution. In summary to improve energy resolution, increasing the PMT hit statistics is critical whereas the energy estimator model resolution has a small effect on the total energy resolution. Additionally this study finds that for every 1% improvement in total energy resolution, the number of

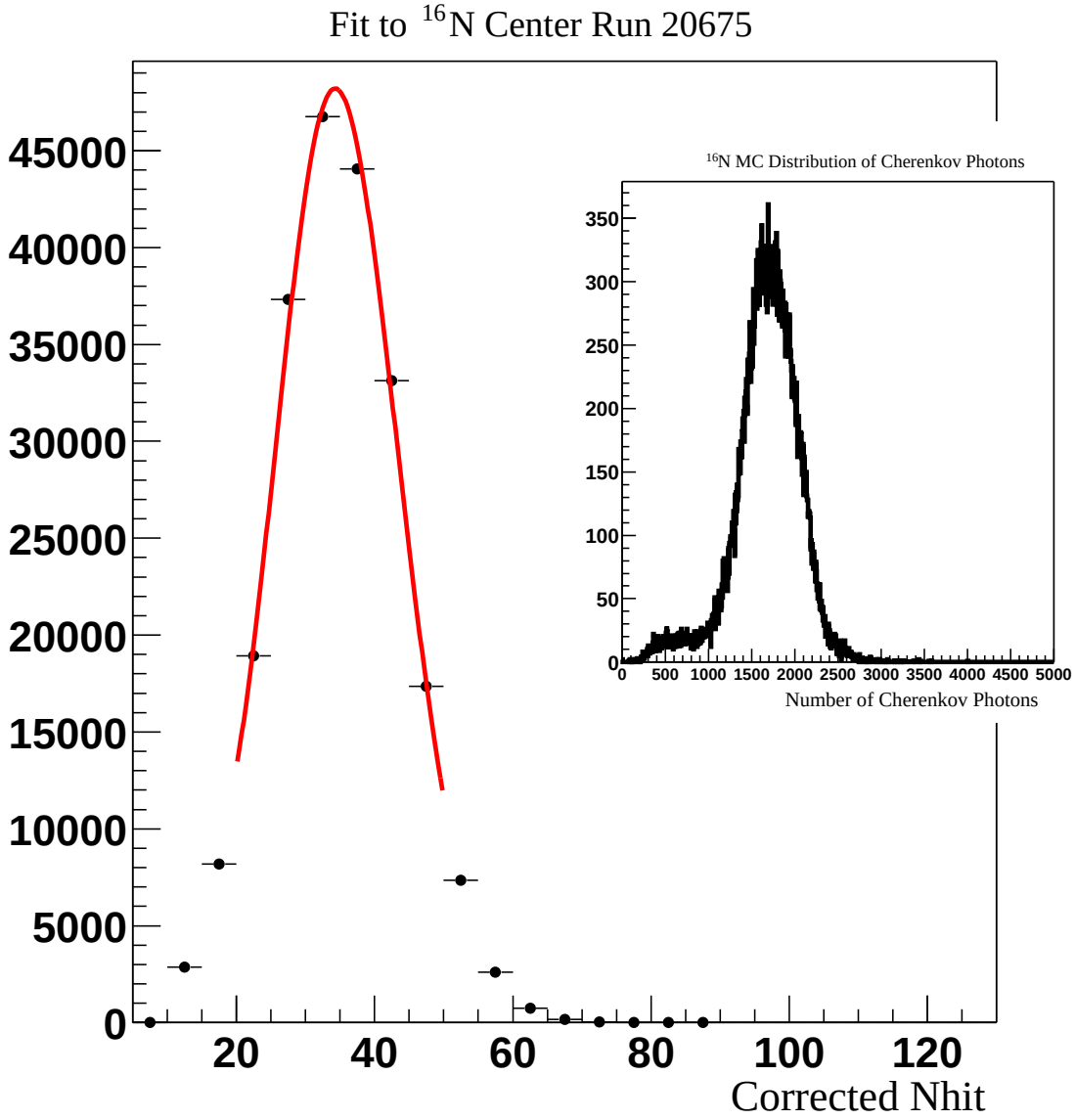

Fig. 4.7: Corrected-N_{Hit} (N_{Corr} , see Section 3.2.1 for a definition) for a ^{16}N center run. In the inset the ^{16}N Monte Carlo distribution of the number Cherenkov photons is shown. This distribution in the inset is convolved with the detector response function to reproduce the data shown in the main figure. Statistical errors are shown for the data, but are smaller than the data points.

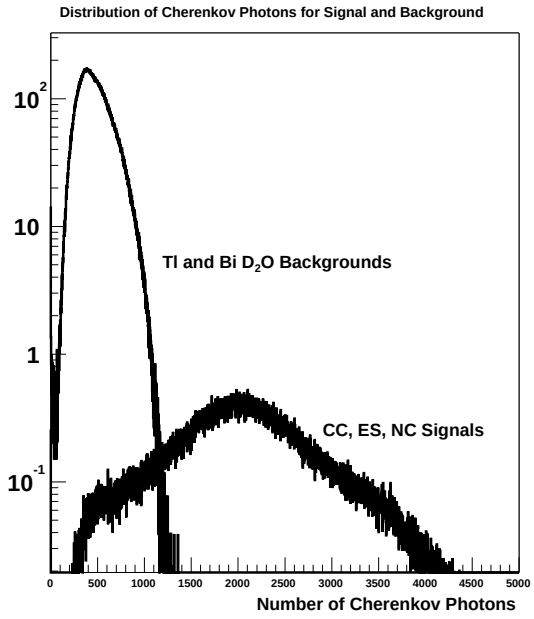

Fig. 4.8: Monte Carlo distribution of the number of Cherenkov photons for internal ^{214}Bi and ^{208}Tl D_2O backgrounds and CC, ES and NC signals for the salt phase.

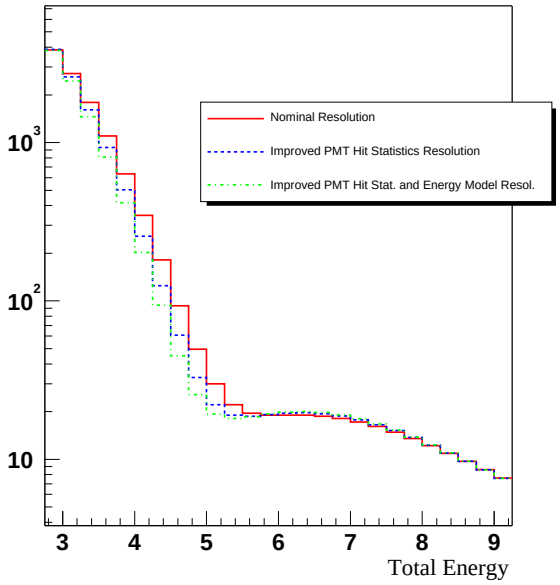

Fig. 4.9: Energy distributions for different PMT hits statistics and energy estimator model resolutions.

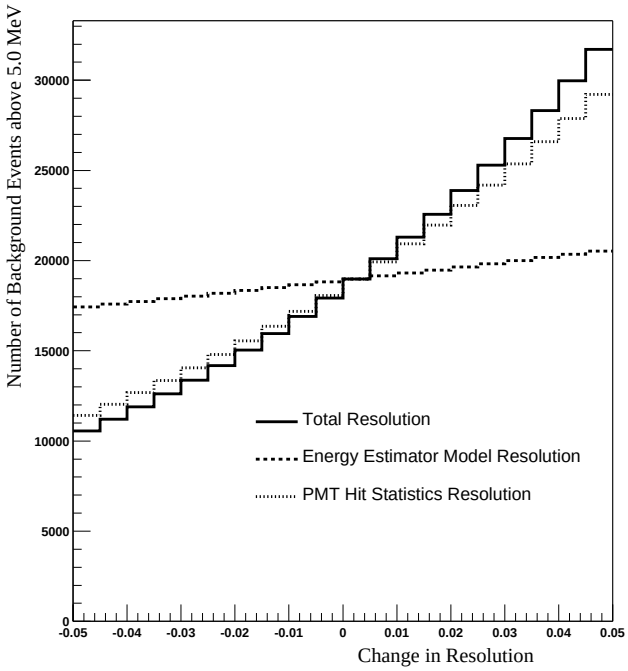

Fig. 4.10: Dependence of the number of background events above 5.0 MeV on changes in the PMT hits statistics and energy estimator model resolutions.

background events in the signal region is reduced by 10%. Including the late light in the energy estimator is expected to reduce the resolution by 6% which extrapolating the results of this study would result in a 60% reduction in the number of background events in the signal region.

4.3 Removing Cross Talk

As discussed in the previous section, using scattered and reflected light in the energy estimator improves the energy resolution. In the RSP energy estimator (see Section 3.2.1) the prompt PMT timing cut of 10 ns is designed not only to remove hits from scattered and reflected light that are complicated to model but also to remove

hits from a known front end electronics phenomenon, cross talk. In order to include late light in the energy estimator, cross talk hits must be removed.

If a PMT has a high charge, an adjacent channel on the daughter board which is capacitively coupled to that channel, can fire its discriminator but the integrated charge will be very low, around the channel's pedestal value. While cross talk is a known detector characteristic, it has never been effectively modeled in the Monte Carlo or removed from the data. In the past, there have been attempts to remove cross talk from the data by cutting on the charge of the cross talk channel but these primitive cuts were highly sensitive to changes in event rate and shifts in the PMT charge spectrum. The following section details a new method of cutting cross talk channels that is based upon channel location, charge and timing information.

4.3.1 The Cross Talk Cut

The greatest challenge in removing cross talk from the data is to make the cut impervious to rate dependent changes in the charge spectrum. As seen in Figure 4.11, the charge distributions for cross talk hits in low and high rate ^{16}N differ by several ADC counts. Using only a charge cut of 5 ADC counts above pedestal results in a highly rate dependent cut. Relaxing the charge cut to 10 ADC counts removes rate dependencies but the cut acceptance of non-cross talk hits being tagged as cross talk is too high. (1 photo-electron is approximately 35 ADC counts.)

To loosen the dependence on charge, an adjacency requirement is made. This requires that a low charge hit must be adjacent in electronics space to a high charge hit, only extending to nearest neighbors on the same FEC. While there is a possibility of producing cross talk on a channel that is two or more channels away from the

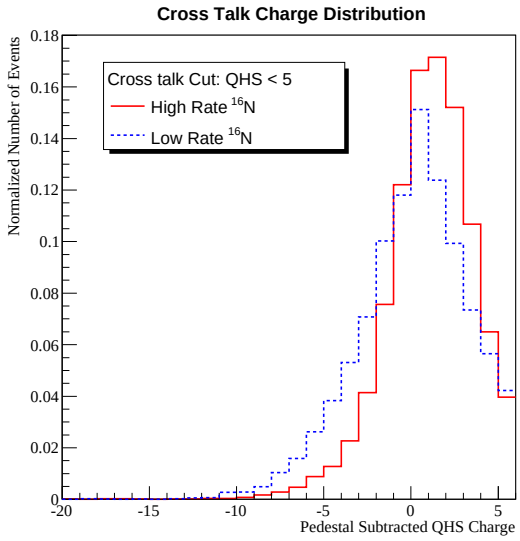

Fig. 4.11: The charge distribution of cross talk for high and low rate ^{16}N data

high charge tube, this is a second order effect that is not taken into account here. Additionally extremely high charge PMT pulses can produce cross talk in the PMT cable bundles, but this is also a significantly smaller effect.

To further relax the cut's dependence on charge, the out-of-time nature of cross talk hits is utilized. With respect to the high charge adjacent channel, the timing of cross talk channels has an ECA time that is approximately 10 ns late in time. The reason for this out of time nature is not understood.

To summarize the cut, a hit is tagged as cross talk[2] if the following criteria are met

1. **Charge:** The channel has a pedestal-subtracted QHS value less than 10 ADC counts and greater than -30 ADC counts

[2]Cross talk channels are flagged by setting bits 0 and 26 in SNOMAN's PF bank. Currently, all of the fitters and energy estimators ignore hits with the cross talk bit set but classifier routines such as $\langle\theta_{ij}\rangle$and ITR do not.

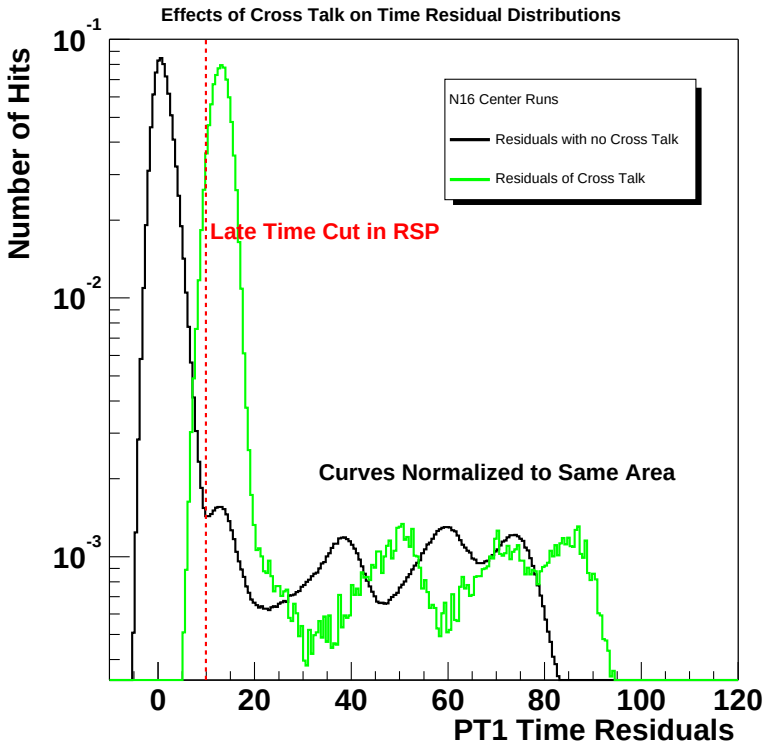

Fig. 4.12: Comparison of time residuals for cross talk hits and all other hits. Note that the distributions are normalized to the same area.

2. **Adjacency:** The channel is the adjacent channel on the FEC to a high charge channel (pedestal subtracted QHS value must be greater than 50 ADC counts).

3. **Timing:** The channel has an ECA time that is between 8 ns and 25 ns late in time with respect to the high charge channel's timing.

Lower limits of -30 QHS for the charge cut and 25 ns for the timing difference are applied to avoid flagging miscalibrated channels as cross talk.

Since cross talk is late in time, only the tail end of the cross talk distribution falls within the RSP prompt time window (Figure 4.12). Quantitatively, 21.5% of cross talk hits lie within the prompt time window, which is 0.3% of the total prompt time

hits, and approximately 1% of all PMT hits.

4.3.2 Rate Stability of the Cross Talk Cut

As previous attempts at cutting cross talk hits failed because the cut was sensitive to changes in the detector's event rate, the rate stability of this cut has been checked using high and low rate ^{16}N source data. Additionally, to verify that the cut does not have a radial dependence, a comparison between ^{16}N at the center and off-axis can be made. Shown in Figure 4.13, the number of cross talk hits in each event is consistent for low, high and off-axis ^{16}N data. Furthermore, the difference between high and low rate ^{16}N in the distribution of the number of cross talk hits per event is smaller for this cross talk cut compared to the traditional cut which requires that the cross talk channel has a charge less than 5 QHS and is adjacent to a high charge channel (Figure 4.14).

4.4 Summary of Cross Talk Cut

Using channel charge, timing and location information, a cut of cross talk hits has been developed which is insensitive to the detector's event rate. Cross talk hits contribute only 0.3% of the hits in the RSP prompt timing window but to include late light in the energy estimators it is critical that these electronic-produced hits are removed from the data.

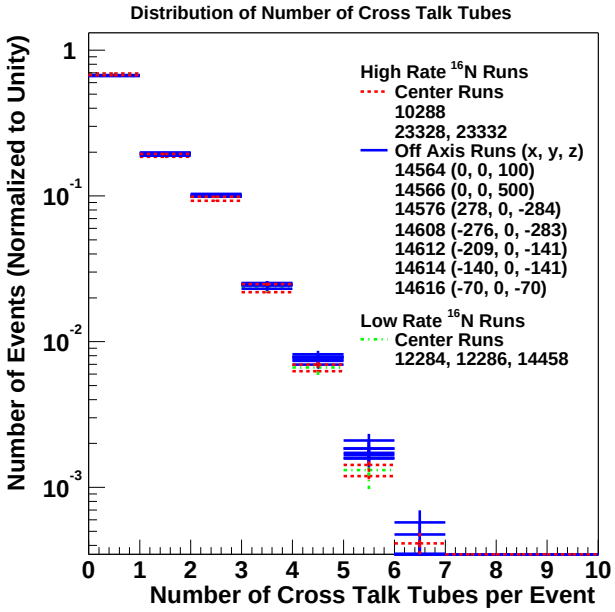

Fig. 4.13: Comparison of the number of cross talk hits per event for high rate, off-axis, and low rate ^{16}N.

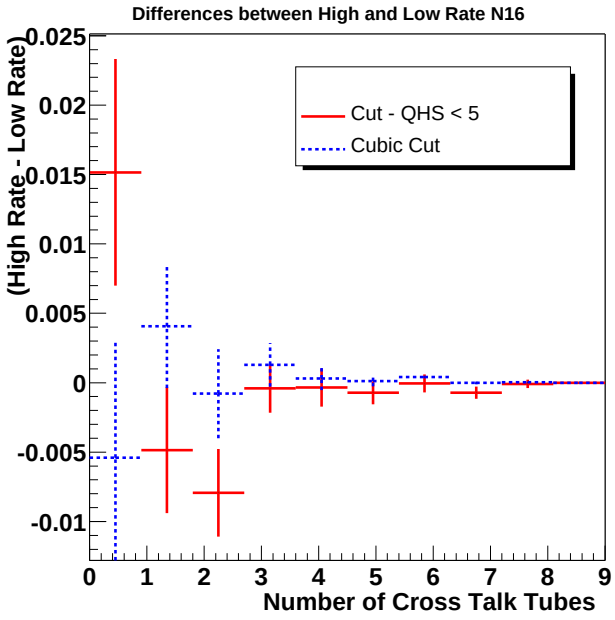

Fig. 4.14: Comparison between high and low Rate ^{16}N for two different cross talk cuts. Cut(1): QHS of adjacent tube is less than 5 QHS (solid line), Cut(2): Standard cut outlined in 4.3.1 (dashed line).

Ch. 5

Improving SNO's Energy Resolution Using a Maximum Likelihood Energy Fitter

As discussed in Section 4.2, estimating the energy of events using all available light increases the number of observed hits per MeV by 12%, which by itself would give a 6% improvement in energy resolution. An improvement in energy resolution of this magnitude is predicted to reduce the number of background events in the signal region by up to 60%. Prior to the work described here, only prompt hits have been used to estimate the energy of events in SNO (see Section 3.2.1). Prompt light has the advantage that it is simple to model. Including late light, therefore raises a new challenge: modeling all optical processes for all event positions, directions and times to better than 1% accuracy. Clearly, artifacts such as electronic-produced cross talk hits can not be modeled and therefore the cross talk cut described in Section 4.3 is critical.

To lower the analysis energy threshold, a new energy estimator (FTK) was developed that includes *all* the light in an event and is successfully able to model this late light at all positions in the D_2O. To include late light in the energy estimation, *all* possible paths of light in the detector need to be modeled accurately (to much better than 1%) and quickly (less than 1 second). In other words, the energy estimator must reproduce the entire MC simulation but 1000 times faster. The FTK algorithm uses both analytic and MC style methods to estimate the prompt and late light, achieving both the required accuracy and speed. MC studies indicate that FTK's energy resolution is approximately 6% narrower relative to prompt light energy estimators and reduces the number of ^{214}Bi and ^{208}Tl events in the signal region by over 60%.

5.1 Motivation for a Maximum Likelihood Energy Fitter

The FTK maximum likelihood energy fitter differs from traditional SNO energy estimators in several keys ways.

- FTK uses a maximum likelihood optimization technique and it returns not only the most probable energy but also the uncertainty on that energy. These uncertainties are used to cut poor fits and reduce the number of background events in the signal window.

- FTK uses no energy look-up table (see Section 3.2.1). This has the advantage that FTK naturally commutes with the MC. For example if the PMT responses or media attenuations change in the MC, FTK will automatically adapt to those changes.

- FTK naturally accounts for the location of offline tubes and therefore corrects for local detector variations.

- FTK utilizes the SNOMAN geometry code as its model of the detector and therefore can accurately model the neck, the belly plates, belly plate grooves[1], kevlar ropes, NCDs and even the source container if a source is deployed.

- FTK is calibrated to estimate the energy of events in the light water. This is extremely useful for estimating rates of the external backgrounds.

This chapter is organized into the following sections: Section 5.2 gives a general outline of this maximum likelihood energy fitter and Sections 5.3-5.5 gives details about the inner workings of the fitter. An in-depth technical description of the FTK algorithm can be found in Appendix A. This fitter's performance on MC is discussed in Section 5.6. Performance on calibration data is shown in Chapter 6 which discusses systematic uncertainties in energy estimation.

5.2 FTK Overview

The basic strategy of FTK is very simple; calculate the number of hits expected for this event and compare that number to the number of hits actually observed. The fitted energy is varied until the number of expected hits has the best agreement with the number of observed hits. Since FTK does not have a prompt timing cut, the number of expected hits is a sum of the number of expected hits produced by direct photons, Rayleigh scattered photons, photons reflecting off the AV, photons reflecting

[1]The belly plates are additional layers of acrylic in the AV where the AV support ropes are mounted. The grooves are cuts in the belly plates for the ropes

off the PMTs and PMT noise. These different paths of light in the SNO detector are graphically represented in Figure 5.1. With the exception of PMT noise, the number of hits produced from different photon paths is highly dependent on the electron's position and direction and must be calculated for each event.

To find the number of direct photons expected in an event, FTK first calculates the probability that a photon will fire a given PMT. In SNO, a photon can be lost or re-routed in many ways. It can be absorbed in the D_2O, acrylic or H_2O, scattered, reflected off the AV or PMTs, miss the PMT entirely and be lost in the PSUP, or reach the PMT but fail to fire the tube. For each tube, FTK calculates the probability that none of the above fates occurs. This probability times the number of Cherenkov photons produced is the mean number of direct photons expected for that tube. The total detector-wide number of direct photons is the sum of the mean number expected at each tube. The number of Cherenkov photons used to determine the mean number of photons for each tube depends on the energy of the electron. As the energy in the FTK fit varies, the number of Cherenkov photons changes accordingly.

Similarly, the mean number of expected scattered hits at a given tube is the number of Cherenkov photons produced times the probability that a photon will scatter, not be absorbed or reflected enroute, reach the PMT in question and then cause it to fire. The sum of the mean number of scattered hits from each tube is the total number of expected scattered hits. Determining the number of AV or PMT reflected hits uses a similar approach.

The following section discusses how the calculation of the number of expected hits is achieved.

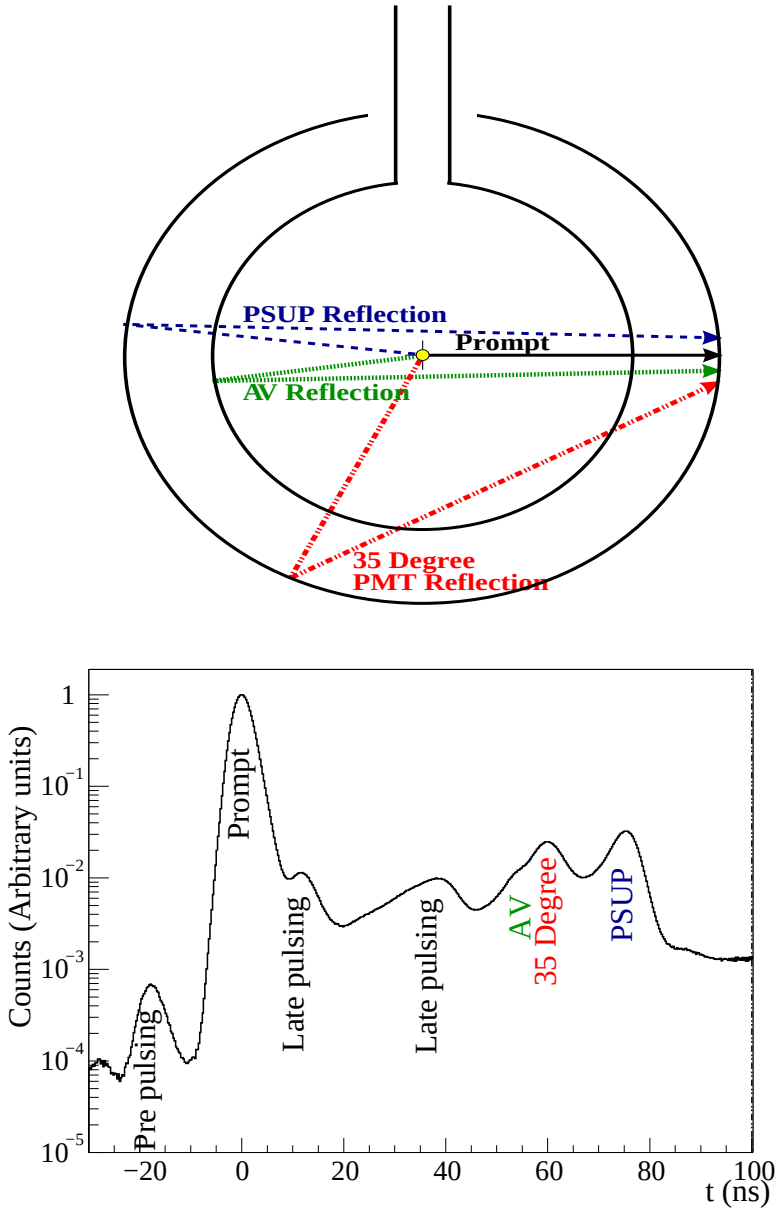

Fig. 5.1: Top: Graphical representation of the different paths of light in SNO. Bottom: The time residual distribution for light produced at the center of the detector where the timing for each path of light has been labeled. Figure courtesy of Bryce Moffat.

5.3 The Approach of the FTK Energy Fitter

The premise of the FTK energy fitter is to calculate the probability that a given PMT was hit by a direct photon, a scattered photon, or a photon reflected off the PMTs or AV. Let the probability of the i^{th} PMT being hit by a single direct photon, which is dependent upon the electron's position and direction, be ρ_i^{dir}. Using this notation, the probability that a single photon hits *any* tube in the detector is given by

$$\rho_{dir} = \sum_{\text{All PMTs}} \rho_i^{dir} \tag{5.1}$$

Therefore the number of expected direct photons in the detector, n_{exp}^{dir}, given the electron's position, direction and energy is

$$n_{exp}^{dir} = N_\gamma \rho_{dir} \tag{5.2}$$

where N_γ is the number of Cherenkov photons produced by the electron. Similarly, the probabilities of the i^{th} PMT being hit by a scattered photon, an AV reflected photon, or a PMT reflected photon are defined as ρ_i^{scat}, ρ_i^{av}, and ρ_i^{pmt} respectively. Analogous to Equation 5.1, the number of expected scattered, n_{exp}^{scat}, AV reflected, n_{exp}^{av}, and PMT reflected photons, n_{exp}^{pmt} in the detector are given by the following equations,

$$n_{exp}^{scat} = N_\gamma \rho_{scat} = N_\gamma \sum_{\text{All PMTs}} \rho_i^{scat} \tag{5.3}$$

$$n_{exp}^{av} = N_\gamma \rho_{av} = N_\gamma \sum_{\text{All PMTs}} \rho_i^{av} \tag{5.4}$$

$$n_{exp}^{pmt} = N_\gamma \rho_{pmt} = N_\gamma \sum_{\text{All PMTs}} \rho_i^{pmt} \tag{5.5}$$

The total number of expected detected photons in the detector is simply the sum of all possible paths for the light,

$$n_{exp}(N_\gamma) = n_{exp}^{dir} + n_{exp}^{scat} + n_{exp}^{av} + n_{exp}^{pmt} + n_{exp}^{noise} \tag{5.6}$$

where n_{exp}^{noise} is the number of expected noise hits, which does not scale with the number of Cherenkov photons. Let the number of observed photons in the detector for a given event be N_{obs}. Then the likelihood of observing N_{obs} photons given a hypothesis of N_γ photons produced is dictated by Poisson statistics and is

$$\mathcal{L}(N_\gamma) = \frac{(n_{exp}(N_\gamma))^{N_{obs}} e^{-n_{exp}(N_\gamma)}}{N_{obs}!} \tag{5.7}$$

Several extensions need to be made to this likelihood function. First, while SNO's unit of measurement is the number of Cherenkov photons produced in an event, we are interested in estimating the event's energy in MeV. For a given electron energy, the number of Cherenkov photons produced is a distribution, not a delta function. To find the likelihood of observing N_{obs} photons given a hypothesis of an electron energy, E, we must integrate over all possible Cherenkov photons for this electron energy:

$$\mathcal{L}(\mathrm{E}) = \int \frac{n_{exp}(N_\gamma)^{N_{obs}} e^{-n_{exp}(N_\gamma)}}{N_{obs}!} \times P\left(\mathrm{N}_\gamma; E\right) d\mathrm{N}_\gamma \tag{5.8}$$

where $P\left(\mathrm{N}_\gamma; E\right)$ is the probability of producing N_γ Cherenkov photons given an electron energy, E. More on the distribution of the number of Cherenkov photons can be found in Section 5.4.1.

The second complication to the likelihood function is that we cannot distinguish multiple photons detected by a given tube and therefore do not measure the number

of observed photons in an event but only the number of hits, N_{hit}. In view of this, the number of expected hits, N_{exp} (not the number of expected photons, n_{exp}) needs to be determined. A detailed discussion of the calculation of the number of multi-photon hits is in Section 5.3.2. Knowing the number of hits, N_{exp}, the final likelihood is

$$\mathcal{L}(\mathrm{E}) = \int \frac{(N_{exp})^{N_{hit}} e^{-N_{exp}}}{N_{hit}!} \times P\left(\mathrm{N}_\gamma; E\right) d\mathrm{N}_\gamma \tag{5.9}$$

This likelihood function appears to be very simple but the difficultly lies in calculating ρ_{dir}, ρ_{scat}, etc. Since these probabilities are functions of electron position and direction, they must be calculated for each event. This can be very CPU intensive.

Roughly 88% of all photons in an event are direct photons, therefore ρ_{dir} must be calculated very accurately. The number of direct hits in FTK is estimated using an analytic integration of photon paths in the detector. This integration includes effects such as distortion of the PMT's solid angle due to light refraction in the AV and the energy dependence to the angular distribution of Cherenkov light. The late light which constitutes a smaller fraction of the total light in an event needs to modeled less accurately. For these calculations, a variety of techniques include MC methods and analytic integrations of photon paths is used. The next section highlights the ρ_{scat} calculation which uses a MC method to estimate the number of scattered hits. The specifics of the direct, AV reflected, PMT reflected and noise hit calculations can be found in Appendix A.

Another possible method of calculating the likelihood is

$$\mathcal{L}(\mathrm{E}) = \prod_{NPMT} \int \frac{(\mu_i)^{n_i} e^{-\mu_i}}{n_i!} \times P\left(\mathrm{N}_\gamma; E\right) d\mathrm{N}_\gamma \tag{5.10}$$

where $\mu_i = N_\gamma \rho_i$ and is the mean number of hits expected at the i^{th} PMT, n_i is the

number of observed hits, either zero or one, and the product is over all PMTs. This likelihood in principle would give a better estimate of the event's energy because it tests the probability of a specific tube being hit or not hit compared to Equation 5.9 which tests only the integrated number of hit tubes. The above likelihood is not used for computational reasons only. First, integrating over the distribution of the number of Cherenkov photons for each tube is very CPU intensive. Second, as discussed in Section 5.3.1, it is computationally not feasible to calculate ρ_i^{scat} for each tube, only the detector integrated probability ρ_{scat} and therefore ρ_i is not known for each tube.

5.3.1 Rayleigh Scattered Light Calculation

This section gives an example of how one of the hit probabilities (the scattering probability) in FTK is calculated. A discussion of the calculation of the direct, AV reflected, PMT reflected and noise hit probabilities can be found in Appendix A.

The probability that the i^{th} PMT is hit by a Rayleigh scattered photon, is the probability that a photon reaches an arbitrary scatter point S within the PSUP volume V, scatters at that point and then is detected by the i^{th} PMT. This is represented in Figure 5.2 and also shown in the following equation,

$$P_i^S = \lambda_{\text{Norm}} \int_{\lambda_1}^{\lambda_2} \frac{d\lambda}{\lambda^2} P_1^s \times P_2^s \times P_3^s \times P_4^s \times P_5^s \times P_6^s \tag{5.11}$$

where the probabilities are listed below:

$$\begin{aligned} P_1^s &= g(\cos\alpha) \qquad (5.12) \\ &= \text{Probability that the Cherenkov photon is produced} \end{aligned}$$

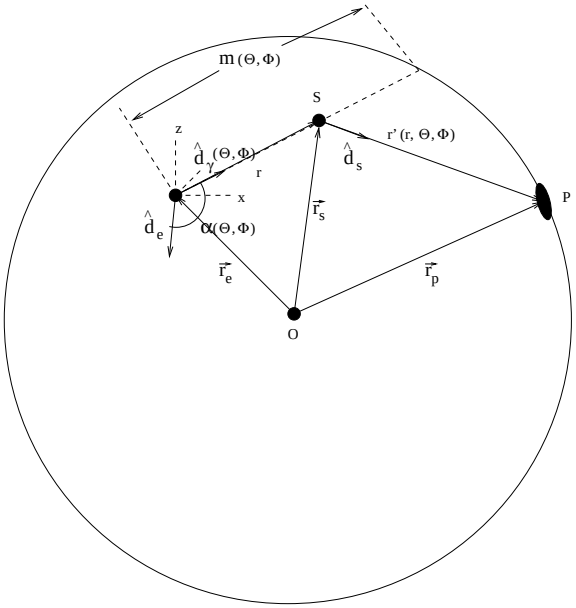

Fig. 5.2: Graphical representation of the path of a scattered photon. Figure taken from [38].

at an angle α with respect

to the electron direction, $\hat{d}_e$

$$P_2^s = e^{-(d_d\mu_d + d_a\mu_a + d_h\mu_h)} \tag{5.13}$$

$=$ Probability of the photon not being absorbed enroute

to the scatter point where d is the distance through each

medium from the electron's position to the scatter point and

μ is the attenuation factor and where the subscript

d is D_2O , a is acrylic and h is H_2O

$$P_3^s = 1 - e^{-(d_d\mu'_d + d_h\mu'_h)} \tag{5.14}$$

$=$ Probability of the photon scattering at point S

where d is the distance through each medium from the

electron's position to the scatter point and μ'

is the scattering coefficient for D_2O and H_2O.

Currently, scattering in the acrylic is not accounted for.

$$P_4^s = g'(\cos\alpha_s) \tag{5.15}$$

$=$ Probability that the photon is scattered into angle α_s

$$P_5^s = e^{-(d'_d\mu_d + d'_a\mu_a + d'_h\mu_h)} \tag{5.16}$$

$=$ Probability of the photon not being absorbed from the

scatter point to the PMT, where d' is the distance

through each medium from the scatter point to the PMT and

μ is the absorption factor

$$P_6^s = R_{\text{pmt}}(\theta,\lambda)\frac{\Omega_0}{2\pi} \tag{5.17}$$

$=$ Probability that the photon reaches and fires the PMT

$\frac{\Omega_0}{2\pi}$ is the solid angle of the tube

$R_{\text{pmt}}(\theta,\lambda)$ is the PMT angular and

wavelength response

θ is the photon's angle with respect to the

PMT's normal direction

$$\lambda_{\text{Norm}} = \frac{1}{\lambda_1^{-1} - \lambda_2^{-1}} \tag{5.18}$$

$$\lambda_1 = 220\text{nm is the lower wavelength cutoff value} \tag{5.19}$$

$$\lambda_2 = 710\text{nm is the upper wavelength cutoff value} \tag{5.20}$$

$$d\lambda = 10\text{nm} \tag{5.21}$$

The $\frac{1}{\lambda^2}$ weighting factor in the integration accounts for the fact that Cherenkov photons are produced flat in frequency ($dN_\gamma(\nu) \propto d\nu$ where N_γ is the number of photons and ν is their frequency).

To calculate the probability of single photon scattering and being detected by the i^{th} PMT, we must integrate over all possible scatter points S in the volume

$$\rho_i^{scat} = \int_{S \epsilon V} P_i^S \tag{5.22}$$

This integration is given by

$$\rho_i^{scat} = \frac{1}{V} \int_0^{2\pi} \int_0^{\pi} \int_0^{m(\theta,\phi)} P_i^S \sin\theta \; r^2 \; dr d\theta d\phi \tag{5.23}$$

where V is the volume of the detector and

$$m(\theta,\phi) = -\vec{r_e} \cdot \hat{d}_\gamma(\theta,\phi) + \sqrt{\left(\vec{r_e} \cdot \hat{d}_\gamma(\theta,\phi)\right)^2 - (r_e^2 - R^2)} \tag{5.24}$$

$m(\theta,\phi)$ is the distance from the event position to the PSUP given a direction, θ and ϕ. See Figure 5.2 for explanation of the above variables.

The total detector wide probability of detecting a scattered photon is given by

$$\rho_{scat} = \sum_{\text{All PMTs}} \rho_i^{scat} \tag{5.25}$$

Computing the integration in Equation 5.22 numerically for each PMT is computationally not feasible. For a single event, this integration takes roughly 45 minutes! Alternatively, the scattering probability is calculated using a "photon bomb". This technique consists of randomly generating Cherenkov photons at the electron's position, forcing the photons to scatter at an arbitrary point in the detector, propagating the photons through the detector and determining the probability of a PMT being hit. The photon bomb technique is advantageous in that the computational speed is entirely determined by the number of photons in the bomb. Unlike the numerical integration method, the bomb technique does not calculate the individual probability of hitting the i^{th} PMT as given by Equation 5.22 but rather the detector wide scattering probability (Equation 5.25).

In the scattering photon bomb calculation, photons are generated at the electron's position and given an isotropic direction, with a Cherenkov-like wavelength distribution (flat in frequency). The $g(\cos\alpha)$ angular distribution is a function of electron energy while the remaining terms in Equation 5.11 are independent of energy. By decoupling this energy dependent term from the calculation the computationally intensive terms in the scattering bomb need only be calculated once per event.

To minimize the number of photons needed in the bomb, all photons are forced to scatter. The probability that the photon will scatter along the path from the electron position to the PSUP, $m(\theta, \phi)$, is given by

$$P = \int_0^{m(\theta,\phi)} \mu' e^{-\mu' x} dx \tag{5.26}$$

where μ' is the scattering coefficient in the medium. There exists a normalization term N_s such that the probability of scattering inside the detector is one. N_s is determined in the following equation,

$$N_s \int_0^{m(\theta,\phi)} \mu' e^{-\mu' x} dx = N_s(1 - e^{-(d_d \mu'_d + d_h \mu'_h)}) = 1 \tag{5.27}$$

where is d_d and d_h are the distances traveled through D_2O and H_2O respectively, μ'_d and μ'_h are the scattering coefficient in each medium. Scattering in the acrylic is not accounted for in this model nor is it accounted for in the SNOMAN MC. Knowing N_s, the scattering point, S, is determined from the cumulative distribution of Equation 5.26.

At the scattering point, the direction of the scattered photon is determined by the angular distribution of Rayleigh scattered photons which is

$$g'(\cos \alpha_s) = 1 + \cos^2(\alpha_s) \tag{5.28}$$

where α_s is the angle between the incoming photon's polarization vector and the scattered photon's polarization vector.

To account for the loss of photons due to absorption, a trick similar to the scattering normalization is played. The probability of a photon being absorbed from the electron position to S is given by Equation 5.13. An absorption normalization term, N_a can be defined such that the probability of the photon not being absorbed is one, as seen below

$$N_a e^{-(d_d \mu_d + d_a \mu_a + d_h \mu_h)} = 1 \tag{5.29}$$

Similarly from S to the PSUP the absorption normalization term, N'_a is given by

$$N'_a e^{-(d'_d\mu_d + d'_a\mu_a + d'_h\mu_h)} = 1 \tag{5.30}$$

Second order paths such as photons that have multiple Rayleigh scatters or scattered photons that reflect off a PMT are not directly modeled in the photon bomb. Since Rayleigh scattering is largely forward scattering the probability of multiple Rayleigh scatters for a given photon is accounted to first order by not including the scattering probability in Equation 5.30. Further capitalizing on the forward scattering nature of Rayleigh scattering, the scattering-PMT reflection probability is estimated by taking the ratio of the probability of a PMT reflected hit (Appendix A.3) to the probability of a direct hit, which estimates the fraction of reflected hits given this position and direction[2].

The distances through each media used in Equations 5.27, 5.29 and 5.30 are calculated using a simplified model of the detector. This simplified model includes a spherical AV of 5.5 cm thickness, no neck and no belly plates. Additionally the photon is propagated using point-to-point geometry and refraction through the AV are not modeled. Since the number of scattering hits is roughly an order of magnitude smaller than the number of direct hits, these simplifications have negligible effects on the overall energy scale.

From the scattering point, the photon is propagated to the PSUP to determine if the photon reaches a PMT or is absorbed in the PSUP[3]. If so, the probability that the PMT will fire, given the wavelength and angle of incidence of the photon ($R_{\rm pmt}(\theta, \lambda)$)

[2]In the past second order effects were estimated from MC and loaded through the TFTK bank in word TFTK_SCAT_COR. This word is now obsolete and should be set to 1.0

[3]The photon is passed to the SNOMAN GEO code at a radius of 820 cm to determine if a PMT was hit. This is to avoid GE_TELL errors that result when making the pass closer.

is determined[4].

The detector-wide scattering probability for an isotropic photon distribution is

$$\rho'_{scat} = \frac{1}{N_\gamma} \sum_{N_\gamma} \frac{R_{\rm pmt}(\theta, \lambda)}{N_a N'_a N_s} \tag{5.31}$$

where N_γ is the number of photons in the bomb, $R_{\rm pmt}(\theta, \lambda)$ is the PMT angular and wavelength response and N_s, N_a and N'_a are the scattering and absorption normalization terms defined by Equations 5.27, 5.29 and 5.30 respectively. For photons distributed according to the Cherenkov photon angular distribution, the scattering probability of Equation 5.31 becomes

$$\rho_{scat} = \frac{1}{\sum_{N_\gamma} g(\cos\alpha)} \sum_{N_\gamma} \frac{R_{\rm pmt}(\theta, \lambda) g(\cos\alpha)}{N_a N'_a N_s} \tag{5.32}$$

Clearly, in the isotropic case, where $g(\cos\alpha) = 1$ for all α, Equation 5.32 reduces to Equation 5.31.

5.3.2 Multi-Photon Calculation

The FTK calculation of the direct, Rayleigh scattered and reflected light estimates the number of expected detected *photons* but in the detector only the number of *hits* is measured. To estimate the number of detected hits, the number of multi-photon hits (MPE), which are hits caused by two or more photons, needs to be determined. For solar neutrino energies, several simplifying assumptions are made. First, three or more photons firing a given tube is very rare and therefore neglected in FTK. Second, an MPE hit where one photon was a direct photon and the other was non-direct or

[4]The PMT response is estimated using Grey Disk and scaled by a normalization factor (see Appendix A.1) to account for differences in the overall response with 3d-PMT

where both photons were non-direct is less than 0.01% of total number of hits in an event and is also neglected. Under these assumptions, only MPE hits involving two direct photons are considered in the following MPE calculation.

Historically, when estimating the number of multi-photon hits (MPE) in a given event the distribution of the number of Cherenkov photons produced in the direction of the tube was assumed to be a Poisson distribution. Under this assumption, the Poisson probability that the PMT was hit is the probability of one or more photons hitting the tube or one minus the probability of no photons hitting the tube as seen below,

$$P_i(n \geq 1) = 1 - P(n = 0) = 1 - \exp^{-\gamma_i} \tag{5.33}$$

where n is the number of detected photons and γ_i is the Poisson mean number of expected photons. Taylor expanding the above equation and dropping terms involving three or more photons gives

$$P_i(n \geq 1) = \gamma_i - \frac{1}{2}\gamma_i^2 \tag{5.34}$$

where the γ_i^2 term is the MPE correction term. For direct light and a single photon wavelength, the Poisson mean is given by

$$\gamma_i = N_\gamma g(cos\alpha) F e^{-\mu d} R_{pmt} \frac{\Omega_0}{2\pi} \tag{5.35}$$

where N_γ is the number of Cherenkov photons, $g(cos\alpha)$ is the probability that a Cherenkov photon was produced at angle α with respect to the electron's direction, F is the probability that the photon does not reflect off the AV acrylic, $e^{-\mu d}$ is the

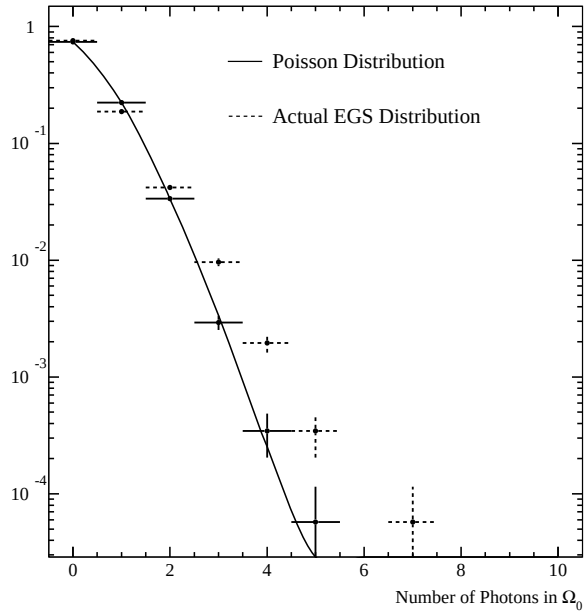

Fig. 5.3: Number of photons produced within a given solid angle for a fixed number of total Cherenkov photons for a Poisson distribution (solid lines with fit shown) and the distribution generated using EGS (dashed lines).

probability of photon attenuation, R_{pmt} is the PMT response and $\frac{\Omega_0}{2\pi}$ is the PMT's solid angle.

The above derivation is *only* valid under the assumption that the distribution of the number of photons produced for a given solid angle by the electron is a Poisson. For isotropic light, this assumption is valid but not for Cherenkov light. As seen in Figure 5.3, the actual distribution of the number of photons as determined using the Electron-Gamma-Shower (EGS) simulation in the MC (dashed line) has a longer tail than a Poisson distribution with the same mean number of photons (solid line). The difference between these distributions might seem trivial, but using a Poisson distribution underestimates the number of expected MPE hits by approximately a factor of two.

To better estimate the number of MPE hits, the PMT hit probability, P_i must be calculated without assumptions about the shape of the distribution of the number of produced photons. Assuming a single wavelength for simplicity of the calculation, the probability of the i^{th} PMT being hit by a Cherenkov photon is given by

$$P_i = \sum_{N_g=1}^{N_\gamma} \frac{dP(N_g)}{d\Omega_0} e^{-\mu d} F \sum_{n=1}^{N_g} \frac{N_g!}{n!(N_g-n)!} R_{pmt}^n (1-R_{pmt})^{(N_g-n)} \tag{5.36}$$

where N_γ is the number of Cherenkov photons in the event, N_g is the number of photons produced within the tube's solid angle, $\frac{dP(N_g)}{d\Omega_0}$ is the probability of producing N_g photons within the tube's solid angle (plotted in Figure 5.3), $e^{-\mu d}$ is the probability of photons attenuating enroute to the PMT, F is the probability of not reflecting off the AV, R_{pmt} is the PMT response and n is the number of detected photons. In other words, P_i is the product of the probability of N_g photons being produced in the direction of the tube, the probability of those N_g photons not being absorbed enroute and the binomial probability of those N_g photons being detected.

Expanding the summation of n gives the following

$$\begin{aligned} P_i \;=\; & \sum_{N_g=1}^{N_\gamma} \frac{dP(N_g)}{d\Omega_0} e^{-\mu d} F \Big(\frac{N_g!}{(N_g-1)!} R_{pmt} + \\ & \frac{N_g!}{(N_g-1)!}(-1)(N_g-1)R_{pmt}^2 + \frac{N_g!}{2(N_g-2)!} R_{pmt}^2 + \mathcal{O}(R_{pmt}^3) \Big) \end{aligned} \tag{5.37}$$

where the binomial formula of

$$(1-x)^m = 1 - mx + \frac{m(m-1)}{2!}x^2 + ... \tag{5.38}$$

has been used. The above equation can be further simplified to

$$P_i = \sum_{N_g=1}^{N_\gamma} \frac{dP(N_g)}{d\Omega_0} e^{-\mu d} F \left(N_g R_{pmt} - \frac{1}{2}(N_g^2 - N_g) R_{pmt}^2 + \mathcal{O}(R_{pmt}^3) \right) \tag{5.39}$$

Assuming the electron's energy is in a regime where the probability of three or more photons firing the same tube is small, terms of $\mathcal{O}(R_{pmt}^3)$ can be neglected.

By definition, for discrete distributions ranging from zero to infinity the mean and variance are given respectively by

$$M \equiv E[x] = \sum xP(x) \tag{5.40}$$

$$V \equiv E[x^2] - (E[x])^2 = \sum x^2 P(x) - M^2 \tag{5.41}$$

In Equation 5.39, the summation over N_g ranges from one to N_γ, but this summation can be changed to start at $N_g = 0$ since the value of P_i is zero at $N_g = 0$. Furthermore for the purpose of this calculation N_γ is essentially infinity. Using the above definitions, Equation 5.39 becomes

$$P_i = e^{-\mu d} F \left(M R_i - \frac{1}{2}(V + M^2 - M) R_i^2 \right) \tag{5.42}$$

If $\frac{dP(N_g)}{d\Omega_0}$ is Poissonian, $V = M$ and Equation 5.42 reduces to

$$P_i \;=\; e^{-\mu d} F \left(M R_i - \frac{1}{2} M^2 R_i^2 \right) \tag{5.43}$$

$$= e^{-\mu d} F N_\gamma g(\cos\alpha) \frac{\Omega_0}{2\pi} R_{pmt} - \frac{1}{2} e^{-\mu d} F \left(N_\gamma g(\cos\alpha) \frac{\Omega_0}{2\pi} R_{pmt} \right)^2 \quad (5.44)$$

where $M = N_\gamma g(\cos\alpha)\frac{\Omega_0}{2\pi}$ has been substituted. Using the Poisson assumption, we get back Equation 5.34 with the exception of a factor of the attenuation.

Equation 5.42 is very powerful in that by knowing only the mean and variance of the true $\frac{dP(N_g)}{d\Omega_0}$ distribution the correct number of MPE hits can be calculated. Unfortunately, the mean and variance of $\frac{dP(N_g)}{d\Omega_0}$ is a function of N_γ, the solid angle of the tube, $\cos\alpha$ and the electron's energy. But hope is not lost, for several simplifications can be made. First, the mean of the true $\frac{dP(N_g)}{d\Omega_0}$ distribution is equal to $N_\gamma g(\cos\alpha)\frac{\Omega_0}{2\pi}$ (the mean of the Poisson). This can be seen in the upper plot of Figure 5.4, which plots the ratio of

$$\frac{\text{Mean of true } \frac{dP(N_g)}{d\Omega_0}}{N_\gamma g(\cos\alpha)\frac{\Omega_0}{2\pi}} \quad (5.45)$$

for a given electron energy as a function of $\cos\alpha$. Furthermore, the ratio

$$R = \frac{E[N_g^2] \text{ for the true } \frac{dP(N_g)}{d\Omega_0}}{E[N_g^2] \text{ for a Poisson with mean } N_\gamma g(\cos\alpha)\frac{\Omega_0}{2\pi}} \quad (5.46)$$

can be approximated as a constant as a function of

$cos\alpha$ as seen in Figure 5.4.

With the above relationships, Equation 5.42 simplifies to

$$\begin{aligned} P_i &= e^{-\mu d} F N_\gamma g(\cos\alpha) \frac{\Omega_0}{2\pi} R_{pmt} \\ &\quad -\frac{1}{2} e^{-\mu d} F \left[(R-1) \left(N_\gamma g(\cos\alpha) \frac{\Omega_0}{2\pi} \right) + R \left(N_\gamma g(\cos\alpha) \frac{\Omega_0}{2\pi} \right)^2 \right] R_{pmt}^2 \quad (5.47) \end{aligned}$$

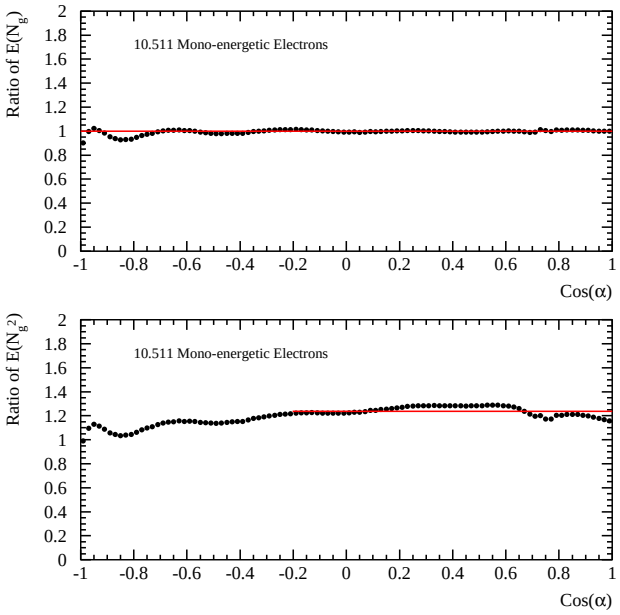

Fig. 5.4: Top Figure: Ratio of the mean of the true $\frac{dP(N_g)}{d\Omega_0}$ distribution and the mean of the Poisson distribution. Bottom Figure: Ratio of $E[N_g^2]$ for the true distribution and Poisson distribution.

R is dependent on the electron energy and can be well quantified by a third degree polynomial[5] (Figure 5.5).

For simplicity, the above equation was derived for a single wavelength. Integrating over the distribution of wavelengths for Cherenkov light, the MPE correction term becomes

$$-\frac{1}{2}\lambda_{\text{Norm}}\int_{\lambda_1}^{\lambda_2}\frac{d\lambda}{\lambda^2}\left(e^{-\mu d}F\right)\left[(R-1)\left(N_\gamma g(\cos\alpha)\frac{\Omega_0}{2\pi}\right)\right.$$
$$\left.+R\left(N_\gamma g(\cos\alpha)\frac{\Omega_0}{2\pi}\right)^2\right]\lambda_{\text{Norm}}\int_{\lambda_1}^{\lambda_2}\frac{d\lambda}{\lambda^2}R_{pmt}^2 \tag{5.48}$$

[5]The parameters of the polynomial are stored in the DFTK 4 bank

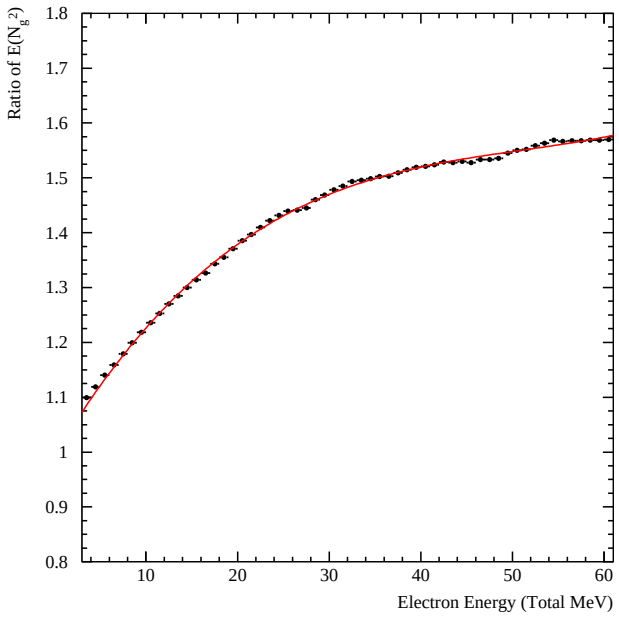

Fig. 5.5: Ratio of $E[N_g^2]$ for the true distribution and Poisson distribution as a function of electron energy.

where $\lambda_{Norm} = \frac{1}{\lambda_1^{-1} - \lambda_2^{-1}}$, $\lambda_1 = 220$ nm and $\lambda_2 = 710$ nm. This equation is not strictly correct for in the λ integration over R_{pmt}^2, the wavelength should not be weighted by $\frac{1}{\lambda^2}$ which is the initial distribution of wavelengths for Cherenkov light, rather it should be weighted by the distribution of photon wavelengths after those photons have been attenuated by the D_2O , acrylic and H_2O . For simplicity of the calculation, the $\frac{1}{\lambda^2}$ weighting factor is used as the weighting term has a small effect on the MPE correction.

Equation 5.48 nicely tracks the positional and directional dependencies of the MPE correction as indicated in Figures 5.6 and 5.7. The difference between the number of MPE hits between MC and FTK integrating over all positions and directions is 0.02% and 0.015% of the total number of hits for 5 MeV and 10 MeV electrons respectively. This is compared to a 1% shift when using the Poisson calculation (Equation 5.33).

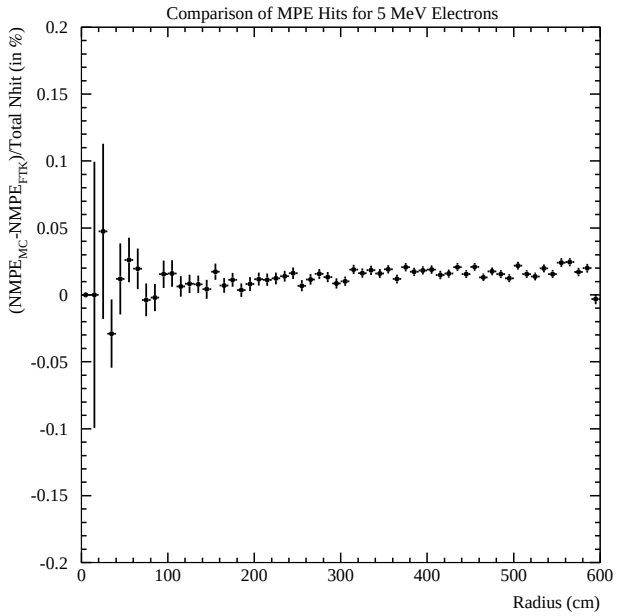

Fig. 5.6: Difference in the number of MPE hits between the MC and FTK in terms of the percent of the total number of hits in the event for 5 MeV isotropic electrons.

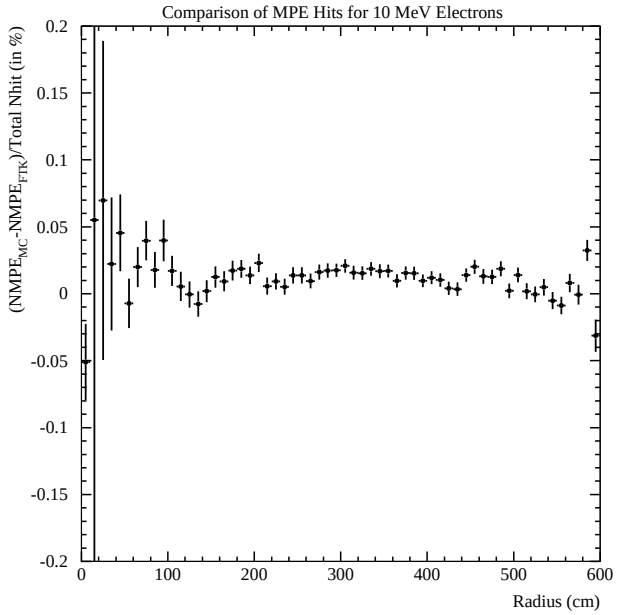

Fig. 5.7: Difference in the number of MPE hits between the MC and FTK in terms of the percent of the total number of hits in the event for 10 MeV isotropic electrons.

5.3.3 Energy Correction to the Likelihood Bias

The likelihood function in FTK only has a single data point, N_{Hit}. As a result, there is an inherent bias in the energy due to this small sample size. Toy MCs have shown that the bias is enhanced by the skewed nature of the log-normal distribution used to parameterize the number of Cherenkov photons. (Flipping the skew of the log-normal, changes the sign of the energy bias.) Furthermore, when using a symmetric distribution of the number of Cherenkov photons (such as a Gaussian), there is no bias in energy. Since the energy bias is the consequence of the likelihood function's small sample size, the MC is used to correct for it. Figure 5.8 plots the difference between the generated energy and FTK's reconstructed energy for mono-energetic electrons isotropically distributed throughout the volume. A flat correction is applied to account for the energy bias. Applying this correction, Figure 5.9 plots the residual difference between generated and FTK energy. These differences are less than 0.25%.

5.4 Cherenkov Photon and $\cos\alpha$ Distributions

5.4.1 Parameterization of the Number of Cherenkov Photons

SNO's fundamental unit of measurement is the number of Cherenkov photons produced in an event. To convert from the number of Cherenkov photons, which is a medium-dependent number, to energy in MeV, the distribution of the number of Cherenkov photons for a given electron energy was determined using SNOMAN MC. For a mono-energetic electron, this distribution is nicely parameterized by an offset (or left-right reflected) log-normal function as seen in Figure 5.10 and given by the following equation

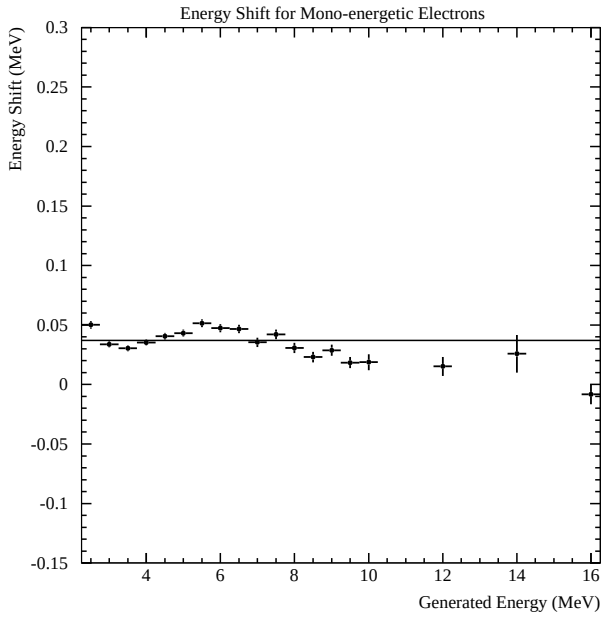

Fig. 5.8: Difference between generated energy and FTK's reconstructed energy for mono-energetic electrons as a function of generated energy. The inherent energy bias in the likelihood function is roughly 0.04 MeV.

$$P(N_\gamma) = \frac{1}{\sqrt{2\pi}(\theta - N_\gamma)\sigma} e^{\left(\frac{-(\ln(\theta - N_\gamma) - \ln\mu)^2}{2\sigma^2}\right)} \tag{5.49}$$

where N_γ is the number of Cherenkov photons, θ the offset, μ is the mean and σ is the width. The parameters of the offset log-normal function have simple dependence on energy, given by

$$\mu = a_1 + a_2 \times E \tag{5.50}$$

$$\sigma = a_3 + \frac{a_4}{E} \tag{5.51}$$

$$\theta = a_5 + a_6 \times E \tag{5.52}$$

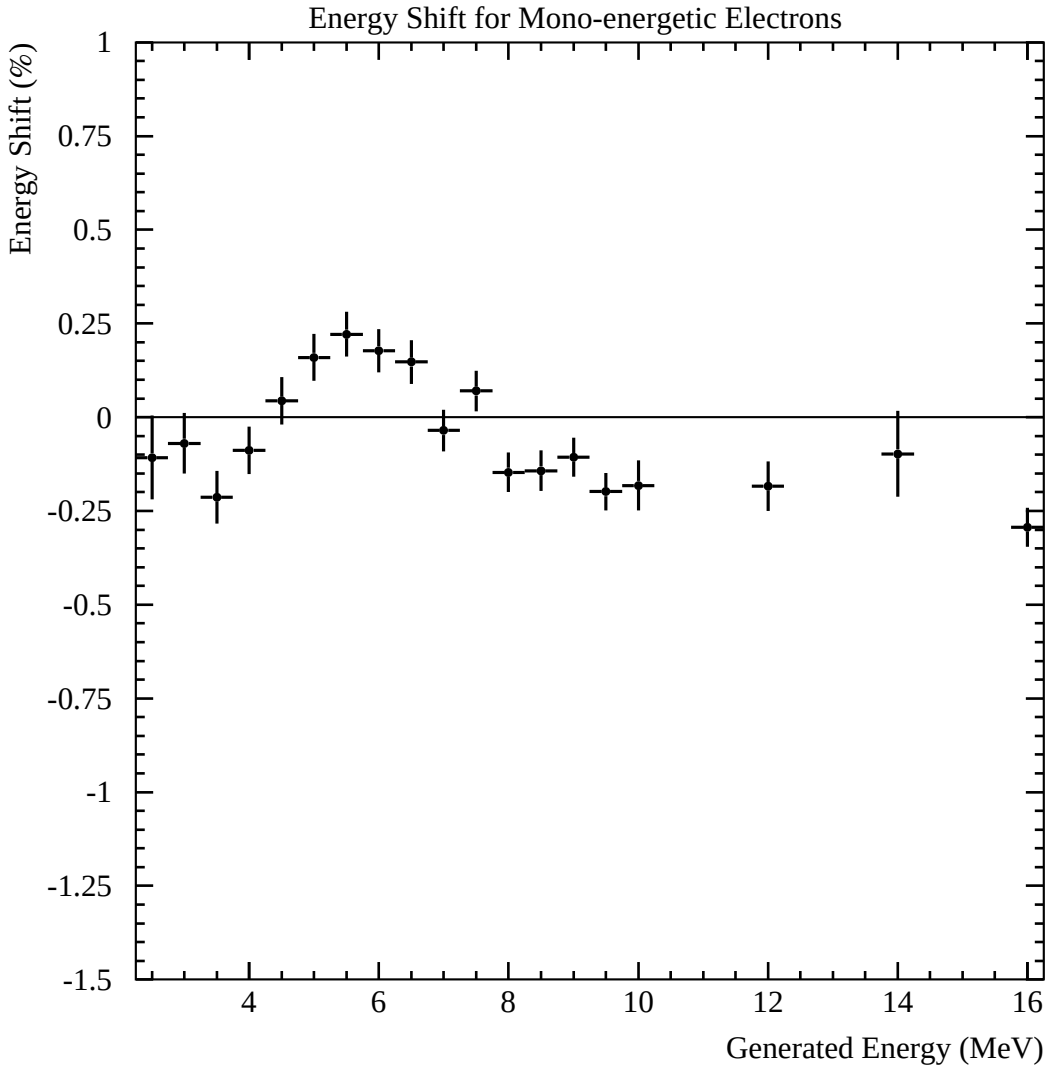

Fig. 5.9: Difference between generated energy and FTK's reconstructed energy for mono-energetic electrons in percent of the generated energy as a function of generated energy. The energy bias has been corrected. There appears to be large differences between the generated and FTK energies but this is due to the scale in the figure being very small.

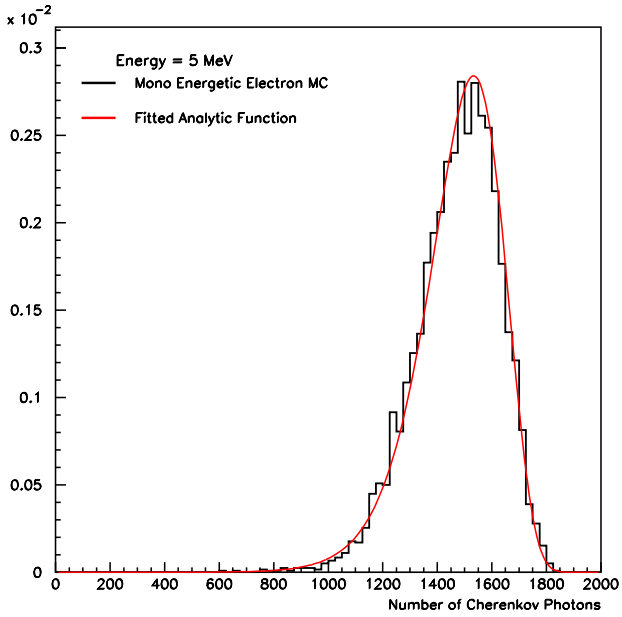

Fig. 5.10: Distribution of the number of Cherenkov photons for 5 MeV electrons with fit to an offset log-normal function.

The a_i parameters are derived from fits to mono-energetic electron Monte-Carlos of total energy E in MeV and the fitted parameters, μ, σ and θ are shown in Figure 5.11. This simple parameterization allows FTK to interpolate the distribution of the number of Cherenkov photons to any energy as seen in Figure 5.12.

In practice, the distribution of the number of Cherenkov photons can not be parameterized by the same values of a_i for SNO's energy range of 2 MeV for low energy βs to 60 MeV for the Michel electrons. To cover the entire dynamic range, the fit to mono-energetic electron MC is done in five energy ranges, 2 to 3 MeV, 3 to 6.5 MeV, 6.5 to 15 MeV, 15 MeV to 30 MeV and 30 MeV to 95 MeV[6]. At the boundaries, the variables, μ, σ, and θ are required to be first order continuous, but the derivative allowed to be discontinuous[7]. These particular energy ranges were chosen

[6]The fit parameters are stored in the DFTK 3 titles file.

[7]At the 30 MeV boundary, there is no continuity requirement. This was done in order to achieve

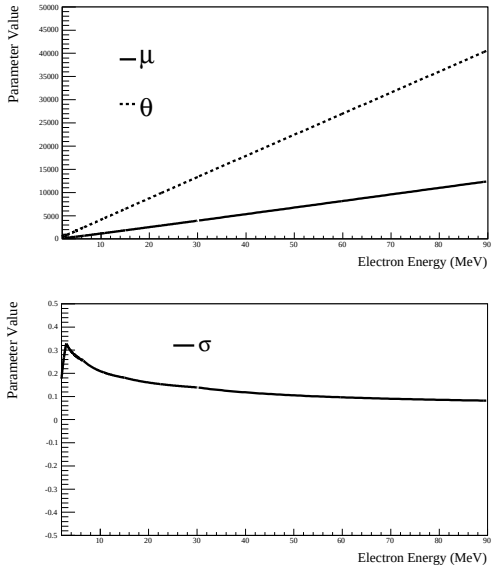

Fig. 5.11: Parameter values for μ, σ and θ as a function of electron energy used in the offset-lognormal function to describe the number of Cherenkov photons.

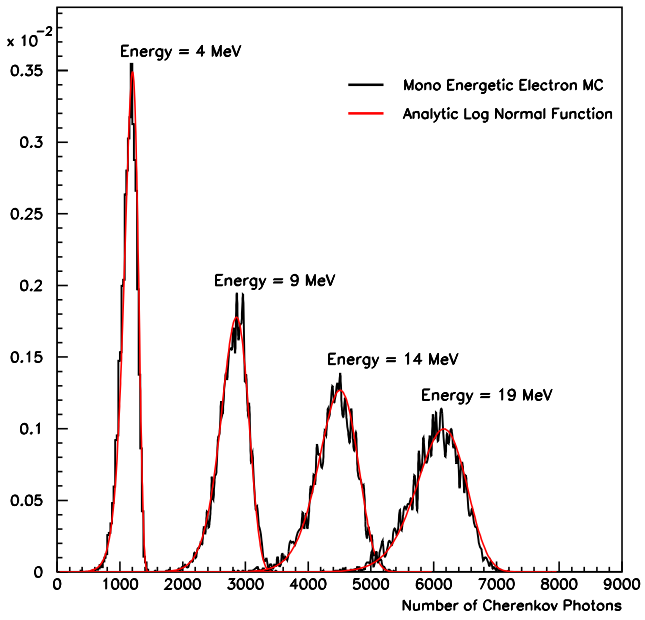

Fig. 5.12: Distribution of the number of Cherenkov photons for multiple electron energies. Also shown is the offset log-normal function using the parameterization of Equations 5.50-5.52.

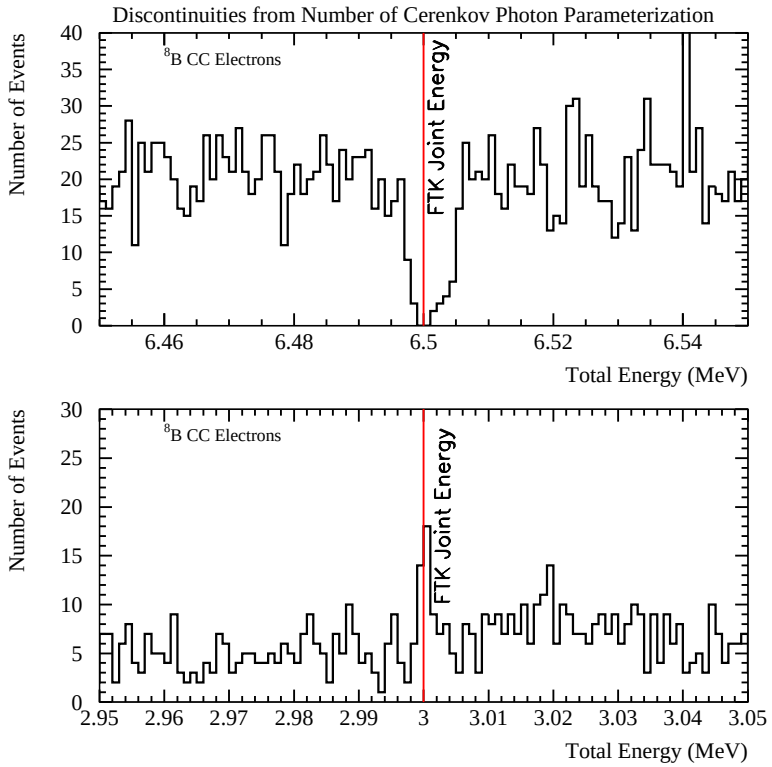

Fig. 5.13: Discontinuities in the ^{8}B CC energy spectrum at the boundaries of the log-normal parameter fit. The top figure is at the 6.5MeV boundary, the bottom figure at the 3.0MeV boundary.

because they allow for the best fit to the log-normal function.

Using ^{8}B CC MC, the fitted energy spectrum was scrutinized to determine if the piece-wise log-normal fit was creating discontinuities in the fitted energy. At the 6.5MeV boundary, there is clearly a discontinuity as seen in Figure 5.13. The size of the energy gap is 0.01 MeV, which is much smaller than any reasonable energy bin size. At the 3.0 MeV boundary, there is a slight excess of events, although the width of the excess is 0.05 MeV. In both cases, the size of the discontinuity is too small to affect the energy distribution and is therefore considered negligible.

a better fit at the higher energies

5.4.2 Parameterization of the $\cos\alpha$ Distributions

The distribution of directions of Cherenkov photons with respect to the electron direction ($\cos\alpha$) is dependent on the energy of the electron. A more energetic electron scatters fewer times and therefore the $\cos\alpha$ distribution is more sharply peaked. Using the energy information encoded in the $\cos\alpha$ distribution serves as an additional handle in the FTK likelihood. The best parameterization found for the $\cos\alpha$ distribution for a given electron energy is the following

$$P(\cos\alpha) = \begin{cases} 10^{th} \text{ degree polynomial} & \text{if } \cos\alpha \leq 0.73 \\ \text{Gaussian} & \text{if } 0.73 < \cos\alpha < 0.772 \\ 3^{rd} \text{ degree polynomial} & \text{if } \cos\alpha \geq 0.772 \end{cases} \tag{5.53}$$

At the boundaries, the $\cos\alpha$ distribution is required to be continuous, but the derivative allowed to be discontinuous. Figure 5.14 shows this fit to the $\cos\alpha$ distribution for 5 MeV electrons. The sharpening of the angular distribution with electron energy can clearly be seen in Figure 5.15 which plots the $\cos\alpha$ fit for several different energies.

Unlike the distribution of the number of Cherenkov photons, parameters of the fit to the $\cos\alpha$ distribution have no well defined energy dependence. Instead, the $\cos\alpha$ distribution is fit at many different mono-energetic electron energies and a linear interpolation is used for energies in between the fit points. Specifically, the fitted electron energies (in total energy, kinetic energy plus the electron rest mass of 0.511 MeV) are 2.011 MeV to 10.011 MeV with 0.1 MeV spacings, 10.011 MeV to 20.011 MeV with 0.25 MeV spacing, 20.011 MeV to 50.011 MeV with 1.0 MeV spacing and 50.011 MeV

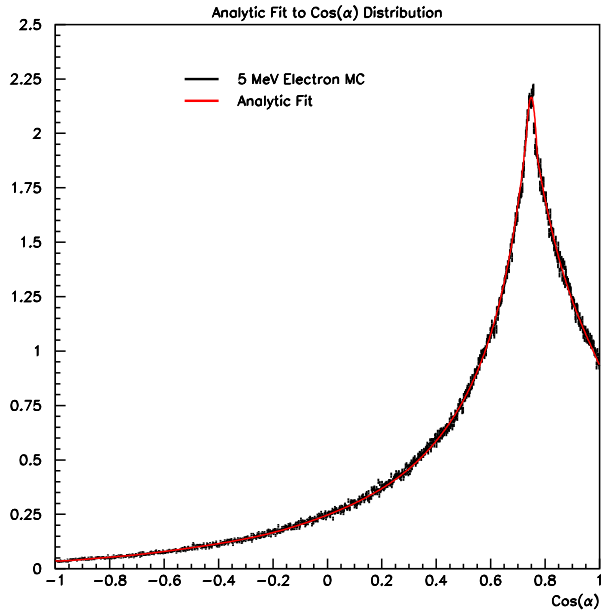

Fig. 5.14: $\cos\alpha$ distribution for 5 MeV electrons with parameterization fit shown.

to 95.011 MeV with 5.0 MeV spacings. Changing the spacing between the electron energies used in the fit is a matter of practicality, in order to reduce the number of parameters needed to be stored[8]. This change in spacing in the $\cos\alpha$ fits does not create any discontinuities in the fitted FTK energy, as can be seen in Figure 5.16, which highlights the 10.011 MeV boundary.

5.5 Determining PMT Reflectivity and Rayleigh Scattering from ^{16}N Data

FTK's large timing window presents new problems in tuning the MC to agree with the data. The prompt timing window used by RSP (see Section 3.2.1) includes

[8]The $\cos\alpha$ parameters are stored in titles bank DFTK 4

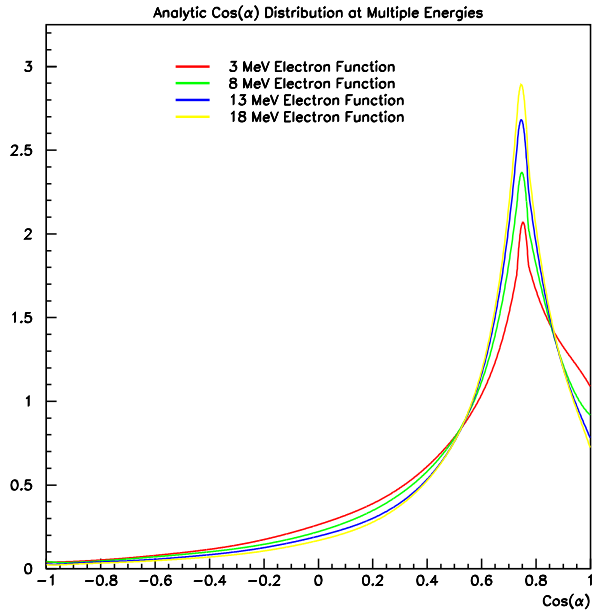

Fig. 5.15: $\cos\alpha$ fits for several electron energies. The $\cos\alpha$ distribution sharpens with larger electron energies.

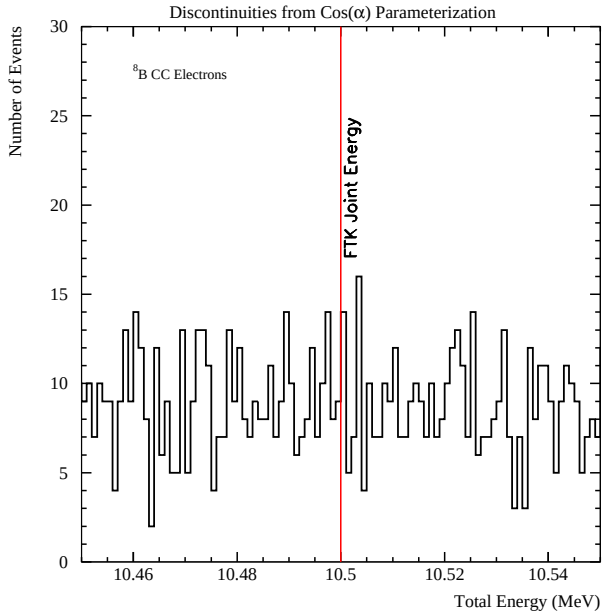

Fig. 5.16: Search for discontinuities in the energy spectrum of ^{8}B CC electrons due to changes in the $\cos\alpha$ linear interpolation step size. Ten MeV is where the first change in step size takes place.

just direct hits with a fraction of Rayleigh scattered hits and therefore only a single parameter, the collection efficiency, is needed to match MC to calibration data. For FTK, discrepancies between data and MC can be due to an overall collection efficiency or normalization differences in non-direct light (Rayleigh scattering, AV reflections and PMT reflections). As differences in the non-direct light between data and MC can affect FTK's energy resolution, a maximum likelihood fit using the PMT time residuals of ^{16}N data and MC was developed to tune the late light in the MC. The largest discrepancy between data and MC in the late light is the PMT reflections. To tune the amount of PMT reflections in the MC, the reflectivity of the PMT concentrators is scaled in a way that changes the overall number of PMT reflected hits but preserves the PMT angular response and the angular distribution of the reflected photons. Additionally this section discusses comparisons of the amount of Rayleigh scattered hits between data and MC.

5.5.1 Increasing PMT Reflections in the 3d-PMT Model

Since the 3d-PMT model of the phototube in the MC propagates individual photons through the complicated tube geometry to determine the photon's fate (see Section 2.4), increasing the overall number of PMT reflections but leaving the angular distribution of those reflected photons the same is not a straightforward problem because this PMT model has no easily tunable parameters. In SNO's phototubes, a photon can reflect out of the PMT bucket either by reflecting from the glass, reflecting once from the concentrator, reflecting twice from the concentrator or in more rare cases reflecting more than twice from the concentrator. Figure 5.17 shows the time residual distribution for each of these types of PMT reflections. The 35° peak (peak

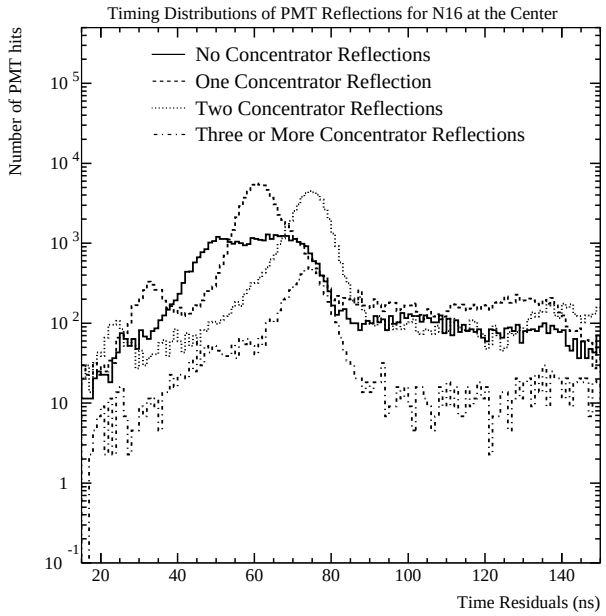

Fig. 5.17: Time residual distributions of PMT reflections for ^{16}N at the center. Note that majority of the light which is in the prompt peak is not shown in this figure.

around 60 ns) is mainly composed of single reflections from the concentrator, while the 180° peak (peak around 75 ns) usually has two reflections from the concentrator.

The overall number of PMT reflected hits can be scaled in the MC either by changing the reflectivity of the concentrator or by varying the photo-cathode response over the PMT face in a way that would change the ratio between the number of prompt photons and PMT reflected photons. Since the 180° reflections generally have two reflections from the concentrator, increasing the concentrator reflectivity will increase the 180° reflections by a factor of two with respect to the 35° reflections, which is motivated by the data. As shown in Figure 5.18, although the 35° reflections in the MC are shifted in time with respect to the data, the area of that peak is roughly 7% smaller in the MC compared to data. On the other hand, the 180° peak is 15% smaller in MC than in data.

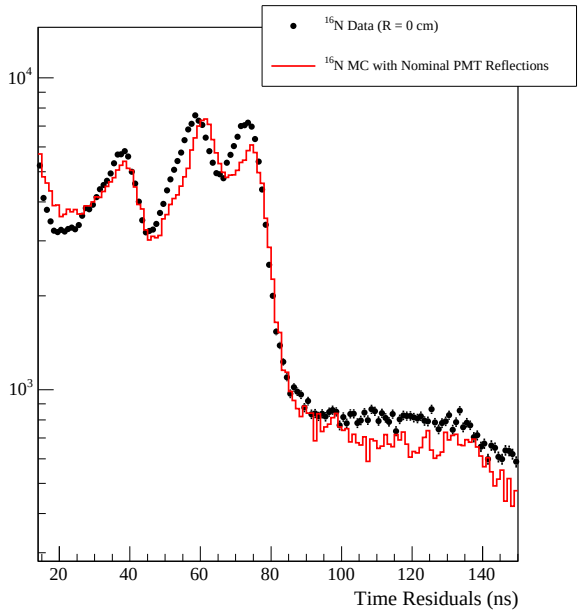

Fig. 5.18: Time residual distribution for ^{16}N data and MC at the center. The 35° degree peak is located at 60 ns, the 180° peak is located at 75 ns.

Scaling the concentrator reflectivity will change not only the number of photons that reflect out of the PMT bucket but also the number of photons that strike the concentrator and reflect inward to the photo-cathode. Thus, the reflectivity of the concentrator has to be modified in such a way that does not destroy the angular response of the PMT. Let $P_{35}(\kappa)$, where κ is the concentrator reflectivity, be the probability of a photon reflecting once from the concentrator and out of the PMT bucket. $P_{35}(\kappa)$ is linearly dependent on the concentrator reflectivity, κ. Additionally, let $P_{prompt}(\kappa)$ be the probability of a photon striking the photo-cathode. $P_{prompt}(\kappa)$ is composed of a constant plus linear reflectivity term, accounting for photons that strike the photo-cathode directly and photons that strike the concentrator and then the photo-cathode. This is expressed as

$$P_{prompt}(\kappa) = N_{pc} + N_c(\kappa) \tag{5.54}$$

where N_{pc} is the fraction of prompt photons that do not strike the concentrator and N_c is the fraction of prompt photons that do strike the concentrator. To increase the number of PMT reflections, we want to find a concentrator reflectivity κ' such that the number of PMT reflected hits with respect to the number of prompt hits is increased by N_p, as shown below

$$\frac{P_{35}(\kappa')}{P_{prompt}(\kappa')} = N_p \frac{P_{35}(\kappa)}{P_{prompt}(\kappa)} \tag{5.55}$$

Assuming that the concentrator reflectivity can be scaled by a constant factor, s for all angles in which the photon might strike the concentrator[9] the scaled reflectivity is $\kappa' \equiv s\kappa$. With this definition and Equation 5.54, the above equation becomes

$$\frac{sP_{35}(\kappa)}{N_{pc}(1+s\beta)} = N_p \frac{P_{35}(\kappa)}{N_{pc}(1+\beta)} \tag{5.56}$$

where $\beta \equiv \frac{N_c}{N_{pc}}$. Solving for the reflectivity scale factor, s yields

$$s = \frac{N_p}{1+(1-N_p)\beta} \tag{5.57}$$

The value of N_p is determined in a maximum likelihood fit to the ^{16}N time residual distribution (see Section A.5.1) and β which is a function of the angle of incidence and the wavelength of the photon is calculated from the MC[10] as seen in Figure 5.19.

[9] For photons striking the concentrator at large angles with respect to the concentrator normal this is not true. In these cases, the scale factor is capped so that the concentrator reflectivity is never greater than one.

[10] β is stored in the PRAT titles bank in 1° angular bins and 10 nm wavelength steps

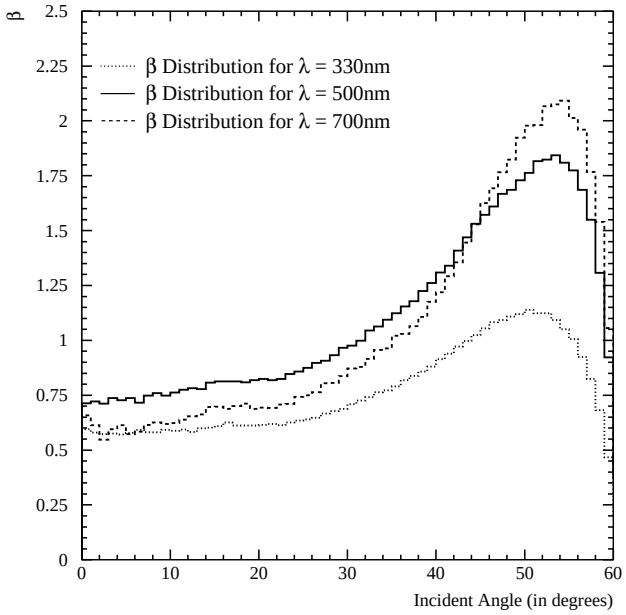

Fig. 5.19: β as a function of the angle of incidence of the photon for several different wavelengths.

Scaling the PMT reflectivity with this method correctly increases the overall number of PMT reflected hits while preserving the ratio of 35° and 180° reflections (Figure 5.20). At large angles of incidence the PMT angular response is slightly distorted by this scaling in concentrator reflectivity and is corrected by tuning the photocathode response in the 3d-PMT model [58]. To determine the PMT reflectivity scale factor, N_p, the time residual distributions for direct, scattered, av reflected and PMT reflected hits (derived from ^{16}N MC) are fit to the ^{16}N data. Details of this fit can be found in Appendix A.5.1.

Scaling the concentrator reflectivity by N_p, the MC timing residual distributions has significantly better agreement to the data. Figures 5.20-5.22 compare MC with nominal PMT reflections and MC with the PMT reflections increased by the fitted value of N_p for several different source positions. By changing the concentrator re-

flectivity, the PMT reflections in the MC are in much better agreement with the data.

5.5.2 Determining Rayleigh Scattering with ^{16}N Data

To a first approximation, the sum of the number of direct and Rayleigh scattered hits should be independent of the Rayleigh scattering length making FTK very insensitive to mis-measurement of the scattering length. Yet, an incorrect measurement of the scattering length does lead to differences in FTK's and RSP's measurement of the energy because the RSP prompt window does not include all Rayleigh scattered light. To determine the scattering coefficient in the detector, the ever familiar ^{16}N timing residual distribution is utilized. Ideally a masked laserball (a collimated laserball beam used to study scattering) or laserball timing residual distribution could be used for this analysis. The masked laserball was not deployed in the D_2O phase and the MC modeling of the laserball for times later than 10 ns is very poor. Since ^{16}N is used to estimate the energy systematic uncertainties, this analysis serves only to demonstrate whether or not the scattering length in the detector is consistent with the MC value.

Using the masked laserball in the salt phase, Jeanne Wilson showed that the scattering length should be 1.289 times larger than the nominal MC value [68]. For the D_2O phase, this value appears to be too large as can be seen in Figure 5.20, where Rayleigh scattering dominates in the region of 15 to 30 ns. Using the maximum likelihood technique discussed in Appendix A.5.1 and fitting for N_c and N_r in the region of -10 to 50 ns with 1 ns bins, the preferred Rayleigh scattering length is consistent with the nominal MC value (Figure 5.23). Furthermore, extractions of

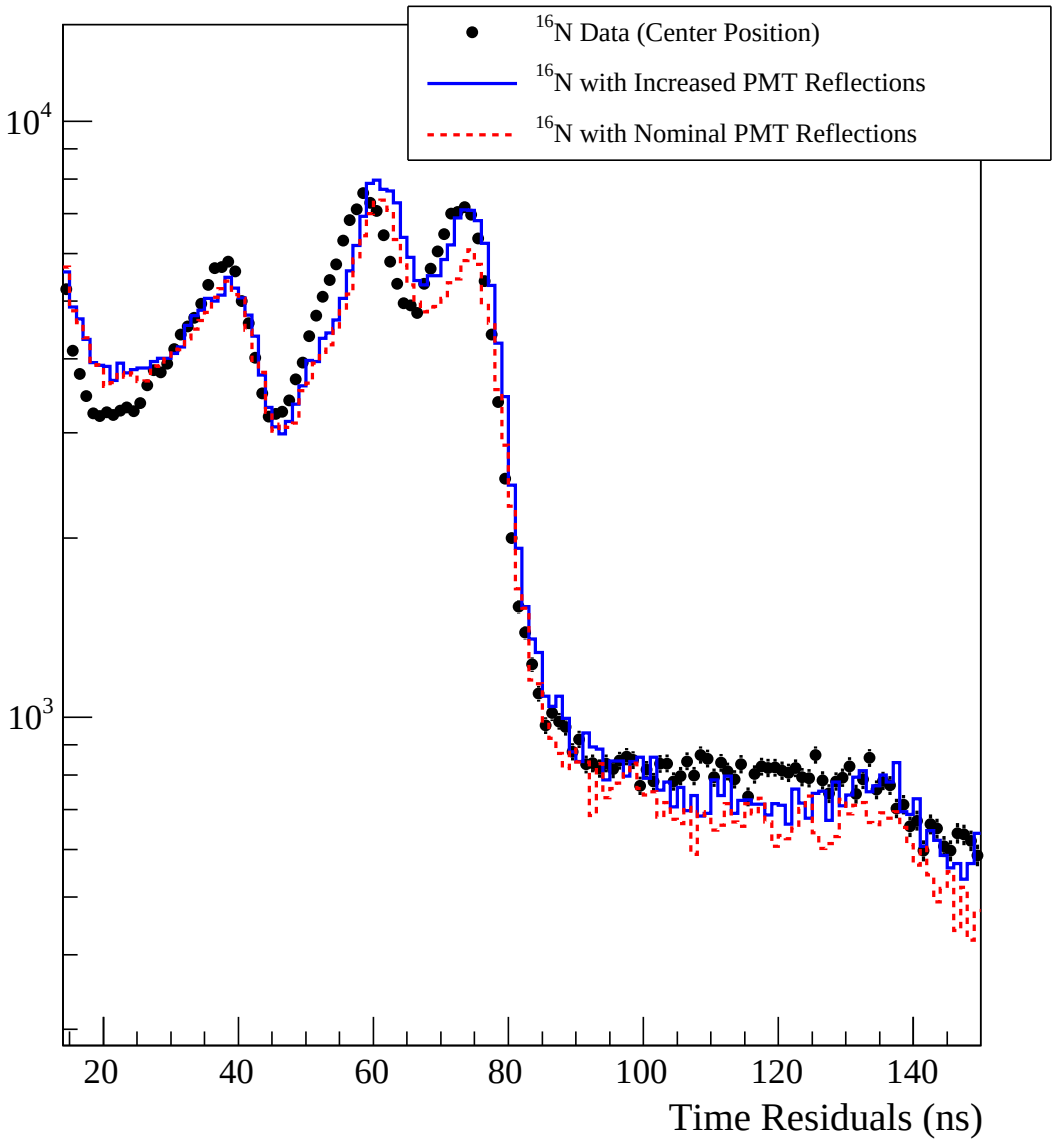

Fig. 5.20: Late light timing residual distributions for ^{16}N data (points), MC with nominal PMT reflections (red-dashed) and MC with PMT reflections increased by 8.3% (blue-solid) in the center. The distributions were normalized to equal area in the prompt peak (-2 to 2 ns).

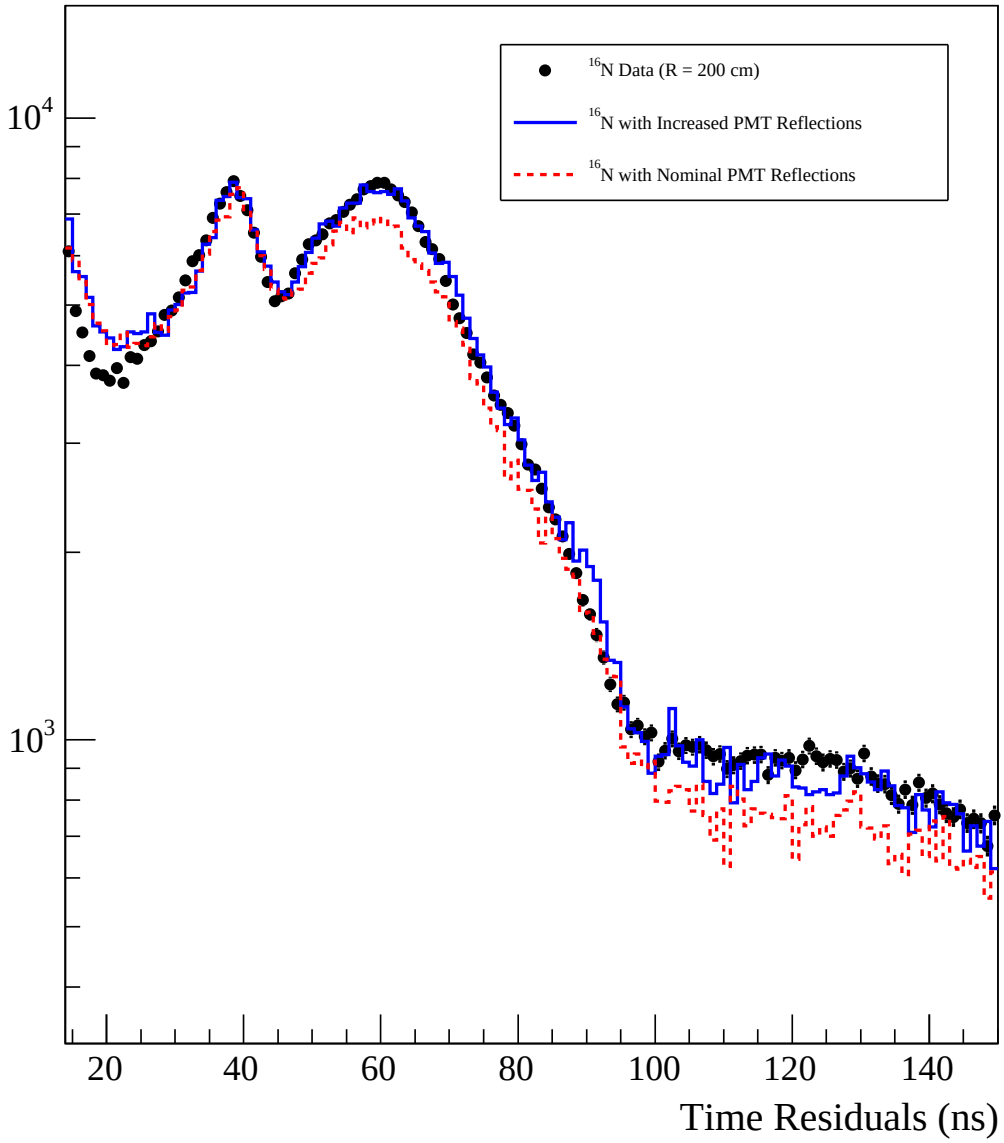

Fig. 5.21: Late light timing residual distributions for ^{16}N data (points), MC with nominal PMT reflections (red-dashed) and MC with PMT reflections increased by 8.3% (blue-solid) at 200 cm. The distributions were normalized to equal area in the prompt peak (-2 to 2 ns).

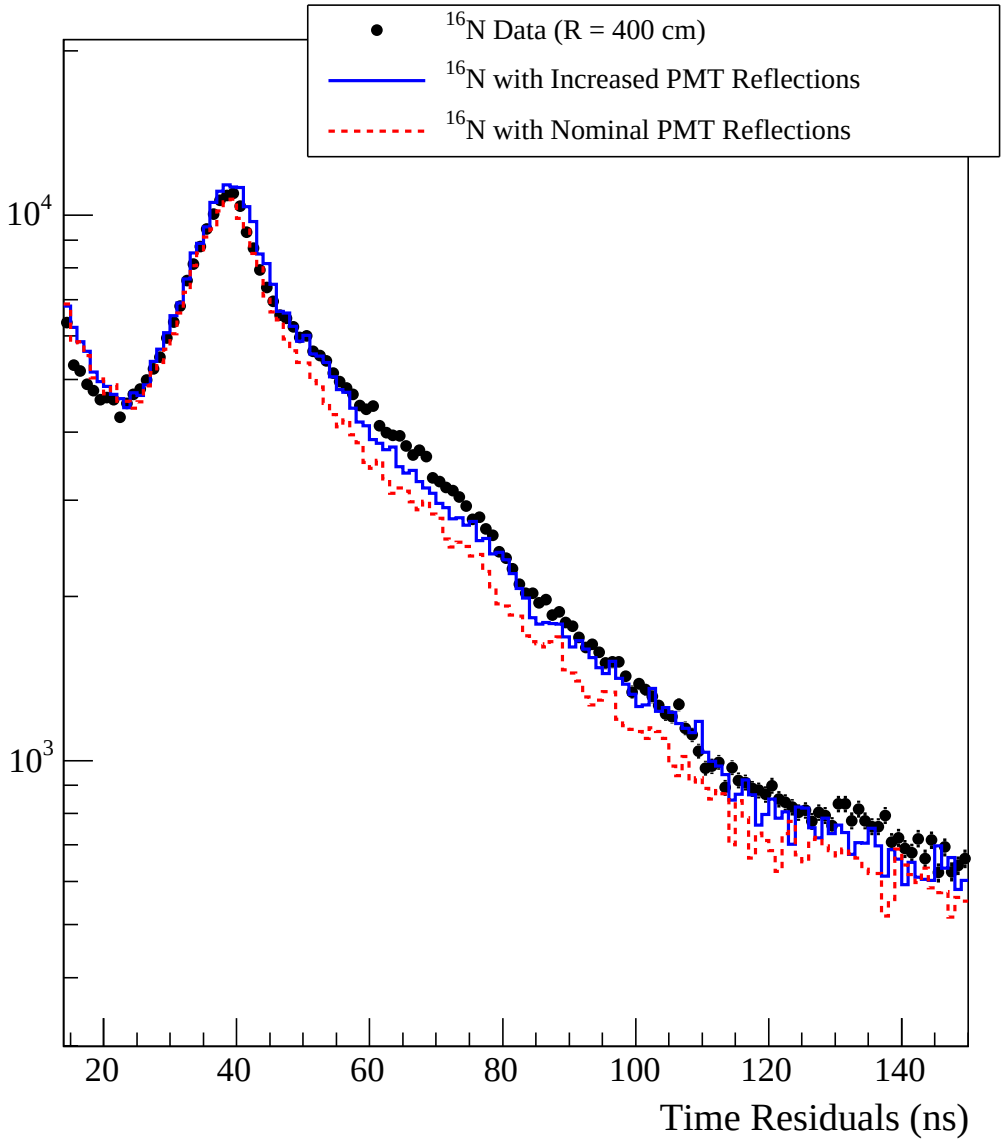

Fig. 5.22: Late light timing residual distributions for ^{16}N data (points), MC with nominal PMT reflections (red-dashed) and MC with PMT reflections increased by 8.3% (blue-solid) at 400 cm. The distributions were normalized to equal area in the prompt peak (-2 to 2 ns).

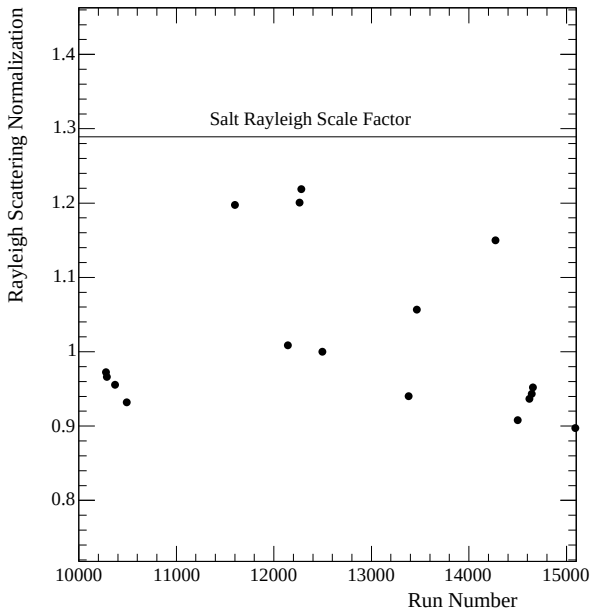

Fig. 5.23: Rayleigh scattering normalization in the D_2O phase using a maximum likelihood fit to ^{16}N data and MC timing residuals as a function of run number. The MC nominal scale factor is 1.0. The salt masked laserball measurement is also shown.

the optical attenuations in the D_2O using the laserball also prefers the nominal MC scattering length [69]. In light of these suggestive conclusions and with the lack of a proper calibration source for this measurement, it was decided to set the scattering length for the D_2O phase to the nominal MC value.

5.6 FTK Performance

As seen in Figure 5.24, FTK's prediction of the number of hits reproduces the expected number of hits determined from mono-energetic electron MC. The MC N_{Hit} distribution seen in the figure required approximately 2 hours of CPU time where as FTK's calculation of the expected number of hits took less than a second. The

accuracy of FTK's prediction of the number of hits is evaluated by comparing this prediction to the number of direct hits, Rayleigh scattered hits, AV reflected and PMT reflected hits in the MC. To determine the number of direct and non-direct hits in the MC, every photon in an event that fires a tube in the MC is tracked from the electron's position to the PMT to determine if the photon scattered or reflected enroute. Figure 5.25 shows the difference in the number of total hits observed in the MC to the total number of hits FTK predicts per MeV for 5 MeV mono-energetic electrons in the D_2O phase as a function of ρ, where $\rho = \left(\frac{r}{r_{av}}\right)^3$ and r_{av} is the radius of the AV. Also shown is the difference in the number of direct hits per MeV. A negative difference between MC and FTK corresponds to FTK over-predicting the number of hits, which results in an under-prediction of the energy. FTK's prediction of the number of total and direct hits is accurate to 0.5% and flat as a function of ρ to 1%. The structure in ρ is due to residual differences between the 3d-PMT angular response (used in the MC, see Section 2.4) and the Grey Disk angular response (used by FTK to predict the hit probability).

Similarly, Figure 5.26 plots the difference between the MC and FTK for non-direct light; Rayleigh scattering, PMT reflections, AV reflections from the first and second AV boundaries, noise and other hits, for 5 MeV electrons as a function of ρ. Other hits are defined as any type of reflection or scattering that FTK does not currently model. The only significant interactions not modeled by FTK are reflections from the PSUP steel and reflections from the Kevlar ropes, which together account for less than 0.06 hits for 5 MeV electrons. For non-direct light, FTK has excellent agreement with the MC for all radii in the D_2O volume.

In Figures 5.27 and 5.28 showing similar comparisons for 10 MeV electrons in the D_2O phase, FTK continues to correctly estimate the number of direct and non-

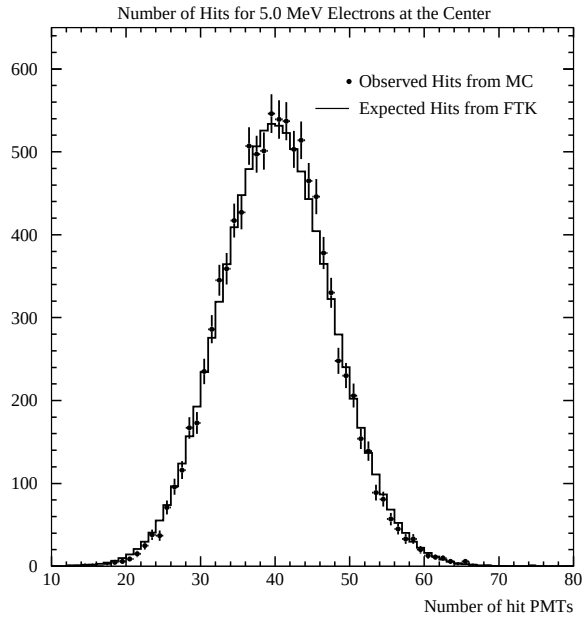

Fig. 5.24: Distribution of number of hits for 5 MeV electrons at the center of the detector determined using the MC. The solid line distribution is FTK's prediction of the number of hits.

direct hits. In the salt phase, the residual difference between 3d-PMT and Grey Disk angular response is much less significant and therefore, as seen in Figure 5.29, this results in better agreement between MC and FTK as a function of ρ. Figure 5.30 compares MC and FTK for non-direct light for 5 MeV electrons in the salt phase, which also shows good agreement.

FTK's energy scale in the MC as a function of ρ is also flat in the D_2O phase to 1%. Figures 5.31 and 5.32 show this energy scale normalized by the generated electron energy for 5 and 10 MeV electrons. As with the number of predicted hits, the radial structure is due to 3d-PMT and Grey Disk angular response differences. In Figure 5.33, which shows the energy scale in the salt phase as a function of ρ the radial profile is much flatter. The bottom plots in these figures show FTK's energy

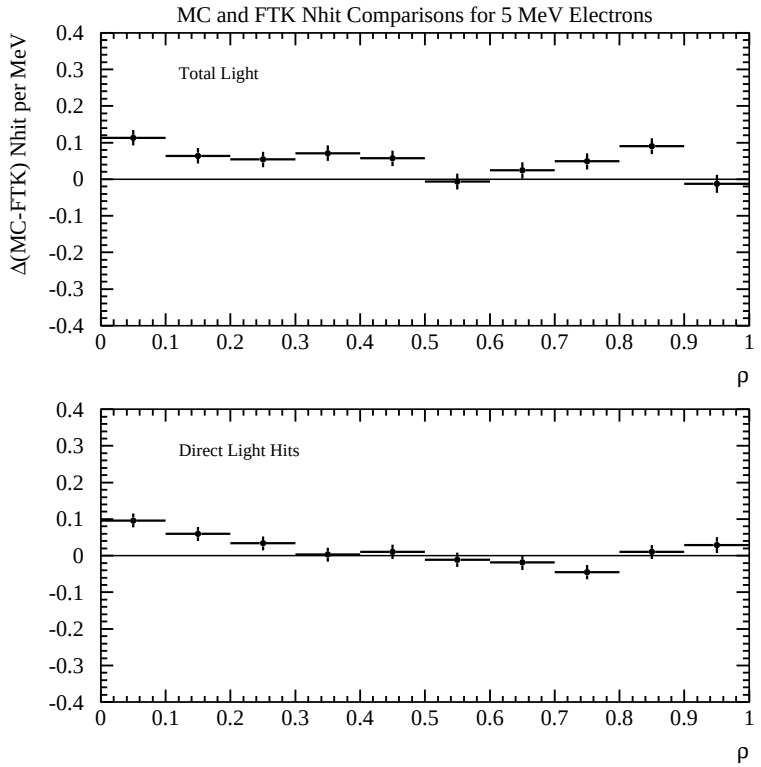

Fig. 5.25: Difference in predicted hits per MeV between MC and FTK for the number of total hits (top) and the number of direct hits (bottom) for 5 MeV electrons in the D_2O phase.

resolution as a function of ρ. As seen in Figure 5.34 FTK's resolution is approximately 6% narrower at 5 MeV than the RSP resolution in previous measurements

5.7 Summary

The FTK energy fitter is a new approach to estimating the energy of events in SNO which uses the difficult to model late light in addition to the prompt light. As a result of including this light, the FTK's energy resolution is approximately 6% better than prompt light energy estimators. Previous MC studies indicated that an improvement

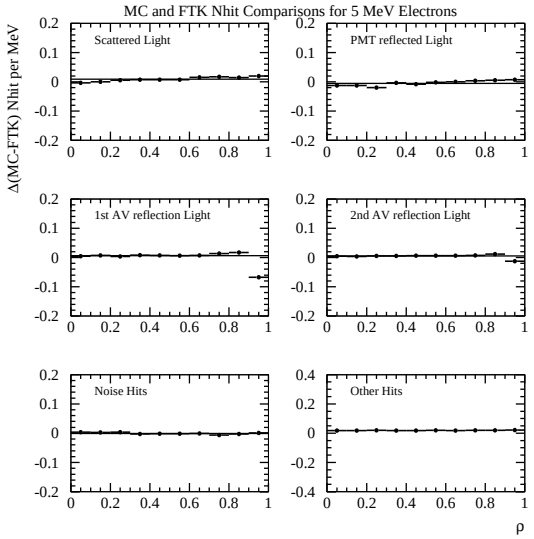

Fig. 5.26: Difference in predicted hits per MeV between MC and FTK for the number of non-direct hits, including Rayleigh scatter hits, PMT reflections, AV reflections, noise and other hits for 5 MeV electrons in the D_2O phase.

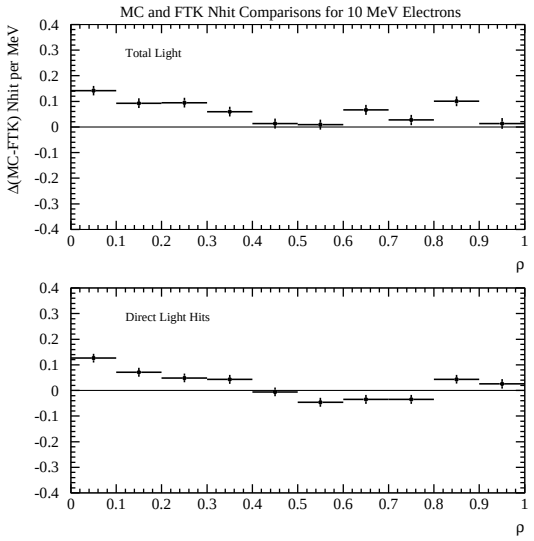

Fig. 5.27: Difference in predicted hits per MeV between MC and FTK for the number of total hits (top) and the number of direct hits (bottom) for 10 MeV electrons for D_2O phase.

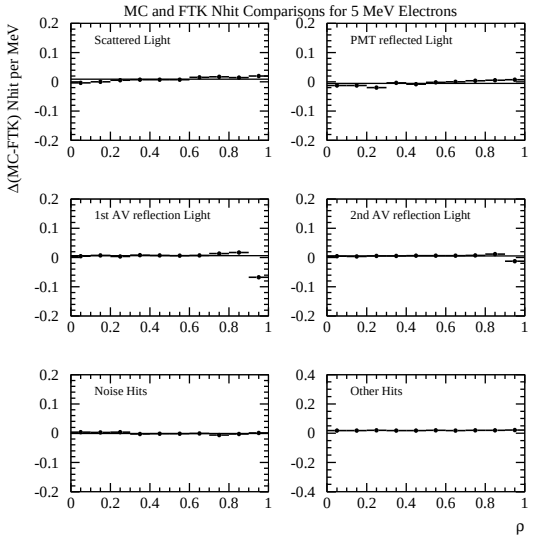

Fig. 5.28: Difference in predicted hits per MeV between MC and FTK for the number of non-direct hits, including Rayleigh scatter hits, PMT reflections, AV reflections, noise and other hits for 10 MeV electrons in the D_2O phase.

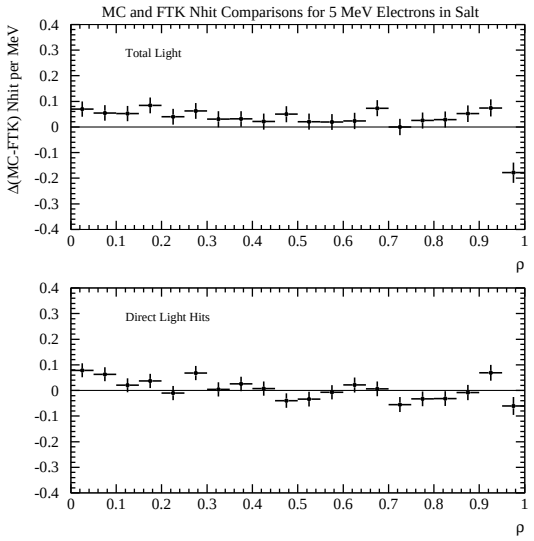

Fig. 5.29: Difference in predicted hits per MeV between MC and FTK for the number of total hits (top) and the number of direct hits (bottom) for 5 MeV electrons in the salt phase.

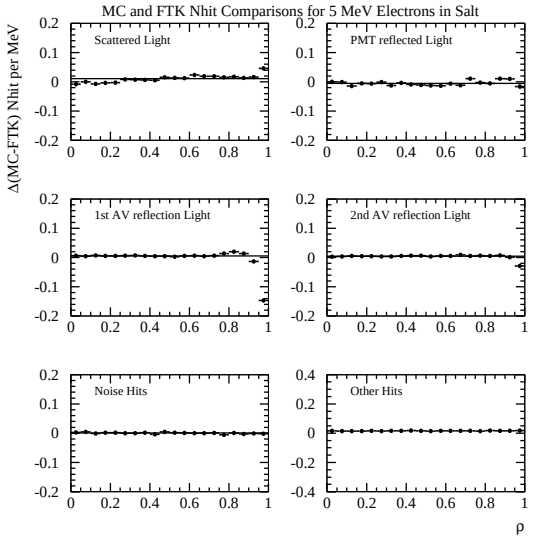

Fig. 5.30: Difference in predicted hits per MeV between MC and FTK for the number of non-direct hits, including Rayleigh scatter hits, PMT reflections, AV reflections, noise and other hits for 5 MeV electrons in the salt phase.

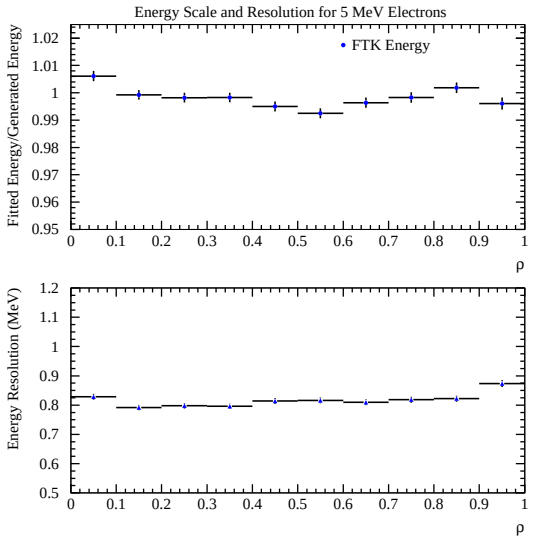

Fig. 5.31: Top Figure: FTK fitted energy over the generated energy for 5 MeV electrons as a function of ρ for the D_2O phase. Bottom Figure: FTK energy resolution as a function of ρ for the D_2O phase.

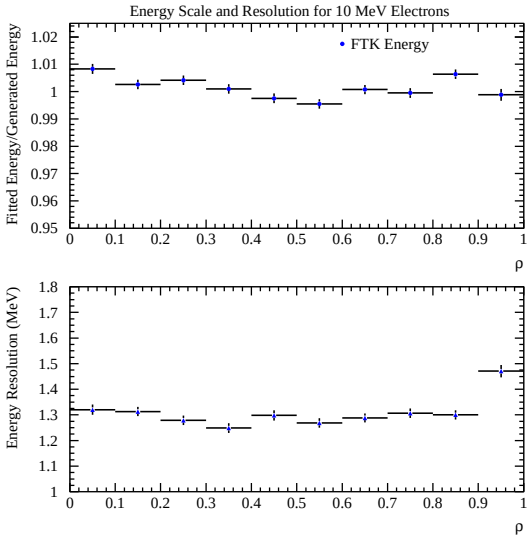

Fig. 5.32: Top Figure: FTK fitted energy over the generated energy for 10 MeV electrons as a function of ρ for the D_2O phase. Bottom Figure: FTK energy resolution as a function of ρ for the D_2O phase.

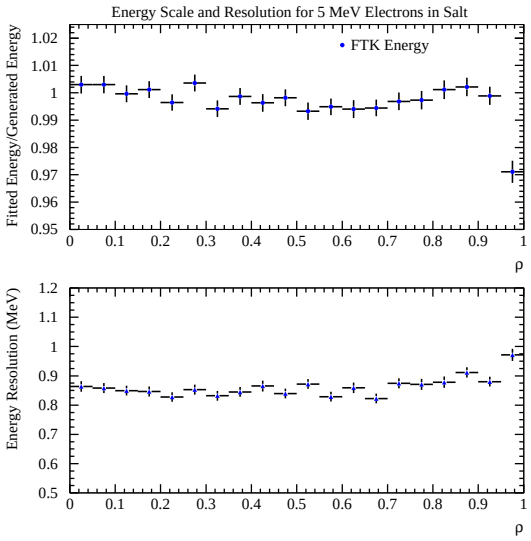

Fig. 5.33: Top Figure: FTK fitted energy over the generated energy for 5 MeV electrons as a function of ρ for the salt phase. Bottom Figure: FTK energy resolution as a function of ρ for the salt phase.

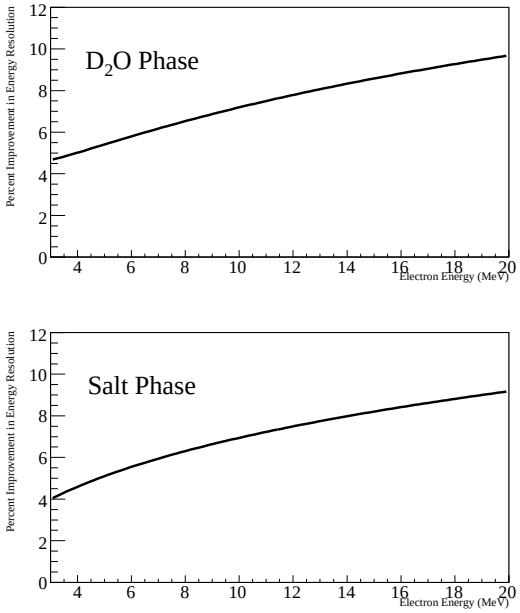

Fig. 5.34: Percent improvement in energy resolution between FTK and RSP for the D_2O (top figure) and Salt phases (bottom figure).

in energy resolution of this magnitude would reduce the number of ^{214}Bi and ^{208}Tl backgrounds in the signal region by 60% (see Section 4.2). Figures 5.35 and 5.36 show the number of background events above 4 MeV for MC ^{214}Bi and ^{208}Tl respectively in the salt phase using the prompt light energy estimator and FTK energy. With this new energy estimator, the reduction in the integrated number of background events above 4 MeV is reduced by roughly a factor of 2.5. Reduction of background events in the signal region is critical for the low energy ^{8}B flux and CC and ES spectral measurements to be discussed in Chapter 9.

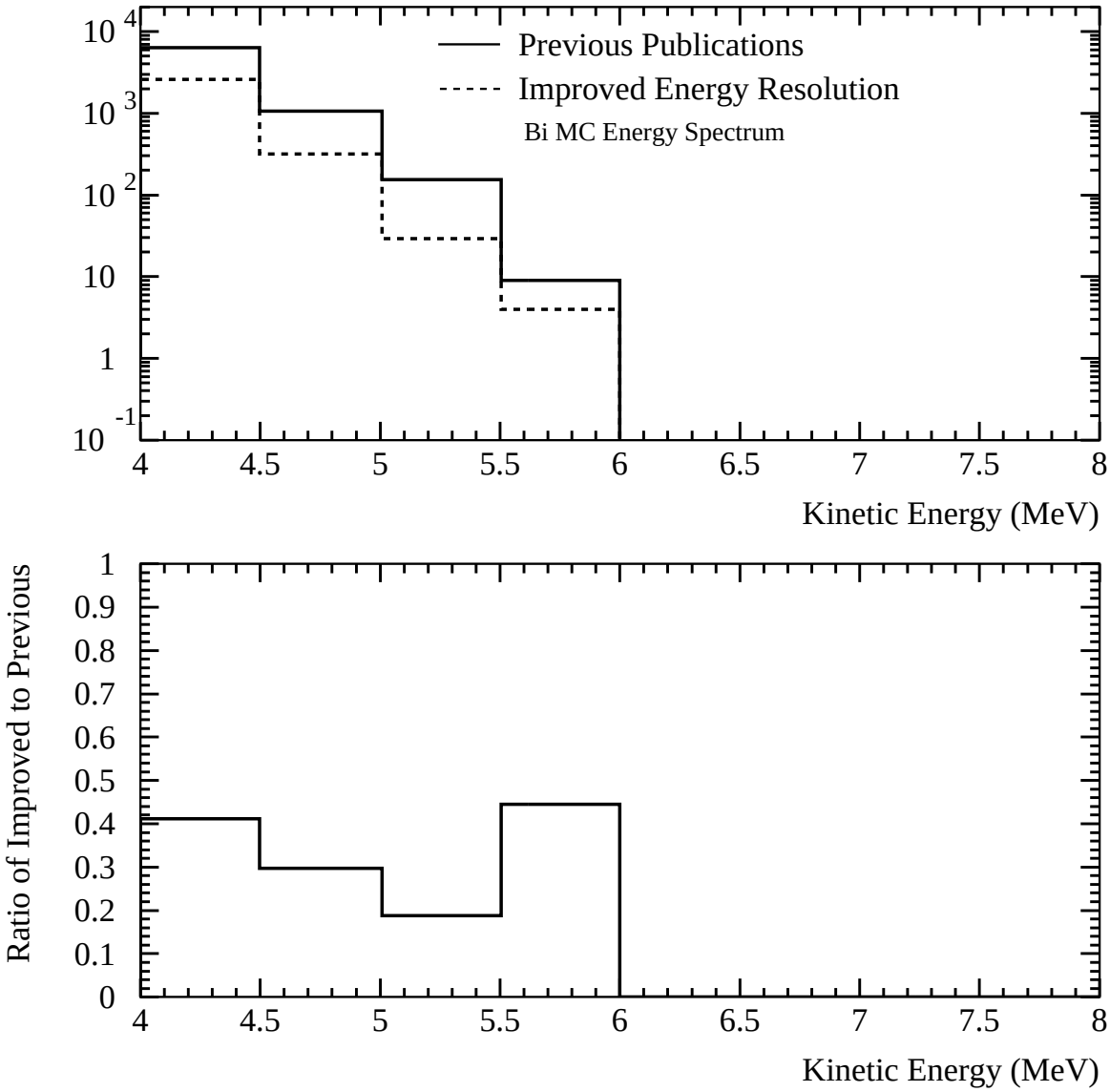

Fig. 5.35: Energy spectrum of ^{214}Bi MC events inside the fiducial volume using the RSP energy (solid line) and FTK energy (dashed line). The lower figure is the ratio of two spectra.

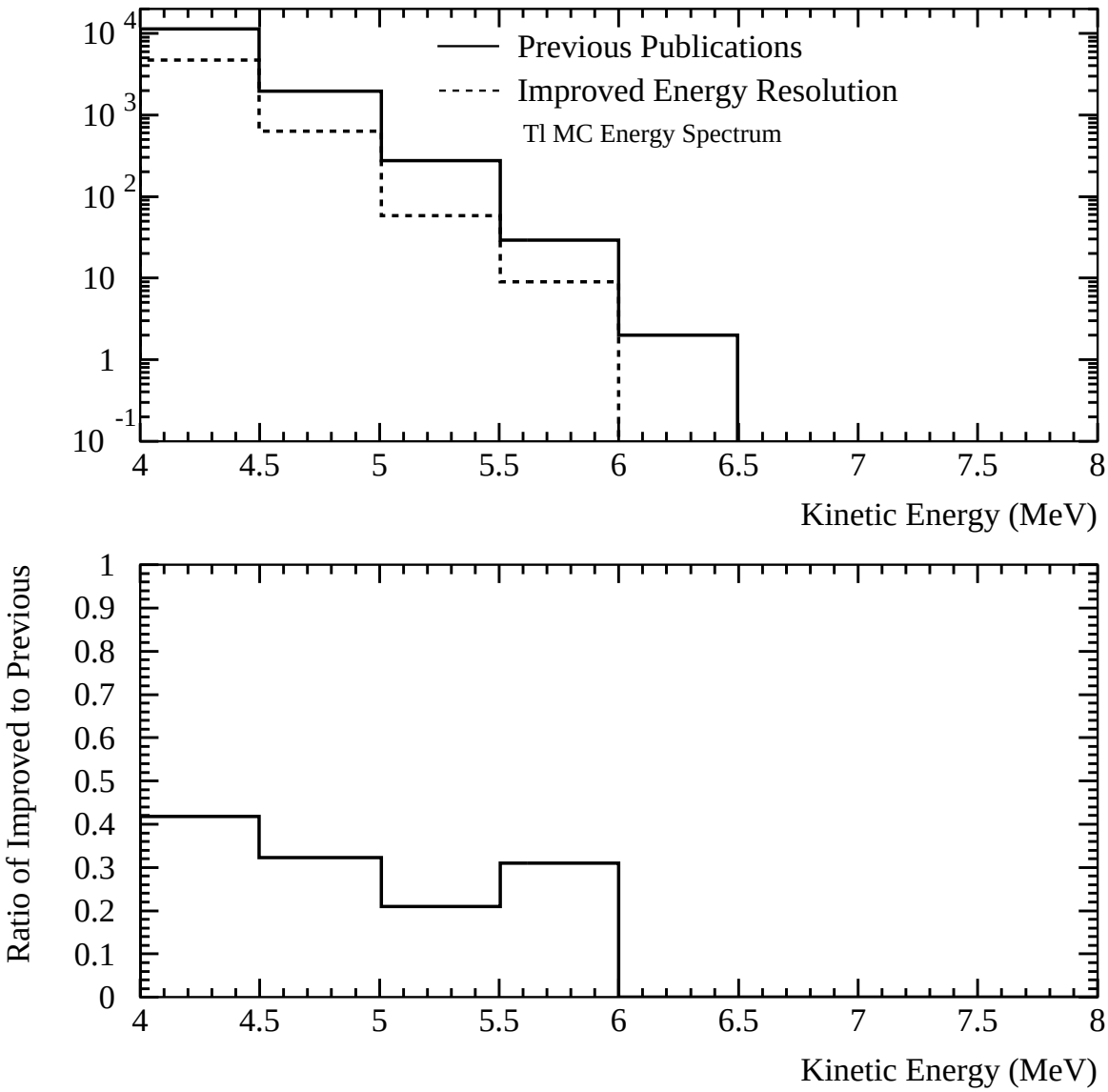

Fig. 5.36: Energy spectrum of ^{208}Tl MC events inside the fiducial volume using the RSP energy (solid line) and FTK energy (dashed line). The lower figure is the ratio of two spectra.

Ch. 6

Determining Energy Systematic Uncertainties

The previous chapter demonstrates that the FTK energy estimator successfully reproduces the energy response of the MC simulation. To study the FTK's ability to reproduce the data, the ^{16}N source (see Section 2.3.2) is used to determine FTK's energy response throughout the D_2O volume. The energy response in data is determined by comparing the FTK energy distribution of ^{16}N data at various locations in the detector to the expected energy distribution derived using the MC. Any differences in the means (the energy scale) of those distributions are taken as the energy scale systematic uncertainty. Differences in the width of the ^{16}N energy distributions between data and MC is the systematic uncertainty in the energy resolution. Energy scale and resolution systematic uncertainties directly affect the measurement of the neutrino fluxes and CC and ES energy spectra. Therefore, it is critical to minimize any differences in energy scale and resolution between data and MC.

Traditionally SNO's energy scale and resolution systematic uncertainties were de-

termined by fitting a simple Gaussian to the peak of the ^{16}N energy distribution. The reconstructed energy of ^{16}N is not, however, a Gaussian, since the 6.13 MeV γ produced from the ^{16}N de-excitation can Compton scatter multiple electrons with a range of energies. A better fit with higher precision to the ^{16}N energy distribution can be achieved by exploiting the multi-electron energy nature of the ^{16}N response. Such a fit has the added benefit of being able to simultaneously determine the energy dependence of the resolution uncertainties.

The following chapter discusses a new method of fitting the ^{16}N energy distribution using the spectrum of electron energies produced by ^{16}N γs. With this fitting technique, the energy dependence of the resolution can be derived independently of the mono-energetic electron MC used in prior analyses. Since ^{16}N is SNO's most reliable and understood calibration source, using ^{16}N as a multi-energy electron source allows for better estimation of the energy systematic uncertainties over the range of energies important to the solar neutrino analysis.

6.1 The Pitfalls and Limitations to Fitting ^{16}N Energy to a Gaussian

There are numerous shortcomings to determining the ^{16}N energy mean and resolution by fitting the energy distribution to a Gaussian. First, the ^{16}N energy distribution is only approximately a Gaussian at the peak of the distribution. Therefore, in order to achieve a reasonable χ^2 the Gaussian fit is done over a very limited range of energies, approximately $\pm 1.6\sigma$ around the energy mean. The measurement of the mean and resolution is sensitive to the fit range although the difference between data and MC

in either the mean or resolution is more resilient to changes in the fit range. Second, since ^{16}N is not a mono-energetic electron source, the measured energy resolution does not agree with the energy resolution measured from mono-energetic electron MC as indicated in Figure 6.1. The distribution of the number of Cherenkov photons is much broader for mono-energetic γs compared to electrons with the same energy and this is reflected in the measured resolution. Yet, for the CC and ES signals the resolution systematic uncertainties for electrons - *not* γs - needs to be determined. Since the distribution of the number of Cherenkov photons is broader for γs, the component of the energy resolution associated with the inherent width of the number of photons produced is also larger, mitigating the effects on the resolution uncertainty due to detector mis-modelings. Therefore, calculating the resolution uncertainties using the measured resolution from a γ source will result in an underestimated electron resolution uncertainty. To calculate the resolution uncertainty for electrons, the effect on the uncertainty due to the additional broadening of the energy resolution in γs must be taken into account or the ^{16}N source must be treated as a multi-energetic electron source to extract the electron resolution. The latter method is discussed in the following section.

6.2 Determining the Most Probable Energy Spectrum for ^{16}N

While the γ produced from ^{16}N de-excitation can Compton scatter multiple electrons, the energies of these low energy electrons can not be individually resolved and only the summed energy of all scattered electrons in an event is measured *as if* the event had

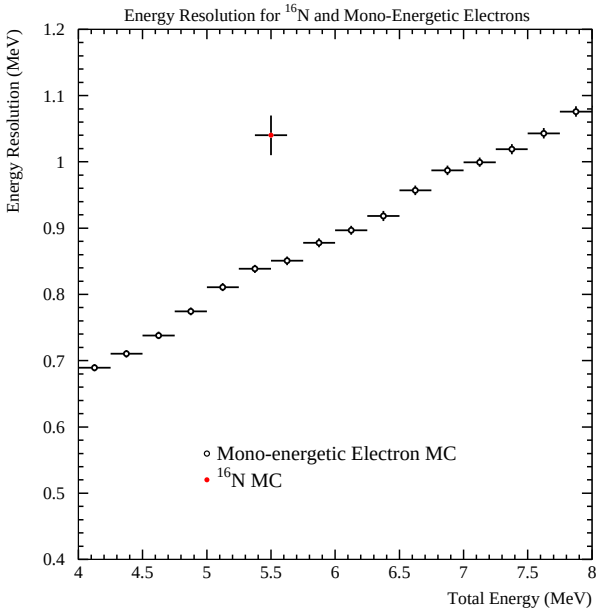

Fig. 6.1: Energy resolution for ^{16}N MC (fitted to a Gaussian) and for mono-energetic electron MC.

occurred from a single electron. Due to the energy threshold required for electrons to produce Cherenkov light, the energies of multiple Compton scattered electrons can not be directly added to determine the summed energy of the event. To find the ^{16}N electron energy spectrum, a more natural unit of measure of an event's energy is the number of Cherenkov photons produced. The number of produced photons can then be converted to the most probable mono-energetic electron energy that would produce that number of photons. The parameterization of the number of Cherenkov photons for mono-energetic electrons utilized by FTK (Section 5.4.1) is employed to make this conversion. MC is used to find the distribution of the number of Cherenkov photons for ^{16}N γs (Figure 6.2), which results in the most probable electron energy distribution indicated in Figure 6.3. The distribution of the number of Cherenkov photons and the most probable electron energy distribution have the same shape due

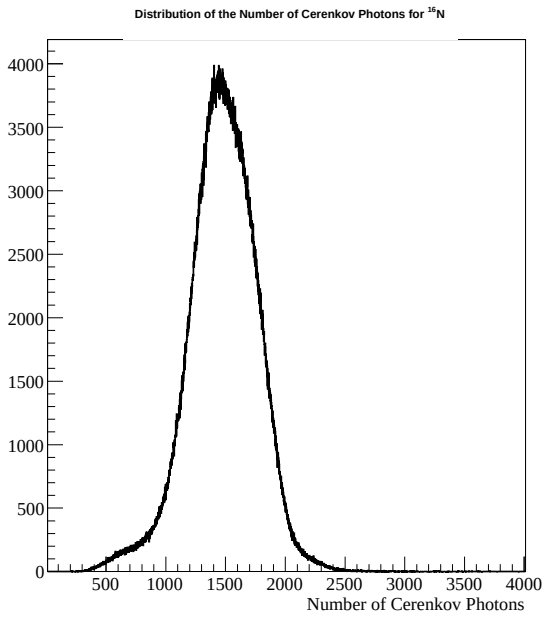

Fig. 6.2: Distribution of the number of Cherenkov photons for ^{16}N.

to the one-to-one mapping used to build the energy distribution. The most probable energy distribution represents SNO's fundamental energy resolution, in other words Figure 6.3 indicates the energy resolution in SNO if every Cherenkov photon could be detected and the detector was modeled perfectly. The most probable electron energy distribution can be used as the basis of a fit to the ^{16}N reconstructed energy distribution.

6.3 Fitting ^{16}N Energy to the Most Probable Electron Energy Spectrum

To determine the detector's energy scale and resolution for electrons, the most probable electron energy distribution (Figure 6.3) is convolved with a Gaussian that rep-

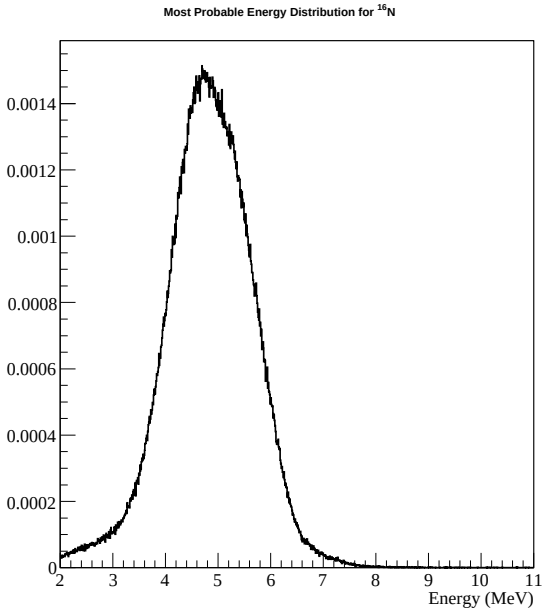

Fig. 6.3: Most probable electron energy distribution for ^{16}N.

resents the broadening in energy due to limited photon statistics (not detecting every photon) and detector mis-modeling (non-perfect detector model). (Using the Cherenkov photon distribution to determine the energy resolution was first explored in Section 4.2.) The Gaussian used to smear the most probable energy distribution has three free parameters: a shift which represents offsets in the energy scale (p_3) and two resolution parameters. The energy dependence of the resolution is $\sigma = p_1 + p_2\sqrt{E_{elec}}$, where E_{elec} is the kinetic energy of the electron. The convolution is mathematically illustrated in the following equation,

$$P(E) = \int \frac{N}{\sqrt{2\pi}\sigma} P_{prob}(E_{elec}) e^{\left(\frac{(E-E_{elec}-p_3)^2}{2\sigma^2}\right)} dE_{elec} \tag{6.1}$$

where $P(E)$ is the Gaussian convolved most probable electron energy distribution, E is the reconstructed energy, E_{elec} is the electron energy and integration variable, N

is a normalization parameter floated in the fit, and $P_{prob}(E_{elec})$ is the most probable electron energy distribution for ^{16}N.

SNO's energy resolution is composed of three parts; the inherent resolution from the width of the number of Cherenkov photons produced, the photon statistics resolution which is governed by the detection efficiency of Cherenkov photons and the energy estimator resolution which is due to detector mis-modelings in the energy estimator. The inherent resolution for mono-energetic electrons has already been incorporated into $P_{prob}(E_{elec})$, therefore the energy resolution obtained from the fit, σ, is composed of the photon statistics and energy estimator resolution only. To determine the total electron energy resolution, the inherent resolution can not simply be added in quadrature with σ since σ is not independent of $P_{prob}(E_{elec})$ in the convolution described in Equation 6.1. Section 6.3.2 discusses how the total energy resolution and uncertainty is determined.

To determine the fit parameters, p_i, Equation 6.1 is fit to the ^{16}N energy distribution for both data and MC over the fit range of 3 to 10 MeV as shown in Figure 6.4. Compared to the traditional Gaussian fit, the χ^2 per degree of freedom with this fit is significantly better as demonstrated in Figure 6.5 and the fit range is much larger compared to the $\sim$ 4 to 6 MeV fit range for the Gaussian fit. To optimize the fit range and to ensure there is no sensitivity to it, the fit was repeated on a handful of ^{16}N data and MC energy distributions varying the starting and ending energies. As demonstrated in Figures 6.6 and 6.7 the fitted scale and resolution is very stable as long as neither the starting or ending fit range is close to the ^{16}N mean. Also using a starting energy below 2.5 MeV leads to variable fit results, since the energy spectrum can be distorted by triggering effects which are not modeled in the fit.

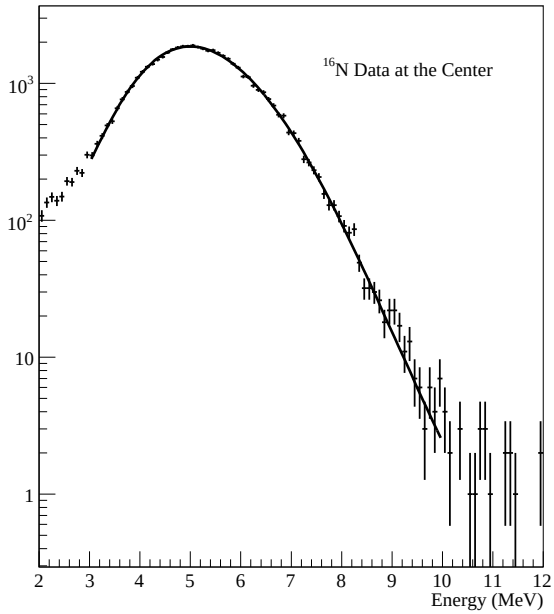

Fig. 6.4: Most Probable electron energy fit to ^{16}N data at the center. The χ^2 is 67.2 for 66 degrees of freedom.

6.3.1 Selecting Events Without Source Container Shadowing

Since FTK accounts for all detector geometry modeled in the MC, including the source container, it has the negative side effect that for events that are mis-reconstructed and point towards the source the energy will be greatly overestimated to compensate for tubes believed to be shadowed by the source. This problem results from the position reconstruction algorithms not including the source geometry in their model. As a net result the FTK energy distribution for ^{16}N has a very long energy tail compared to RSP which does not account for source shadowing (Figure 6.8). To remove these events, events within 50 cm of the source's center must be traveling outward (the angle between the reconstructed direction and the directional vector from the source center to the reconstructed position is less than 90°). Applying this selection criteria successfully eliminates FTK's high energy tail (Figure 6.8). In theory shadowed events

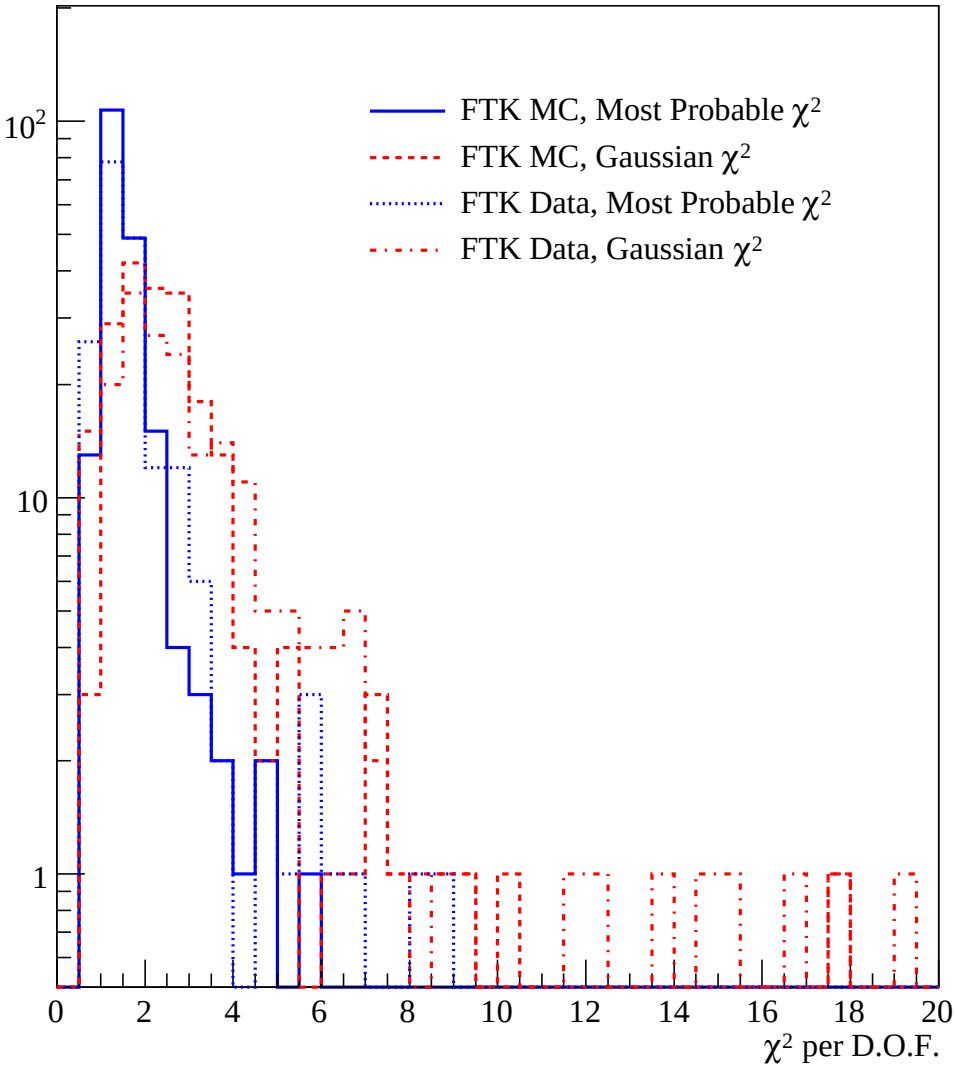

Fig. 6.5: χ^2 per degree of freedom when fitting ^{16}N data and MC to the most probable electron energy fit and a traditional Gaussian fit. There are approximately 66 degrees of freedom in the most probable electron energy fit and 34 degrees of freedom in the Gaussian fit. The χ^2 per degree of freedom is much better when using the most probable electron energy fit compared to a Gaussian fit.

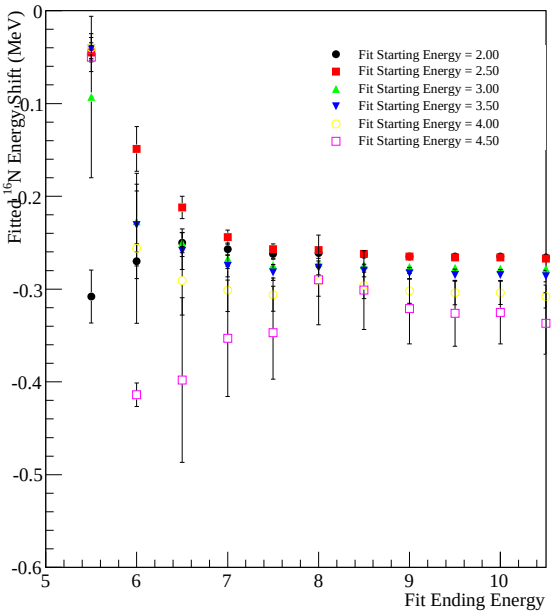

Fig. 6.6: ^{16}N energy mean extracted using the most probable electron energy fit. The abscissa indicates the upper energy fit range. The points indicate the lower energy fit range. The energy mean obtained from the fit is stable for different starting and ending fit ranges.

do not need to be cut because they are present in both data and MC, but in practice the high energy tail in FTK distorts the most probable electron energy fit leading to non-sensible results.

To remove pathological events from the data, the standard data cleaning cuts (without the burst cut) and the FECD tag are applied (see Appendix B). Additionally all the new high level cuts that will be discussed in Section 7.2 using cut levels from [70] are applied with the exception of the QPDT cut and the energy ratio cut.

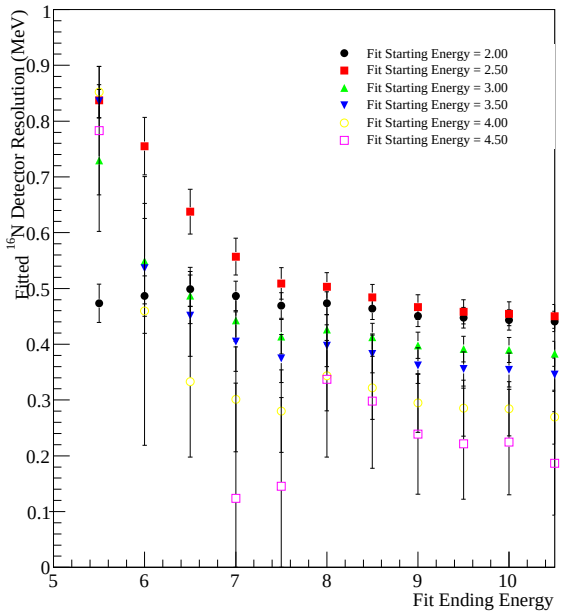

Fig. 6.7: ^{16}N energy resolution extracted using the most probable electron energy fit. The abscissa indicates the upper energy fit range. The points indicate the lower energy fit range. The energy resolution obtained from the fit is stable for different starting and ending fit ranges.

6.3.2 Determining the Total Energy Resolution and Propagation of Fit Uncertainties

The fitted energy resolution in the most probable electron energy fit is the PMT hit statistics and energy estimator model resolution (see Section 4.2 for an additional discussion) and does not include the width of the distribution of the number of Cherenkov photons for mono-energetic electrons. To evaluate the systematic uncertainty in the electron energy resolution, the total resolution (including inherent resolution) must be compared between data and MC. To calculate the total resolution for electrons, the most probable electron energy distribution for a mono-energetic electron is convolved with a Gaussian where the parameters p_i (see Equation 6.1) are determined

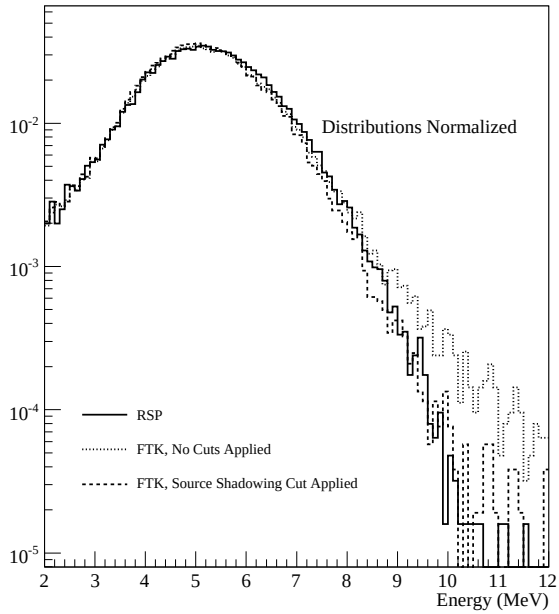

Fig. 6.8: ^{16}N energy distribution showing FTK's high energy tail (dotted line) caused by mis-reconstructed events shadowed by the source, FTK's energy cutting shadowed events (dashed line) and RSP energy for comparison (solid line).

from a fit to ^{16}N data and MC. The total electron resolution is the variance of this convolved distribution. The most probable electron distribution for 5 MeV electron MC is shown in Figure 6.9.

Incorporating the uncertainties of the fit parameters, p_i into the uncertainty on the total energy resolution is a more complicated matter. If the fit parameters were completely uncorrelated, the uncertainty on the total resolution would be $\sqrt{\delta p_1^2 + \delta p_2^2}$ where δp_1^2 and δp_2^2 are the uncertainties on p_1 and p_2 respectively. Although the shift in energy scale parameter (p_3) is largely (and therefore taken to be) uncorrelated with the resolution parameters, the two resolution parameters are correlated with a known correlation matrix.

The total resolution uncertainty can be determined by diagonalizing the correla-

tion matrix and propagating the parameter uncertainties in the diagonalized basis. If the correlation matrix between p_1 and p_2 is

$$V = \begin{pmatrix} v_{11} & v_{12} \\ v_{12} & v_{22} \end{pmatrix} \tag{6.2}$$

the eigenvectors of the diagonalized matrix are p_1' and p_2' with eigenvalues given by

$$\lambda_{\pm} = \frac{v_{11} + v_{22} \pm \sqrt{(v_{11} + v_{22})^2 - 4(v_{11}v_{22} - v_{12}^2)}}{2} \tag{6.3}$$

The eigenvectors can be expressed in terms of the original basis as

$$p_1' = p_1 \cos(\theta) + p_2 \sin(\theta) \tag{6.4}$$

$$p_2' = -p_1 \sin(\theta) + p_2 \cos(\theta) \tag{6.5}$$

where

$$\theta = \frac{1}{2} \tan^{-1} \left(\frac{2v_{12}}{v_{11}^2 - v_{22}^2} \right) \tag{6.6}$$

To calculate the uncertainty on the total resolution, p_1' and p_2' are shifted by $\pm\lambda_+$ and $\pm\lambda_-$ respectively and p_3 is shifted by its positive and negative uncertainty, one at a time. For each of these parameter shifts, the most probable electron energy distribution for mono-energetic electrons is again convolved with a Gaussian using the new shifted parameters to determine the new total resolution. The uncertainty in the best fit total resolution is taken to be the difference in the resolution calculated using the shifted parameters and the resolution calculated using the best fit parameters. Since the parameters were shifted in an uncorrelated manner, the final uncertainty

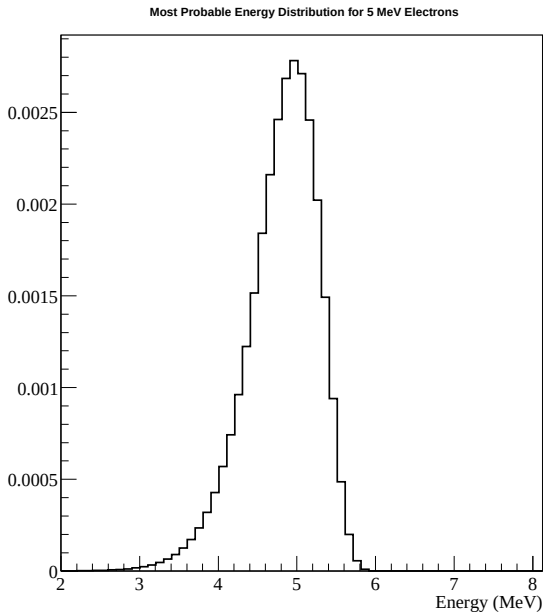

Fig. 6.9: Most probable electron energy distribution for 5 MeV mono-energetic electrons.

on the total resolution is the uncertainty in the resolution from each of the parameter shifts added in quadrature.

6.4 D_2O Phase Energy Systematic Uncertainties

6.4.1 FTK Energy Drift Correction and Other Corrections

To evaluate the FTK energy scale and resolution systematic uncertainties in the D_2O phase, a scale correction as a function of time needs to be applied to the MC as seen in Figure 6.10. For the processing of the D_2O data and MC, the collection efficiency drift used to model time dependent changes in the data was determined using RSP's prompt time window, not FTK's timing window. Since there is an indication that the concentrator reflectivity and thus the late light began to change in the latter half

of the D_2O phase, the drift function used for RSP does not represent the drift in FTK's timing window as determined from ^{16}N data. To account for this, a correction function is applied to FTK energy in the data only. The correction function used for FTK energy is a constant for the first segment of the collection efficiency drift function and a linear function for the second segment. Using the path fitter reconstruction (see [38] for a description), the correction function is

$$C(JD) = \begin{cases} 1.00371 & \text{if JD} < 9363 \\ 1.2308 - 2.4254e^{-5} * \text{JD} & \text{otherwise} \end{cases} \tag{6.7}$$

where JD is the Julian Day.

Additionally radial and energy corrections need to be applied to FTK energy. Unlike the energy drift correction, these corrections equally affect both data and MC and therefore do not have any affect on the determination of energy systematic uncertainties but are necessary so that the absolute FTK energy scale is correct. The radial bias in absolute energy scale is due to differences between the PMT angular response model used by FTK and the response model used by the MC. The energy bias in absolute energy scale is the result of FTK's MPE correction breaking down at higher energies (greater than 15 MeV). The application of these corrections including the drift correction is given below

$$\begin{aligned} C(\rho) &= 1.0126 - 0.044882\rho + 0.032725\rho^2 \\ T'_{data} &= -0.10872 + 1.0277\left(\frac{T_{data}}{C(\rho)C(JD)}\right) - 0.0012247\left(\frac{T_{data}}{C(\rho)C(JD)}\right)^2 \\ T'_{mc} &= -0.10872 + 1.0277\left(\frac{T_{mc}}{C(\rho)}\right) - 0.0012247\left(\frac{T_{mc}}{C(\rho)}\right)^2 \end{aligned}$$

where $C(\rho)$ is the radial correction, $C(JD)$ is the drift correction given in the previous equation, T_{data} is the FTK energy for data, T'_{data} is the corrected FTK energy for data, T_{mc} is the FTK energy for MC and T'_{MC} is the corrected FTK energy for MC. Note that all energies are in kinetic energy.

6.4.2 Energy Scale Uncertainties

To estimate the energy scale uncertainties, the difference between data and MC energy scales is calculated for ^{16}N data and MC for each run and is shown as a function of source radius in Figure 6.11. The detector is divided into six radial slices (indicated by the vertical lines in the figure) and the average energy scale difference in each radial slice is weighted by its relative volume to determine the volume weighted average scale uncertainty. For comparison, Figure 6.12 plots the energy scale uncertainty as determined using the traditional Gaussian fit, which has similar volume weighted uncertainties and is shown for comparison.

The large spread in energy scale for ^{16}N points at the same radii results from mis-modeling different regions in the detector, mainly misunderstanding the top and bottom regions of the detector. As demonstrated in Figure 6.13, the data and MC difference in energy scale is dramatically different at the top of the detector, compared to points in the x-y plane only and compared to points near the bottom of the detector. Since many of the high radii ^{16}N points are deployed on the z-axis by blindly volume weighting all ^{16}N points, the bottom of the detector is oversampled and the energy scale uncertainty is overestimated for most the detector's volume. To more judiciously measure the scale uncertainties for all regions, the energy uncertainties should be calculated for the regions away from the detector top and bottom and then

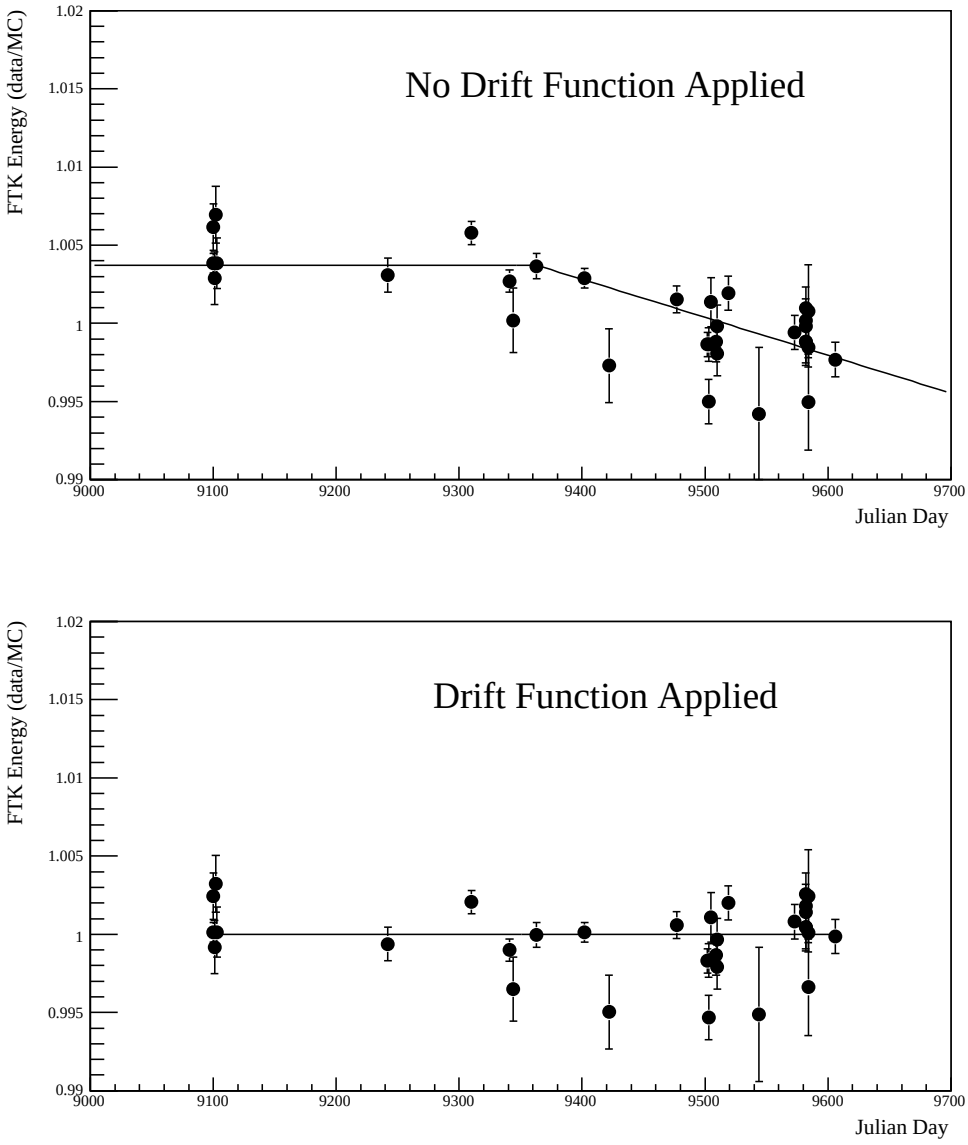

Fig. 6.10: Difference in FTK energy scale between D_2O ^{16}N data and MC at the center before the correction function is applied (top figure) and after apply correction function (bottom figure).

separately for these regions.

Events are excluded if they illuminate a significant fraction of the top and bottom regions. This cut is defined by finding the intersection point of the reconstructed directional vector with the AV. If the z component of this intersection point is less than -500 cm (removes bottom region) or greater than 500 cm (removes top region) the event is eliminated. The z component, $Z_{intersect}$ is mathematically given as follows,

$$Z_{intersect} = r_3 + u_3 \left(\sqrt{(\vec{r} \cdot \vec{u})^2 - |\vec{r}^2| + r_{av}^2} - \vec{r} \cdot \vec{u} \right) \tag{6.8}$$

where $\vec{r} = (r_1, r_2, r_3)$ is the reconstructed positional vector, $\vec{u} = (u_1, u_2, u_3)$ is the reconstructed directional vector and r_{av}^2 is the radius of the AV. For events isotropically distributed in both position and direction, roughly 17% of events illuminate either the top or bottom regions of the detector with these definitions. With this cut applied, Figure 6.14 plots the data and MC difference in energy scale. The detector asymmetry is significantly reduced and the uniformity in energy scale between the top and bottom regions is much improved as seen in Figure 6.15. Comparing Figures 6.13 and 6.15, the energy scale for ^{16}N points on the x-y plane changes very little when applying the cut of $Z_{intersect}$ and it is the ^{16}N points in the negative plane that rise to agree. As a result, the radial bias is flat to $\sim$ 475cm and then a distinct jump can be seen. It is unknown what could be causing this rise.

To estimate the energy scale uncertainties for events which illuminate the top and bottom regions, the ^{16}N data and MC is compared using only events illuminating these regions. Figure 6.16 shows the energy scale difference for events illuminating the bottom region, using only ^{16}N points in the negative z-hemisphere. Clearly, the energy scale uncertainty is significantly worse for these events. Using only events that

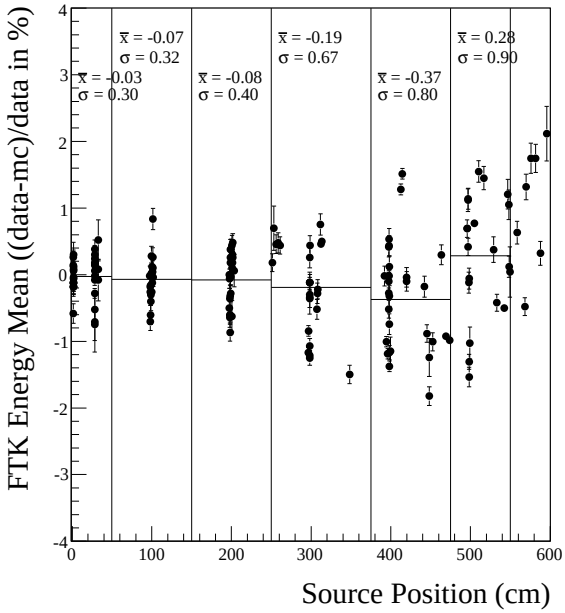

Fig. 6.11: Difference in FTK energy scale as a function of source radius. The energy means were obtained using the most probable electron energy fit.

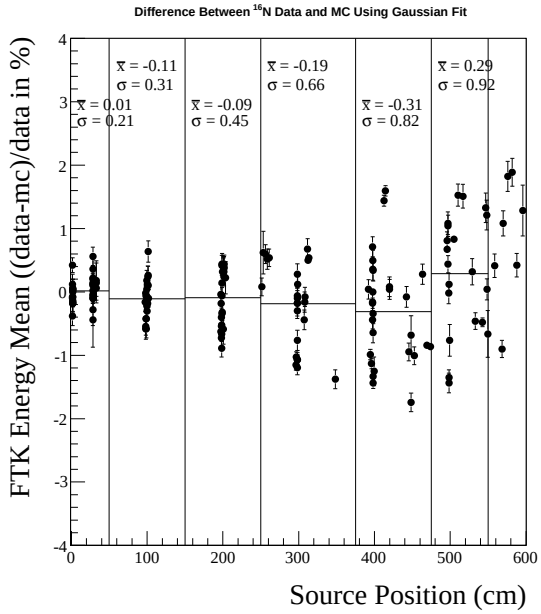

Fig. 6.12: Difference in FTK energy scale as a function of source radius. The energy means were obtained using a Gaussian fit.

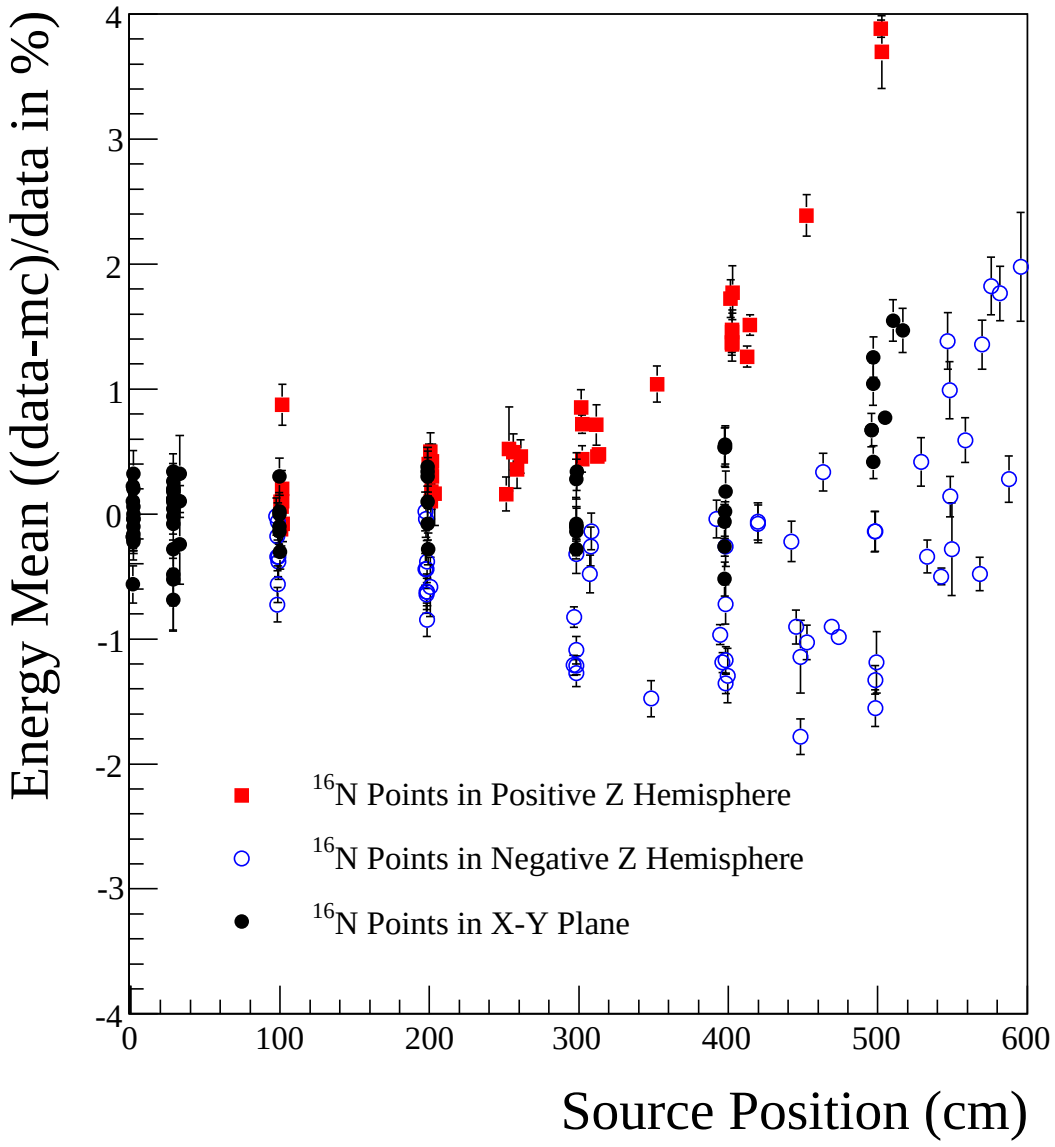

Fig. 6.13: Difference in FTK energy scale as a function of source radius for source positions above the x-y plane (red squares), below the x-y plane (blue open circles) and on the x-y plane (black circles).

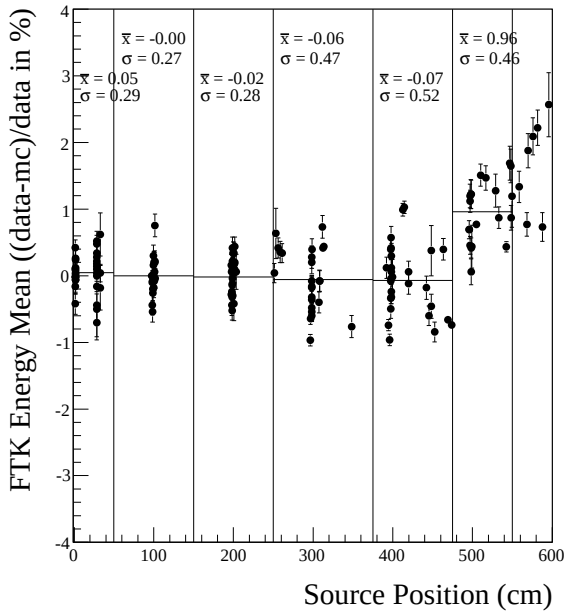

Fig. 6.14: Difference in FTK energy scale as a function of source radius where events that illuminate the top and bottom regions have been removed. The energy means were obtained using the most probable electron energy fit.

illuminate the top region results in a high number of failures in the most probable electron energy fit, therefore the results for the Gaussian fit to the mean are used to determine the scale uncertainty for this region. For events illuminating the top region, the energy scale uncertainty is embarrassing as shown in Figure 6.17. Since in the top regions events within $r_{fit} < 375$cm have significantly smaller uncertainties, different uncertainties are applied for events inside and outside of 375 cm. To summarize, the application of the energy scale uncertainties for all regions in the detector is

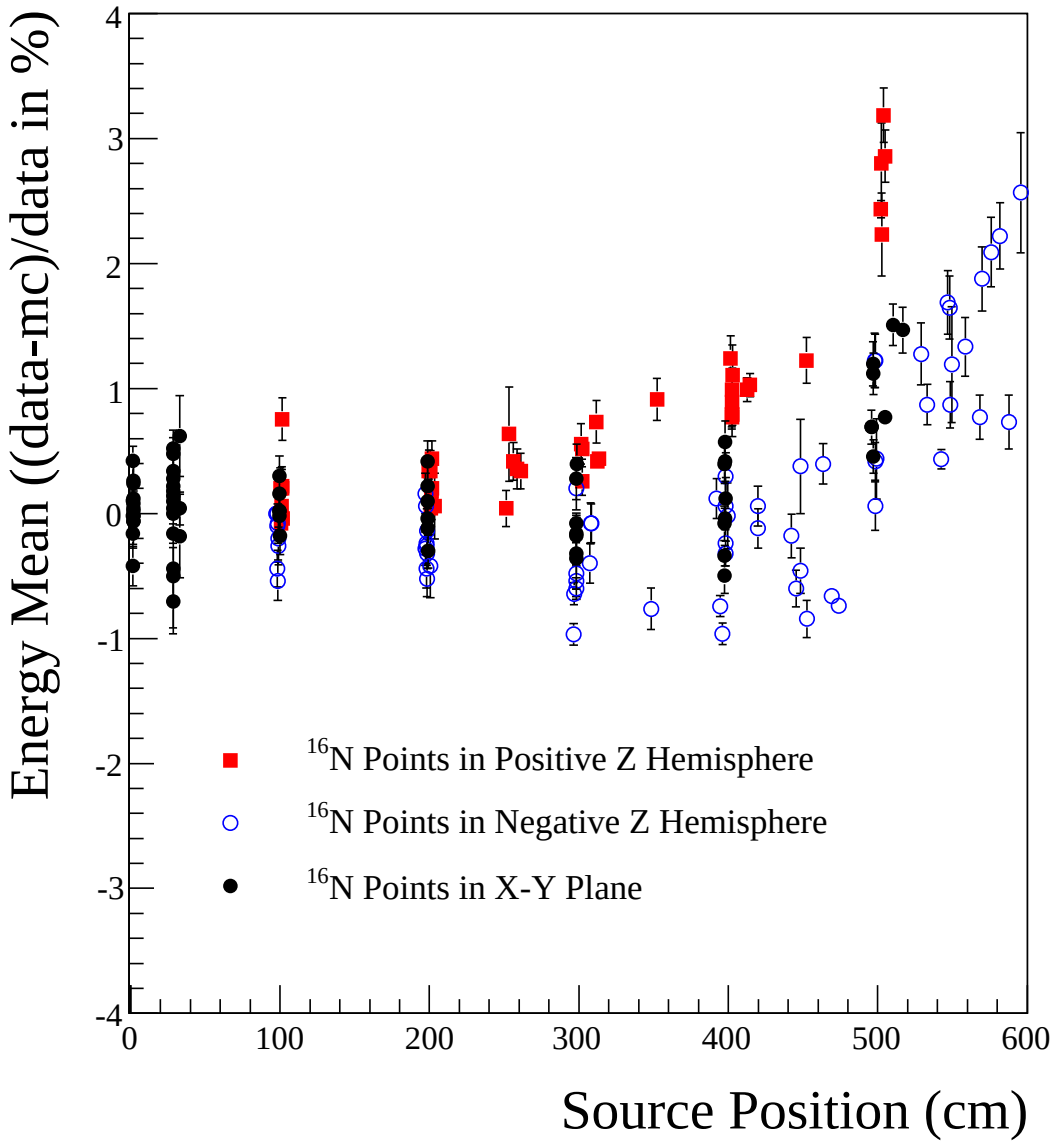

Fig. 6.15: Removing events that illuminate the detector top and bottom regions, the difference in FTK energy scale is shown as a function of source radius for source positions above the x-y plane (red squares), below the x-y plane (blue open circles) and on the x-y plane (black circles).

$$\text{Scale Uncertainty} = \begin{cases} \text{Top} & \text{if } Z_{intersect} > 500\text{cm} \\ \text{Inner Top} & \text{if } Z_{intersect} > 500\text{cm and } r_{fit} < 375\text{cm} \\ \text{Bottom} & \text{if } Z_{intersect} < -500\text{cm} \\ \text{Middle} & \text{otherwise} \end{cases} \tag{6.9}$$

where the uncertainty values are listed in Table 6.1. For the top and bottom regions, the energy scale offsets were applied as a systematic uncertainty and not as a correction to the MC. Although there is currently some indication that the top/bottom asymmetry is due to different PMT angular responses for PMTs near the bottom versus elsewhere [71], at the time of this writing it was unclear if the asymmetry was due to the detector or a source effect. Given this uncertainty, the energy scale was not corrected in the MC.

With the charge rate correction (QRC) application [72], it is once again possible to use walk corrected (PT) times in the energy estimators. To evaluate residual rate dependent changes in energy scale, low rate ^{16}N is compared to MC. As seen in Figure 6.18, there is a small residual rate dependence, which is significantly smaller than the 3% rate dependences on the energy scale without QRC applied. The time dependent uncertainty in energy scale is taken as the spread in the high rate ^{16}N points.

All energy scale systematic uncertainties using the path fitter position reconstruction (an event position and direction reconstruction algorithm which both PMT timing and hit information [38]) are summarized in Table 6.1. Many of the scale uncertainties are one sided and therefore should not simply be summed in quadrature

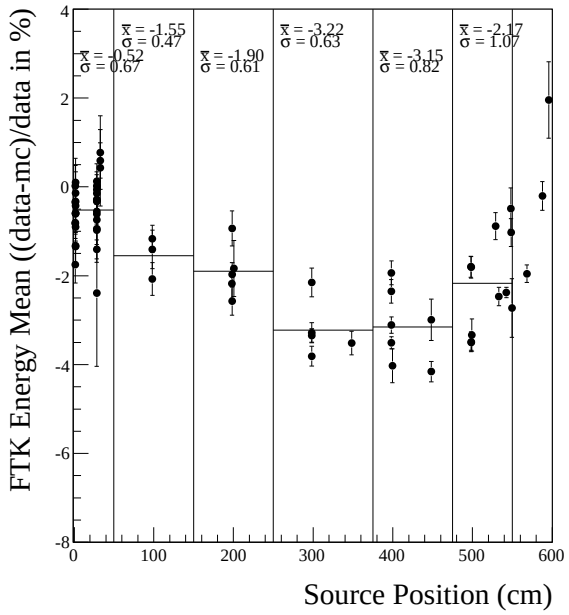

Fig. 6.16: Using only events that illuminate the bottom region, the difference in FTK energy scale is shown as a function of source radius. The energy means were obtained using the most probable electron energy fit.

as symmetrically distributed scale uncertainties. Instead to determine the total scale uncertainty for each detector region a MC method is used. The radial distribution uncertainty for each region is assumed to be a uniform distribution between zero and the mean offset and is convolved with a Gaussian with a width that is the standard deviation around the mean offset. The electronics rate effect uncertainty is also assumed to be a uniform distribution with a Gaussian convolution. All other scale uncertainties are taken to be a Gaussian centered at zero and a width shown in the table. Throwing many random trials, selecting an uncertainty from each of these distributions and linearly adding them, Figure 6.19 plots the resulting distribution of the total scale uncertainty for the middle detector region. Table 6.2 summaries the total scale uncertainties for all regions. Since the mean value for the total scale

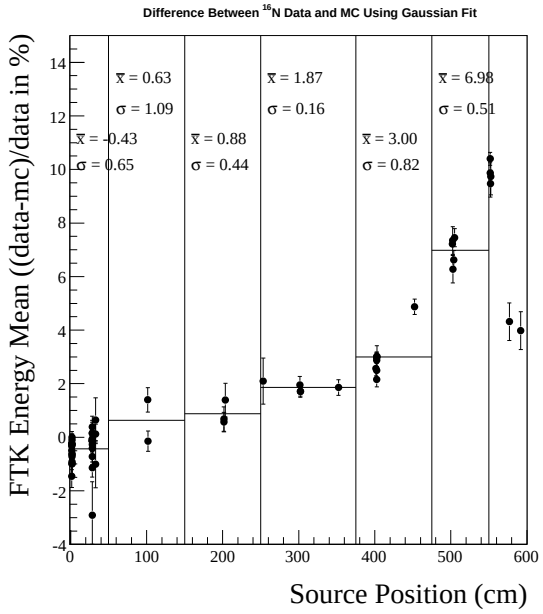

Fig. 6.17: Using only events that illuminate the top region, the difference in FTK energy scale is shown as a function of source radius. The energy means were obtained using a Gaussian fit.

uncertainty is offset from zero for all regions, the uncertainty is applied negative and positive uncertainties as tabulated in the summary table are applied to the energy distributions used in the signal extraction (see Chapter 9).

6.4.3 Energy Resolution Uncertainties

The advantage of the most probable electron energy fit is the ability to determine the energy resolution uncertainties over a range of electron energies. Averaging over many ^{16}N runs at various points in the detector, the resolution function extracted using the most probable electron energy fit is directly compared to the resolution function determined from MC mono-energetic electrons (Figure 6.20). Perfect agreement between ^{16}N resolution and the mono-energetic electron energy resolution is

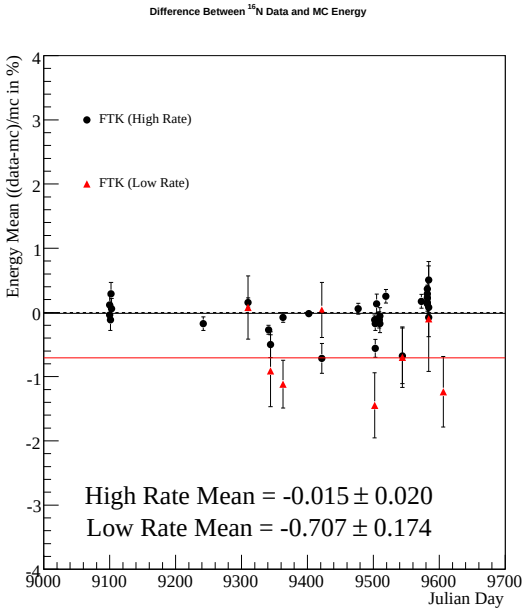

Fig. 6.18: Difference in FTK energy scale for ^{16}N high rate and low rate ^{16}N center runs as a function of Julian day. The energy means were obtained using the most probable electron energy fit.

Source		Uncertainty
Detector PMT status		0.01%
Electronics threshold		0.20%
Electronics gain		0.40%
Electronics rate effect		$-0.69 \pm 0.17\%$
Time drift/stability: data-MC		0.02%
^{16}N source modeling		0.65%
Radial distribution: data-MC	Top ($r_{fit} > 375$cm)	$+5.07 \pm 0.66\%$
	Top ($r_{fit} < 375$cm)	$+1.55 \pm 0.29\%$
	Middle ($r_{fit} < 475$cm)	$-0.06 \pm 0.47\%$
	Middle ($r_{fit} > 475$cm)	$+0.96 \pm 0.46\%$
	Bottom	$-2.69 \pm 0.84\%$

Table 6.1: Energy scale uncertainties using FTK energy with path fitter reconstruction. The positive and negative uncertainties listed are the error on the energy scale uncertainty.

Region	Total Uncertainty	Negative Shift	Positive Shift
Top ($r_{fit} > 375$cm)	$+2.20 \pm 1.76\%$	-1.76%	+3.96%
Top ($r_{fit} < 375$cm)	$+0.43 \pm 0.99\%$	-0.99%	+1.42%
Middle ($r_{fit} < 475$cm)	$-0.37 \pm 0.95\%$	+0.95%	-1.32%
Middle ($r_{fit} > 475$cm)	$+0.14 \pm 0.99\%$	-0.99%	+1.13%
Bottom	$-1.69 \pm 1.41\%$	+1.41%	-3.10%

Table 6.2: Summary of the total scale uncertainties and the recommended positive and negative shifts.

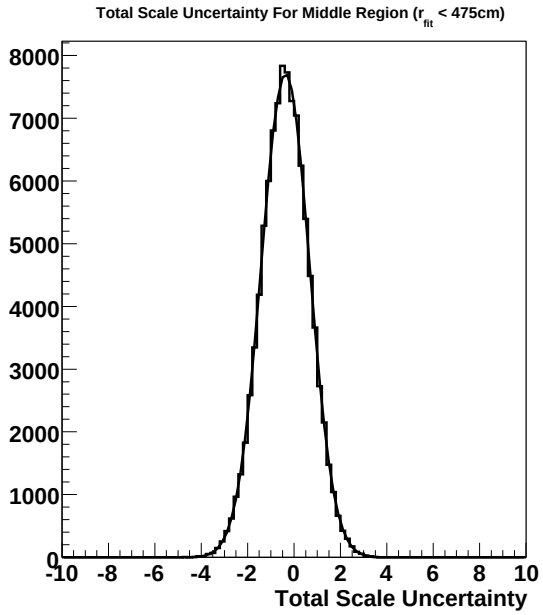

Fig. 6.19: Total scale uncertainty for the middle region of the detector with $r_{fit} <$ 475cm. The distribution has been fit to a Gaussian to determine the uncertainties listed in Table 6.2.

not expected because the ^{16}N resolution only has two terms in the resolution function, (see Equation 6.1) while the mono-energetic electron resolution function has an additional term, linear in energy.

Comparing the energy resolution at 5 MeV for ^{16}N data and MC (see Section 6.3.2 for discussion on this calculation), the uncertainty in the resolution is close to 2% and relatively constant throughout the entire volume, as seen in Figure 6.21. As with the energy scale, there is quite a broad spread for ^{16}N points at the same radii, although applying a cut on $Z_{intersect}$ has little effect on the resolution uncertainty. As expected, the uncertainty in energy resolution is slightly larger using the most probable electron fit compared to the Gaussian fit (Figure 6.22) because the Gaussian fit measures energy resolution for γs while the most probable electron fit measures the resolution for electrons.

To estimate the uncertainty in energy resolution for various electron energies, the resolution for each ^{16}N data and MC point is calculated in the energy range of 2.5 to 10 MeV in 0.25 MeV steps. For each energy step, the mean data and MC resolution difference is calculated for ^{16}N points in the radial slices as shown in Figure 6.23, where the points indicate the different radial slices. In this figure the error bars indicate the standard deviation around the mean for the ^{16}N points in each radial slice. As in Figure 6.21 the uncertainties in energy resolution for each electron energy is very similar for each radial slice. The results of volume weighting all radial slices for a given electron energy is shown in Figure 6.24, where the error bars indicate the volume weighted standard deviation.

Since the resolution uncertainty in Figure 6.21 is flat with radius, the overall uncertainty is taken as the volume weighted radial bias and spread. For 5 MeV electrons, the resolution uncertainties are summarized in Table 6.3. When determining the en-

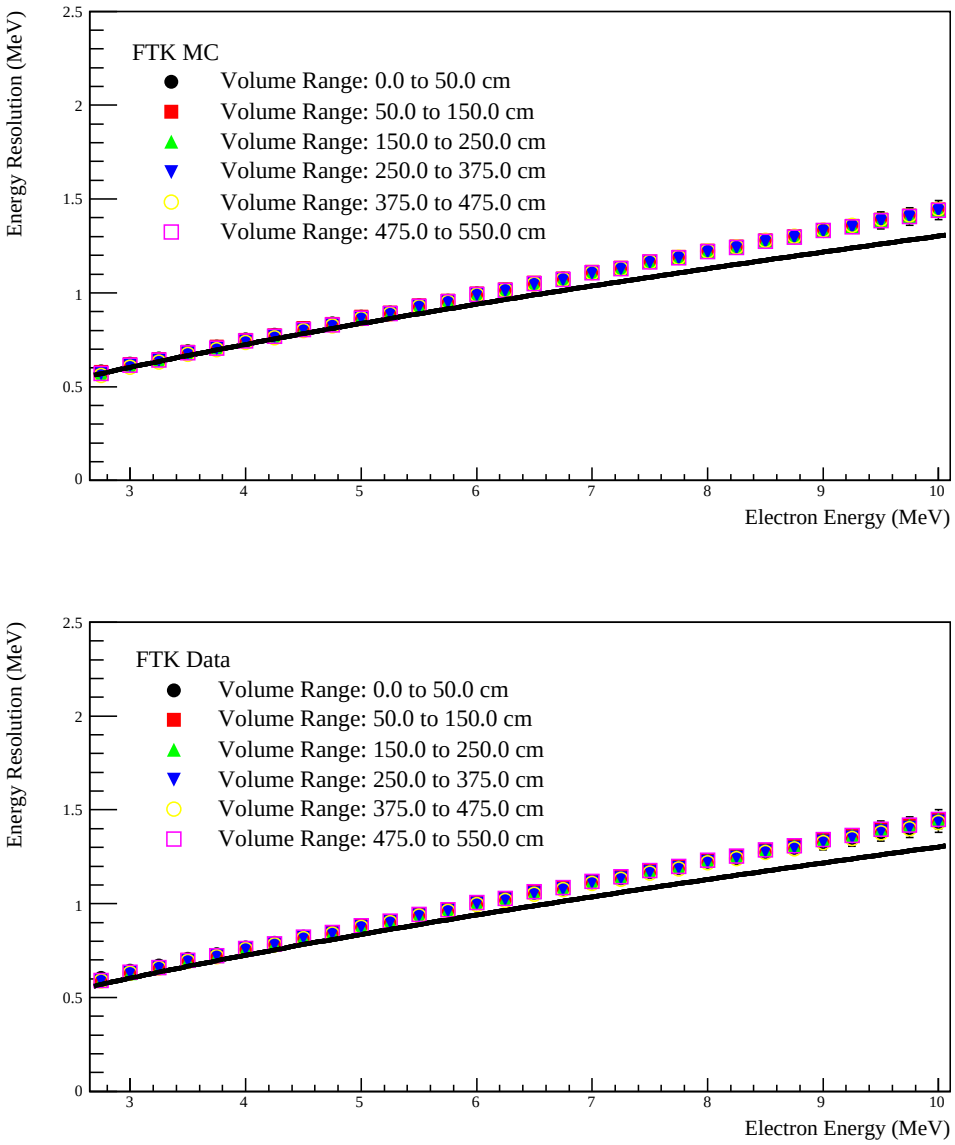

Fig. 6.20: Average resolution function extracted using the most probable electron energy fit for MC (top figure) and data (bottom figure) for various radial slices. The solid line indicates the resolution function measured from mono-energetic MC.

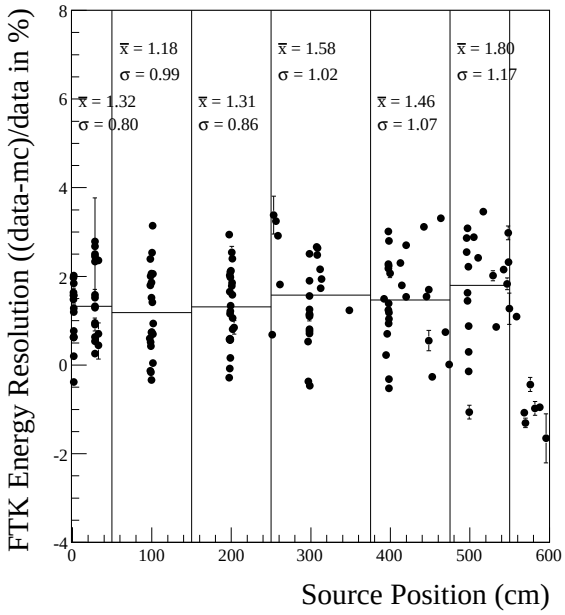

Fig. 6.21: Difference in total electron energy resolution at 5 MeV between ^{16}N data and MC as a function of source radius. The total resolution was obtained using the most probable electron energy fit.

Source	Resolution Uncertainty
Radial distribution: data-MC	$1.60 \pm 1.09\%$

Table 6.3: Energy resolution uncertainties at 5 MeV using FTK energy with path fitter reconstruction.

ergy dependence of the resolution uncertainties only the electron energy range of 4.5 to 6 MeV is considered. This energy range roughly corresponds to the one sigma limits of the most probable electron energy (Figure 6.3). Beyond this range the fitted resolution is very sensitive to fluctuations on the energy tail. Over this energy range, the mean offset and spread in the resolution uncertainty can be parameterized by a polynomial as listed in Table 6.4. The mean offset and spread is added linearly when applying this systematic uncertainty to energy distribution used in the signal extraction.

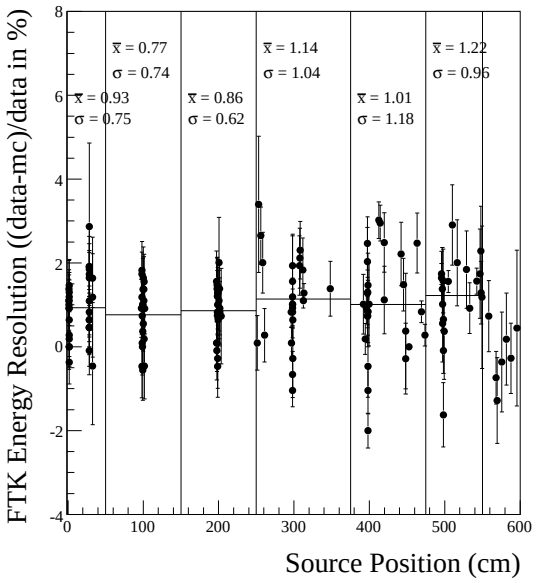

Fig. 6.22: Difference in energy resolution between ^{16}N data and MC as a function of source radius. The total resolution was obtained using a Gaussian fit.

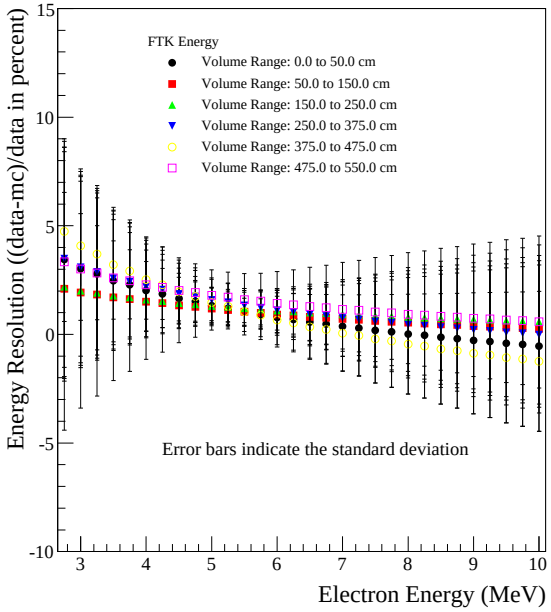

Fig. 6.23: Average difference in total resolution between ^{16}N data and MC for various radial slices (points) as a function of electron energy. The uncertainties shown are the standard deviation of the average.

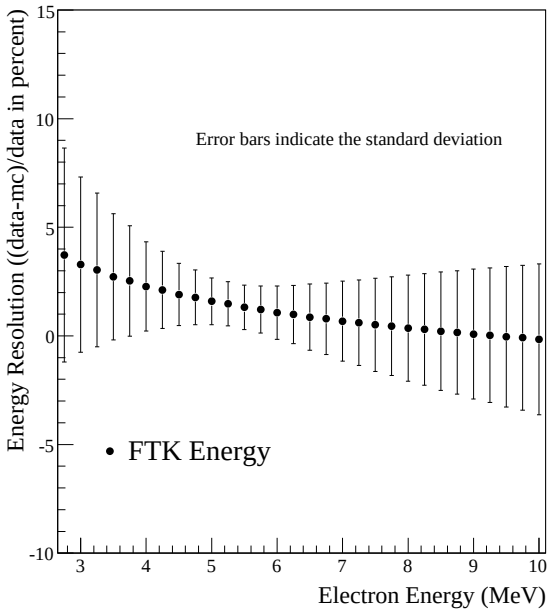

Fig. 6.24: Volume-weighted difference in total resolution between ^{16}N data and MC as a function of electron energy. The uncertainties shown are the standard deviation of the volume-weighted average.

Source	Resolution Uncertainty (in %)
Radial distribution: Offset	$4.4306 - 0.55569E_{elec}$
Radial distribution: Spread	$21.798 - 7.7212E_{elec} + 0.71592E_{elec}^2$

Table 6.4: Energy resolution uncertainties for the electron energy range of 4.5 to 6 MeV using FTK energy with path fitter reconstruction. E_{elec} is the electron energy.

6.5 Salt Phase Energy Systematic Uncertainties

For the salt phase, the energy systematic uncertainties are evaluated using the same methods as the D_2O phase. Unlike the D_2O phase, only an energy correction needs to be applied to FTK energy for both data and MC. This correction given below is applied to rectify FTK's MPE calculation which breaks down at energies greater than 15 MeV.

$$T' = -0.10872 + 1.0277T - 0.0012247T^2 \tag{6.10}$$

where T is the kinetic FTK energy.

6.5.1 Energy Scale Uncertainties

When comparing ^{16}N data and MC in the salt phase as a function of source radius, the energy scale asymmetry near the bottom of the detector observed in the D_2O phase is pointedly worse (Figure 6.25). Additionally studies of the energy scale in the NCD phase indicate a further worsening of the energy response near the bottom [73], suggesting that this effect might be due to non-uniform aging of the PMT light concentrators. As the bottom asymmetry is more enhanced in the salt phase, the $Z_{intersect}$ cut (Equation 6.8) used to determine if an event illuminates the bottom of the detector is modified to $Z_{intersect} < -450$cm. With this expanded cut criteria, 12% of event distributed uniformly throughout the volume will be selected as illuminating the bottom of the detector (compared to 8.5% with the D_2O phase cut).

Removing events that illuminate both the top and bottom, the difference between ^{16}N data and MC in energy scale determined using the most probable electron energy fit is shown in Figure 6.26. In contrast to the D_2O phase, the energy response is

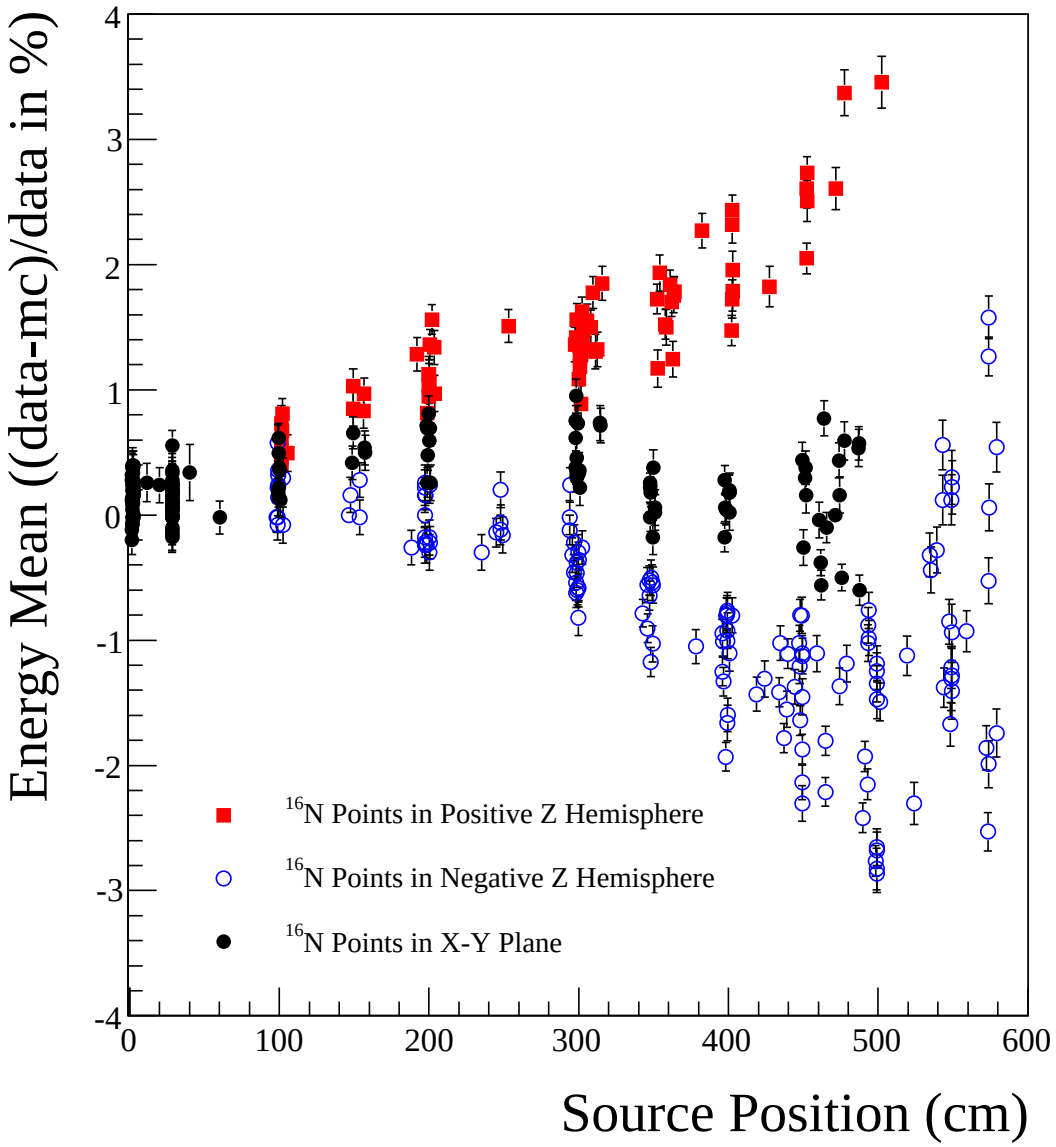

Fig. 6.25: Difference in FTK energy scale for ^{16}N in the salt phase as a function of source radius for source positions above the x-y plane (red squares), below the x-y plane (blue open circles) and on the x-y plane (black circles).

relatively flat to the edge of the fiducial volume. Therefore, the energy scale uncertainty is taken as the volume weighted uncertainty over the entire fiducial volume. Figures 6.27 and 6.28 show the energy scale differences between data and MC for events that illuminate the bottom and top regions of the detector respectively. For events that illuminate the top, the detector is divided into two regions (above and below 375 cm) and the energy scale uncertainties are volume weighted separately in each region. The detector regions used to estimate the energy scale uncertainties for the salt phase are summarized below

$$\text{Scale Uncertainty} = \begin{cases} \text{Top} & \text{if } Z_{intersect} > 500\text{cm} \\ \text{Inner Top} & \text{if } Z_{intersect} > 500\text{cm and } r_{fit} < 375\text{cm} \\ \text{Bottom} & \text{if } Z_{intersect} < -450\text{cm} \\ \text{Middle} & \text{otherwise} \end{cases} \tag{6.11}$$

where the uncertainty values are listed in Table 6.5.

Uncertainties due to detector rate dependent effects are evaluated by comparing the difference between ^{16}N data and MC for high rate and low rate calibration data (Figure 6.29). In the salt phase, rate dependent effects are a much smaller effect and there are significantly more low rate ^{16}N runs. The time dependent uncertainty in the detector response is taken as the variation in energy scale for high rate ^{16}N which is also quoted in the figure.

As with the D_2O phase, many of the energy scale systematic uncertainties are one-sided and a MC method is used to evaluate the positive and negative contributions for each detector region (see Section 6.4.2). The total energy scale uncertainties with

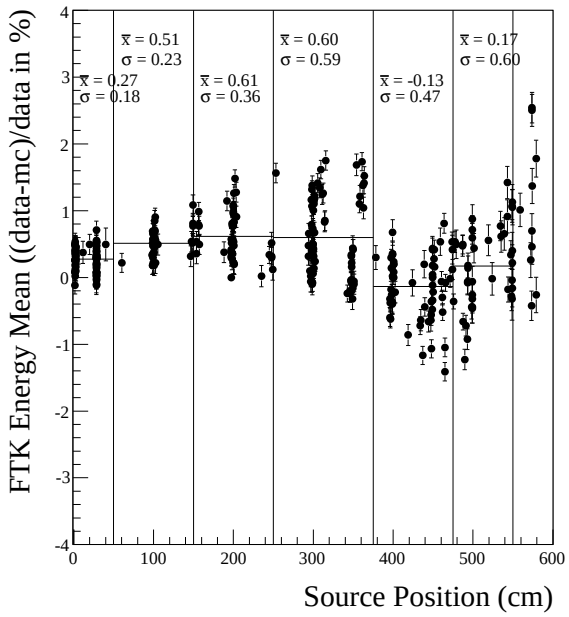

Fig. 6.26: Removing events that illuminate the top and bottom regions, the difference in FTK energy scale for ^{16}N in the salt phase is shown as a function of source radius. The energy means were obtained using the most probable electron energy fit.

Source	Uncertainty	
Detector PMT status		0.01%
Electronics threshold		0.20%
Electronics gain		0.40%
Electronics rate effect		-0.29 ± 0.09%
Time drift/stability: data-MC		0.015%
^{16}N source modeling		0.65%
Radial distribution: data-MC	Top ($r_{fit} > 375$cm)	$+3.20 \pm 0.71$%
	Top ($r_{fit} < 375$cm)	$+1.44 \pm 0.21$%
	Middle	$+0.21 \pm 0.53$%
	Bottom	-3.05 ± 0.83%

Table 6.5: Energy scale uncertainties for the salt phase using FTK energy with path fitter reconstruction.

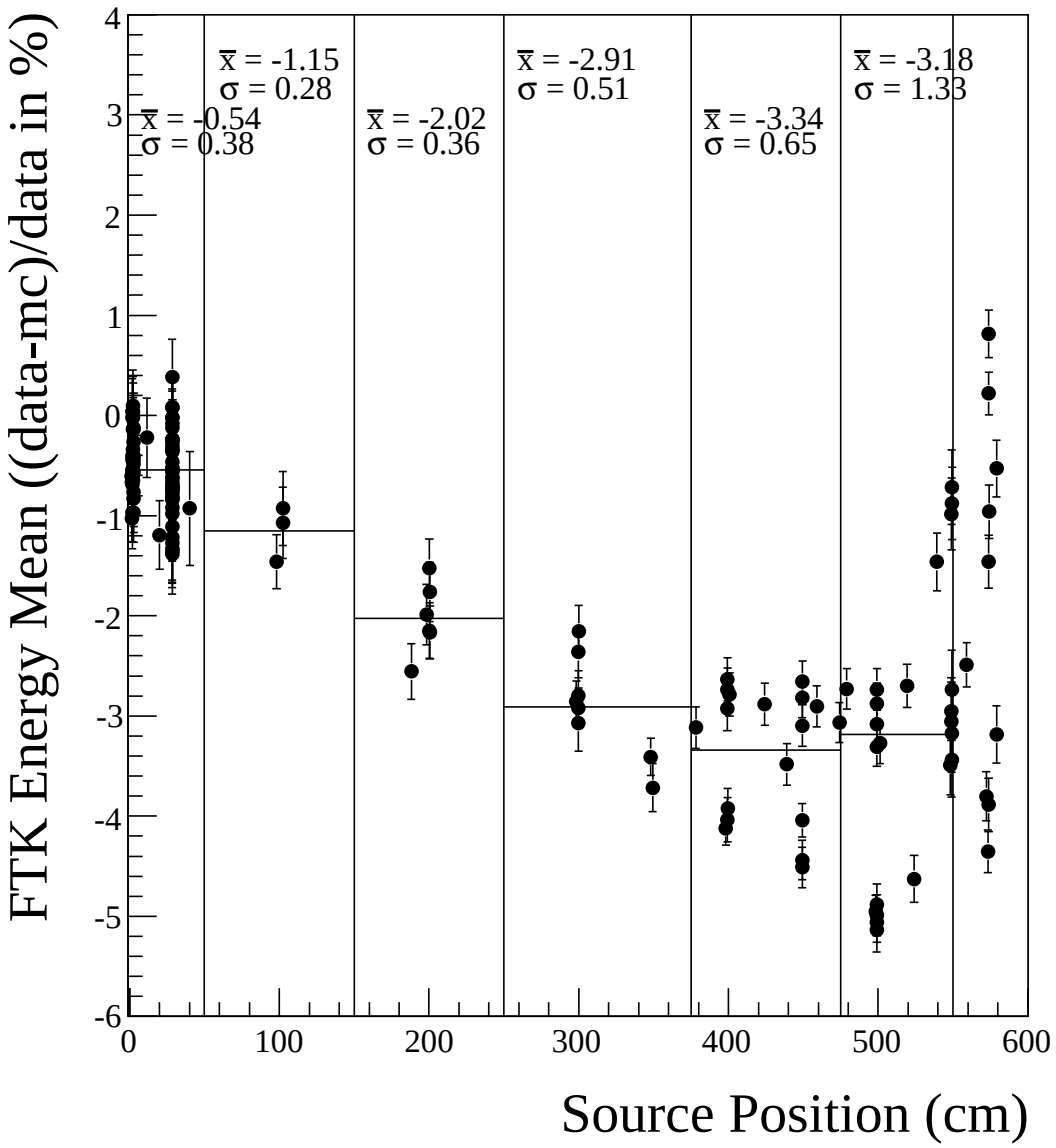

Fig. 6.27: Using only events that illuminate bottom region, the difference in FTK energy scale is shown as a function of source radius for ^{16}N in the salt phase. The energy means were obtained using the most probable electron energy fit.

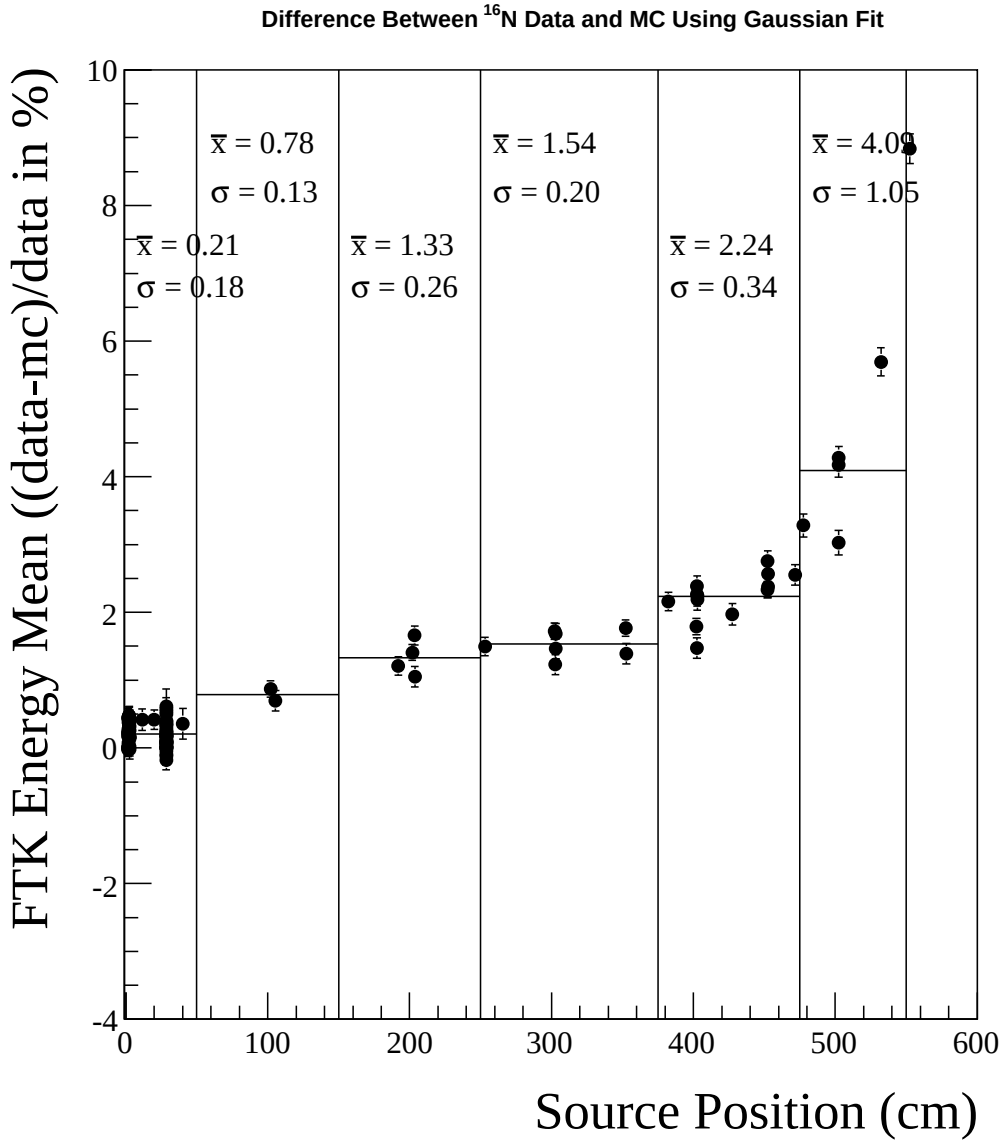

Fig. 6.28: Using only events that illuminate top region, the difference in FTK energy scale is shown as a function of source radius. The energy means were obtained using a Gaussian fit.

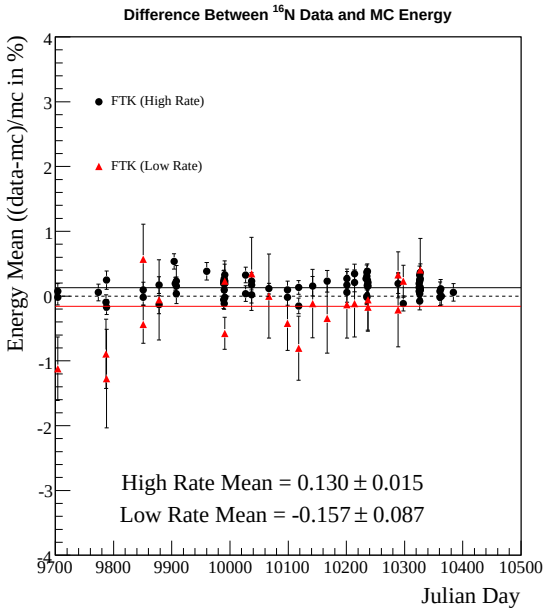

Fig. 6.29: Difference in FTK energy scale for ^{16}N high rate and low rate ^{16}N center runs taken during the salt phase as a function of Julian day. The energy means were obtained using the most probable electron energy fit.

positive and negative shifts are listed in Table 6.6.

6.5.2 Energy Resolution Uncertainties

To evaluate uncertainties on the energy resolution, only ^{16}N events which do not illuminate the top or bottom are considered. This was not necessary when evaluating energy resolution uncertainties in the D_2O phase but in the salt phase, since the energy scale differences between regions are much larger. These large differences in energy scale result in an underprediction of the energy resolution uncertainty for those regions.

Using the most probable electron energy fit, the energy resolution as a function of electron energy is shown in Figure 6.30 which has good agreement with the resolution

Region	Total Uncertainty	Negative Shift	Positive Shift
Top ($r_{fit} > 375$cm)	$+1.46 \pm 1.422\%$	-1.42%	+2.88%
Top ($r_{fit} < 375$cm)	$+0.58 \pm 0.92\%$	-0.92%	+1.50%
Middle	$-0.04 \pm 0.96\%$	+0.96%	-1.00%
Bottom	$-1.67 \pm 1.44\%$	+1.44%	-3.11%

Table 6.6: Summary of the total scale uncertainties and the recommended positive and negative shifts for the salt phase.

Source	Resolution Uncertainty
Radial distribution: data-MC	$1.47 \pm 1.14\%$

Table 6.7: Energy resolution uncertainties at 5 MeV using FTK energy with path fitter reconstruction and ^{16}N in the salt phase.

function determined using mono-energetic electron MC. Comparing the difference in energy resolution between ^{16}N data and MC (Figure 6.31) at an electron energy of 5 MeV, the uncertainty in energy resolution is constant with radius and the overall resolution uncertainty is taken to be the volume weighted average of all ^{16}N points, listed in Table 6.7. Over the range of electron energies from 4.5 to 6.0 MeV, the uncertainty in energy resolution is described by a polynomial listed in Table 6.8 and seen in Figure 6.32. When apply this systematic uncertainty the mean offset and spread should be added linearly.

Source	Resolution Uncertainty (in %)
Radial distribution: Offset	$4.3402 - 0.56796E_{elec}$
Radial distribution: Spread	$20.960 - 7.2172E_{elec} + 0.65110E_{elec}^2$

Table 6.8: Energy resolution uncertainties for the electron energy range of 4.5 to 6 MeV using FTK energy with path fitter reconstruction and ^{16}N in the salt phase. E_{elec} is the electron energy.

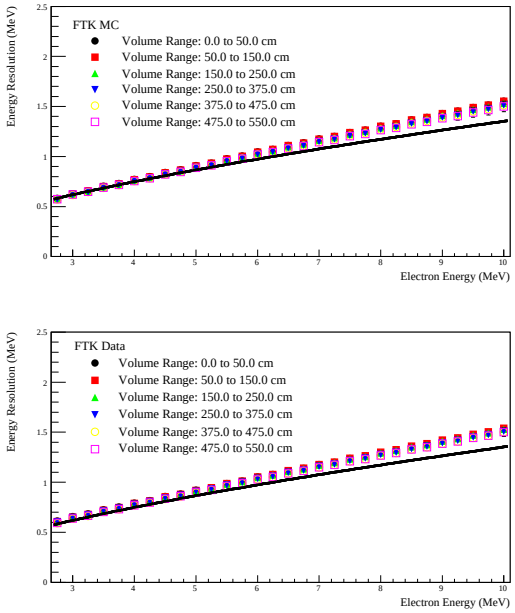

Fig. 6.30: Average resolution function extracted using the most probable electron energy fit for MC (top figure) and data (bottom figure) for various radial slices using ^{16}N taken in the salt phase. The solid line indicates the resolution function measured from mono-energetic MC.

6.6 Summary

This chapter discusses a new method for fitting the ^{16}N energy distribution which utilizes the multi-energetic electron energy nature of this source. Using this fitting method it is possible to determine the energy scale uncertainties as well as the energy resolution uncertainties as a function of electron energy. Detailed comparisons of ^{16}N data to MC indicate that there are is a large asymmetry in energy scale between the top and bottom of the detector. As a result, the energy systematic uncertainties are evaluated separately for the top, bottom and middle regions of the detector. Studying ^{16}N in both the D_2O and salt phases, energy uncertainties (both scale and resolution) have been determined for all regions of the detector using the most probable electron

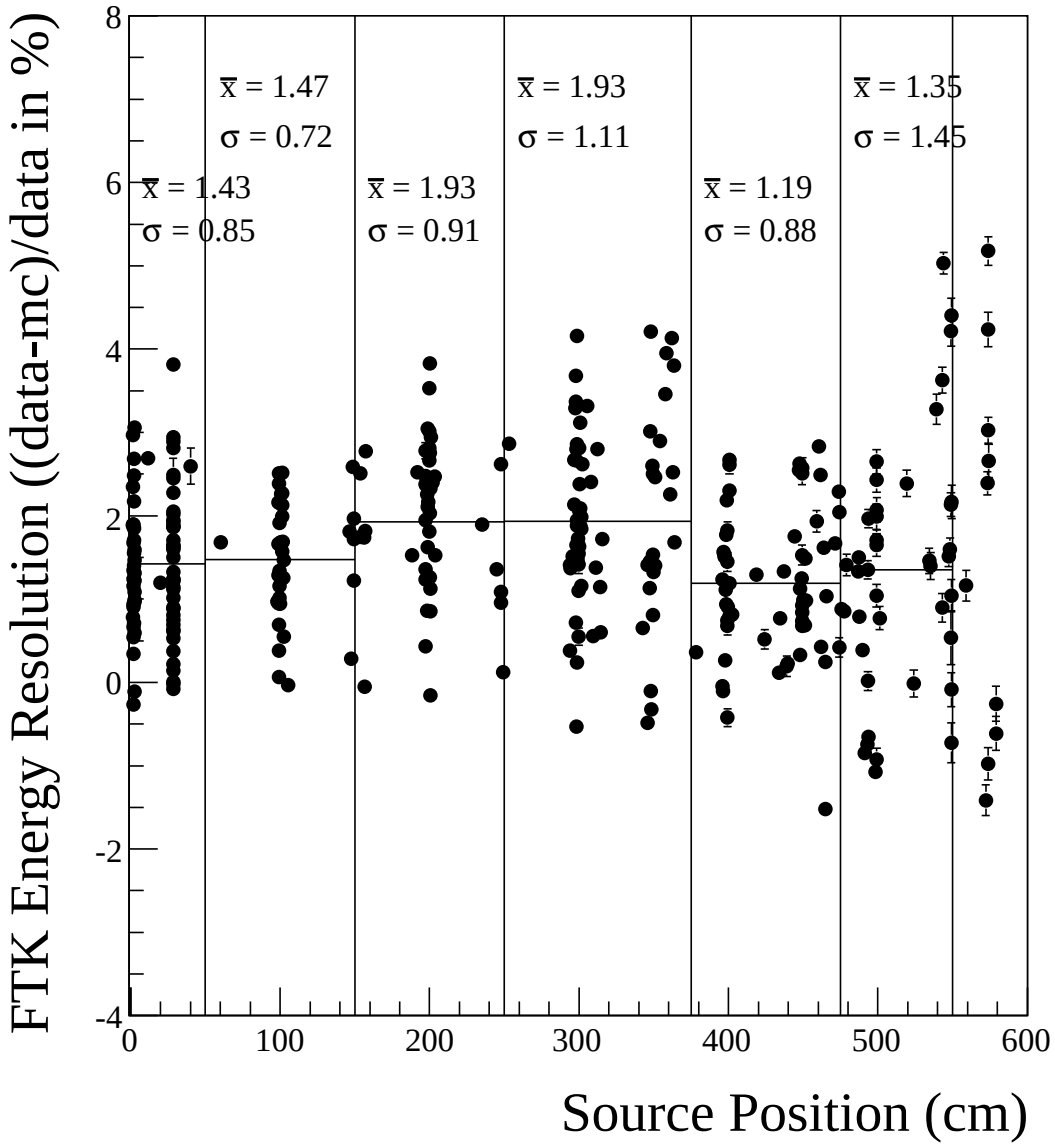

Fig. 6.31: Difference in total electron energy resolution at 5 MeV between ^{16}N data and MC as a function of source radii. The total resolution was obtained using the most probable electron energy fit. Events with illuminate the top and bottom have been eliminated.

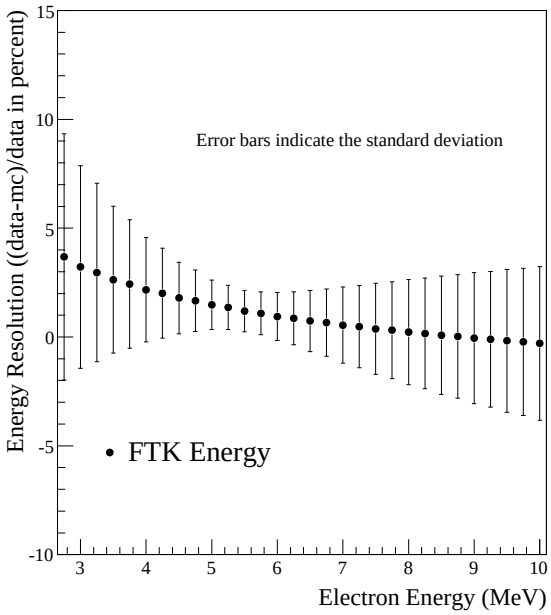

Fig. 6.32: Volume weighted difference in total resolution between ^{16}N data and MC as a function of electron energy using ^{16}N in the salt phase.

energy fitting technique.

Ch. 7

The Data Set

Most of the events collected from the detector are uninteresting for physics analysis. These events are instrumental backgrounds - events that are not caused by Cherenkov light in the detector. To remove these events from the data set, several algorithms were developed which tag instrumental events so that these events can be removed from consideration in the physics analysis. Additionally all the data must pass selection criteria to ensure that the detector was functioning properly when the data were taken. The following section discusses these selection criteria, the various cuts used to flag instrumental events and measurement of the residual contamination of these events in the data set.

In addition to instrumental events, events from low energy ^{214}Bi and ^{208}Tl decays are also present in the data set. This section also discusses the different types of low energy backgrounds and the methods used to estimate the concentrations of these events.

7.1 Data Selection

To ensure the quality of the data taken, all runs where the detector was running in neutrino data taking mode must pass both human and software checks. First, the shift report for each neutrino run is reviewed and discussed by two members of a trained run selection committee. If a neutrino run passes the committee's selection, the run must also pass two software quality checks: first pass selection (FPS) and second pass selection (SPS). For a run to pass all quality checks all functioning PMTs must have high voltage, there can be no sources deployed in the detector, no circulation of the water or radioassays which can produce light in the detector must be running and all trigger and PMT electronics setting must be set to run in neutrino data taking mode. A detailed list of the selection criteria, FPS and SPS can be found in Appendix B.3, [68] and [40].

7.2 Removing Instrumental Backgrounds

In addition to the signal and low energy background events detected by SNO, the detector can produce non-physics events, called instrumental events in the detector. These events are a serious problem since they are produced at a rate much higher than the rate of the signal and low energy background events combined. Fortunately, instrumental events have very different topologies, PMT charge and/or PMT timing distributions from neutrino interaction events and calibration events, which allow these events to be removed from the data.

Flashers, a spontaneous emission of light by a PMT, were first discovered to be a significant source of background before the detector was filled with water and

only air was being used as a medium. A large charge on the flashing tube with associated pick-up in the flanking tubes is typical of such events. Additionally, an elliptical ring of light is detected on the opposite wall one light crossing time later. While it is unknown what causes PMTs to flash, each tube is estimated to do so roughly once a week, resulting in an overall detector flasher rate of once per minute. This is approximately 100 times the neutrino interaction rate. Another PMT based background is flat TAC events, so named because the PMT timing distribution is flat over the trigger window. These events are due to DC light being emitted in the PMT base and are usually associated with the tube's death.

The front-end electronics is prone to pick-up if there is increased personnel activity on the deck or the cavity is shaken from blasting in the mine. Pick-up events have a very distinct topology. There are a large number of hits in a single crate and the hits have a small amount of charge. For these events the ratio of the number of hits to the total amount of charge is very different from events caused by Cherenkov light in the detector.

During the commissioning of the detector, it was discovered that there were unexplained downward going events that appeared to originate in the neck of the AV. The exact origin is unknown (possibly electrical discharge of insulators in the N_2 atmosphere) but these events can be tagged by veto tubes located in the neck.

To remove these events, a group of cuts called the Data Analysis Mask Number (DAMN) cuts were designed. All of the DAMN cuts are based on low level event or PMT charge, timing and location information. These cuts are summarized in Appendix B (also included is a detailed discussion of one of the DAMN cuts; the AMB cut).

A second set of cuts called the high level cuts (HLC) are a more sophisticated

set of cuts use the reconstruction position of the event to remove non-physics events. These are summarized below. The high level cuts are also effective at removing low energy backgrounds [70].

- **High Level Cuts (HLC)**
  - **In-Time Ratio (ITR):** A cut based on the PMT time residual distribution using the reconstructed event position and time. ITR is the ratio of the number of hits which have a time residual between -2.5 and 5.0 ns to the total number of hits in the event. Events with a small value of ITR have very few prompt hits. ITR is extremely effective at removing light water low energy background events which mis-reconstruct inside the fiducial volume.
  - **Beta Parameters:** This is a parameter used to measure an event's isotropy. The $l^{th}\beta$ parameter is defined as the average value of the Legendre polynomial, P_l, of the cosine of the angle with respect to the reconstructed position between each pair of PMT hits in the event. The combination $\beta_{14} \equiv \beta_1 + 4\beta_4$ is used to estimate the event's isotropy. Smaller values of β_{14} indicate the event is more isotropic. See [74] for more details.
  - θ_{ij}**:** Another parameter used to measure an event's isotropy is θ_{ij} which is the average of the angles between each pair of PMT hits in an event with respect to the reconstructed position. Larger values of θ_{ij} indicate the event is more isotropic.
  - **Charge Weighted** θ_{ij}**:** Analogous to θ_{ij} but with each PMT being weighted by its measured charge.

– **In-cone Timing KS Test (ICT) :** A Kolmogorov-Smirnov (KS) test on the time residual distribution of hits inside the Cherenkov cone ($0.6 < \cos\alpha < 0.7$ where α is the angle between the reconstructed direction and the vector from the reconstructed position to the hit PMT). Only hits in the cone are considered because the time residual distribution for hits outside the cone (such as reflected and scattered hits) is strongly dependent upon the event position and is difficult to determine quickly. This KS test is used to cut poorly reconstructed events, especially events which have a poor Cherenkov cone.

– Φ **Angular KS Test:** A KS test that compares the distribution of the Φ angle (azimuthal angle of the vector from the reconstructed position to the hit PMT) of hit PMTs to a uniform distribution (Cherenkov light is produced uniformly about the reconstructed electron direction). Two KS tests are calculated; one using only hits in the cone (see definition in ICT description) and the other using all hits in the event. These tests are effective at removing mis-reconstructed events.

– **2-dimensional Angular KS Test:** A 2-dimensional KS test which compares both the polar and azimuthal angles of the vector from the reconstructed position to the hit PMTs. The event is compared to an energy dependent $\cos\alpha$ distribution derived from mono-energetic electron MC (see 5.4.2) where the event's energy is the RSP estimated energy. As with the Φ Angular KS Test, the 2-d angular KS is calculated twice, once using only hits in the cone, and again with all hits in the event. These tests are effective at removing mis-reconstructed events.

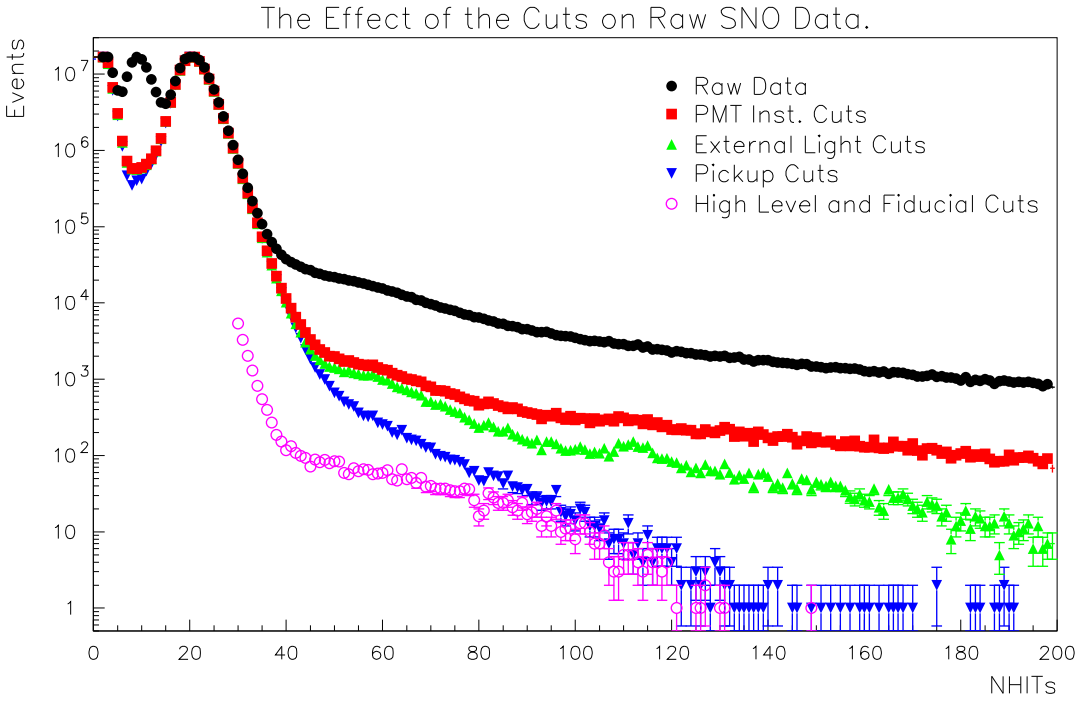

Fig. 7.1: N_{Hit} distribution for the raw data and data with DAMN, θ_{ij} and ITR cuts applied. Figure taken from [75].

– **Charge Probability versus ΔT (QPDT):** A cut designed to remove events that are low energy decays inside the PMT glass that mis-reconstruct inside the signal region. These events tend to have a tube with very large charge (tube nearest the decay) that is early in time with respect to the rest of the light (the remaining light is reflected light with long path lengths). The QPDT cut removes events that have an unusual number of PMTs early in time or have an unusually high charge early in time.

The results of the DAMN, θ_{ij} and ITR cuts on the raw data can be seen in Figure 7.1.

7.3 Contamination Measurement of Instrumental Backgrounds

To estimate the residual contamination of instrumental events remaining in the data sample after the DAMN and HLC cuts have been applied, the bifurcated analysis technique is used [76]. This analysis technique was first developed for SNO by Vadim Rusu but has been expanded to include a more sophisticated box relaxation method and contamination limit calculation. While bifurcated analysis is a very powerful method to estimate residual contamination in a data sample, this technique relies on several assumptions. First, there is only a single background type. For this analysis, all classes of instrumental background events are assumed to be a single background type of non-Cherenkov like events. Second, two orthogonal sets of cuts can be defined, conventionally called the normalized and rejection branches. Orthogonality of the cuts is important as each cut branch is used to cross calibrate the other branch. Correlations between the two cut branches lead to incorrect results. Lastly, bifurcated analysis is only sensitive to the types of backgrounds that the cut branches are designed to eliminate and cannot measure the contamination from backgrounds to which the cuts are not sensitive.

With two cut branches the events in the data set can be categorized to determine the number of events that pass both cuts (a), the number that pass the normalized branch only (b), the number that only pass the rejection branch (c) and number that fail both cuts (d). This is shown graphically in Figure 7.2. Defining y_1 as the fraction of background events that pass the rejection branch and x_1 as the fraction of signal events that pass this branch, the total number of events passing this branch ($a + c$) can be expressed as

$$\text{Rejection Branch:} \qquad a + c = x_1\nu + y_1\beta \tag{7.1}$$

where ν is the number of signal events and β is the number of background events. Similarly the number of events passing the normalized branch is

$$\text{Normalized Branch:} \qquad a + b = x_2\nu + y_2\beta \tag{7.2}$$

where x_2 is the fraction of signal events passing this branch and y_2 is the fraction of background events passing this branch. Since the two cut branches are orthogonal, the number of events passing both cuts is given by

$$a = x_1x_2\nu + y_1y_2\beta \tag{7.3}$$

The number of background events passing both cuts (the contamination) is $y_1y_2\beta$.

In the above equations, a, b and c are known, and x_i can be measured using tagged calibration sources. Assuming the x_i are unity (a valid assumption for the DAMN cuts) Equations 7.1 to 7.3 with some substitutions reduce to

$$c = \nu + y_1(1 - y_2)\beta \tag{7.4}$$

$$b = \nu + y_2(1 - y_1)\beta \tag{7.5}$$

$$a = \nu + y_1y_2\beta \tag{7.6}$$

$$\beta + \nu = a + b + c + d \tag{7.7}$$

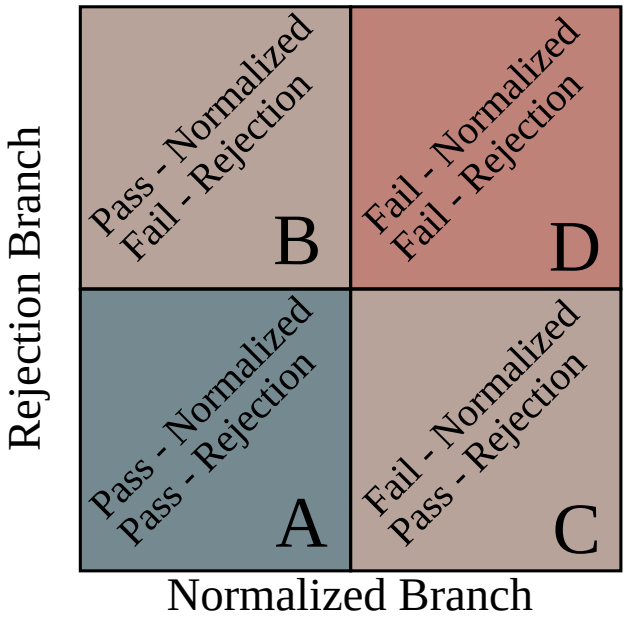

Fig. 7.2: Graphical representation of the pass and fail regions for the normalized and rejection branches used in the bifurcated analysis.

Solving for $y_1 y_2 \beta$, the residual contamination in the data sample is simply

$$y_1 y_2 \beta = \frac{bc}{d} \tag{7.8}$$

Although this equation appears to be very simple, the difficulty lies in verifying the orthogonality of the cut branches.

7.3.1 Bifurcated Analysis: Cut Branches and Results

While both the DAMN cuts and the high level cuts are effective at removing instrumental events, the former uses basic hit geometry, charge and timing information while the latter is based upon the reconstructed vertex position of the event. To define two orthogonal cuts, a first guess might be to use the DAMN cuts that use geometry,

charge, veto tubes and event rate information (QVT, Q/N_{Hit} , QCluster, AMB, Owl, Neck, OwlEHi, crate isotropy, FGC) and the beta parameters, which also uses hit geometry as the normalized branch. The rejection branch would consist of timing based DAMN cuts (FTS and ITC) and ITR which also uses timing. While these cut branches are orthogonal from a cut definition basis, breaking up the DAMN and high level cuts destroys the single background assumption. As a whole, the DAMN cuts remove non-Cherenkov like events but individually they remove specific types of instrumental events. For example, AMB and QCluster are correlated because they both use charge information but also because they are both designed to eliminate flashers. Similarly, the high level cuts are correlated as they both accept events that are Cherenkov like even though one uses timing information and the other isotropy. For the single background assumption to remain true, neither the DAMN cuts nor the high level cuts can be spread among the two branches. Although some of the DAMN cuts which use geometry and timing information might be correlated with the beta parameters and ITR, these correlations, if any were found to be negligible. In [19], the cut branches are defined as

- **First Pass:** Muon Follower Short, Junk, Esum, Retrigger, N_{Hit} Burst, ITC, Energy > 5.5, and Radius < 550
- **Normalized Branch:** AMB, Q/N_{Hit} , Owl, Neck, QVT, Crate Isotropy, FGC, FTS, QCluster, and OwlEhi
- **Rejection Branch:** $-0.12 < \beta_{14} < 0.95$ and ITR > 0.55

where the first pass branch refers to cuts that are preapplied to remove pathological events[1].

[1]ITC is applied in this branch as it is already preapplied in MCProd

Using the cut branches described above and Equation 7.8, the level of contamination for the salt data sample is 0.04 ± 0.01 events or $0.0012 \pm 0.0003\%$ where the errors given are statistical only.

7.3.2 Testing Orthogonality: Relaxing the Box

Orthogonality of the two cut branches can be tested by relaxing the cut branches, remeasuring the contamination and comparing that measurement to the number of additional events in the relaxed box. If the normalized and rejection branches are orthogonal, then the number of new events inside the relaxed box (counted contamination) should be consistent with the value measured by the bifurcated analysis (measured contamination). For this orthogonality test, only the AMB and Owl cut are relaxed in the normalized branch and the ITR in the rejection branch.

For the normalized branch only the AMB and Owl cut can be easily relaxed. The AMB cut is relaxed from 3.7 to 4.0 sigma and the Owl cut from 3 to 5 tubes, For the rejection branch, ITR is relaxed from 0.55 to 0.45. β_{14} is not relaxed to prevent contamination from AV isotropic background events. (These events are thought to be the result of stress relief in the acrylic tiles and are largely eliminated by the β_{14} cut.) Relaxing the β_{14} would include these events breaking the single background assumption. Contamination in the data set from these events is estimated independently [77].

When relaxing the box not all of the events inside the pass-pass region are background events. Figure 7.3, which is a graphical representation of the ITR, beta parameter box, indicates that there is a tail of signal events just outside the ITR box for both ^{16}N and neutrino candidates. When estimating the counted contamination in the relaxed box, the expected number of signal events must be accounted for. Using

Type	Measured Contamination	Counted Contamination	Signal Events	FC Lower Limit	FC Upper Limit
Total	0.18 ± 0.05	6	5.15	0.0	4.13
Day	0.04 ± 0.02	1	2.31	0.0	0.79
Night	0.14 ± 0.04	4	2.84	0.01	3.9

Table 7.1: Summary of the measured contamination value using the bifurcated analysis technique and the counted contamination value found when relaxing the box. Also included is the Feldman-Cousins (FC) limits given the estimated signal events. The FC limits are for 68% confidence levels.

the ^{16}N source, ITR cuts 0.1% of signal events between 0.45 and 0.55. The number of signal events expected when relaxing ITR is 3.2 events. Using high rate ^{8}Li in the center, the number of signal events cut between 3.7 and 4.0 sigma for the AMB cut is $0.005 \pm 0.005\%$ or 1.9 events.

Relaxing the box yields a measured contamination of 0.18 ± 0.05 events and a counted contamination of 6 events with 5.15 expected signal events. These results along with diurnal measurements of the relaxed contamination are summarized in Table 7.1. Feldman-Cousins limits were calculated to determine if the signal subtracted counted contamination is consistent with the measured contamination (also shown in the table). Since the measured contamination of the relaxed box is consistent with the Feldman-Cousins limits, the normalization and rejection branches are orthogonal.

7.4 Summary of Instrumental Backgrounds

Although instrumental background events dominate the rate of events in the detector, many different algorithms have been developed that successfully eliminate these events from the data set. The bifurcated analysis technique, used to measure the number of instrumental background events remaining in the data set, finds the con-

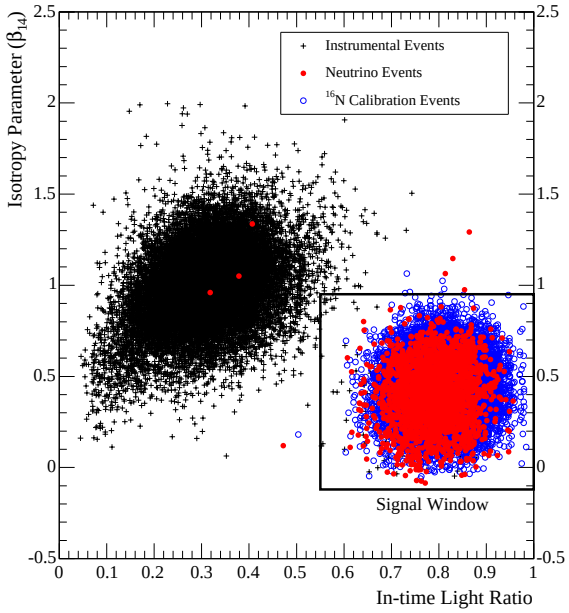

Fig. 7.3: The Beta parameters versus ITR for instrumental events, neutrino candidates, and ^{16}N for the salt data set.

tamination is very small.

7.5 Low Energy Cherenkov Background Estimates

Below electron kinetic energies of 4.5 MeV, the signal region becomes dominated by events from low energy decays in the ^{238}U and ^{232}Th chains. These events are classified into two categories; internal and external Cherenkov background events. The internal Cherenkov backgrounds are events from decays in the ^{238}U and ^{232}Th chains, the most energetic of which are ^{214}Bi and ^{208}Tl decays inside the heavy water. These events are isotropically distributed through the D_2O volume and can only be distinguished from the signal events using the energy spectrum, the isotropy parameters and the event direction with respect to the Sun. The second class of backgrounds, ex-

ternal Cherenkov backgrounds, are decays in the ^{238}U and ^{232}Th chains in the acrylic, light water and PMT glass. Since these events are produced in the light water but mis-reconstruct inside the signal volume, the HLCs discussed in Section 7.2 are effective at removing them. External background events remaining in the signal region after applying all analysis cuts can be distinguished from the signal using the energy spectrum, the isotropy parameters, the event direction with respect to the Sun, and the radial distribution of the backgrounds. External Cherenkov backgrounds tend to be near the outer volume of the detector rather than uniform throughout the detector.

In SNO's measurements to date, the number of internal Cherenkov background events inside the signal region has been estimated by measuring the number of ^{214}Bi and ^{208}Tl events in a very low energy region (approximately 4.0 to 4.5 MeV) where backgrounds dominate over the signal events. These rates are extrapolated to the analysis energy region. The number of expected background events in the signal region is subtracted from the lowest bin of the CC energy spectrum. Similarly for the external background events, the rate of ^{214}Bi and ^{208}Tl is determined outside the fiducial volume, in the light water. These event rates for the AV, H_2O and PMT external Cherenkov backgrounds are then extrapolated into the fiducial volume.

This thesis takes a different approach which is to fit for both the internal and external Cherenkov background events simultaneously with the signal (see Chapter 8 for further details). A difficulty with this approach is that at energies below 4.5 MeV, the Cherenkov backgrounds are difficult to distinguish from CC electrons. To mitigate this problem, constraints on the rates of ^{214}Bi and ^{208}Tl in the detector are useful. For the internal Cherenkov backgrounds, since the neutrino data is used in the signal extraction fit, it can not be used to constrain the background rates. Instead, to set constraints on these rates, measurements from the radioassays are used.

These measurements are a completely independent measurement of the background rates and are discussed in the next section. For the external Cherenkov background events, radioassay measurements of the ^{238}U and ^{232}Th rates are also available for the light water but not the AV or PMT regions. Since most of the information about the external background rates can be obtained outside the signal region, a method of determining the background rates for the AV, H_2O and PMT regions using the neutrino data in the light water can be used to constrain the number of these events inside the signal region. Appendix C discusses the methodology of obtaining these rates and the analysis that was used to estimate the number of external background events for [19]. For the extraction of the signals in this thesis, the only constraints on the external Cherenkov backgrounds in the H_2O from radioassays were used but using the method discussed in Appendix C to constrain the external backgrounds could reduce the statistical uncertainties in the signal extraction fits.

7.5.1 Internal Cherenkov Backgrounds

Several radioassays are used in SNO to measure both the ^{238}U and ^{232}Th concentration in the D_2O volume, the details of which can be found in [62] and [63]. These assays are taken roughly on a bi-monthly basis and therefore cannot monitor spikes in the radioactivity. The measured ^{238}U and ^{232}Th rates for both the D_2O phase and salt phase data sets are listed in Table 7.2.

During the salt phase, there was a leak in the assay system used to measure ^{222}Rn in the ^{238}U chain which was not discovered until after the salt phase data taking had ended. As a result, it is only possible to set an upper limit on the amount of ^{222}Rn in the D_2O during this time period. A second radioassay method which measures ^{226}Ra

Type	D_2O Phase (g per g of D_2O)	Salt Phase (g per g of D_2O)
^{238}U	$1.01^{+0.34}_{-0.20} \times 10^{-14}$	Upper Limit 2.0×10^{-14} Lower Limit $1.41 \pm 0.46 \times 10^{-16}$
^{232}Th	$2.09 \pm 0.21(stat.)^{+0.96}_{-0.91}(sys.) \times 10^{-15}$	$1.76 \pm 0.44(stat.)^{+0.70}_{-0.94}(sys.) \times 10^{-15}$

Table 7.2: Summary of ^{238}U of ^{232}Th concentrations in the D_2O volume determined from the radioassays in the D_2O and salt phases.

Type	D_2O Phase (g per g of H_2O)	Salt Phase (g per g of H_2O)
^{238}U	$29.5 \pm 5.1 \times 10^{-14}$	$20.6 \pm 5.0 \times 10^{-14}$
^{232}Th	$8.1^{+2.7}_{-2.3} \times 10^{-14}$	$5.2 \pm 1.6 \times 10^{-14}$

Table 7.3: Summary of ^{238}U of ^{232}Th concentrations in the H_2O volume determined from the radioassays in the D_2O and salt phases.

(also in the ^{238}U chain) can be used to set a lower limit on the ^{238}U concentration for the salt phase. Measurements of ^{226}Ra can only be used as a lower limit since it tends to diffuse out of the water into the pipes and o-rings of the water systems.

Aside from the salt phase measurement of the ^{238}U concentration which is very poor, the radioassays provide nice constraints on the rates of internal Cherenkov backgrounds.

7.5.2 External Cherenkov Backgrounds

Using similar methods as used for the radioassays of the internal Cherenkov backgrounds, the measurements of the ^{238}U and ^{232}Th concentrations in the light water for both the D_2O and salt phase data sets are shown in Table 7.3. Compared to the D_2O volume, the requirements for the cleanliness of the H_2O are more relaxed leading to concentrations that are generally a factor of 10 larger.

7.6 Summary of Cherenkov Backgrounds

To set constraints on the rate of internal and external ^{238}U and ^{232}Th backgrounds, measurements of the D_2O and H_2O background concentrations from the radioassays are used. With these constraints the backgrounds can be fit simultaneously with the signal.

Ch. 8

Signal Extraction Technique

Since only the Cherenkov light from a recoil or Compton scattered electron is observed in CC, ES and NC events (Section 1.4.2), it is impossible to distinguish events from each interaction individually. To estimate the amount of each signal in the data set, a maximum likelihood fit is used. This signal extraction approach uses a set of observables (energy, event direction with respect to the Sun, event position and isotropy) to distinguish the signals. This chapter introduces the signal extraction method and discusses fitting using multiple phases of data with the inclusion of low energy backgrounds.

8.1 The Maximum Likelihood Method

Although CC, ES and NC events can not be distinguished event-by-event, the electrons observed from each of these interactions have properties which can be exploited to determine the amount of each signal in the data set. The most powerful observables used to distinguish the signals are the event's energy (E), the event's reconstructed

direction with respect to the direction from the Sun ($\cos\theta_\odot$), the event's reconstructed radial position ($\rho \equiv (\frac{r}{r_{\rm AV}})^3$), and an isotropy parameter (β_{14}, see Section 7.2). For the CC, ES and NC signals, distributions of these observables are shown in Figures 8.1 and 8.2 for the D_2O and salt phases respectively.

The energy spectra are quite different between the signals and this gives some handle in separating the signals. However, the CC and ES energy spectra can be distorted by matter effects and/or new physics as discussed in Chapter 1. To search for distortions, the CC and ES energy spectra are not constrained when extracting the number of signal events in the data set. A fit without using the CC and ES energy spectra is called an unconstrained fit. The free neutron produced from the NC interaction has no memory of the neutrino energy and therefore the neutron energy spectrum is included in the fit.

The observable $\cos\theta_\odot$ is very effective at distinguishing the ES signal. For this interaction the $\cos\theta_\odot$ distribution is strongly correlated with the Sun's direction. The CC interaction has a slight correlation with the Sun's direction of $\approx 1 - \frac{1}{3}\cos\theta_\odot$, whereas the direction of the γ produced from the captured NC neutron is completely uncorrelated with the Sun's location.

Each event's radial position[1] also offers some discrimination between the signals. While the CC and ES signals are uniform in the radial variable ρ, NC neutrons produced at large radii have a greater probability of wandering into the light water where their capture produces a γ with an energy too low to be observed. As a result the radial distribution for neutrons tends fall off at high radii. This effect is enhanced in the D_2O phase where the capture efficiency is smaller and neutrons travel much

[1]For this analysis the path fitter reconstruction algorithm is used (see [38] for a detailed description).

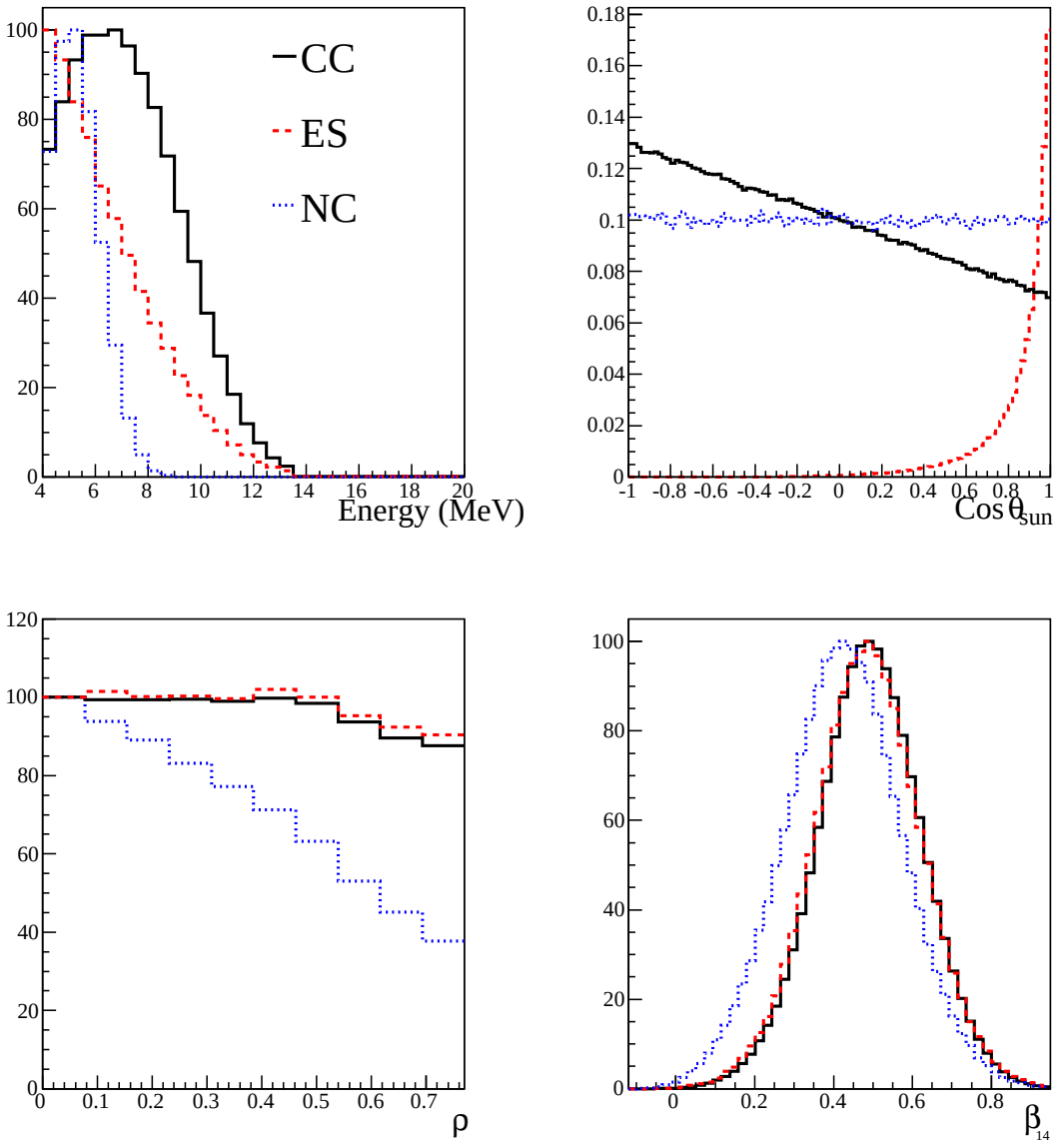

Fig. 8.1: Distributions of the signal extraction observables for CC, ES and NC events in the D_2O phase.

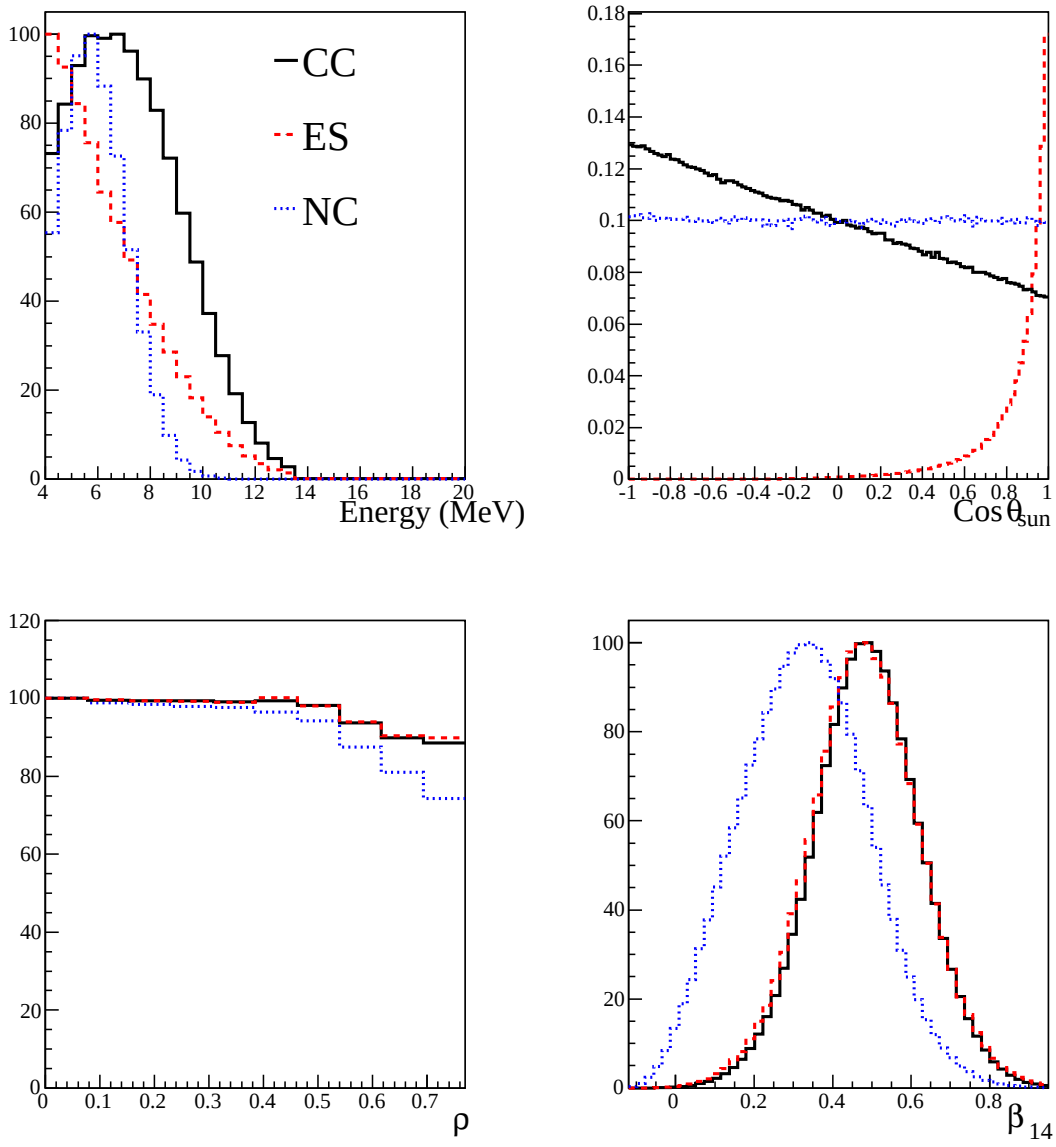

Fig. 8.2: Distributions of the signal extraction observables for CC, ES and NC events in the salt phase.

further distances before capturing. Although the radial distribution offers little handle on separating the signals, this distribution is very useful in separating signal events from external backgrounds (see Section 8.3).

The fourth observable used to distinguish the signals is the isotropy parameter β_{14} which is a measure of the spatial distribution of PMT hits. In the pure D_2O phase, neutron capture on deuterium produces a single 6.25 MeV γ. This γ can Compton scatter an electron, which if energetic enough produces Cherenkov light. The γ losses most of its energy to one electron therefore the isotropy distribution between NC, CC and ES signals tend to be very similar in this phase. In the salt phase, neutron capture on chlorine produces multiple, isotropically-distributed γs which then scatter multiple electrons. Although it is not possible to reconstruct individual electrons in an event, multiple isotropic electrons tend to make the distribution of PMT hits more isotropic (smaller values of the β_{14} observable). This allows better separation of NC events from CC and ES electrons.

To obtain the number of CC, ES and NC signal events in data set, the distributions of these observables are used in a maximum likelihood fit to the data. The maximum likelihood technique finds the *most probable* parameter values of the parameter set $\overline{x}_d$ by maximizing the product of probabilities. Known as the likelihood function, this product of probabilities can be expressed as

$$\mathcal{L} = \prod_{d=1}^{N_{data}} f(\overline{x}_d; \overline{\theta}) \tag{8.1}$$

where N_{data} is the number of events in the data set and $f(\overline{x}_d; \overline{\theta})$ is the probability density function (PDF) for measuring the observables, $\overline{x}_d$ for a given parameter set, $\overline{\theta}$. The number of events in the data set, N_{data} is Poisson distributed around the true

mean number of events μ_0. This Poisson probability can be included in the likelihood as follows

$$\mathcal{L} = \mu_0^{N_{data}} \frac{e^{-\mu_0}}{N_{data}!} \prod_{d=1}^{N_{data}} f(\overline{x}_d; \overline{\theta}) = \frac{e^{-\mu_0}}{N_{data}!} \prod_{d=1}^{N_{data}} \mu_0 f(\overline{x}_d; \overline{\theta}). \tag{8.2}$$

which is called the extended maximum likelihood function (see [78] for a detailed discussion).

For signal extraction in SNO, the parameter set $\overline{\theta}$ is the number of CC, ES and NC events. In this case, the PDFs $f(\overline{x}_d; \overline{\theta})$ are a linear function of $\overline{\theta}$ and simplify to

$$f(\overline{x}_d; \overline{\theta}) = \sum_{i=1}^{N_s} n_i f_i(\overline{x}_d) \tag{8.3}$$

where N_s is the number of signal types (CC, ES and NC) and $n_i \equiv \theta_i$ is the number of events of signal type i and is also the parameter being varied in the fit. The observable parameters, $\overline{x}_d$ are energy, $\cos\theta_\odot$, ρ and β_{14}.

Computationally the logarithm of the likelihood function is maximized as this is more practical. The log likelihood, L is expressed as

$$L = \log \mathcal{L} = \sum_{d=1}^{N_{data}} \log \left(\sum_{i=1}^{N_s} n_i f(\overline{x}_d) \right) - \sum_{i=1}^{N_s} n_i \tag{8.4}$$

where the equalities $\mu_0 = \sum_{i=1}^{N_s} \mu_i$ and $\mu_i = \mu_0 \frac{n_i}{N_{data}}$ have been used. (Constant terms of μ_0 and $\log(N_{data}!)$ have been omitted since they contribute only to the overall offset of the likelihood.) The likelihood calculation is done numerically using a signal extraction routine (called MXF) installed in SNOMAN. CERN's MINUIT minimization package [79] is utilized. The MXF code has been extensively tested and was used as the extraction algorithm for the analysis in SNO's publication of the salt data set [19]. For the purpose of this analysis, it has been expanded to include fitting

using multiple phases of data. For a beautiful description of the MXF verification and features see [68].

8.2 Fitting Using Multiple Phases

To combine two phases of data, the log likelihood function is expanded to

$$L = \sum_{d=1}^{N_{data}} \log\left(\sum_{i=1}^{N_s} n_i f_i(\overline{x}_d)\right) - \sum_{i=1}^{N_s} n_i + \sum_{d'=1}^{N'_{data}} \log\left(\sum_{i=1}^{N_s} n'_i f'_i(\overline{x}'_d)\right) - \sum_{i=1}^{N_s} n'_i \tag{8.5}$$

where $f_i(\overline{x}_d)$ are the PDFs for the D_2O phase, $f'_i(\overline{x}'_d)$ are the PDFs for the salt phase, and n_i and n'_i are the number of events of signal type i in the D_2O and salt phases respectively. For each signal, n_i and n'_i are not independent between the two phases and can be related by

$$n_i = F_i \times E_i \times t_i \times \epsilon_i \tag{8.6}$$

$$n'_i = F_i \times E'_i \times t'_i \times \epsilon'_i \tag{8.7}$$

where F_i is the fraction of the number of expected events observed for signal i and the parameters that are maximized in the fit. E_i and E'_i are the number of expected events per unit time predicted by the Standard Solar Model for this signal in the D_2O and salt phases respectively, t_i and t'_i is the duration of the D_2O and salt phases and ϵ_i and ϵ'_i is the efficiency of detecting signal events for each phase. These efficiency terms includes acceptances on signal events due to the energy and fiducial volume cuts. Assuming no time variation in the neutrino survival probability, F_i is the same for both phases and using these relations in the likelihood function, the number of

signal events of type i in each phase can not vary independently. The remaining terms, E_i, E_i', t_i, t_i', ϵ_i and ϵ_i' are determined from the signal MC used to make the PDFs.

Equation 8.5 describes the likelihood function for a constrained fit where the shape of the CC and ES energy spectra are included in the PDFs. To test for matter effects, it is desirable to fit for the shape of the CC and ES energy spectra. In such an unconstrained fit, each energy bin for the CC and ES signals is treated as a separate parameter in the fit and the likelihood function for an individual event in a single phase becomes

$$\mathcal{L}_d = \sum_{i=CC,ES} \left(\sum_{k=1}^{N_{spec}} n_{i_k} f_{ik}(\overline{x}_d) \right) + \sum_{i=NC} (n_i f_i(\overline{x}_d)) \tag{8.8}$$

where n_{i_k} is the number of events in the spectral bin k and N_{spec} is the number of spectral bins.

8.3 Including Backgrounds in the Likelihood Fit

In the SNO publications [2, 19, 28, 64], the energy threshold of the analysis was high enough that events from internal and external radioactivity (see Section 7.5) were very small and therefore not included in the signal extraction fit. At lower energy thresholds, the number of background events is significant and therefore must be included directly in the fit with the signals. The low energy backgrounds that need to be included in the signal extraction consist of internal ^{214}Bi and ^{208}Tl, ^{214}Bi and ^{208}Tl in the AV, ^{214}Bi and ^{208}Tl in the H_2O and PMT β-γ (^{214}Bi and ^{208}Tl decays in the PMT glass). With the exception of the PMT β-γ backgrounds, the PDFs for

^{214}Bi and ^{208}Tl backgrounds for each region are built using MC. Photo-disintegration neutrons produced from γs in the ^{214}Bi and ^{208}Tl decays are also included in the background PDFs. The PMT β-γ PDF for each phase is built using a very hot ^{232}Th source near the PSUP (see Appendix C.1.3 for a description).

In addition to ^{214}Bi and ^{208}Tl backgrounds, neutron backgrounds from (α, n) reactions on ^{13}C, ^{17}O and ^{18}O initiated by Radon daughters that accumulated on the surface of the AV during construction are also included for both phases. These neutrons are distinguishable from NC produced neutrons because they tend to capture near the AV. Although the number of (α, n) neutrons is expected to be small, they are included in the fit. Additionally in the salt phase, backgrounds from ^{24}Na are also present. ^{24}Na is produced by a neutron capture on ^{23}Na and β-decays to ^{24}Mg (the half life of ^{24}Na is 15 hours). This decay produces a low energy β which mimics CC electrons and a 2.75 MeV γ which can photo-disintegrated a deuteron. ^{24}N is mainly introduced into the detector via the neck or the water system pipes during water circulation.

The observable distributions for the internal backgrounds are shown in Figures 8.3 and 8.4 for the D_2O and salt phases, respectively. These backgrounds have very similar radial, $\cos\theta_\odot$ and β_{14} distributions to the CC signal and are very difficult to distinguish from that signal. Similarly, Figures 8.5 and 8.6 show the distributions for the external backgrounds for both phases. The external backgrounds have a distinct radial distribution allowing for better separation from the signal.

To include backgrounds in the signal extraction, the likelihood function (Equa-

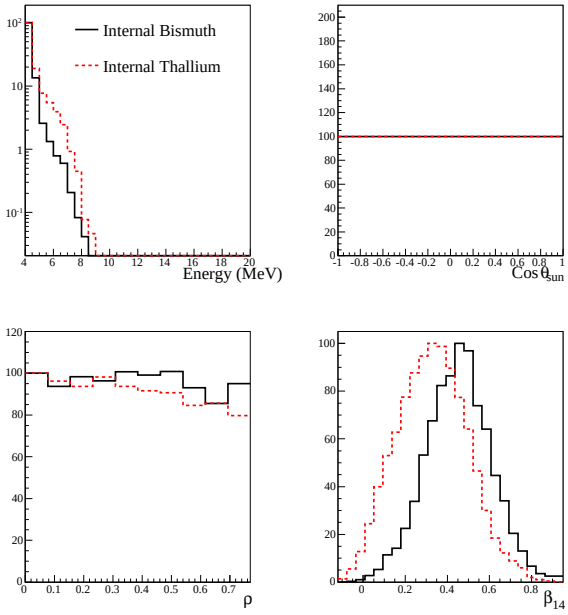

Fig. 8.3: Distributions of the signal extraction observables for internal ^{214}Bi and ^{208}Tl events in the D_2O phase.

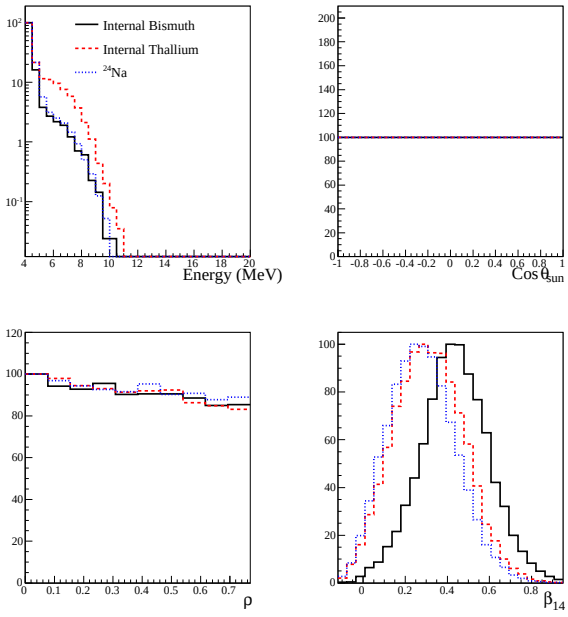

Fig. 8.4: Distributions of the signal extraction observables for internal ^{214}Bi, ^{208}Tl and ^{24}Na events in the salt phase.

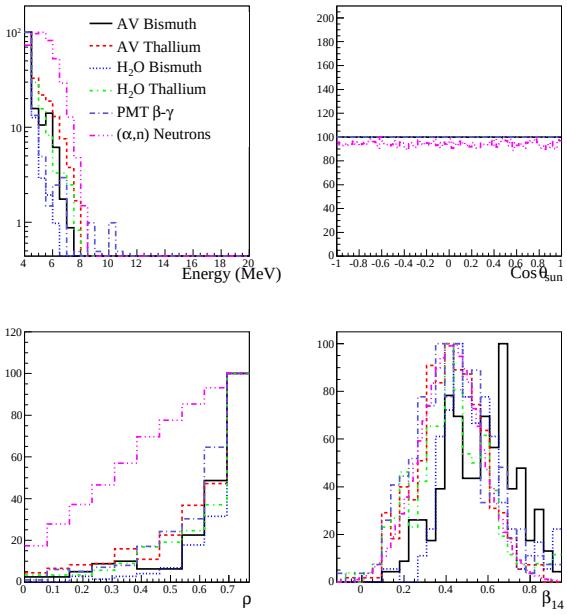

Fig. 8.5: Distributions of the signal extraction observables for external ^{214}Bi and ^{208}Tl, PMT β-γ and (α, n) neutron events in the D_2O phase.

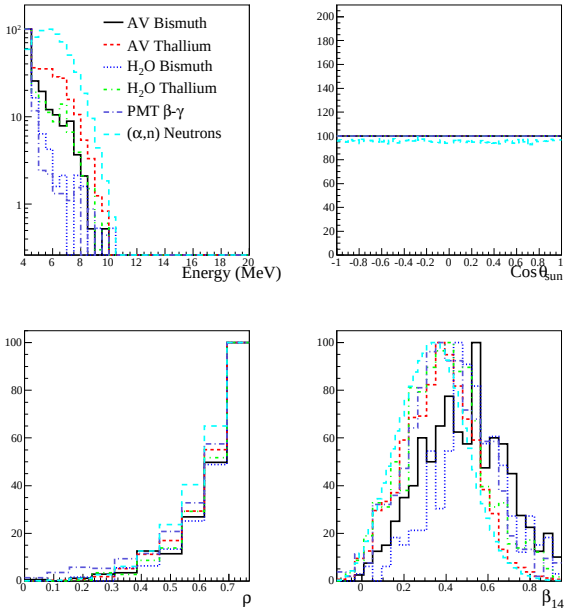

Fig. 8.6: Distributions of the signal extraction observables for external ^{214}Bi and ^{208}Tl, PMT β-γ and (α, n) neutron events in the salt phase.

tion 8.5) is modified to

$$\begin{aligned} L &= \sum_{d=1}^{N_{data}} \log\left(\sum_{i=1}^{N_s} n_i f_i(\overline{x}_d) + \sum_{j=1}^{N_b} m_j g_j(\overline{x}_d)\right) - \sum_{i=1}^{N_s} n_i - \sum_{j=1}^{N_b} m_j \\ &+ \sum_{d'=1}^{N'_{data}} \log\left(\sum_{i=1}^{N_s} n'_i f'_i(\overline{x}'_d) + \sum_{j=1}^{N'_b} m'_j g'_j(\overline{x}'_d)\right) - \sum_{i=1}^{N_s} n'_i - \sum_{j=1}^{N'_b} m'_j \end{aligned} \tag{8.9}$$

where N_b and N'_b are the total number of backgrounds types in the D_2O and salt phases respectively, m_j and m'_j is the number of events of background type j in the D_2O and salt phases and $g_j(\overline{x}_d)$ and $g'_j(\overline{x}_d)$ are the PDFs for each background type. Unlike the signals, the number of background events of a given type is not correlated between the two phases[2]; therefore each background is treated as an independent parameter in the fit.

For the D_2O and H_2O backgrounds, the radioassays place constraints on the concentrations of ^{214}Bi and ^{208}Tl (see Tables 7.2 and 7.3). These constraints are taken to be a Gaussian with asymmetric upper and lower 1σ limits. This constraint adds to the log-likelihood function (Equation 8.9) the term

$$\sum_{j=1}^{N_b} \log(C_j(m_j)) \tag{8.10}$$

where C_j is the Gaussian probability of obtaining m_j background events. If no constraint is applied to a certain background $C_j(m_j) = 1$.

[2] (α, n) Neutrons, AV backgrounds and PMT β-γ could be constrained between the two phases but are not for this analysis.

8.4 Evaluating Fit Biases

The maximum likelihood method can produce a bias in the extracted fit parameters if either a correlation between the observables is neglected in the PDFs or the PDF statistics are not sufficient. To completely account for correlations between observables, the PDF for each signal and background type would be multi-dimensional where the number of dimensions would be equal to the number of observables. In practice, the MC statistics are too poor for this dimensionality. To optimize both the dimensionality of the PDFs and the bin sizes, artificial data sets (built from MC for both D_2O and salt phases) are used to determine if any biases are present in this signal extraction. The number of events for each signal and background type in the artificial data sets is Poisson distributed and is approximately the number of events expected in the data. For verification of the signal extraction, 10 artificial data sets were assembled including CC, ES, and NC signals, internal ^{214}Bi and ^{208}Tl events, and external neutrons (including (α, n) neutrons and external photo-disintegration neutrons) for both phases. Only 10 artificial data sets were assembled due to limited statistics in the background MCs. When including external backgrounds (^{214}Bi and ^{208}Tl in the AV and H_2O) in the artificial data sets, 10 data sets were generated but the number of events in each set was reduced by a factor of 10. Due to computational limitations, the statistics of the H_2O MCs are poor therefore building both the PDFs and multiple artificial data sets with a realistic number of events is not possible.

To verify that the maximum likelihood method is not biased, the signal extraction fit is repeated on each of the artificial data sets to determine if there is any pulls or

biases, defined as

$$\text{Pull} = \frac{N(X) - E(X)}{\sigma(X)} \tag{8.11}$$

$$\text{Bias} = \frac{N(X) - E(X)}{E(X)} \tag{8.12}$$

where $N(X)$ is the fitted number of events for signal or background type X, $E(X)$ is the number of true number of events of that type in the artificial data set and $\sigma(X)$ is the statistical uncertainty on the fitted number of events. Both the pull (quoted in terms of sigma) and bias (quoted in terms of percent) should be distributed around zero if the fit is unbiased.

As four dimensional PDFs of energy, $\cos\theta_{\odot}$, ρ and β_{14} are not possible due to limited MC statistics, the PDFs are factorized into a three dimensional PDF of energy, ρ and β_{14} and one dimensional PDF of $\cos\theta_{\odot}$ as seen below

$$f_i(\overline{x}_d) = f_i(E, \rho, \beta_{14}) \times f_i(\cos\theta_{\odot}). \tag{8.13}$$

Energy and β_{14} are highly correlated since low energy electrons scatter more and therefore produce more isotropic PMT hit patterns. Including correlations between energy and ρ was shown in [68] to reduce biases in the ES signal. The parameter ranges and bin sizes are quoted in Table 8.1. Using this parameterization in an unconstrained fit to 10 artificial data sets, including the signal, external neutrons and internal backgrounds resulted in huge pulls on the order of 10σ in the 4.0 to 4.5 MeV CC spectral bin. This bias was determined to be due to poor statistics in

the background PDFs. Instead the following parameterization is adopted

$$f_i(\overline{x}_d) = f_i(E, \rho, \beta_{14}) \times f_i(\cos\theta_\odot) \quad (8.14)$$

$$g_j(\overline{x}_d) = g_j(E, \beta_{14}) \times g_j(\rho) \times g_j(\cos\theta_\odot) \quad (8.15)$$

where $f_i(\overline{x}_d)$ is the PDF parameterization used for the signals and $g_j(\overline{x}_d)$ is the parameterization used for the background PDFs. Ranges and bin sizes for $f_i(\overline{x}_d)$ are quoted in Table 8.1 and Table 8.2 for $g_j(\overline{x}_d)$. Using this factorization in an unconstrained fit on 10 artificial data sets, the mean pull (Figure 8.7) and mean bias (Figure 8.8) in the lowest energy bin is significantly reduced although not consistent with zero. The remaining bias is most likely due to correlations between energy and ρ in the background PDFs which are not included in this factorization. Better MC statistics in the background MC, specifically internal ^{214}Bi would help to eliminate this bias but for the purpose of this analysis the bias is included in model testing (see Section 9.3.2). In a constrained fit, there is no bias in the extracted CC, ES and NC rates using the parameterization in Equation 8.15. Including AV and H_2O backgrounds in the artificial data sets introduces no new biases in either the constrained or unconstrained fits.

The artificial data sets can also be used to estimate the expected statistical uncertainty on the extracted signal rates. As seen in Figure 8.9 , the fractional uncertainty (defined as $\sigma(X)/N(X)$) in the 4 MeV CC energy bin (CC1 in the figure) is large, roughly 25%. This uncertainty can be significantly reduced by lowering the energy threshold further to 3.5 MeV. Between 3.5 and 4.0 MeV, low energy backgrounds dominate by a factor of 10 over the expected signal rate. Including this energy bin in the fit serves to normalize the number of background events, improving the statistical

Observable	Lower Limit	Upper Limit	Bin Size
Energy (con)	4.0 MeV	20.0 MeV	0.5 MeV (4 to 13.5 MeV) 6.5 MeV (13.5 to 20 MeV)
Energy (uncon)	4.0 MeV	12.0 MeV	0.5 MeV
$\cos\theta_{\odot}$	-1.0	1.0	0.02
ρ	0.0	0.77	0.077
β_{14}	-0.12	0.95	0.0214

Table 8.1: Ranges of the PDF observables and the bin sizes used for the signal and (α, n) neutron PDFs. 'Con' and 'uncon' refer to the range and binning used in a constrained and unconstrained fit respectively.

Observable	Lower Limit	Upper Limit	Bin Size
Energy (con)	4.0 MeV	20.0 MeV	0.5 MeV (4 to 13.5 MeV) 6.5 MeV (13.5 to 20 MeV)
Energy (uncon)	4.0 MeV	12.0 MeV	0.5 MeV
$\cos\theta_{\odot}$	-1.0	1.0	2.0
ρ	0.0	0.77	0.077
β_{14}	-0.12	0.95	0.0428

Table 8.2: Ranges of the PDF observables and the bin sizes used for the background PDFs. 'Con' and 'uncon' refer to the range and binning used in a constrained and unconstrained fit respectively.

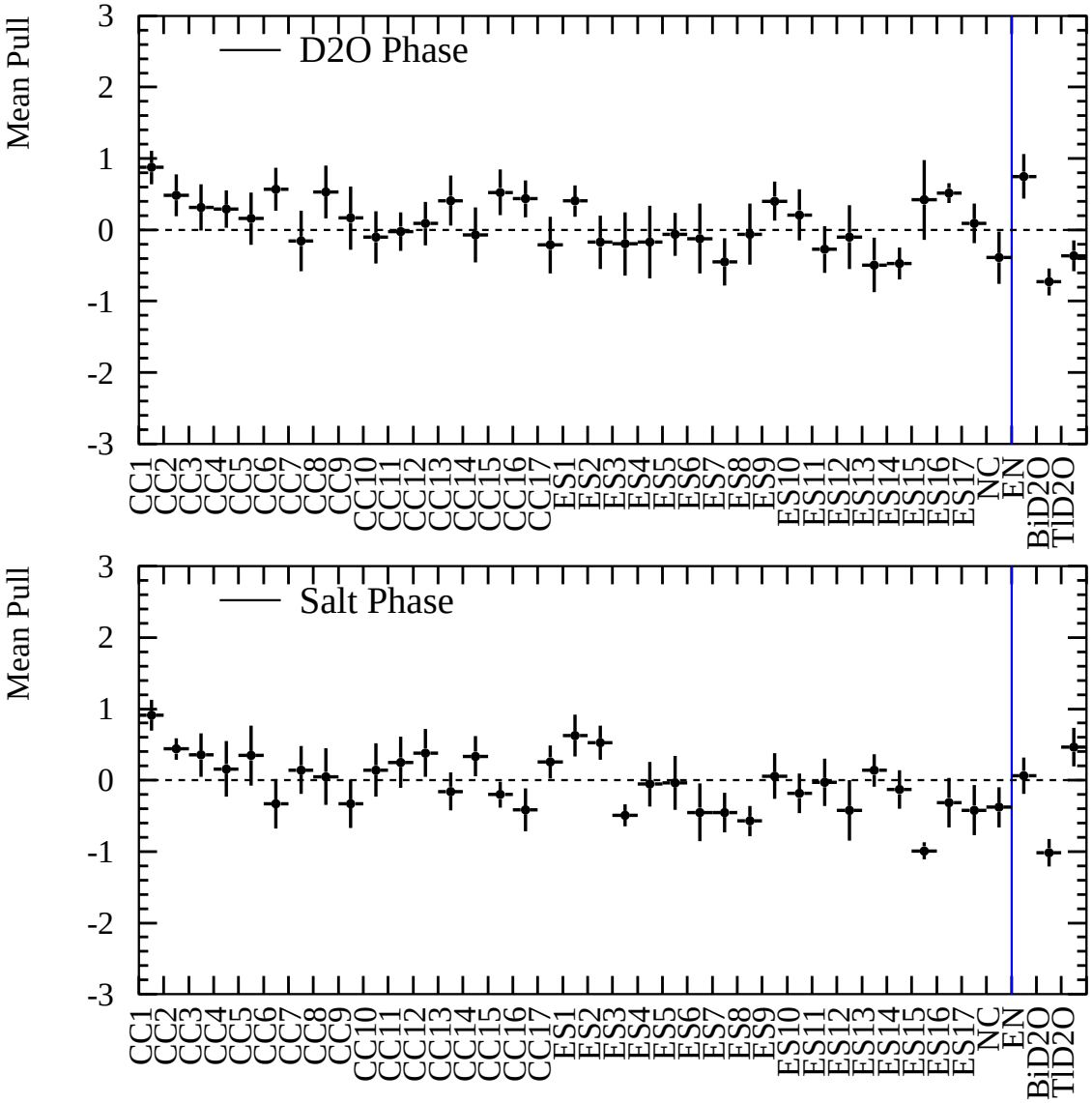

Fig. 8.7: Mean pull (in terms of sigma) for the D_2O (top figure) and salt (bottom figure) phases in a two phase fit to 10 artificial data sets. The PDF parameterization used is Equation 8.15. CC1 refers to the first CC energy bin and the energy range is 4.0 to 12.5 MeV in 0.5 MeV bins. The blue-solid line indicates the division between the CC, ES and NC signals from the backgrounds.

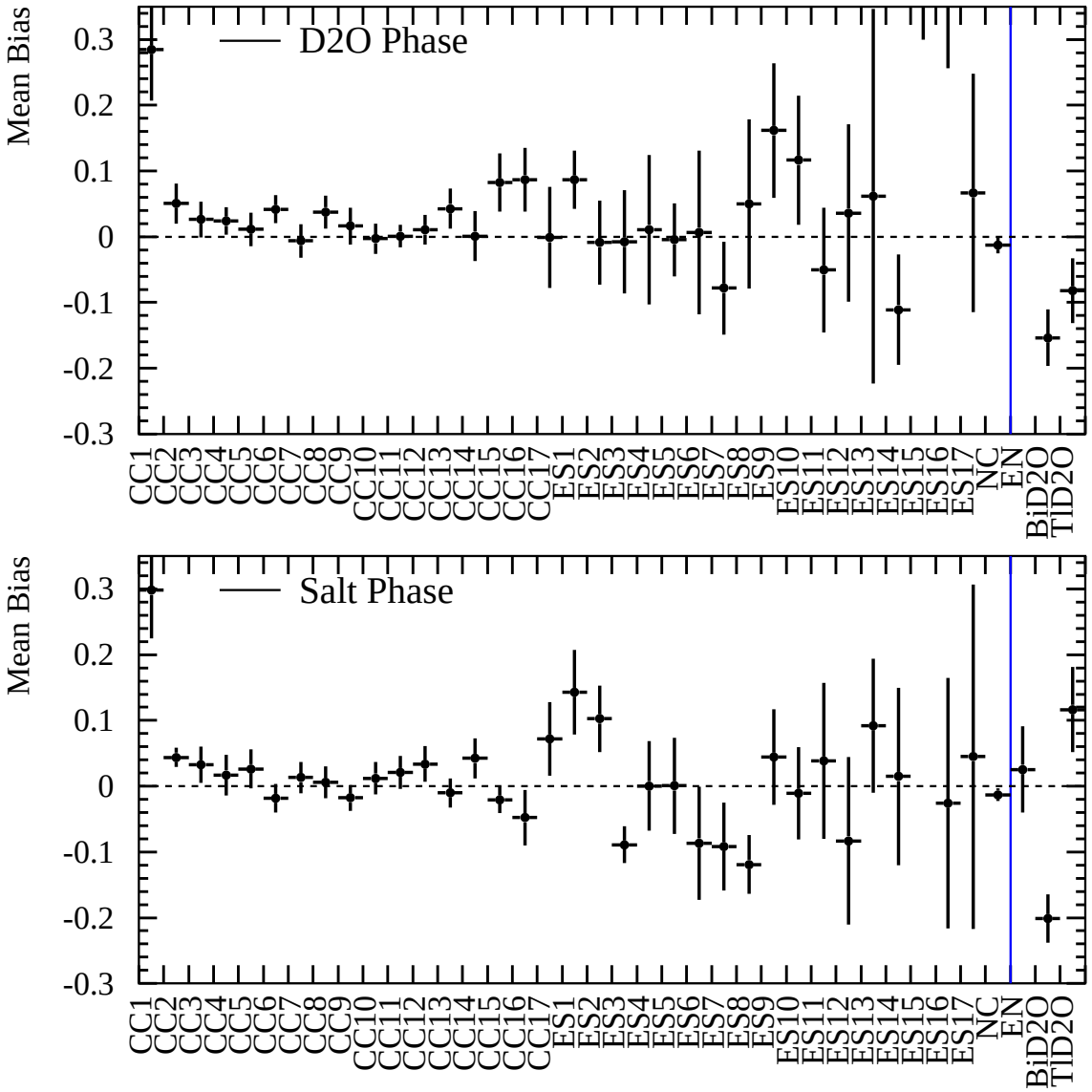

Fig. 8.8: Mean bias for the D_2O (top figure) and salt (bottom figure) phases in a two phase fit to 10 artificial data sets. The PDF parameterization used is Equation 8.15. CC1 refers to the first CC energy bin and the energy range is 4.0 to 12.5 MeV in 0.5 MeV bins. The blue-solid line indicates the division between the CC, ES and NC signals from the backgrounds.

uncertainty in the 4.0-4.5 MeV bin. As seen in Figure 8.10, by using a 3.5 MeV energy threshold the statistical uncertainty at 4.0 MeV (CC2 in the figure) is now 12%. Although fitting using an energy threshold of 3.5 MeV improves the fitted uncertainty in the 4.0 MeV spectral bin, the believability of the PDFs to represent the data at this energy is questionable and needs to be studied in more detail before such fits on the data can be performed. For this analysis, the fit was done using an energy threshold of 4.0 MeV, the PDF parameterization specified in Equation 8.15 with bin sizes summarized in Tables 8.1 and 8.2.

8.5 Summary

In this chapter the signal extraction technique used to determine the number of signal events in the data set has been introduced. To fit at a lower energy threshold and using multiple phases of data, the maximum likelihood fit has been expanded to include both the D_2O and salt phase data sets and simultaneously fit for the low energy background PDFs. Fits to artificial data sets have shown that the extraction method and PDF parameterization produces tolerable biases in the fitted number of signal events at the energy threshold of 4.0 MeV.

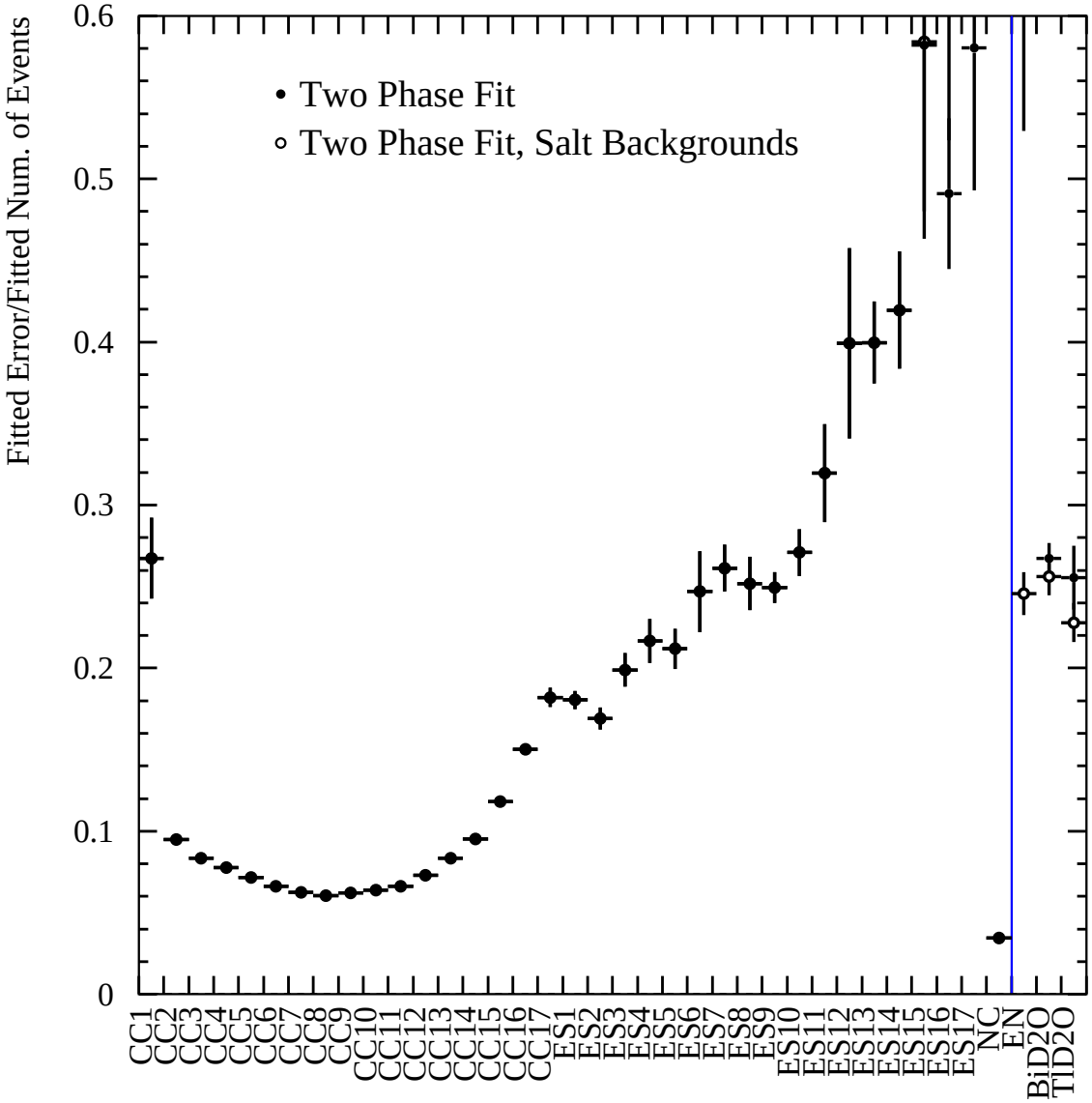

Fig. 8.9: The mean fractional uncertainty on the fitted CC, ES and NC rates in a two phase fit to 10 artificial data sets at an energy threshold of 4 MeV. CC1 refers to the first CC energy bin and the energy range is 4.0 to 12.5 MeV in 0.5 MeV bins. The blue-solid line indicates the division between the CC, ES and NC signals from the backgrounds.

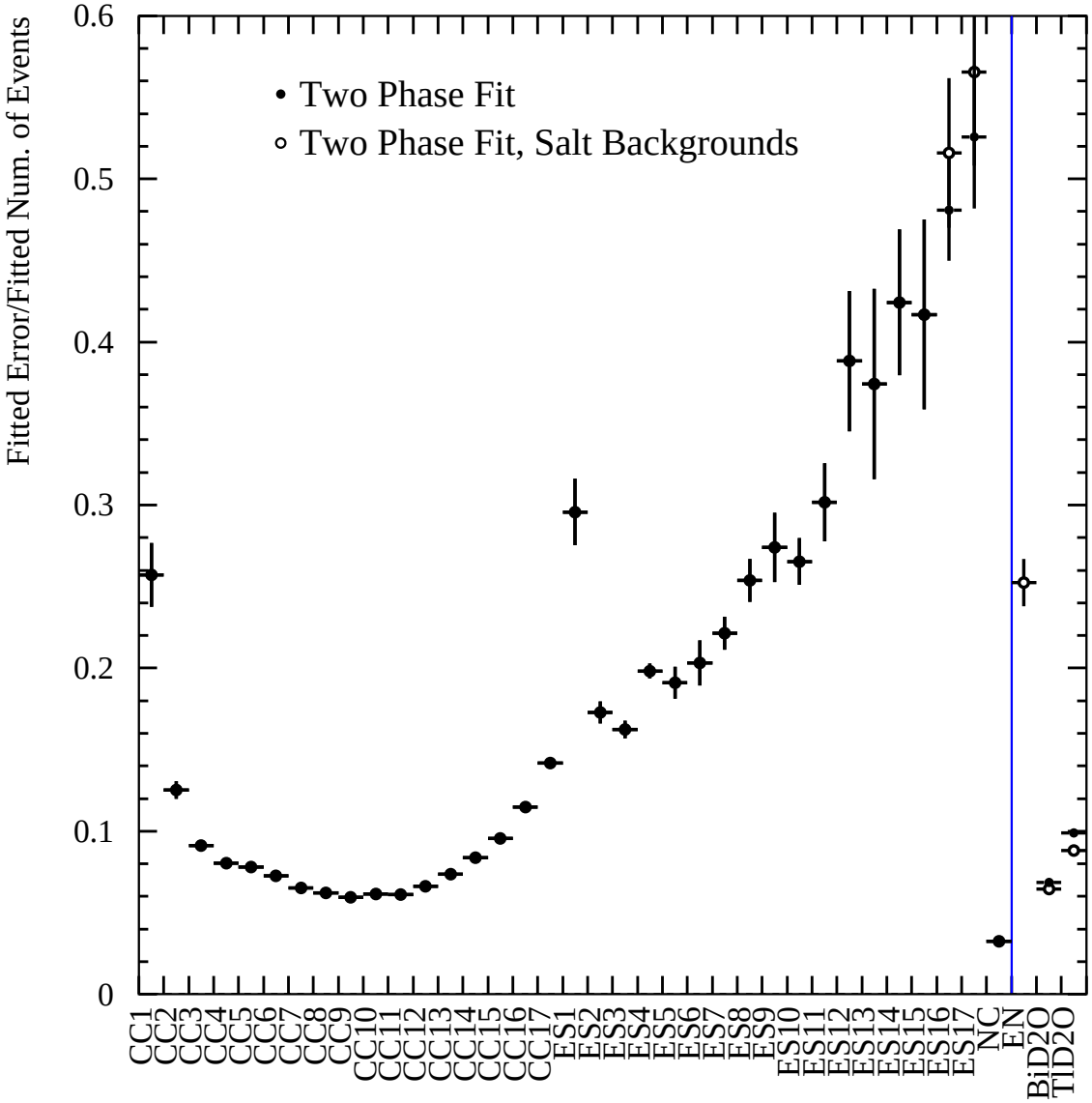

Fig. 8.10: The mean fractional uncertainty on the fitted CC, ES and NC rates in a two phase fit to 10 artificial data sets at an energy threshold of 3.5 MeV. CC1 refers to the first CC energy bin and the energy range is 3.5 to 12.0 MeV in 0.5 MeV bins. The blue-solid line indicates the division between the CC, ES and NC signals from the backgrounds. Note that the CC2 bin is the 4.0-4.5 MeV CC energy bin.

Ch. 9

Fluxes and Energy Spectra

With improvements to the energy resolution and new analysis cuts, the number of background events above 4.0 MeV has been reduced by 60%. Capitalizing on this improvement in signal and background separation, this analysis uses an energy threshold of 4 MeV to extract the CC, ES and NC fluxes as well as the CC and ES energy spectra. This is 1.5 MeV lower than the analysis in [19] and 1.0 MeV lower than the analysis in [2]. Including both the D_2O and salt phase data sets at this lower energy threshold, the measurement of the CC, ES and NC fluxes is more precise than any previous measurement using SNO's data. Additionally the lower energy threshold is critical for searching for spectral distortions in the CC and ES energy spectra, which are sensitive to MSW distortions as well as new physics (see Chapter 1). This chapter discusses the evaluation of systematic uncertainties in the PDF's of observables, needed to evaluate systematic uncertainties on the fluxes and energy spectra. The extracted CC, ES and NC fluxes are presented as well as the extracted CC and ES energy spectra.

9.1 Systematic Uncertainties in Observables

To account for systematic differences in the PDFs obtained from MC and the data, the signal extraction is repeated using shifted or distorted PDFs to evaluate the systematic uncertainties on the fit parameters. The uncertainty on the fit parameters due to an observable systematic uncertainty s is defined as

$$\delta_s(X) = N_s^{\text{shift}}(X) - N(X) \tag{9.1}$$

where $N(X)$ is the nominal (unshifted) fitted parameter value and $N_s^{\text{shift}}(X)$ is the fitted parameter value using the modified PDF. The observables used in the PDFs are energy, β_{14}, event position and $\cos\theta_\odot$ and the systematic uncertainties on each of these observables are discussed in the next sections. The systematic uncertainty on the fit parameters due to an observable systematic uncertainty is taken to be uncorrelated with other observable systematic uncertainties. The uncorrelated uncertainties are all added in quadrature.

When fitting using two or more phases of data, the observable systematic uncertainties (such as energy scale) in one phase are not necessarily uncorrelated with the other phase. The exact correlation coefficient for systematic uncertainties between the phases is very difficult to determine but to first approximation the observable uncertainties can be broken into uncorrelated and fully correlated uncertainties. For example, time dependent uncertainties in the energy scale are uncorrelated between phases as they depend on the fluctuations of the moment. In contrast, the ^{16}N source model uncertainty would be fully correlated as the same ^{16}N source is used during both phases. For observable systematic uncertainties that are uncorrelated between

the two phases, the method represented by Equation 9.1 is repeated separately for each uncertainty in each phase. For observable systematic uncertainties that are fully correlated between the two phases, the PDF observables are shifted by the systematic uncertainty in both phases simultaneously.

For each observable systematic uncertainty, the fit is repeated for the positive and negative uncertainty value as well as the correlated and uncorrelated uncertainties. Accounting for all observable systematic uncertainties in this analysis requires that the fit is repeated approximately 40 times with different modifications to the PDFs. The following sections outlines the application of each observable systematic uncertainty in the PDFs and also discusses correlations between phases in the observable systematic uncertainties.

9.1.1 Energy Uncertainties

Systematic uncertainties in the energy observable can be classified into two types: energy scale and energy resolution. Determination of these uncertainties is discussed in detail in Chapter 6 and summarized in Table 9.1. All uncertainties due to time dependent changes in the detector are taken to be uncorrelated. Energy scale uncertainties due to the ^{16}N source modeling, the detector radial distribution and electronic rate effects are 100% correlated between the D_2O and salt phases. These uncertainties are the result of mis-modeling of the source, the angular response, optics and the electronic rate correction. Since the same MC model is used in both phases, uncertainties due to these effects are not independent between the phases. The total uncorrelated and correlated energy scale uncertainties listed in Table 9.2 were determined using the MC method discussed in Section 6.4.2. Energy scale uncertainties are applied to

the PDF by shifting the value of the estimated energy by the $\pm 1\sigma$ shifts summarized in the table.

To account for differences in data and MC energy as function of energy, an energy non-linearity uncertainty, determined by comparing the energy scale as a function of energy between ^{8}Li data and MC, is also applied. A discussion of the calculation of the non-linearity uncertainty can be found in Appendix D.2. This uncertainty is applied to the PDFs

$$E' = \delta_e E \tag{9.2}$$

where E' is the modified energy, E is the event energy and δ_e includes the non-linearity uncertainty. The uncertainty is the ratio between the data and MC energy scale determined from ^{8}Li, given as

$$\delta_e = \frac{a_1 + a_2 E}{a_3 + a_4 E} \tag{9.3}$$

where the values of a_i are listed in Table D.1. This uncertainty is taken to be 100% correlated between phases.

Uncertainties in energy resolution (summarized in Table 9.1) are also taken to be 100% correlated between the two phases since these uncertainties are due to detector mis-modeling and are the same for each phase. Resolution uncertainties (δ_{resol}) are applied to the PDFs by smearing the MC energy values:

$$E' = E(1 + g(\delta_{resol})) \tag{9.4}$$

where E' is the smeared energy, E is the original event energy and $g(\delta_{resol})$ is a

Uncertainty	D_2O Phase (%)	Salt Phase (%)	Correlation
Detector PMT status	0.01	0.01	Uncorrelated
Electronics threshold	0.20	0.20	Uncorrelated
Electronics gain	0.40	0.40	Uncorrelated
Electronics rate effect	-0.69 ± 0.17	-0.29 ± 0.09	Correlated
Time drift/stability	0.02	0.015	Uncorrelated
^{16}N source modeling	0.65	0.65	Correlated
Radial Top ($>$ 375cm)	$+5.07 \pm 0.66$	$+3.20 \pm 0.71$	Correlated
Radial Top ($<$ 375cm)	$+1.55 \pm 0.29$	$+1.44 \pm 0.21$	Correlated
Radial Middle ($<$ 475cm)	-0.06 ± 0.47	$+0.21 \pm 0.53$	Correlated
Radial Middle ($>$ 475cm)	$+0.96 \pm 0.46$	$+0.21 \pm 0.53$	Correlated
Radial Bottom	-2.69 ± 0.84	-3.05 ± 0.83	Correlated
Electron Resolution:	See Table 6.4	See Table 6.8	Correlated
Neutron Resolution:	2.69	2.61	Correlated

Table 9.1: Summary of the energy scale and resolution systematic uncertainties for both the D_2O and salt phases. The last column indicates if the uncertainty was treated at uncorrelated or 100% correlated between the two phases.

value randomly selected from a Gaussian distribution with width δ_{resol} and a mean of zero. Resolution uncertainties are applied only by increasing the width of the energy distribution and not by narrowing the distribution since studies of ^{16}N indicate the energy distribution of the data is broader than the MC. Different resolution uncertainties are used for electron versus neutron events to account for the differences in the width of the underlying distribution of the number of Cherenkov photons.

9.1.2 Isotropy Uncertainties

Systematic uncertainties in the β_{14} observable can lead to mis-identification of neutron versus electron events. Appendix D.1 discusses how the isotropy uncertainties used in this analysis were obtained (summarized in Table 9.3). Between the two phases, the uncertainties in the β_{14} mean and width for both electron and neutrons are taken

Type	D_2O Phase (%)		Salt Phase (%)	
	-1σ	$+1\sigma$	-1σ	$+1\sigma$
Uncorrelated	-0.45	+0.45	-0.45	+0.45
Correlated Top (> 375cm)	-1.67	+3.87	-1.33	+2.79
Correlated Top (< 375cm)	-0.88	+1.31	-0.81	+1.38
Correlated Middle (< 475cm)	+0.85	-1.22	+0.85	-0.89
Correlated Middle (> 475cm)	-0.88	+1.02	+0.85	-0.89
Correlated Bottom	+1.33	-3.02	+1.37	-3.04

Table 9.2: Energy scale uncertainties for the D_2O and salt phases. The $\pm 1\sigma$ values listed for each detector region are the magnitude and sign of the energy observable shifts applied to the PDFs.

to be 100% correlated. An event's value of β_{14} is dependent upon its energy. This is due to low energy electrons scattering more and producing more isotropic PMT hits pattern. As a result, the β_{14} systematic uncertainties are applied by a fractional uncertainty to the mean value of β_{14} for a given event energy:

$$\beta'_{14} = \beta_{14} + \overline{\beta}_{14}\delta_{bm} \tag{9.5}$$

where β'_{14} is the shifted β_{14} value, $\overline{\beta}_{14}$ is the mean β_{14} value given the event's energy (listed in Table 9.4) and δ_{bm} is the fractional uncertainty summarized in Table 9.3.

To estimate effects of uncertainties in the β_{14} width, the β_{14} values in the PDFs are modified by

$$\beta'_{14} = \beta_{14} + (\beta_{14} - \overline{\beta}_{14})\delta_{bw} \tag{9.6}$$

where δ_{bw} is the uncertainty in the width listed in Table 9.3 and the remaining variables are defined in Equation 9.5.

Uncertainty	D_2O Phase	Salt Phase	Correlation
Mean (δ_{bm}): -1σ	-1.23%	-0.52%	Correlated
Mean (δ_{bm}): $+1\sigma$	+0.47%	+0.40%	Correlated
Width (δ_{bw}): -1σ	-0.57%	-0.53%	Correlated
Width (δ_{bw}): $+1\sigma$	+0.57%	+0.60%	Correlated

Table 9.3: Uncertainties in the β_{14} mean and width for the D_2O and salt phases. All β_{14} uncertainties are taken to be 100% correlated between the phases.

Type	Phase	β_{14} Mean
Electron	D_2O	$0.4516 + 0.00450E + 0.000148E^2$
	Salt	$0.4154 + 0.01552E - 0.000755E^2$
Neutron	D_2O	$0.1806 + 0.06459E - 0.003512E^2$
	Salt	$0.0267 + 0.06845E - 0.003098E^2$

Table 9.4: Mean β_{14} values of electrons and neutrons in the D_2O and salt phases.

9.1.3 Position and Direction Uncertainties

Uncertainties in the reconstructed position and direction can affect the ρ and $\cos\theta_\odot$ distributions. The signals and internal background PDFs are insensitive to position uncertainties since their radial distribution is flat. The external backgrounds are more affected by uncertainties in the reconstructed position since those radial distribution are steeply sloped near the AV.

Uncertainties in the reconstructed direction most strongly affect the $\cos\theta_\odot$ distribution for the ES signal. NC and all backgrounds are unaffected by direction uncertainties since their $\cos\theta_\odot$ distribution is flat. Each of the position and direction uncertainties and their application to the PDFs is discussed below.

Position and Vertex Resolution Uncertainties

The position uncertainties used for this analysis were taken from [19, 80, 81] but a preliminary updated analysis indicates that these uncertainties could be reduced [82]. The position systematic uncertainties consist of uncertainties in the reconstructed x, y and z positions and radial accuracy. The magnitude of each of these uncertainties is listed in Table 9.5. Position systematic uncertainties are the result of mis-modeling the PMT timing and charge distributions. Since these uncertainties are due to the detector model, they are treated as 100% correlated between the two phases. To apply these uncertainties, the x,y, z position or radius of all events in the PDFs are modified by the $\pm 1\sigma$ uncertainty.

The radial accuracy can also have an energy dependent component which effectively changes the fiducial volume for higher energy events. Using ^{8}Li, the energy dependence to the radial position was found to have a gradient of $0.32 \pm 0.31\%$ per MeV [68]. This results in a 1.6% change in the fiducial volume for 10 MeV events compared to 5 MeV events. This gradient is applied to all MC PDFs during the nominal fit and the systematic uncertainty on this measurement is applied by shifting the gradient by the $\pm 1\sigma$ value. This uncertainty is also treated as fully correlated between the two phases.

To account for uncertainties in vertex resolution, the radial distribution in the PDFs is broadened by 15% over the nominal width of 16 cm, determined from ^{16}N. This broadening is applied as

$$R' = R(1 + g(\delta_{vresol})) \tag{9.7}$$

where R' is the modified reconstructed radius, R is the original reconstructed radius

and $g(\delta_{vresol})$ is a value randomly selected from a Gaussian distribution with a mean of zero and a width of δ_{vresol}. Since the vertex uncertainty is also due to detector mis-modeling in the MC, this uncertainty is treated as fully correlated between the two phases.

Angular Resolution Uncertainties

Uncertainties in the angular resolution affect the $\cos\theta_{\odot}$ observable in the MC PDFs. To estimate effects on the extracted number of signal events due to this uncertainty, the event direction is modified by an angle, θ_R. This modified angle is randomly selected from a Gaussian distribution in $\cos\theta_R$ where the width of the Gaussian is

$$W(\cos\theta_R) = e^{-2.935-0.145\times E}. \tag{9.8}$$

E is the event's energy. The new event direction is randomly selected from a cone of angle, θ_R around the original event direction and the $\cos\theta_{\odot}$ value is recalculated. As with the other reconstruction uncertainties, the angular resolution uncertainty is taken as 100% correlated between the two phases.

PMT Background PDF Radial Distribution Uncertainties

The PMT background PDF is obtained using a very hot ^{232}Th source near the PSUP. Since data is used for this PDF, the energy, β_{14}, position and neutron capture uncertainties discussed above are not applied. As discussed in Appendix C.1.3, the position of the ^{232}Th source near the PSUP is uncertain to several centimeters. To account for uncertainties in the source position, the radial position for the PMT source is shifted by $\pm 2\%$. This position uncertainty was taken to be 100% correlated between

Uncertainty	D_2O Phase	Salt Phase	Correlation
x	±2cm	±2cm	Correlated
y	±2cm	±2cm	Correlated
z	±6cm	±6cm	Correlated
R scale	±1%	±1%	Correlated
R scale (energy dep.)	±0.31%	±0.31%	Correlated
R resolution	0.15×16cm	0.15×16cm	Correlated
Angular resolution	see text	see text	Correlated
PMT PDF	±2%	±2%	Correlated
^{24}Na Radial Model	—	see text	—

Table 9.5: Summary of position and direction uncertainties in the D_2O and salt phases. All position and direction uncertainties are treated as 100% correlated between the phases.

the D_2O and salt phases.

^{24}Na Radial Model Uncertainties

The radial distribution of ^{24}Na in the detector is not well known but is thought to be introduced into the detector via the neck and water pipes (located at the bottom of the AV) [83]. During the nominal fit, the ^{24}Na PDF radial distribution is taken to be uniform throughout the D_2O volume. To estimate effects due the radial distribution of this background, the signal extraction fit is repeated using two different radial models: a linear distribution in the reconstructed z position originating from the neck and a linear distribution in the reconstructed z position originating from the bottom of the AV. The linear model uses a 10% gradient from the origin point.

9.1.4 Neutron Capture and Photo-disintegration Cross Section Uncertainties

Uncertainties in the capture efficiency of neutrons directly affects the number of extracted NC events. Additionally uncertainties in the photo-disintegration cross section affect the predicted number of ^{214}Bi and ^{208}Tl produced neutrons. The following section discusses the application of each of these systematic uncertainties.

Neutron Capture Uncertainties

The neutron capture efficiency is measured using ^{252}Cf source deployed at multiple points throughout the D_2O volume. The statistical and systematic uncertainties on the measured efficiencies for each phase are listed in Table 9.6 (taken from [2,19]). The dominant systematic uncertainty in the capture efficiency is the uncertainty in the source strength. Since the same methods were used to measure the source strength in both the D_2O and salt phases, the systematic uncertainty due to the neutron capture is taken to be 100% correlated between the two phases. The statistical uncertainties are treated as uncorrelated between phases. Neutron capture uncertainties are applied by changing the capture efficiency used in the signal extraction by the $\pm 1\sigma$ values listed in the table.

Uncertainties in the neutron capture also affect the detection of neutrons from photo-disintegration included in the background PDFs. To account for this, the ratio of photo-disintegration neutron events to Cherenkov background events is modified to reflect changes in the neutron capture efficiency.

Uncertainty	D_2O Phase	Salt Phase	Correlation
Neutron Capture (stat.)	$\pm 3.9\%$	$\pm 1.2\%$	Uncorrelated
Neutron Capture (sys.)	$\pm 3.0\%$	$+2.2, -2.0\%$	Correlated
PD Cross Section	$\pm 4.0\%$	$\pm 4.0\%$	Correlated

Table 9.6: Summary of position and direction uncertainties in the D_2O and salt phases. 'PD cross section' refers to the photo-disintegration cross section. The last column indicates if the uncertainty was treated at uncorrelated or 100% correlated between the two phases.

Photo-disintegration Cross Section Uncertainties

For the ^{214}Bi and ^{208}Tl background PDFs, the MC used to build these PDFs predicts the ratio of the number of photo-disintegration neutron events to Cherenkov events. For internal ^{214}Bi the number of neutrons to Cherenkov events using a 4.0 MeV threshold is approximately 7% for the D_2O phase and 12% for the salt phase. For internal ^{208}Tl the number of neutrons is 21% and 38% compared to the number Cherenkov events for the D_2O and salt phases, respectively.

Uncertainties in the photo-disintegration cross section changes this ratio which in turn can affect the number of extracted NC events. A summary of the effective field theory calculation used by the MC to predict the photo-disintegration cross section can be found in [83]. Based on this summary, the uncertainty on the cross section is estimated at 4%. To evaluate effects on the extracted number of signal events due to this cross section uncertainty, the ratio of the number of neutron to Cherenkov events in each background PDF is reduced or increased by 4%. Since this cross section uncertainty is a theoretical uncertainty, it is treated as 100% correlated between the D_2O and salt phases.

9.2 Corrections to Observables, PDFs and Fluxes

In addition to systematic uncertainties in the observables, several corrections need to be applied to the data and MC. These corrections account for minor changes in the data and MC that were not included when the data and MC were processed.

9.2.1 Data Corrections

When calibrating the PMT timing (PCA, see Section 2.3.1), the location of the laser-ball was offset by 5 cm in the z-axis from the expected location. As a result of this timing offset, the event reconstructed z position (determined using the PMT times) was shifted by 5 cm. To correct for this offset, all events in the D_2O and salt data sets are shifted by

$$z' = z - 5.0\text{cm} \tag{9.9}$$

where z' is the new reconstructed z position and z is the original z position. Additionally the FTK energy corrections discussed in Sections 6.4.1 and 6.5 are also applied to the data.

9.2.2 PDF and Flux Corrections

The fit parameter F_i, introduced in Equations 8.6 and 8.7, is the fraction of the number of events expected in one Standard Solar Model exposure. To determine the expected number of events in a single SSM exposure, MC is used for the CC and ES signals and an analytic calculation is used for the NC signal. For the CC and ES expected number of events, several corrections to the MC need to be applied. The

magnitude of each of these corrections is listed in Table 9.7[1]. The expected number of events for these signal with corrections is shown below,

$$E(\mathrm{CC}) = N^{\mathrm{MC}}(\mathrm{CC}) R_{\mathrm{model}} N_D S_{ac} R_{\mathrm{O,Na,Cl}} MC_{err} t_{corr} \quad (9.10)$$

$$E(\mathrm{ES}) = N^{\mathrm{MC}}(\mathrm{ES}) R_{\mathrm{model}} N_e S_{ac} MC_{err} t_{corr} \quad (9.11)$$

where

N^{MC}**:** The number of CC or ES events predicted by the MC for one SSM. The number of expected events is recalculated when systematic shifts are applied to the observables.

R_{model}**:** Correction to Standard Solar Model rate. The MC was generated at $5.15 \times 10^6 \mathrm{cm}^{-2}\mathrm{s}^{-1}$using the BP2000 model [84]. This correction factor converts to the B2005 flux [20] of $5.69 \times 10^6 \mathrm{cm}^{-2}\mathrm{s}^{-1}$.

N_D**:** Correction to the number of target deuterons. Relevant to the CC and NC interactions only.

N_e**:** Correction to the number of target electrons. relevant to the ES interaction only.

S_{ac}**:** Correction to the number of MC events to account for differences in the cut acceptances of the DAMN and HLC in the MC with respect to the data (See Section 7.2 for a description of the cuts). The correction is applied as function of energy and is determined from ^{16}N and ^{8}Li calibration sources [85]. See Table D.2 for the correction values.

$R_{0,\mathrm{Na,Cl}}$**:** Correction term to account for CC interactions on ^{18}O, Cl and

[1]Corrections due to the radiation of Bremsstrahlung photons formerly applied at this stage have been included in the MC and are no longer necessary.

Na nuclei in the D_2O which are not included in the MC.

MC_{err}**:** SNOMAN occasionally aborts MC events due to errors in tracking photons. The number of aborted MC events increases with the number of photons in the event. An energy dependent correction to account for these events was derived in [68][2].

t_{corr}**:** A correction to the MC livetime to account for dead time introduced by the DAMN cuts.

The number of expected NC events is calculated using an analytic calculation given as

$$E(\mathrm{NC}) = R_{\mathrm{NC}}\epsilon_n t R_{\mathrm{model}} N_D S_{ac} \tag{9.12}$$

where R_{model}, N_D and S_{ac} are defined above and

R^{NC}**:** The predicted rate of neutrons per day assuming the BP2000 standard solar model ^{8}B and *hep* rates, equal to 13.11. Taken from [65].

ϵ_n**:** The neutron capture efficiency including all cuts. For the D_2O phase the neutron capture efficiency is 0.230 (taken from [2] and corrected for the cuts used by this analysis). For the salt phase the neutron capture efficiency is 0.651 (taken from [19] and corrected for the cuts used by this analysis).

t**:** Livetime for the phase.

[2]This correction was increased by a factor of three for this analysis to account for the fact that Cerfac has been disabled.

Correction	CC	ES	NC
Livetime (D_2O)	0.986	0.986	0.986
Livetime (salt)	0.989	0.989	0.989
Number of electrons	—	1.0151	—
Number of deuterons	1.012	—	1.012
Cut Acceptance	see text	see text	see text
CC on O,NaCl	1.0081	—	—
MC Aborted Events	see text	see text	see text
SSM	1.105	1.105	1.105

Table 9.7: Summary of corrections to the expected number of CC, ES and NC events used in the signal extraction.

9.2.3 *hep* Flux Subtraction

The fit parameters, F_i in the signal extraction include contributions due to *hep* neutrinos. Since the number of expected *hep* neutrinos is less than a percent of the ^{8}B flux (see Table 1.2), the expected rate is subtracted from the CC, ES and NC rates. The B2005 SSM is used for the *hep* flux and MC is used to determine the number of expected *hep* events expected in each CC, ES spectral bin and well as the NC flux.

9.3 Results

With the above corrections applied, the CC, ES and NC fluxes including the CC and ES energy shape in the fit (constrained fit) are

$$\Phi_{\rm CC}^{\rm combined,con} = 1.67^{+0.04}_{-0.04}({\rm stat.})^{+0.09}_{-0.08}\ ({\rm syst.}) \times 10^6 {\rm cm}^{-2}{\rm s}^{-1} \quad (9.13)$$

$$\Phi_{\rm ES}^{\rm combined,con} = 2.35^{+0.15}_{-0.15}({\rm stat.})^{+0.14}_{-0.10}\ ({\rm syst.}) \times 10^6 {\rm cm}^{-2}{\rm s}^{-1} \quad (9.14)$$

$$\Phi_{\rm NC}^{\rm combined,con} = 4.86^{+0.15}_{-0.15}({\rm stat.})^{+0.20}_{-0.19}\ ({\rm syst.}) \times 10^6 {\rm cm}^{-2}{\rm s}^{-1}. \quad (9.15)$$

	CC	ES	NC
CC	1.0	-0.153	-0.319
ES	-0.153	1.0	-0.063
NC	-0.319	-0.063	1.0

Table 9.8: Covariance matrix for the CC, ES and NC signals from the two phase constrained fit.

This fit uses both the D_2O and salt phase data sets and a kinetic energy threshold of 4 MeV. These numbers are consistent with the numbers from previous measurements listed in Table 9.9, but the statistical and systematics uncertainties are greatly reduced. The observable distributions resulting from the fit are shown in Figures 9.1 and 9.2 for the D_2O and salt phases respectively. The covariance matrix for the signals in shown in Table 9.8

For verification, the constrained fit using a 4 MeV energy threshold was repeated for the D_2O and salt phases separately. The fluxes are

$$\Phi_{\rm CC}^{\rm D2O,con} = 1.67^{+0.06}_{-0.05}({\rm stat.})^{+0.05}_{-0.06}\ ({\rm syst.}) \times 10^6 {\rm cm}^{-2}{\rm s}^{-1} \quad (9.16)$$

$$\Phi_{\rm ES}^{\rm D2O,con} = 2.42^{+0.23}_{-0.22}({\rm stat.})^{+0.13}_{-0.06}\ ({\rm syst.}) \times 10^6 {\rm cm}^{-2}{\rm s}^{-1} \quad (9.17)$$

$$\Phi_{\rm NC}^{\rm D2O,con} = 5.38^{+0.44}_{-0.49}({\rm stat.})^{+0.42}_{-0.52}\ ({\rm syst.}) \times 10^6 {\rm cm}^{-2}{\rm s}^{-1} \quad (9.18)$$

for the D_2O phase and

$$\Phi_{\rm CC}^{\rm salt,con} = 1.68^{+0.05}_{-0.05}({\rm stat.})^{+0.07}_{-0.08}\ ({\rm syst.}) \times 10^6 {\rm cm}^{-2}{\rm s}^{-1} \quad (9.19)$$

$$\Phi_{\rm ES}^{\rm salt,con} = 2.30^{+0.20}_{-0.20}({\rm stat.})^{+0.14}_{-0.05}\ ({\rm syst.}) \times 10^6 {\rm cm}^{-2}{\rm s}^{-1} \quad (9.20)$$

$$\Phi_{\rm NC}^{\rm salt,con} = 5.18^{+0.17}_{-0.17}({\rm stat.})^{+0.22}_{-0.21}\ ({\rm syst.}) \times 10^6 {\rm cm}^{-2}{\rm s}^{-1} \quad (9.21)$$

for the salt phase. These fit results are consistent with the combined phase results.

The dominant systematic uncertainties in the constrained fit are energy scale and resolution for the CC, angular resolution for the ES and β_{14} and neutron capture efficiency for the NC. The ES systematic uncertainties are very asymmetric because the angular resolution is applied only as a broadening. The individual contributions to the total uncertainty from each observable systematic uncertainty are listed in Tables 9.10 and 9.11.

The systematic uncertainty on the CC flux using only the D_2O phase is significantly better than the CC flux systematic uncertainty using both the D_2O and salt phases. This is due largely to the radial uncertainty. As seen in Table 9.10, the uncertainty on the CC flux due to the radial uncertainty in the two phase fit is much worse than the uncertainty in the single phase fits. Yet, the radial uncertainty on the NC flux is much better in the two phase fit compared to the D_2O phase only. As a result, the uncertainties on the neutral current flux in the two phase fit are improved at the expense of the uncertainties on the CC flux.

Comparison of the flux uncertainties for the two phase and single phase fits points out that the application of observable systematic uncertainties used in this analysis and in previous SNO measurements overestimates the systematic uncertainties on the fluxes. By combining two phases of data, the systematic uncertainties should improve over those in the single phase only. Yet, as the systematic uncertainties in energy, β_{14}, $\cos\theta_{\odot}$ and ρ are applied to the PDFs independently, cancellations between observable systematic uncertainties are ignored. To evaluate systematic uncertainties in the observables more correctly, all systematic uncertainties would be included as parameters in the fit and constrained by the measured $\pm 1\sigma$ values. This would account for any correlations between observable uncertainties. Including the observable systematic

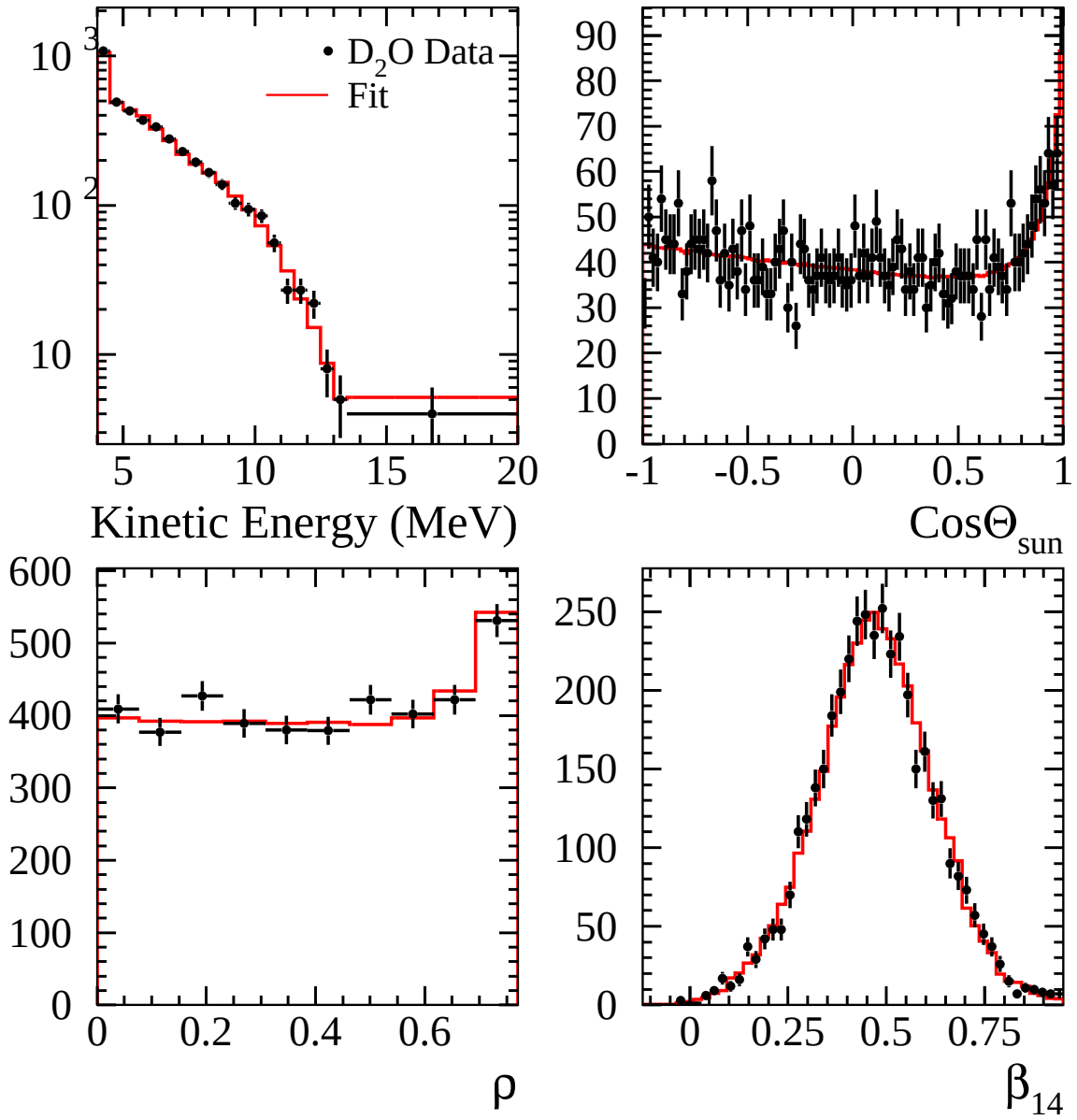

Fig. 9.1: Observable distributions for the D_2O phase data with the two phase constrained fit results with a threshold of 4.0 MeV kinetic energy.

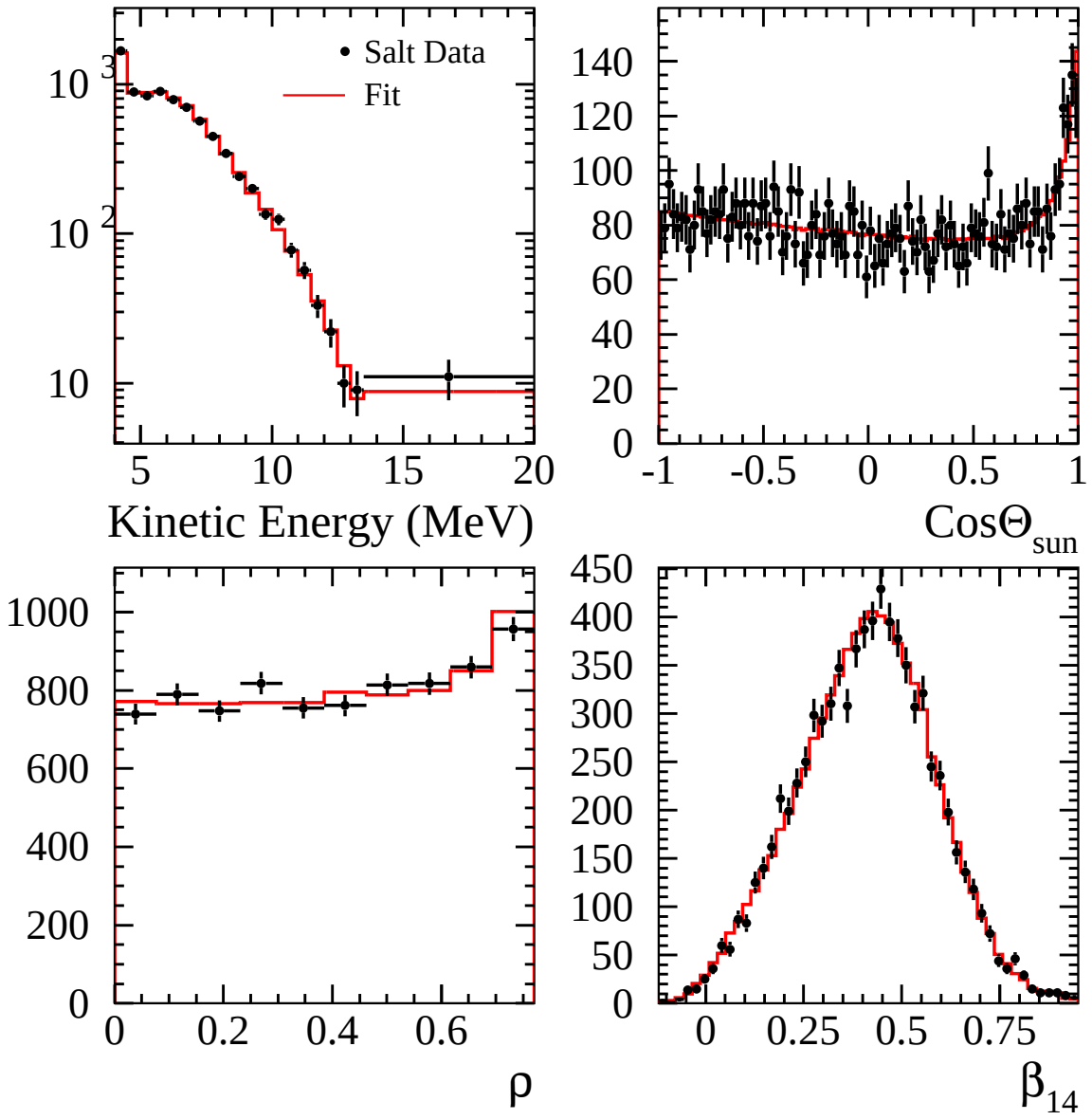

Fig. 9.2: Observable distributions for the salt phase data with the two phase constrained fit results with a threshold of 4.0 MeV kinetic energy.

Type	D_2O (con)	Salt (con)	Salt (uncon)
CC	$1.76^{+0.06+0.09}_{-0.05-0.09}$	$1.72^{+0.05+0.11}_{-0.05-0.11}$	$1.68^{+0.06+0.08}_{-0.06-0.09}$
ES	$2.39^{+0.24+0.12}_{-0.23-0.12}$	$2.34^{+0.23+0.15}_{-0.23-0.14}$	$2.35^{+0.22+0.15}_{-0.22-0.15}$
NC	$5.09^{+0.44+0.46}_{-0.43-0.43}$	$4.81^{+0.19+0.28}_{-0.19-0.27}$	$4.94^{+0.21+0.38}_{-0.21-0.34}$

Table 9.9: Summary of CC, ES and NC fluxes from previous measurements. The D_2O phase results are taken from [2] and the salt phase results taken from [19]. All number are in terms of $\times 10^6$ cm^{-2}s^{-1}. The first set of uncertainties are statistical, the second set are systematic uncertainties.

uncertainties in the fit was attempted in [68] and found to reduce the systematic uncertainties on the fluxes by 25%. Several computational problems due to choppiness in the likelihood space caused by including uncertainties are included in the fit that have not yet been solved. For this reason, the observable systematic uncertainties were evaluated in the traditional manner even though this method overestimates the total systematic uncertainties.

9.3.1 Unconstrained Fit Fluxes

Removing the CC and ES energy shape from the fit (an unconstrained fit), the fluxes obtained using a 4 MeV energy threshold and two phases of data are

$$\Phi_{\rm CC}^{\rm combined,uncon} = 1.67^{+0.04}_{-0.04}({\rm stat.})^{+0.10}_{-0.07}\ ({\rm syst.}) \times 10^6 {\rm cm}^{-2}{\rm s}^{-1} \quad (9.22)$$

$$\Phi_{\rm ES}^{\rm combined,uncon} = 2.27^{+0.15}_{-0.14}({\rm stat.})^{+0.12}_{-0.21}\ ({\rm syst.}) \times 10^6 {\rm cm}^{-2}{\rm s}^{-1} \quad (9.23)$$

$$\Phi_{\rm NC}^{\rm combined,uncon} = 4.98^{+0.17}_{-0.16}({\rm stat.})^{+0.20}_{-0.26}\ ({\rm syst.}) \times 10^6 {\rm cm}^{-2}{\rm s}^{-1}. \quad (9.24)$$

Compared to previous unconstrained fit results (Table 9.9), this measurement has

	CC			ES			NC		
Uncertainty	Two	D_2O	Salt	Two	D_2O	Salt	Two	D_2O	Salt
	In Percent			In Percent			In Percent		
Ene. Scale (+)	-1.53	-0.72	-2.10	-0.44	-0.76	1.06	1.36	1.09	1.70
Ene. Scale (-)	2.15	0.99	2.59	0.44	0.28	-0.69	-1.36	-5.39	-1.36
D2O Ene. Scale (+)	-0.61	-1.22	0.00	-0.66	-0.71	0.00	0.42	1.65	-0.00
D2O Ene. Scale (-)	0.61	1.08	0.00	0.22	0.19	-0.00	-0.31	-1.75	0.00
Salt Ene. Scale (+)	-0.61	-0.00	-1.25	0.22	0.00	0.96	0.42	-0.00	0.66
Salt Ene. Scale (-)	0.92	0.00	1.31	0.44	-0.00	0.11	-0.42	-0.00	-0.70
Ene. Resol	-0.31	-0.30	-1.01	-0.22	-1.30	-0.16	1.46	0.73	1.17
Ene. Non-linear (+)	-2.45	-2.64	-3.23	0.22	-1.56	-0.03	1.98	4.50	1.78
R (+)	2.76	-0.15	-0.17	2.18	-0.31	-0.80	-0.42	-4.17	-0.13
R (-)	-2.45	0.06	0.31	-3.28	-0.08	-0.73	-0.42	-3.03	-0.21
x (+)	0.00	0.04	0.04	-0.22	0.09	-0.35	0.10	-0.36	0.13
x (-)	0.00	-0.07	-0.07	0.00	0.32	-0.23	-0.10	-0.19	-0.05
y (+)	0.31	0.20	0.05	-0.44	-0.30	-0.52	0.21	0.12	0.26
y (-)	0.00	-0.12	-0.00	0.22	0.65	-0.23	-0.21	0.61	-0.26
z (+)	0.00	0.08	-0.19	-0.44	-0.35	-0.49	-0.10	0.14	-0.13
z (-)	0.31	0.11	0.08	-0.22	0.19	-0.69	-0.10	-0.46	-0.06
Vertex Resol	-0.92	0.12	0.23	-1.97	-0.25	0.09	-0.10	-4.14	-0.45
Ang. Resol.	-0.31	-0.38	-0.45	5.24	5.34	5.18	-0.31	-0.29	-0.20
Ene. Fid. Vol. (+)	1.23	0.55	0.57	0.66	0.22	0.16	-0.31	-0.79	-0.25
Ene. Fid. Vol. (-)	-1.23	-0.54	-0.56	-0.66	-0.22	-0.16	0.31	0.77	0.25

Table 9.10: Summary CC, ES and NC flux systematic uncertainties due to energy and reconstruction uncertainties in a two phase constrained fit (labeled 'Two'), the D_2O phase only and the salt phase only.

	CC			ES			NC		
Uncertainty	Two	D_2O	Salt	Two	D_2O	Salt	Two	D_2O	Salt
	In Percent			In Percent			In Percent		
b14 Mean (+)	-1.53	-1.14	-2.07	-0.66	0.07	-1.15	1.46	0.17	1.77
b14 Mean (-)	3.07	2.64	3.09	1.75	0.93	2.32	-2.19	-0.01	-2.45
b14 Width (+)	-1.23	-0.70	-1.73	-0.22	0.32	-0.74	0.42	-0.36	0.65
b14 Width (-)	1.23	0.64	1.60	0.87	0.47	0.95	-0.63	1.68	-1.08
Neutron Cap (+)	0.00	-0.03	0.01	0.00	0.06	-0.03	-2.19	3.00	-2.21
Neutron Cap (-)	0.00	-0.03	-0.01	0.00	-0.03	-0.02	2.09	3.04	2.00
D2O Neutron Cap (+)	0.00	0.02	0.00	0.00	0.04	0.00	-0.31	3.90	-0.00
D2O Neutron Cap (-)	0.31	-0.05	0.00	0.00	0.03	0.00	0.21	-3.91	-0.00
Salt Neutron Cap (+)	0.00	-0.00	-0.01	0.00	-0.00	0.02	-1.15	-0.00	-1.20
Salt Neutron Cap (-)	0.00	0.00	-0.03	0.00	0.00	-0.02	1.15	-0.00	1.21
PMT Source (+)	0.00	-0.15	-0.05	-0.22	-0.21	0.01	-0.63	-0.98	-0.58
PMT Source (-)	0.31	0.23	0.06	0.22	0.16	0.18	0.84	0.21	1.04
PD cross-sect. (+)	0.00	-0.01	-0.04	0.00	0.06	-0.00	-0.21	-0.06	-0.13
PD cross-sect. (-)	0.00	-0.07	-0.00	0.00	-0.01	0.03	0.10	-0.48	0.30
Na24 Model (+)	0.00	0.00	0.03	0.00	-0.00	0.00	0.00	-0.00	-0.00
Na24 Model (-)	0.00	0.00	0.10	0.00	-0.00	0.03	0.00	-0.00	0.02

Table 9.11: Summary CC, ES and NC flux systematic uncertainties due to β_{14}, neutron capture, and PDF radial models uncertainties in a two phase constrained fit (labeled 'Two'), the D_2O phase only and the salt phase only.

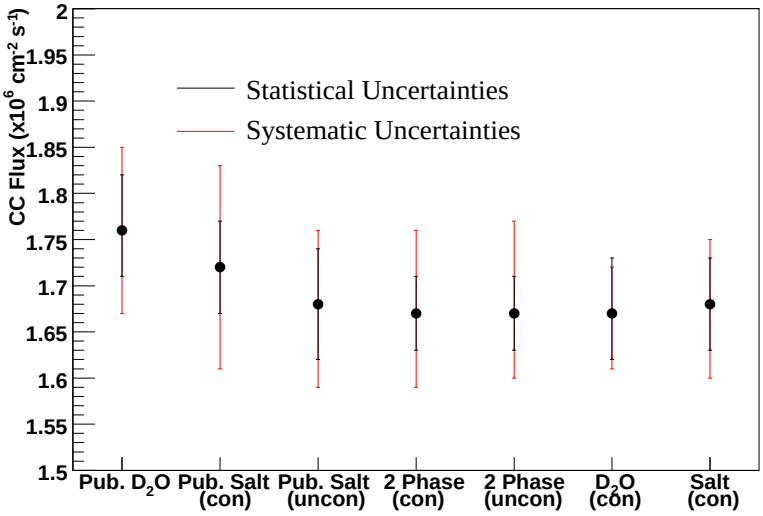

Fig. 9.3: Summary of CC flux measurements. The D_2O publication fluxes were taken from [2] and the salt constrained and unconstrained flux results were taken from [19]. 'Two Phase (con)' refers to the constrained two phase fit in this analysis. 'Two Phase (uncon)' is the unconstrained fit fluxes and 'D_2O (con)' and 'salt (con)' are the single phase constrained fit results.

also greatly improved both the statistical and systematic uncertainties. All of the flux measurements discussed in this section as well as previous flux measurements are summarized in Figures 9.3–9.5 for the CC, ES and NC fluxes respectively. In these figures the improvement in the statistical and systematic uncertainties using the 4 MeV kinetic energy threshold and two phase fit can readily be seen, especially in the measured NC flux.

The number of background events in the fits are summarized in Table 9.12, showing the fit results for the backgrounds for constrained and unconstrained two phase fit, and the constrained single phase fits. For all of the fits, the number of fitted backgrounds of each type is consistent with the other fits although the fitted number of internal ^{214}Bi decreases in the unconstrained fit. This is consistent with the bias studies on artificial data sets (see Section 8.4) where the observed bias is due to

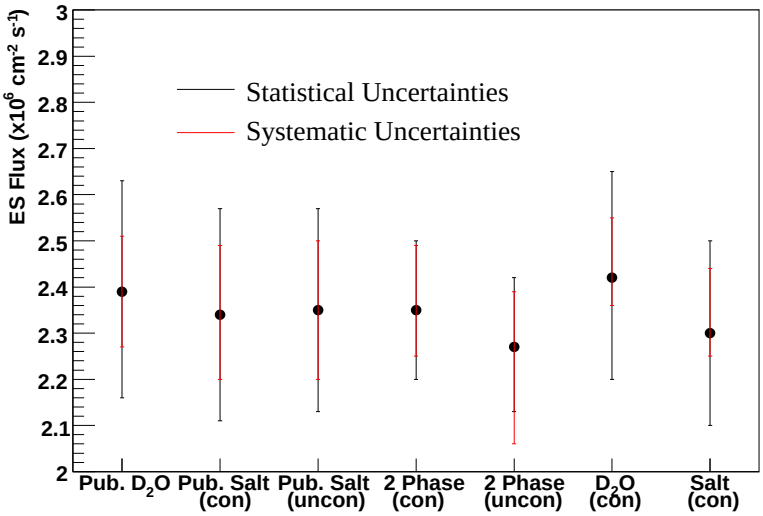

Fig. 9.4: Summary of ES flux measurements. The D_2O publication fluxes were taken from [2] and the salt constrained and unconstrained flux results were taken from [19]. 'Two Phase (con)' refers to the constrained two phase fit in this analysis. 'Two Phase (uncon)' is the unconstrained fit fluxes and 'D_2O (con)' and 'salt (con)' are the single phase constrained fit results.

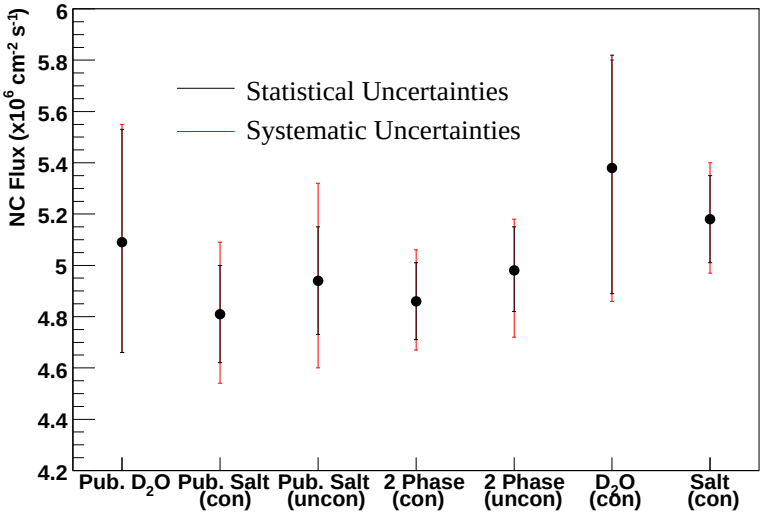

Fig. 9.5: Summary of NC flux measurements. The D_2O publication fluxes were taken from [2] and the salt constrained and unconstrained flux results were taken from [19]. 'Two Phase (con)' refers to the constrained two phase fit in this analysis. 'Two Phase (uncon)' is the unconstrained fit fluxes and 'D_2O (con)' and 'salt (con)' are the single phase constrained fit results.

Background Type	Two Phase (uncon)	Two Phase (con)	Single (con)
D_2O ^{214}Bi	287.4 ± 65.5	358.4 ± 46.0	350.8 ± 45.2
D_2O ^{208}Tl	48.5 ± 34.6	55.2 ± 34.9	49.7 ± 35.3
AV ^{214}Bi	210.7 ± 35.4	213.3 ± 35.3	212.6 ± 35.2
AV ^{208}Tl	22.4 ± 53.1	30.6 ± 53.5	37.3 ± 53.0
H_2O ^{214}Bi	42.0 ± 6.4	42.0 ± 6.4	42.0 ± 6.4
H_2O ^{208}Tl	19.3 ± 6.0	19.4 ± 6.0	19.6 ± 5.9
PMT β-γ	248.9 ± 45.4	256.3 ± 45.5	260.6 ± 45.9
(α, n) neutrons	100.1 ± 64.5	68.5 ± 57.7	16.7 ± 76.8
D_2O ^{214}Bi	370.6 ± 130.1	522.6 ± 67.0	524.1 ± 67.4
D_2O ^{208}Tl	257.0 ± 128.4	251.4 ± 129.2	265.8 ± 128.6
^{24}Na	48.4 ± 104.9	51.9 ± 104.1	46.7 ± 104.5
AV ^{214}Bi	440.5 ± 55.5	443.7 ± 55.3	444.3 ± 55.5
AV ^{208}Tl	22.3 ± 74.9	21.0 ± 74.7	29.3 ± 75.2
H_2O ^{214}Bi	68.5 ± 12.3	68.7 ± 12.3	68.7 ± 12.3
H_2O ^{208}Tl	42.9 ± 12.0	42.8 ± 12.0	42.8 ± 12.0
PMT β-γ	255.6 ± 63.7	251.8 ± 63.6	247.3 ± 64.2
(α, n) neutrons	0.0 ± 21.9	0.0 ± 21.7	0.0 ± 22.7

Table 9.12: Fitted number of background events obtained from the two phase unconstrained fit, two phase constrained fit and single phase constrained fits.

misidentification of low energy CC events and internal ^{214}Bi.

9.3.2 The CC and ES Energy Spectra

The extracted energy spectra for CC and ES signals, expressed in terms of the fraction of one Standard Solar Model are shown in Figures 9.6 and 9.7 respectively. In these figures, an undistorted ^{8}B energy spectrum with no neutrino oscillations would be flat at magnitude one. The lowest energy bin in the CC spectra is expected to be biased high as discussed in Section 8.4. The lowest energy ES bin, however, is not expected to have a signal-extraction-induced bias and is approximately 2σ higher than the other ES bins. The CC and ES spectra values with statistical and systematic uncertainties

are listed in Table 9.13. This table also includes the number of expected events in the D_2O and salt phases for each CC and ES energy bin.

The dominant systematic uncertainties for both the CC and ES spectra are shown in Figures 9.8 and 9.9, respectively. For the CC spectra, energy resolution and β_{14} mean are the dominant systematic uncertainty in the low energy bins. The energy resolution uncertainty used for this analysis was derived using ^{16}N which overestimates the energy resolution uncertainty at lower energies. Using the calibrated Radon spike, to determine energy resolution uncertainties would greatly improve the measurement of this uncertainty at lower energies. The systematic uncertainties in the ES energy spectra are dominated by angular resolution uncertainties.

With the extracted CC and ES energy spectra, the spectral shape predicted by different mixing parameter values in the LMA space can be tested against the data. A full global analysis of the entire Δm^2 and $\tan^2\theta$ parameter space is beyond the scope of this thesis. Instead only a few models are tested (see Figure 1.3 for the current allowed LMA parameter space). The northwest corner of the LMA parameter space is the most sensitive to spectral distortions. An improved energy spectrum measurement would greatly constrain this region, therefore the models selected for this test focus on that region of the LMA parameter space. The models tested include an undistorted ^{8}B energy spectrum and the expected MSW spectral shapes for the previous best fit LMA point from [29] which does not include any CC and ES spectral information from SNO ($\Delta m^2 = 7.9 \times 10^{-5}$ and $\tan^2\theta = 0.40$), a LMA point in the northwest corner of the allowed solar+KamLAND parameter space ($\Delta m^2 = 9.0 \times 10^{-5}$ and $\tan^2\theta = 0.35$), a LMA point in the northwest corner of the allowed solar-only parameter space ($\Delta m^2 = 1.0 \times 10^{-4}$ and $\tan^2\theta = 0.30$) and a LMA point at using the best fit Δm^2 from [29] and larger $\tan^2\theta$ ($\Delta m^2 = 7.9 \times 10^{-5}$ and $\tan^2\theta = 0.45$).

To compare these models to the data, the extracted NC flux is used as the measurement of the total ^{8}B flux and the CC and ES spectra are expressed in terms of the fraction of the NC flux as shown in Figures 9.10 and 9.11. The spectral shapes of the different models discussed above are also included in the figures. For each model in Figure 9.10, the 4–4.5 MeV energy range includes the expected signal extraction bias (see Section 8.4) in the lowest energy CC bin. For the undistorted ^{8}B model, shown in these figures, the fraction of CC and ES events is assumed to be flat and the normalization is the CC/NC and ES/NC ratios extracted from the two phase constrained fit (Equations 9.13–9.15).

To test the significance of each of these models, the χ^2 is defined as

$$\chi^2 = \sum_{i,j=1}^{N_{spec}} \left(Y_i - Y_i^{\text{model}}\right) \left[\sigma_{ij}^2\right]^{-1} \left(Y_j - Y_j^{\text{model}}\right) \tag{9.25}$$

where N_{spec} is the number of spectral bins, equal to 32 for 16 CC and 16 ES bins, Y_i is the data value for bin i, Y_i^{model} is the model prediction for bin i and the total uncertainty is $\sigma_{ij}^2 = \sigma_{ij}^2(\text{stat}) + \sigma_{ij}^2(\text{sys})$. The statistical uncertainties contain the elements of the covariance matrix derived from the signal extraction fit. The systematic uncertainties are calculated as

$$\sigma_{ij}^2(\text{sys}) = \sum_{k=1}^{N_{sys}} \frac{\delta Y_i}{\delta S_k} \frac{\delta Y_j}{\delta S_k} \tag{9.26}$$

where $\frac{\delta Y_i}{\delta S_k}$ is the uncertainty in bin i for the systematic uncertainty, k, and N_{sys} is the total number of systematic uncertainties. This χ^2 accounts for all correlations between the CC and ES energy bins.

The results of the χ^2 for each of these models are listed in Table 9.14. This table

also includes the χ^2 values using statistical uncertainties only. The extracted CC and ES spectra are consistent with an undistorted ^{8}B spectrum but a better fit of these models is the LMA parameters $\Delta m^2 = 7.9 \times 10^{-5}$ and $\tan^2\theta = 0.45$. Additionally the parameters in the northwest corner of the LMA space yield significantly worse χ^2 values. To test the significance of the different LMA models, the $\Delta\chi^2$ method outlined in [86] is taken. Since a global minimization of the LMA parameter space has not been done for this analysis, the best fit point ($\Delta m^2 = 7.9 \times 10^{-5}$ and $\tan^2\theta = 0.45$) of the models sampled in this analysis is used as the global best fit point. For the northwest LMA point $\Delta m^2 = 9.0 \times 10^{-5}$ and $\tan^2\theta = 0.35$ the $\Delta\chi^2$ is more than 2σ from the best fit point, while the LMA point $\Delta m^2 = 1.0 \times 10^{-4}$ and $\tan^2\theta = 0.30$ is more than 3σ from the best fit point. In conclusion, the improved flux measurement and CC and ES energy spectra obtained from this analysis favor higher values of the mixing angle. Including this measurement in a global analysis with other solar experiments and KamLAND should further constrain the LMA parameter space, especially the northwest region.

Type	Fitted Fraction	D_2O Events	Salt Events
CC 4.0 MeV	$0.405^{+0.127+0.302}_{-0.127-0.154}$	156.6 ± 49.5	218.5 ± 69.0
CC 4.5 MeV	$0.327^{+0.034+0.074}_{-0.033-0.055}$	145.6 ± 15.3	204.0 ± 21.4
CC 5.0 MeV	$0.248^{+0.027+0.045}_{-0.026-0.034}$	123.5 ± 13.5	171.9 ± 18.8
CC 5.5 MeV	$0.281^{+0.025+0.043}_{-0.025-0.030}$	148.1 ± 13.6	208.7 ± 19.1
CC 6.0 MeV	$0.289^{+0.023+0.030}_{-0.023-0.028}$	152.9 ± 12.4	214.0 ± 17.3
CC 6.5 MeV	$0.301^{+0.021+0.022}_{-0.021-0.019}$	161.5 ± 11.3	225.6 ± 15.8
CC 7.0 MeV	$0.285^{+0.020+0.017}_{-0.019-0.012}$	147.7 ± 10.1	205.8 ± 14.0
CC 7.5 MeV	$0.296^{+0.019+0.012}_{-0.019-0.011}$	143.6 ± 9.3	199.9 ± 13.0
CC 8.0 MeV	$0.296^{+0.019+0.012}_{-0.018-0.011}$	131.5 ± 8.4	184.3 ± 11.8
CC 8.5 MeV	$0.272^{+0.019+0.013}_{-0.018-0.010}$	105.4 ± 7.4	147.9 ± 10.3
CC 9.0 MeV	$0.288^{+0.021+0.011}_{-0.020-0.018}$	92.0 ± 6.6	129.1 ± 9.3
CC 9.5 MeV	$0.280^{+0.022+0.016}_{-0.022-0.013}$	73.2 ± 5.8	103.4 ± 8.2
CC 10.0 MeV	$0.366^{+0.029+0.020}_{-0.027-0.024}$	72.9 ± 5.6	103.4 ± 8.0
CC 10.5 MeV	$0.311^{+0.030+0.016}_{-0.029-0.025}$	45.7 ± 4.5	65.5 ± 6.4
CC 11.0 MeV	$0.290^{+0.036+0.021}_{-0.033-0.029}$	29.4 ± 3.6	42.6 ± 5.2
CC 11.5 MeV	$0.319^{+0.045+0.025}_{-0.041-0.040}$	20.9 ± 2.9	31.3 ± 4.4
ES 4.0 MeV	$0.711^{+0.111+0.110}_{-0.107-0.042}$	66.1 ± 10.3	92.9 ± 14.5
ES 4.5 MeV	$0.412^{+0.079+0.034}_{-0.075-0.023}$	35.9 ± 6.9	50.1 ± 9.6
ES 5.0 MeV	$0.452^{+0.081+0.039}_{-0.077-0.023}$	35.8 ± 6.4	50.5 ± 9.0
ES 5.5 MeV	$0.289^{+0.076+0.033}_{-0.071-0.006}$	20.8 ± 5.5	29.1 ± 7.7
ES 6.0 MeV	$0.347^{+0.085+0.018}_{-0.079-0.023}$	21.5 ± 5.2	30.0 ± 7.3
ES 6.5 MeV	$0.338^{+0.084+0.012}_{-0.078-0.025}$	18.7 ± 4.6	26.2 ± 6.5
ES 7.0 MeV	$0.466^{+0.097+0.026}_{-0.090-0.029}$	22.2 ± 4.6	30.9 ± 6.4
ES 7.5 MeV	$0.463^{+0.105+0.030}_{-0.098-0.027}$	18.4 ± 4.2	25.9 ± 5.9
ES 8.0 MeV	$0.453^{+0.113+0.027}_{-0.104-0.034}$	15.0 ± 3.7	21.3 ± 5.3
ES 8.5 MeV	$0.491^{+0.129+0.053}_{-0.117-0.022}$	13.6 ± 3.6	19.0 ± 5.0
ES 9.0 MeV	$0.444^{+0.136+0.025}_{-0.122-0.031}$	9.7 ± 3.0	13.8 ± 4.2
ES 9.5 MeV	$0.410^{+0.149+0.023}_{-0.132-0.044}$	7.2 ± 2.6	10.2 ± 3.7
ES 10.0 MeV	$0.223^{+0.156+0.022}_{-0.132-0.025}$	3.0 ± 2.1	4.2 ± 3.0
ES 10.5 MeV	$0.276^{+0.180+0.081}_{-0.148-0.073}$	2.8 ± 1.8	4.0 ± 2.6
ES 11.0 MeV	$0.133^{+0.194+0.049}_{-0.168-0.086}$	0.9 ± 1.4	1.4 ± 2.0
ES 11.5 MeV	$0.053^{+0.188+0.053}_{-0.152-0.051}$	0.3 ± 0.9	0.4 ± 1.4
NC	$0.876^{+0.029+0.036}_{-0.029-0.045}$	746.1 ± 24.9	2975.1 ± 99.2

Table 9.13: Fitted fraction of one SSM and number of events in the D_2O and salt phases obtained from the unconstrained fit. The energy listed in the first column is the lower edge of the energy bin. In the second column the first uncertainty listed is the statistical uncertainty and the second is the systematic uncertainty.

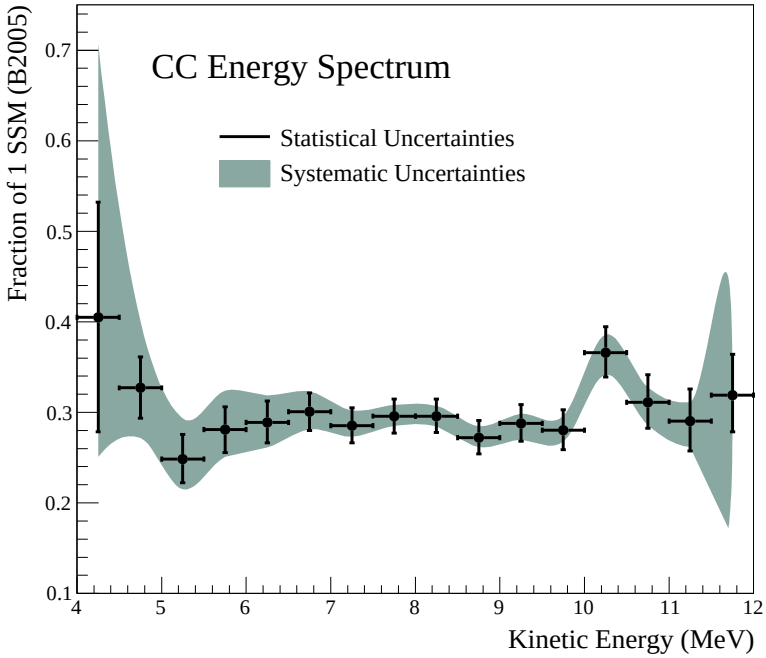

Fig. 9.6: The extracted CC energy spectrum shown in terms of the fraction of the SSM flux.

Model	χ^2 (stat + sys)	χ^2 (stat only)
Undistorted	17.03	33.99
$\Delta m^2 = 7.9 \times 10^{-5}$, $\tan^2\theta = 0.40$	19.03	42.35
$\Delta m^2 = 9.0 \times 10^{-5}$, $\tan^2\theta = 0.35$	22.29	51.08
$\Delta m^2 = 1.0 \times 10^{-4}$, $\tan^2\theta = 0.30$	25.73	60.33
$\Delta m^2 = 7.9 \times 10^{-4}$, $\tan^2\theta = 0.45$	16.00	34.92

Table 9.14: χ^2 values for undistorted ^{8}B energy spectrum and different MSW models. The χ^2 is shown for statistical and systematic uncertainties and statistical uncertainties only. There are 32 degrees of freedom.

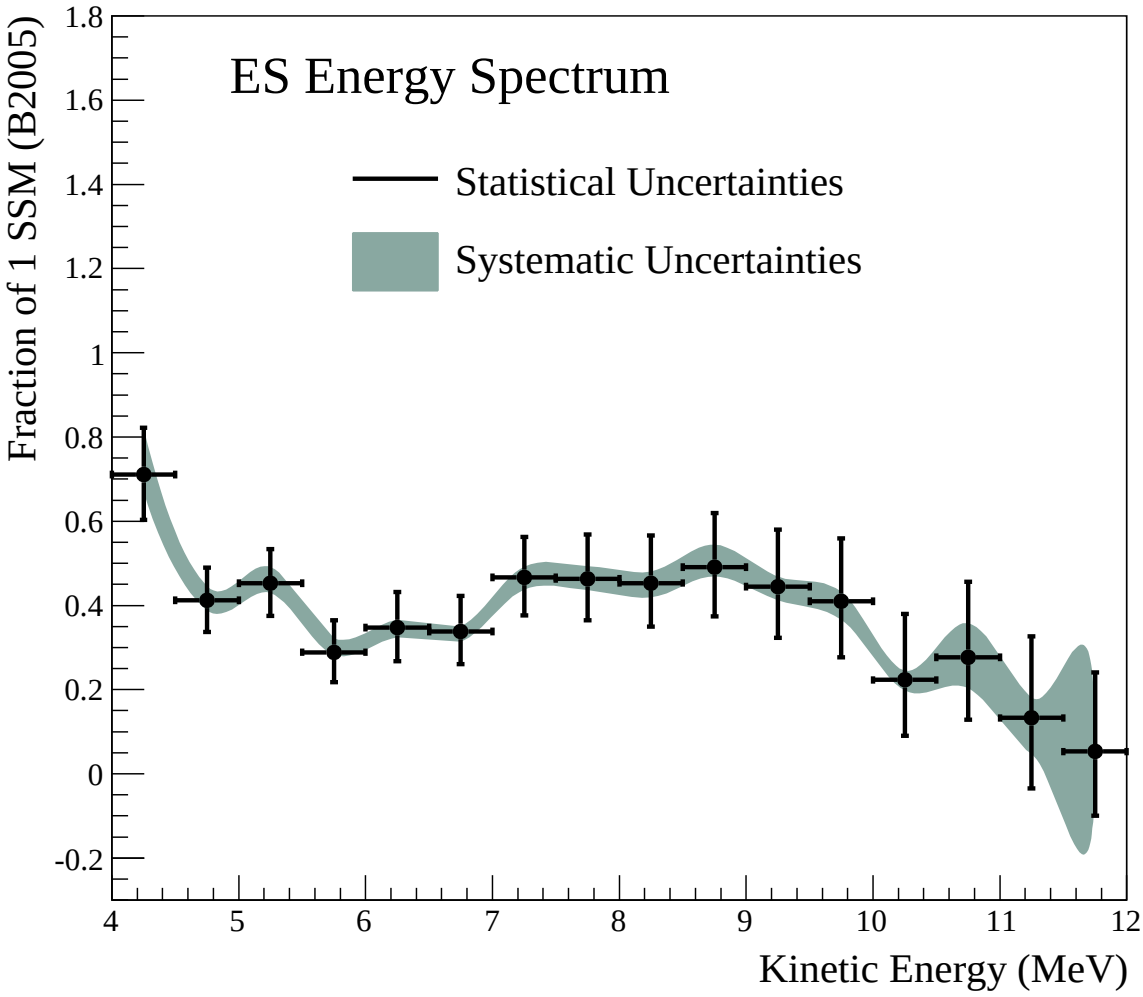

Fig. 9.7: The extracted ES energy spectrum shown in terms of the fraction of the SSM flux.

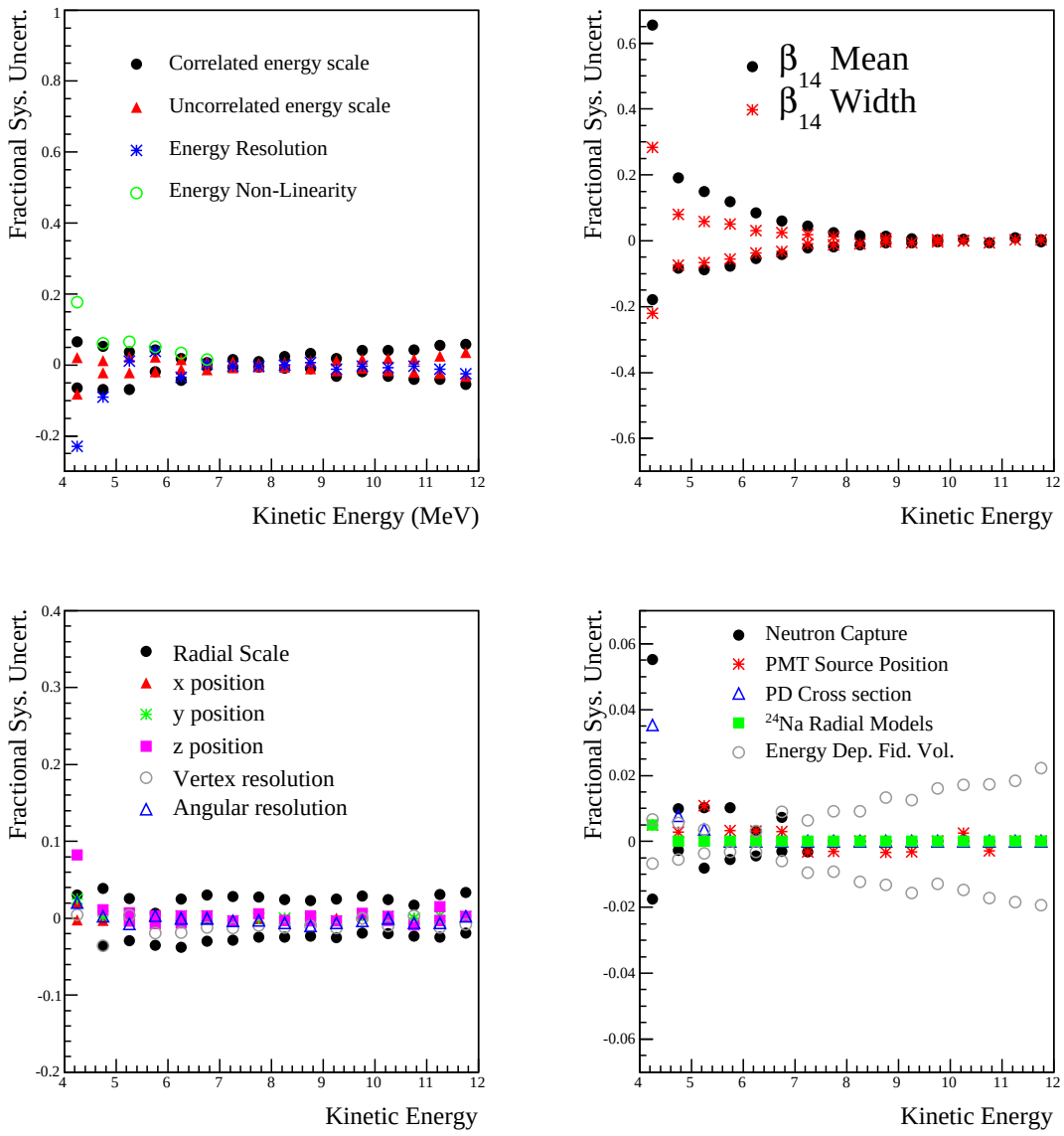

Fig. 9.8: Fractional systematic uncertainty on the fitted rate of CC events due to each observable systematic uncertainty. 'PD cross section' refers to the uncertainty on the photo-disintegration cross section.

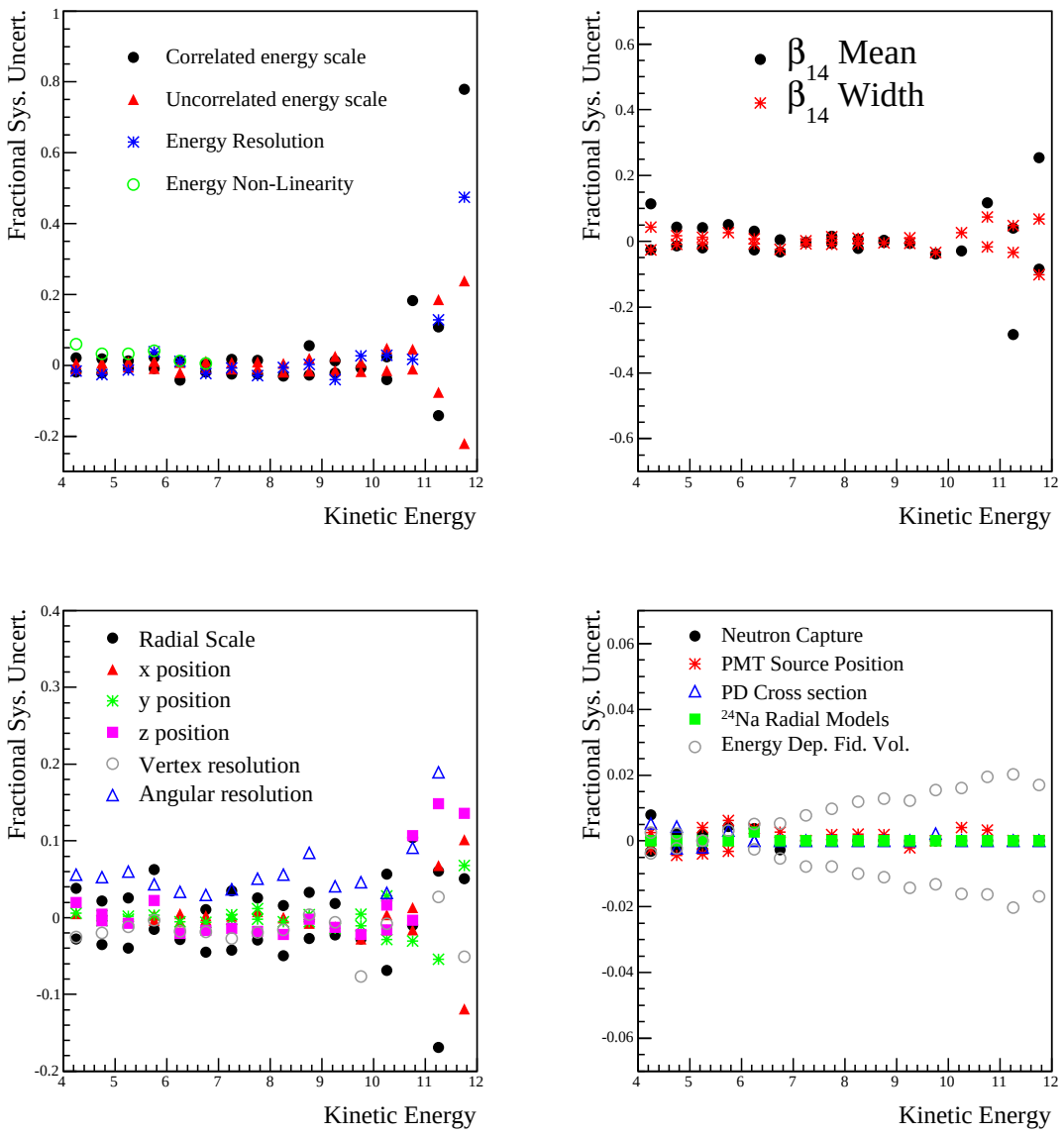

Fig. 9.9: Fractional systematic uncertainty on the fitted rate of ES events due to each observable systematic uncertainty. 'PD cross section' refers to the uncertainty on the photo-disintegration cross section.

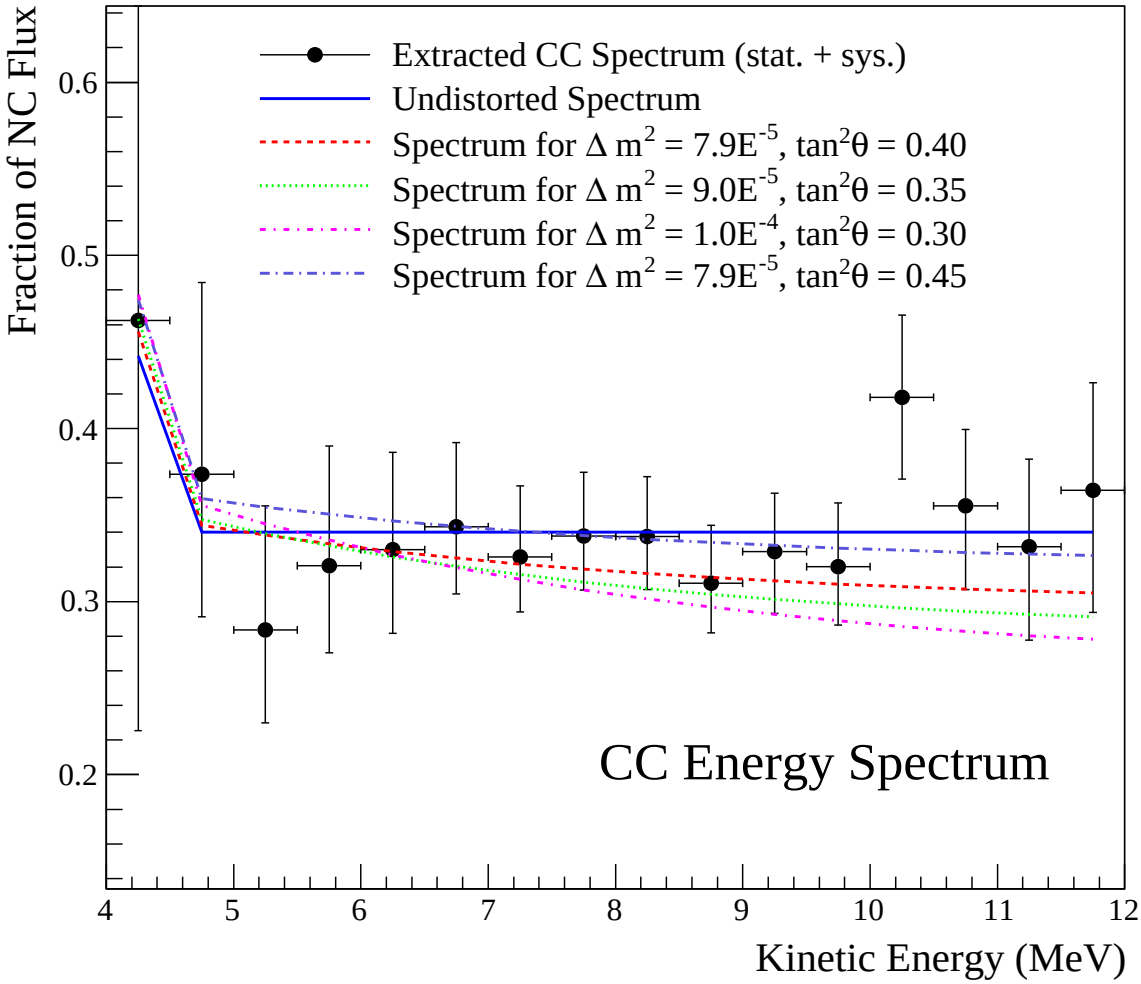

Fig. 9.10: The extracted CC energy spectrum shown in terms of the fraction of the NC flux. The lines indicate the expected fraction for various models including different values of Δm^2 and $\tan^2\theta$ as well as undistorted. The best fit LMA value from [29] is $\Delta m^2 = 7.9 \times 10^{-5}$ and $\tan^2\theta = 0.40$. Note that a bias correction has been applied in the lowest energy bin in all the models.

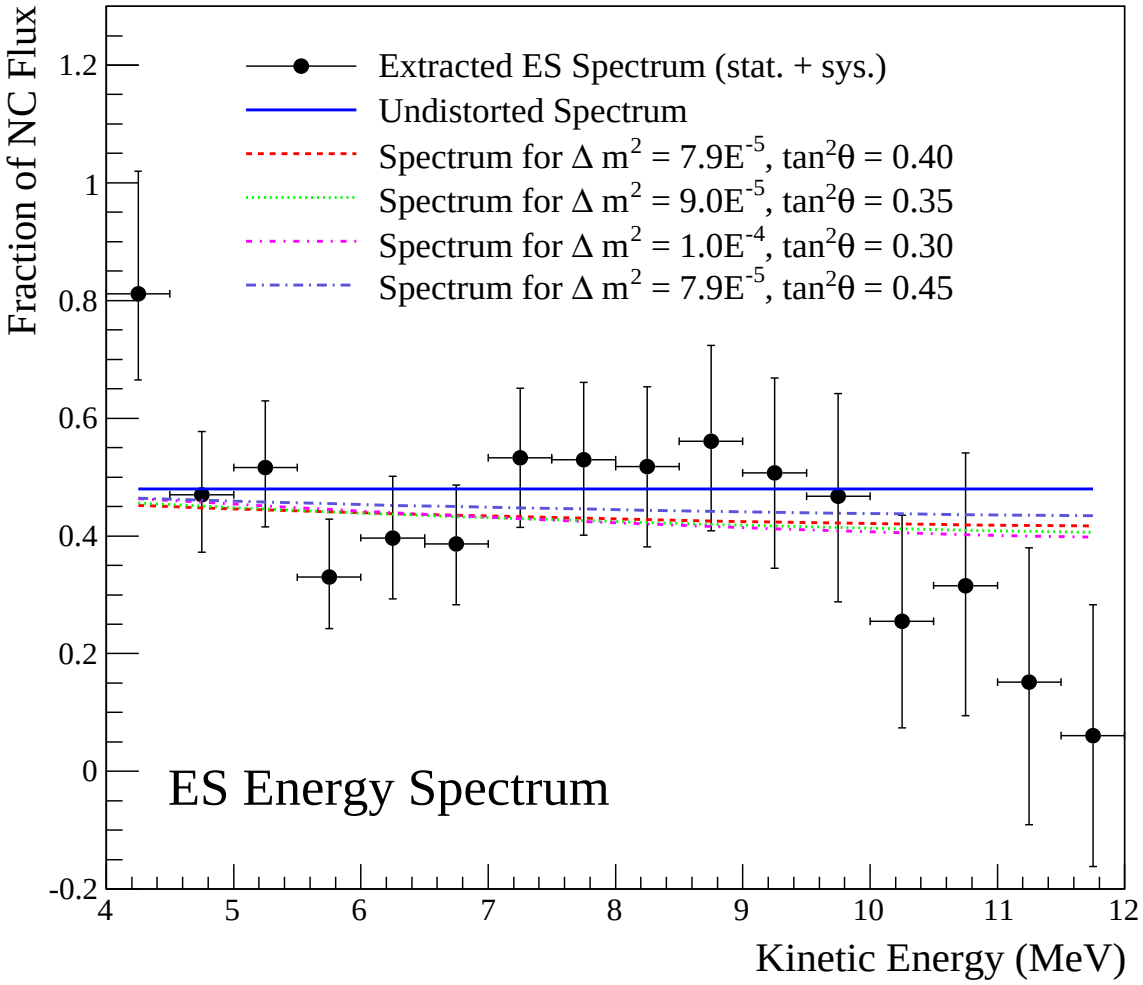

Fig. 9.11: The extracted ES energy spectrum shown in terms of the fraction of the NC flux. The lines indicate the expected fraction for various models including different values of Δm^2 and $\tan^2\theta$ as well as undistorted. The best fit LMA value from [29] is $\Delta m^2 = 7.9 \times 10^{-5}$ and $\tan^2\theta = 0.40$.

Ch. 10

Conclusions

The Sudbury Neutrino Observatory has successfully demonstrated that the solar ^{8}B flux of active neutrinos is consistent with the Standard Solar Model, while the flux of ^{8}B electron neutrinos is suppressed. These results provided the solution to a 40 year old question, first brought to light by Ray Davis about the nature of solar neutrinos. SNO's measurement of the fluxes concludes that solar electron neutrinos are undergoing flavor transformation enroute to Earth.

To improve the measurement of the ^{8}B flux and electron survival probability, this thesis has focused on improving the estimation of energy in SNO in order to lower the analysis energy threshold. The improvement in signal to background separation achieved with the energy estimator developed in this thesis has allowed for a measurement of the CC, ES and NC fluxes at an energy threshold of 4.0 MeV. Combining both the D_2O and salt phases of data in an energy unconstrained fit, the CC, ES and NC fluxes are

$$\Phi_{\rm CC}^{\rm combined,uncon} = 1.67^{+0.04}_{-0.04}({\rm stat.})^{+0.10}_{-0.07}\ ({\rm syst.}) \times 10^6 {\rm cm}^{-2}{\rm s}^{-1} \qquad (10.1)$$

$$\Phi_{\rm ES}^{\rm combined,uncon} = 2.27^{+0.15}_{-0.14}({\rm stat.})^{+0.12}_{-0.21}\ ({\rm syst.}) \times 10^6 {\rm cm}^{-2}{\rm s}^{-1} \quad (10.2)$$

$$\Phi_{\rm NC}^{\rm combined,uncon} = 4.98^{+0.17}_{-0.16}({\rm stat.})^{+0.20}_{-0.26}\ ({\rm syst.}) \times 10^6 {\rm cm}^{-2}{\rm s}^{-1}. \quad (10.3)$$

The total ^{8}B neutrino flux is determined within a statistical and systematic uncertainty of 6.2%. This is compared to uncertainties of 12.5% and 8.9% from previous measurements of the D_2O and salt phases respectively. Further, the CC and ES energy spectra using both the D_2O and salt data sets was extracted at this low energy threshold. The extracted spectra are consistent with an undistorted ^{8}B spectrum but favor larger values of the mixing angle than a recent global analysis obtained. In a full global analysis of the LMA parameter space, these results will improve the constraints on the mixing parameters.

Although this measurement of the CC, ES and NC fluxes is more precise than any previous measurement using SNO data, it can be improved in several ways. First the statistical uncertainty in the 4.0-4.5 MeV energy bin in the CC spectrum can be greatly reduced by lowering the energy threshold further to 3.5 MeV. As discussed in Section 8.4, using a 3.5 MeV threshold helps fix the internal ^{214}Bi rate which in turn helps separate CC electrons from ^{214}Bi events at higher energies. Studies in this thesis indicate this would improve the statistical uncertainty in the 4.0 MeV CC energy bin by 10%. An improved statistical uncertainty in this CC energy bin would be critical in the search for spectral distortions. Second, including systematic uncertainties in the observables as parameters in the fit would greatly improve the total systematic uncertainties on the fluxes. From studies in [68] this could reduce the uncertainties by 25%.

While significant progress has been made in constraining the mixing parameters in the MSNP matrix, our knowledge of the properties of neutrinos is still limited.

Distortions in the neutrino energy spectrum predicted by the MSW effect have not been observed. The sign of ΔM^2_{23} is not known nor is the magnitude of θ_{13}. Is CP violated for leptons? What is the absolute mass of the neutrinos? The past 40 years have revolutionized our knowledge of neutrinos but many fundamental questions still remain. A next generation of experiments strives to solve some of these lingering questions but in the solutions we will perhaps discover even more mysteries.

Appendix A

Calculation of PMT Hit Probabilities and FTK Optimization

This appendix serves to supplement the main overview of the FTK energy estimator found in Chapter 5. The following sections discuss FTK's calculation of the number of direct, AV reflected, PMT reflected and noise hits (a discussion of the scattered hit calculation can be found in Section 5.3.1). Additionally a discussion of the optimization of FTK's timing window and the maximum likelihood method used to tune the late light in the MC is included in this appendix.

A.1 Direct Light Calculation

The probability of a single photon that is not Rayleigh scattered or reflected being detected by the i^{th} PMT is the probability that a photon is produced in the direction

of the PMT, is not attenuated, scattered, or reflected enroute, and that it hits the PMT and is detected. This is expressed as

$$\rho_i^{dir} = \lambda_{\rm Norm} \int_{\lambda_1}^{\lambda_2} \frac{d\lambda}{\lambda^2} P_1 \times P_2 \times P_3 \times P_4 \tag{A.1}$$

where

$$\begin{aligned} P_1 &= g(\cos\alpha) \qquad (A.2) \\ &= \text{Probability that the Cherenkov photon is produced} \\ &\quad \text{at an angle } \alpha \text{ with respect} \\ &\quad \text{to the electron direction, } \hat{d}_e \end{aligned}$$

$$\begin{aligned} P_2 &= e^{-(d_d(\mu_d+\mu'_d)+d_a\mu_a+d_h(\mu_h+\mu'_d))} \qquad (A.3) \\ &= \text{Probability of the photon not being absorbed} \\ &\quad \text{or scattered enroute to the PMT, where } d \\ &\quad \text{is the distance through each medium and} \\ &\quad \mu \text{ is the attenuation factor for each media} \\ &\quad \text{and } \mu' \text{ is the scattering coefficient} \\ &\quad \text{where the subscript } d \text{ is } D_2O \text{ , } a \text{ is acrylic and } h \text{ is } H_2O \end{aligned}$$

$$\begin{aligned} P_3 &= F_1 \times F_2 \qquad (A.4) \\ &= \text{Probability that the photon does not reflect off the AV.} \end{aligned}$$

F_1 is the Fresnel coefficient (including polarization)

for the first AV boundary (if any), F_2 is the coefficient

for the second AV boundary (if any)

$$P_4 = R_{\text{pmt}}(\theta, \lambda)\frac{\Omega_0}{2\pi} \tag{A.5}$$

$$= \text{Probability that the photon reaches and fires the PMT}$$

$\frac{\Omega_0}{2\pi}$ is the solid angle of the tube

$R_{\text{pmt}}(\theta, \lambda)$ is the PMT angular and

wavelength response

θ is the photon's angle with respect to the

PMT's normal direction

$$\lambda_{\text{Norm}} = \frac{1}{\lambda_1^{-1} - \lambda_2^{-1}} \tag{A.6}$$

$$\lambda_1 = 220\text{nm is the lower wavelength cutoff value} \tag{A.7}$$

$$\lambda_2 = 710\text{nm is the upper wavelength cutoff value} \tag{A.8}$$

$$d\lambda = 10\text{nm} \tag{A.9}$$

The $\frac{1}{\lambda^2}$ weighting factor in the integration accounts for the fact that Cherenkov photons are produced flat in frequency ($dN(\nu) \propto d\nu$ where N_γ is the number of photons and ν is their frequency).

To calculate ρ_i^{dir}, the direction of a photon produced at the electron's position is determined, such that the photon will strike the center of the i^{th} PMT, accounting for directional changes caused by refraction through the AV. For events inside 400 cm,

changes in the photon's direction due to refraction is a negligible effect. At larger radii, where the photons strike the AV at large angles, not correcting the photon's initial direction to account for path changes through the AV results in a radial energy bias. Refraction does not change the direction of any one photon significantly, but the AV acts as a lens meaning that while the direction of an individual photon changes only slightly all photons are affected in the same manner. This is especially significant for events at large radii traveling inward, where there are many tubes within the Cherenkov cone.

The probability that a Cherenkov photon would be produced at a given angle (with respect to the electron's direction) is determined using a parameterization as a function of electron energy derived from mono-energetic electron MC. As the electron energy increases, the angular distribution of the Cherenkov photons tightens and the probability of a tube in the Cherenkov cone being hit is greater. FTK uses the energy dependence of the $g(\cos\alpha)$ distribution as an additional handle in fitting for the electron energy. More on the $g(\cos\alpha)$ parameterization can be found in Section 5.4.2.

To estimate photon losses due to absorption and scattering, the SNOMAN geometry code is used to track the amount of material the photon must traverse enroute to the PMT[1]. The advantage of using the SNOMAN geometry code is that the photon's path through the belly plates, the Kevlar ropes, the neck, NCDs and even the source container[2], if deployed, can be accurately modeled. If a photon enters a medium that is not D_2O, acrylic or H_2O, such as the Kevlar ropes or the source container, the

[1]FTK enables the GE error handler in mode KGE_ERH_THROW_ALL_ERR to avoid geometry ZTELL errors and catches all possible geometry errors.

[2]When running on data, the source geometry (if a source run) is not initialized automatically. FTK therefore will initialize the necessary source geometry. This feature can be disabled using word TFTK_ENABLE_GEO. If running on data, FTK will also initialize the collection efficiency from the MCMA bank.

PMT the photon is traveling to is considered to be blocked. The attenuations lengths used in P_2 are taken from laserball measurements. The scattering coefficients are taken from the MC's calculation of the Rayleigh scattering with a correction factor derived from the masked laserball applied [68].

When the photon strikes the front face of the PMT, the angle of incidence with respect to the PMT's normal direction is used to determine the PMT response. The PMT angular and wavelength response used by FTK is derived from the laserball calibration data. To account for normalization differences between the laserball derived PMT responses and SNOMAN's 3d-PMT model of the PMT (see Section 2.4), a constant correction factor is applied to FTK's PMT response[3]. This correction term is calculated by fitting the ratio of the number of direct photons from the 3d-PMT model and the Grey Disk PMT model as a function of radius to a constant (Figure A.1). A direct photon is defined as a photon that does not have any interaction in any media from the production point to the PMT.

The calculation of the PMT's solid angle is an approximation assuming the face of the PMT is flat, given by

$$\Omega_0 = \frac{\pi r_c^2}{d_i^2} \hat{d}_\gamma \cdot \hat{r}_i \tag{A.10}$$

where r_c is the radius of the PMT's concentrator, $\vec{d}_\gamma$ is the directional vector of the photon's initial direction, $\vec{r}_i$ is the vector from the detector's origin to the PMT's center, and d_i is the distance between the electron's position and the photon's perceived location of the PMT. Since refraction through the AV changes the photon's direction, the solid angle of the PMT is the area subtended in the absence of refraction of light

[3]This correction term is load in the TFTK bank using word KTFTK_3DPMT_NORM

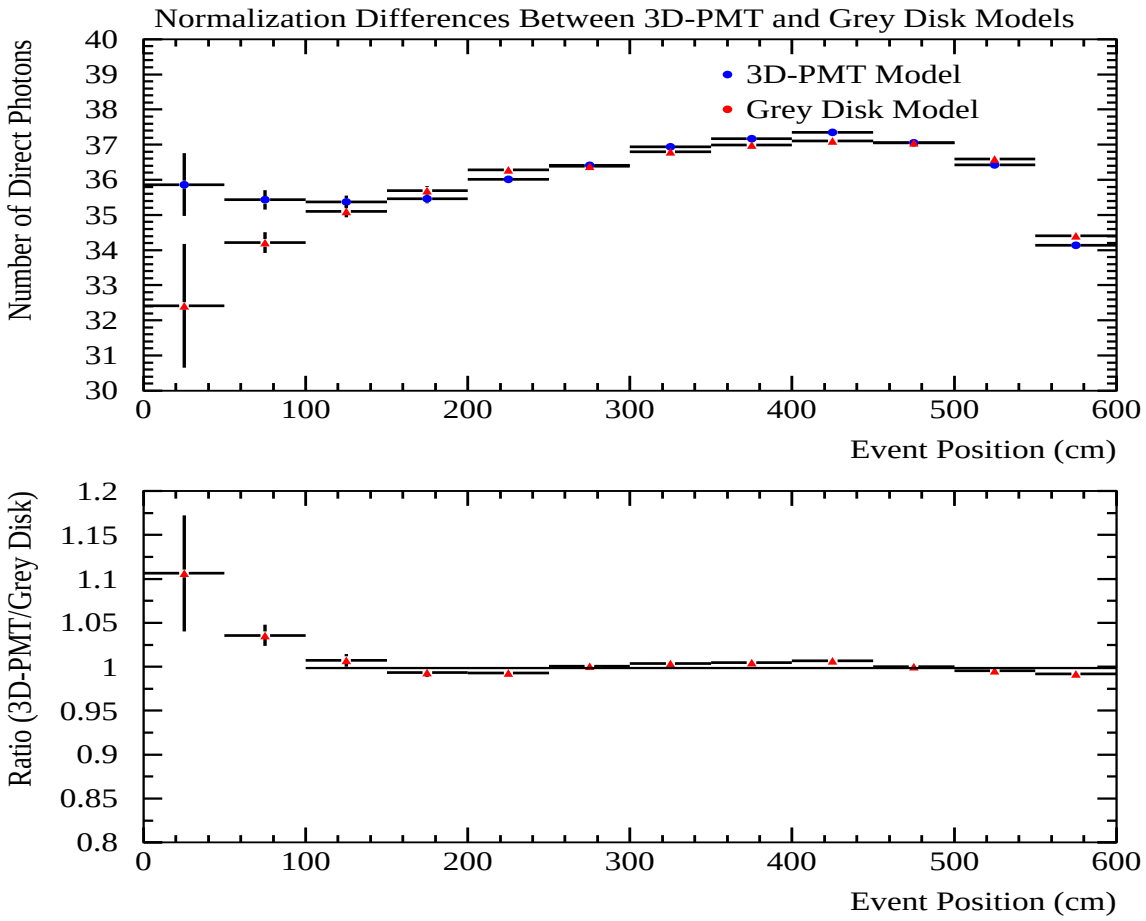

Fig. A.1: Top Figure: The number of direct photons as a function of radius for the two MC PMT model; 3d-PMT and Grey Disk. Bottom Figure: Ratio of the number of direct photons for the two PMT models. The MC shown here was generated for the D_2O phase.

through the AV. (This effect is similar to looking at a coin that is underwater, the location of the coin from the perspective of the viewer is not the same as the coin's actual location.) For the solid angle calculation given in Equation A.10, d_i is not the distance between the electron's position and the actual PMT's location, but the distance between the electron's position and the position where the photon would have struck the PSUP if it were to have traveled unrefracted. For events inside 400 cm, this subtlety has little effect on the direct light calculation. For larger radii, this is more significant. By not correcting it FTK underestimates the energy scale by 1.5% at $R = 550$cm. As with the case of the photon's initial direction, the effect on the solid angle for any given tube is small, but since the AV acts as a lens many tubes are affected in the same way.

Refraction through the AV can also distort the area of the tube from the perspective of the photon. For events inside 500 cm, the distortion of a tube's solid angle is an insignificant effect but for events near the AV, especially outward going events this distortion is non-negligible resulting in a turn-up in the energy scale. To calculate the tube's solid angle taking into account the distorted size, photons are tracked to four points on the perimeter to define a minor and major axis. The solid angle of the tube is then

$$\Omega_{ray} = \frac{\pi R_m R_M}{d_i^2} \hat{d}_\gamma \cdot \hat{r}_i \tag{A.11}$$

where R_m is the radius of the minor axis, R_M is the radius of the major axis and all other variables are defined in Equation A.10. This ray trace solid angle calculation begins to differ significantly from the undistorted solid angle calculation when the distance to the tube from the electron's position is < 700 cm as seen in Figure A.2.

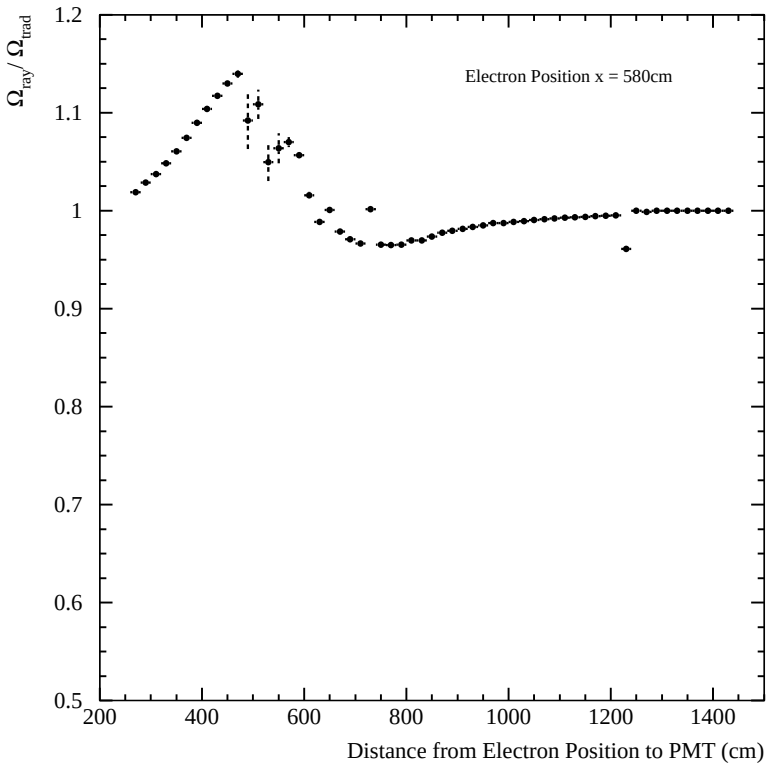

Fig. A.2: Ratio of the solid angle calculations accounting for the distortion in area due to refraction through the AV and not accounting for distortion as a function of distance from the event position to the PMT. The event position is at $x = 580$ cm.

Not using the ray trace solid angle calculation for events near the AV leads to a gross underestimate of the number of direct photons as seen in Figure A.3 which plots the difference between the number of direct photons for MC and FTK per MeV as a function of generated position for outward going events. Switching to the ray trace solid angle calculation when the distance between the event position and tube is < 700 cm, this radial shift disappears (Figure A.4).

The total detector-wide probability of a single photon that is neither scattered nor reflected hitting a PMT is the summation of over all PMTs in the detector.

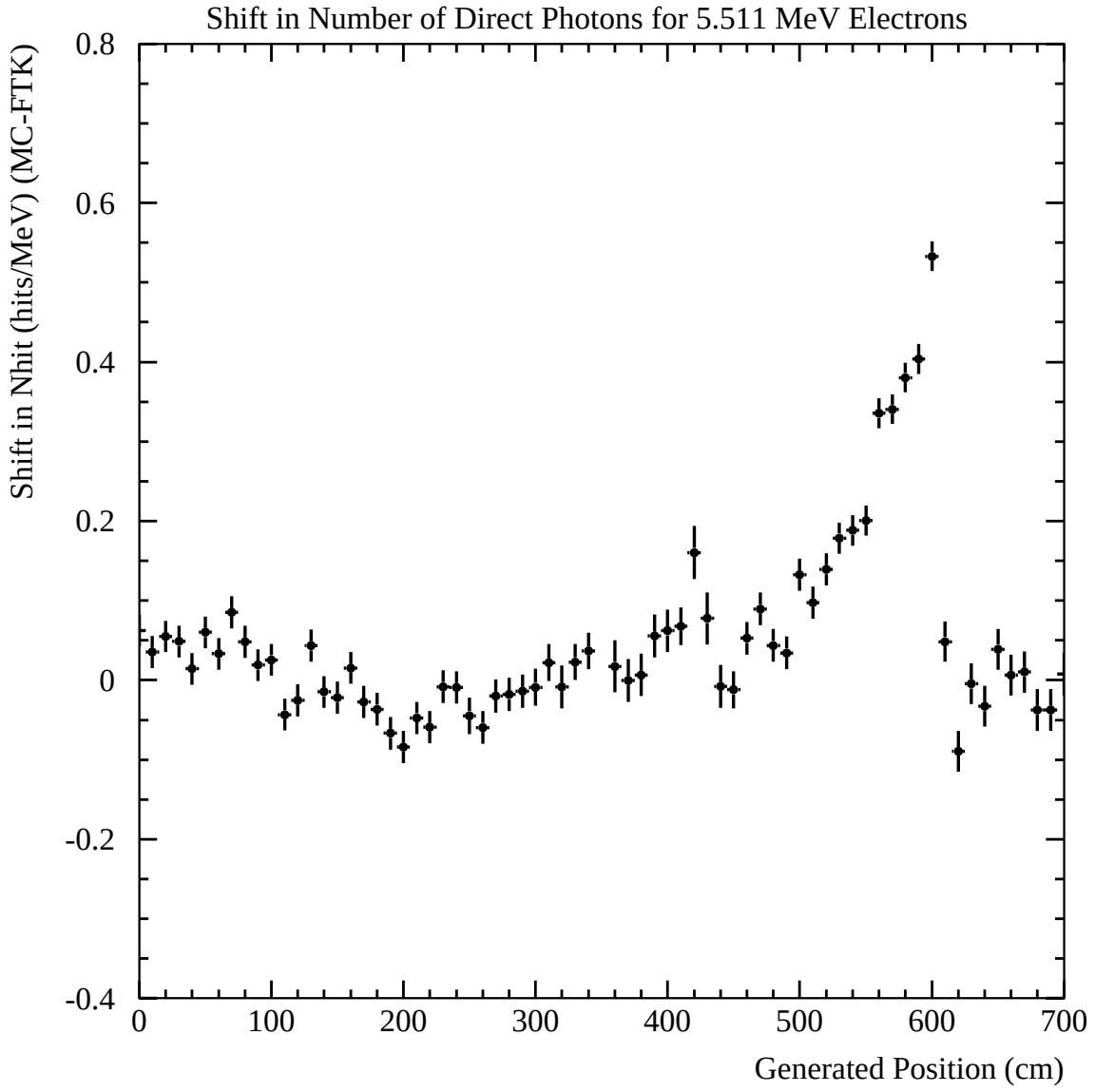

Fig. A.3: Difference in the number of direct photons between MC and FTK per MeV not accounting for distortion of the tube's area due to the AV. Events generated were 5 MeV mono-energetic electrons with position along the x-axis and direction $u = 1$ (outward).

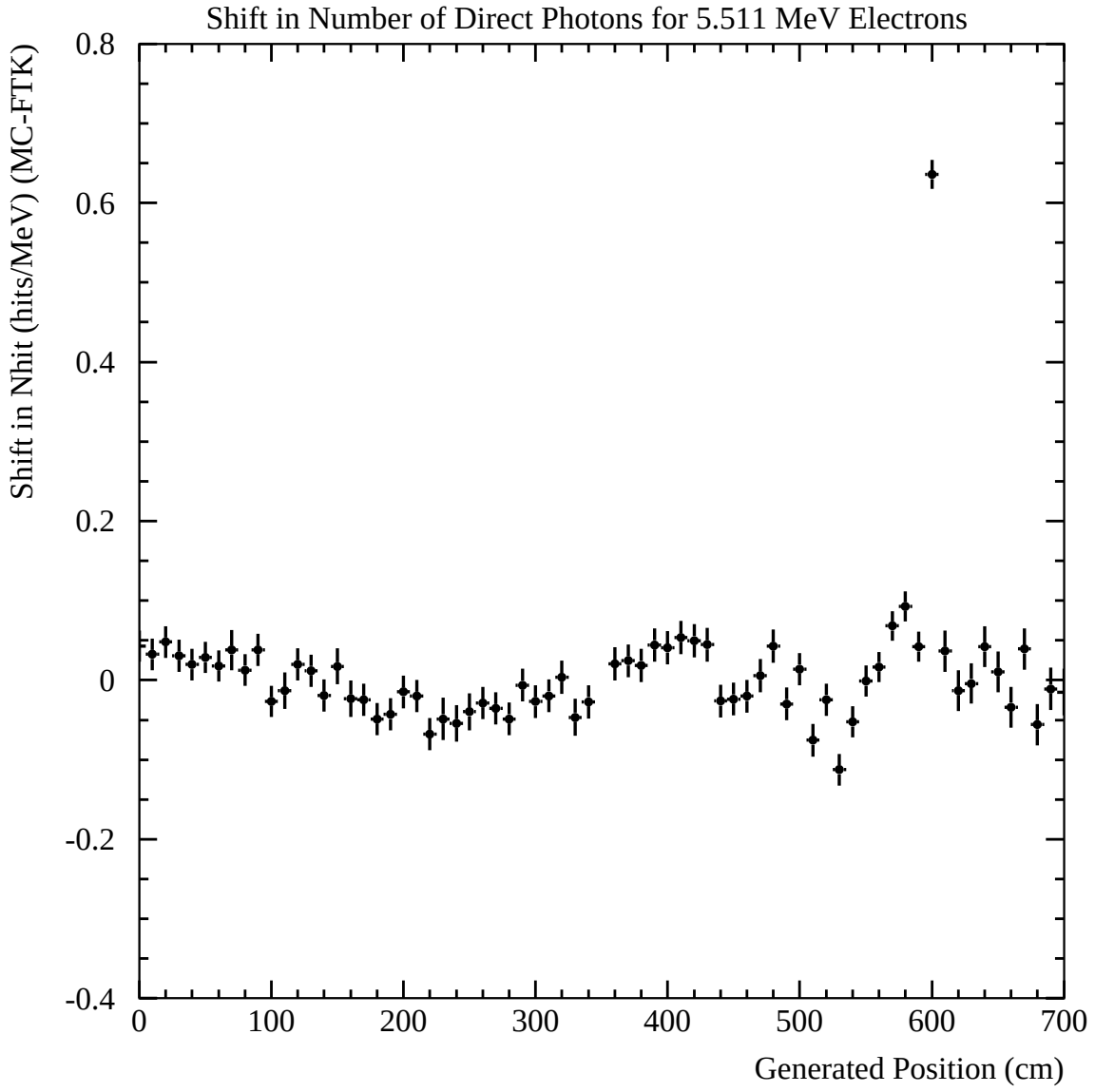

Fig. A.4: Difference in the number of direct photons between MC and FTK per MeV accounting for distortion of the tube's area due to the AV. Events generated were 5 MeV mono-energetic electrons with position along the x-axis and direction $u = 1$ (outward).

$$\rho_{dir} = \sum_{\text{All PMTs}} \rho_i^{dir} \tag{A.12}$$

A.2 AV Reflected Light Calculation

The probability of a photon reflecting off the AV and hitting the i^{th} PMT is given by

$$\rho_i^{av} = \lambda_{\text{Norm}} \int_{\lambda_1}^{\lambda_2} \frac{d\lambda}{\lambda^2} P_1 \times P_1^A \times P_2^A \times P_3^A \times P_4 2 \tag{A.13}$$

where P_1 is defined in A.2, P_4 is defined in A.5 and all other probabilities are listed below

$$\begin{aligned} P_1^A &= e^{-(d_d(\mu_d+\mu'_d)+d_a\mu_a+d_h(\mu_h+\mu'_h))} \qquad (A.14) \\ &= \text{Probability of the photon not being absorbed or scattered} \\ &\quad \text{enroute to the AV where } d \text{ is the distance through each} \\ &\quad \text{medium from the electron's position to the AV and } \mu \text{ is} \\ &\quad \text{the attenuation factor and } \mu' \text{ is the scattering} \\ &\quad \text{coefficient for each medium where the subscript } d \text{ is } D_2O\,, \\ &\quad a \text{ is acrylic and } h \text{ is } H_2O \end{aligned}$$

$$\begin{aligned} P_2^A &= R_1 \text{ (or } F_1 \times R_2) \qquad (A.15) \\ &= \text{Probability that the photon reflects off the first AV surface,} \\ &\quad \text{where } R_1 \text{ is the polarized Fresnel coefficient for reflection.} \end{aligned}$$

Alternatively, the photon can transmit through the first AV surface and reflect off the second surface. In this case, F_1 is the Fresnel coefficient of transmission off the first surface and R_2 is the Fresnel reflection coefficient off the second AV boundary

$$\begin{aligned} P_3^A &= e^{-(d'_d(\mu_d+\mu'_d)+d'_a\mu_a+d'_h(\mu_h+\mu'_h))} \\ &= \text{Probability of the photon not being absorbed or scattered enroute to the PMT from the AV, where } d' \text{ is the distance through each medium from the scatter point to the PMT and } \mu \text{ is the absorption factor and } \mu' \text{ is the scattering coefficient for each medium} \end{aligned} \tag{A.16}$$

The detector wide probability of a photon reflecting off the AV and hitting a PMT is then

$$\rho_{av} = \sum_{\text{All PMTs}} \rho_i^{av} \tag{A.17}$$

As with the scattering calculation, the number of hits from reflections off the AV acrylic is determined using a photon bomb. For events in the D_2O and H_2O photons can reflect off the first AV boundary or transmit through the first boundary and reflect off the second AV boundary. These reflections off the first and second boundaries are handled in two independent photon bombs. For events that reconstruct inside the AV, only a single photon bomb is thrown accounting for reflections off either AV

surface.

For each photon in the bomb, a normalization term, N_a is found such that the probability of *not* being either scattered or absorbed is unity as seen below,

$$N_a e^{-(d_d(\mu_d+\mu'_d)+d_a\mu_a+d_h(\mu_h+\mu'_h))} = 1 \tag{A.18}$$

where μ is the absorption factor and μ' is the scattering coefficient and d are the distances through each media to the AV boundary. Since the angle of incidence at the AV and the amount of acrylic the photon traverses is important to this calculation, path changes due to refraction are modeled, although a simplified model of the detector is used (AV thickness of 5.5 cm, no belly plates, no neck).

At the intersection of the photon trajectory and the AV, the Fresnel coefficient of reflection is found using the standard equations of specular reflection. Diffuse reflections off the AV surfaces are not accounted for in this model. The photon's reflected direction is also determined assuming simple specular reflections. Once reflected, the photon is propagated to the PSUP. Enroute to the PSUP, the photon is not allowed to be absorbed or scattered but the normalization term, N'_a needed to account for such losses is given by

$$N'_a e^{-(d'_d(\mu_d+\mu'_d)+d'_a\mu_a+d'_h(\mu_h+\mu'_h))} = 1 \tag{A.19}$$

At the PSUP, the SNOMAN geometry code is used to determine if the photon strikes a PMT. The PMT responses used for this calculation were derived using laserball calibration data and normalized to agree with the 3d-PMT model's overall efficiency (See Section A.1).

Second order AV reflections, such as AV reflections followed by a Rayleigh scatter

or PMT reflection are negligible and not included in this model.

A.3 PMT Reflected Light Calculation

For reflections off the PMTs, a photon must reach the i^{th} PMT, not produce a hit, reflect off the PMT or concentrator at some angle and be detected by the j^{th} PMT. If the photon reflects off the PMT bucket (PMT and concentrator), there are many possible reflection angles with varying probabilities that that photon can reflect into. Therefore to calculate the number of reflected hits off the PMTs, we must calculate the probability that a photon reaches the bucket and then integrate over all possible reflected angles. The following equation details this calculation

$$\rho_i^{pmt} = \lambda_{\text{Norm}} \int_{\lambda_1}^{\lambda_2} \frac{d\lambda}{\lambda^2} \int_0^{\pi} d\theta' P_1 \times P_2 \times P_3 \times P_1^P \times P_2^P \times P_3^P \tag{A.20}$$

where where P_1 through P_3 are defined in A.1 and all other probabilities are listed below

$$\begin{aligned} P_1^P &= \text{R}_{\text{refl}}(\theta, \theta', \lambda)\frac{\Omega_0}{2\pi} \qquad (A.21) \\ &= \text{Probability that the photon reaches the PMT where } \tfrac{\Omega_0}{2\pi} \\ &\quad \text{is the solid angle of the tube, does } \textit{not} \text{ produce a hit} \\ &\quad \text{in the PMT but reflects with an outgoing angle } \theta' \\ &\quad \text{where } \text{R}_{\text{refl}}(\theta, \theta', \lambda) \text{ is the probability of not firing the tube and} \\ &\quad \text{reflecting given the photon's angle of incidence, } \theta \text{ and} \\ &\quad \text{wavelength, } \lambda \text{ with } \theta \text{ and } \theta' \text{ are with respect} \\ &\quad \text{to the PMT's normal direction} \end{aligned}$$

$$P_2^P = e^{-(d'_d\mu_d + d'_a\mu_a + d'_h\mu_h)} \tag{A.22}$$

$=$ Probability of the reflected photon not being absorbed enroute to the PMT where d' is the distance through each media from the reflection PMT to the PMT and μ is the absorption factor

$$P_3^P = R_{\rm pmt}(\theta'', \lambda)\frac{\Omega_0}{2\pi} \tag{A.23}$$

$=$ Probability that the photon reaches the PMT and is detected

$\frac{\Omega_0}{2\pi}$ is the solid angle of the tube

$R_{\rm pmt}(\theta'', \lambda)$ is the PMT angular and wavelength response

θ'' is the photon's angle with respect to the PMT normal

The detector wide probability of reflecting off a PMT and firing another PMT is

$$\rho_{pmt} = \sum_{\text{All PMTs}} \rho_i^{pmt} \tag{A.24}$$

This calculation can be greatly simplified by capitalizing on the spherical symmetry of SNO. In a coordinate system where the origin is located at the center on the i^{th} PMT and the positive z-axis is the PMT's normal vector to SNO's center, the detector, neglecting the neck, is rotationally invariant. In other words, if one were to sit on the i^{th} PMT and survey the SNO volume, the detector would look exactly the same as if one were to sit on the j^{th} PMT, the two PMTs differing only by an arbitrary rotation.

The integration in Equation A.20 can be factored into two parts,

$$\rho_i^{pmt} = \lambda_{\rm Norm} \int_{\lambda_1}^{\lambda_2} \frac{d\lambda}{\lambda^2} P_1 \times P_2 \times P_1 \times P_{\rm refl}(\theta, \lambda) \tag{A.25}$$

where

$$P_{\rm refl}(\theta, \lambda) = \int_0^{\pi} d\theta' P_1^P \times P_2^P \times P_3^P \tag{A.26}$$

$P_{\rm refl}(\theta, \lambda)$ is independent of electron position and direction, and therefore needs only to be calculated once in the initialization of the fitter. Furthermore, if $P_{\rm refl}(\theta, \lambda)$ is calculated for the i^{th} PMT through rotational symmetry the calculation is the same for the j^{th} PMT. P_1, P_2 and P_3 differ from the direct light calculation (Equations A.2-A.5) only by the $R_{\rm pmt}(\theta', \lambda)$ term allowing the PMT reflection calculation to essentially piggy-back on the direct light calculation adding negligible CPU time to the fitter.

Calculating $P_{\rm refl}(\theta, \lambda)$ can be done with a numerical integration of Equation A.26 but there are several advantages to using a photon bomb as was done with the scattering and AV reflection calculations. First, the calculation of the solid angle, Ω_0, shown in Equation A.10 is an approximation, which is valid when the photon is created relatively far away from the tube (i.e. created in the heavy water). When the solid angle is large from the perspective of the photon, this approximation breaks down. Additionally for angles of incidence larger than 60° it is not possible to fire the tube because it is shadowed by the concentrator. This is known as the concentrator's cutoff angle. In using a photon bomb, no approximation of the solid angle is needed and since the PSUP structure is handled by the SNOMAN geometry code the concentrator cutoff is correctly modeled. Second, the numerical integration would be done from a single tube and symmetry applied to translate the integration value to all other tubes. With the bomb technique photons can be thrown from all tubes to

gain a weighted average of detector asymmetries such as offline tubes and the neck.

For the photon bomb calculation of $P_{\text{refl}}(\theta, \lambda)$, photons are thrown from the face of a given PMT, where the PMT is chosen randomly for each photon in the bomb. The direction of the thrown photon is isotropic within a range of $0 < \cos\theta < 1$ (θ is with respect to the normal vector of the PMT). To account for losses due to absorption, a normalization term, N_a is defined as

$$N_a e^{-(d_d\mu_d + d_a\mu_a + d_h\mu_h)} = 1 \tag{A.27}$$

where μ is the absorption factor and d are the distances through each medium from the photon generation to the PSUP. Refraction through the AV and total internal reflection are modeled. If the photon totally internally reflects more than once, the photon is considered lost. Losses due to Rayleigh scattering after striking a PMT are not included.

Once the photon has reached the PSUP, the SNOMAN geometry code is employed to determine if the photon hits the PMT bucket. The probability it fires the tube is taken from the laserball calibrations of the PMT response. A scaling factor has been applied to account for normalization differences between the 3d-PMT model and the laserball values (see Section A.1).

For a given angle of incidence (θ) and wavelength (λ), the integrated reflection probability term is

$$P_{\text{refl}}(\theta, \lambda) = \frac{1}{N_\gamma} \sum_{N_\gamma} \frac{R_{\text{pmt}}(\theta', \lambda) R_{\text{refl}}(\theta, \theta', \lambda)}{N_a} \tag{A.28}$$

where N_γ is the number of photons in the bomb, $R_{\text{pmt}}(\theta', \lambda)$ is the PMT angular and wavelength response, N_a is the absorption normalization term and $R_{\text{refl}}(\theta, \theta', \lambda)$

is the probability of reflecting into angle θ'. $R_{\text{refl}}(\theta, \theta', \lambda)$ was calculated using an extremely high statistics photon bomb MC with SNOMAN's 3-D PMT model of the PMT. In this MC, photons were created in a shell of radius 820 to 825 cm and given a direction that was radially outward ($\vec{u} \cdot \vec{r} > 0$). Generating photons in this manner is conceptually equivalent to a gigantic 825 cm radius laserball. The reasoning behind only allowing the photons to travel outward is to reduce losses from attenuation or changes in direction from refraction through the AV. If a photon strikes a PMT bucket, its coordinate system is rotated so that the positive z-axis is the PMT's normal vector and the positive x-axis is defined such that the incoming photon's ϕ angle is zero. For every photon that strikes the bucket, the directional coordinates (θ', ϕ') of the outgoing reflected photon, if any, is calculated using the same reference frame as defined above.

The probability that a photon reflects into angle θ' and ϕ' given the angle of incidence θ and wavelength λ is simply

$$P(\theta, \lambda, \theta', \phi') = \frac{N(\theta, \lambda, \theta', \phi')}{N(\theta, \lambda)} \tag{A.29}$$

where $N(\theta, \lambda, \theta', \phi')$ is the number of photons that reflect given the incident photon's direction, wavelength and outgoing photon's direction and $N(\theta, \lambda)$ is the number of photons that strike the bucket with a given incident direction and wavelength. Using a fine binning of 1° for the incoming and outgoing angles requires storage of roughly 100 million words. For reasons of practicality, several approximations are made to reduce the size of the table. First, the outgoing ϕ' direction is roughly uniform from 0 to π for a given angle of incidence. Figures A.5 and A.6 show the reflection probability for the outgoing angles, θ' and ϕ' at two different incoming angles. Clearly, in Figure A.5

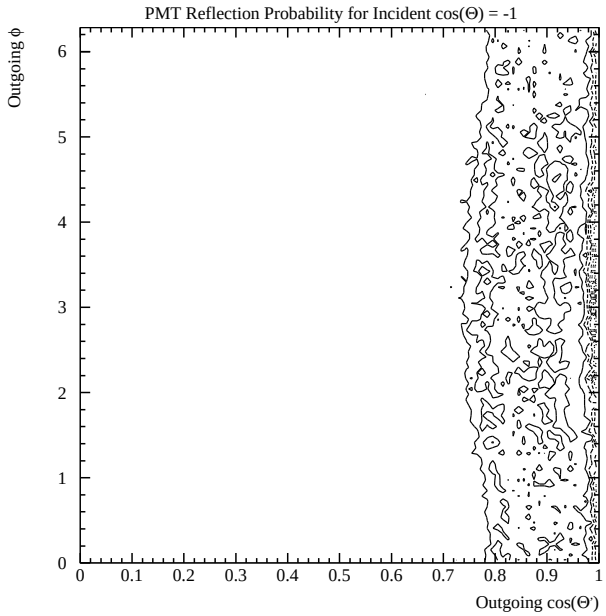

Fig. A.5: Reflection probability as a function of outgoing angle given an angle of incidence of $\cos\theta = -1.0$

there is no obvious structure in the ϕ' direction. For angles of incidence near the concentrator cut off, the outgoing ϕ' angle takes on very discrete values, as seen in Figure A.6. The discreteness the outgoing ϕ' direction is the result of the nature of the reflections at large angle of incidences off the concentrators, as can be seen in photographs in Appendix B of [87]. Photons that strike the tube with angles near the concentrator cut off have a small probability of firing the tube. For practicality we assume the reflected photon is independent of the outgoing ϕ' angle, even at these large angle of incidences.

Another simplification is to break the term $R_{\text{refl}}(\theta, \theta', \lambda)$ into two terms as seen below

$$R_{\text{refl}}(\theta, \theta', \lambda) \equiv R_1(\theta, \lambda) \times R_2(\theta, \theta') \tag{A.30}$$

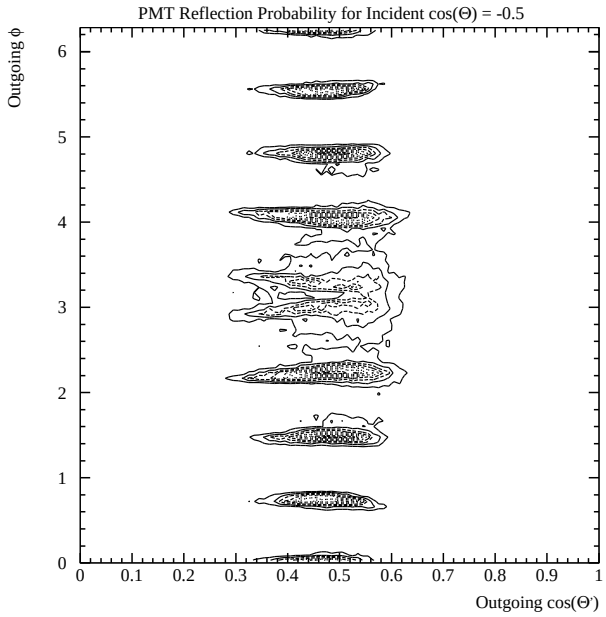

Fig. A.6: Reflection probability as a function of outgoing angle given an angle of incidence of $\cos\theta = -0.5$

This separation is possible only if θ' is not dependent on wavelength, which for our purposes is essentially true[4]. The $R_1(\theta, \lambda)$ reflection probability[5] is shown in Figure A.7.

$R_{\text{refl}}(\theta, \theta', \lambda)$ as determined from MC photon bombs is accurate up to an arbitrary normalization factor [88]. To calculate the normalization factor, the ratio of the number of PMT reflected hits predicted by FTK is compared to the MC's number of hits using mono-energetic electron MC in radial bins of 25 cm in the D_2O volume. To eliminate reconstruction biases, the MC generated electron position and direction was used for FTK. As expected, the normalization scaling factor is independent of

[4]The values of $R_2(\theta, \theta')$ are calculated for 100 $\cos\theta$ and $\cos\theta'$ bins and stored in the DFTK 2 titles bank

[5]The values of $R_1(\theta, \lambda)$ are calculated for 100 $\cos\theta$ bins and 50 bins of λ, ranging from 220 nm to 710 nm in 10 nm steps and are stored in the DFTK 1 bank

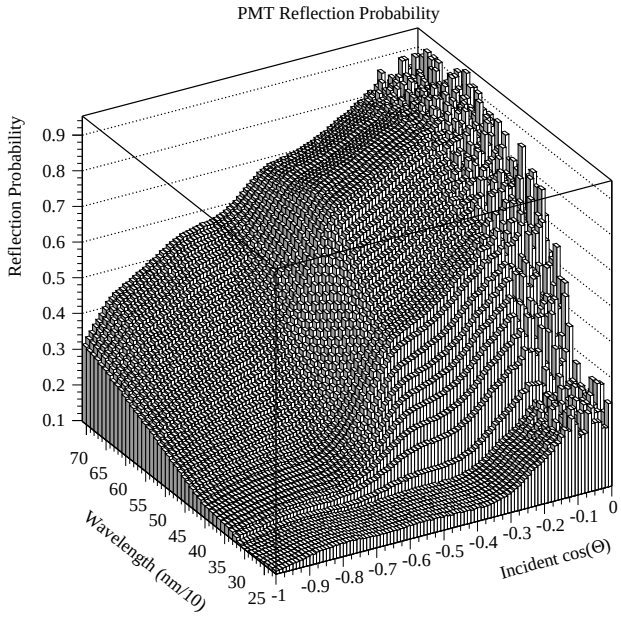

Fig. A.7: Reflection probability, $R_1(\theta, \lambda)$ as a function of incoming angle, θ and wavelength λ

electron position, direction, energy or Julian day[6].

A.4 Optimizing FTK's Timing Window and the Noise Rate Calculation

In theory, there is nothing preventing FTK's timing window being as wide as the trigger window but there are two drawbacks to using a window of this size. First, this window includes noise hits and since noise hits add no information about the energy of an event and only worsen the energy resolution, we want to reduce the amount of noise in the timing window. Second, FTK does not model the number of photons that reflect off two PMTs and reducing the timing window removes many

[6]The correction factor is stored in the TFTK bank word TFTK_PMT_REFL_NORM

such hits. To optimize the timing window, the number of modeled hits (namely PMT reflections and Rayleigh scattering) that fall outside the timing window must be small (modeled hit loss) and the number of double PMT reflections that are not modeled that fall inside the window must be small and constant with radius (not-modeled hit inclusion). The maximum path length for a photon modeled by FTK is a photon from an event vertex at the PSUP, which travels through the detector's center, reflects at 180° off a PMT and returns. The time needed to travel along this path is 135 ns. Figures A.8-A.10 plot the modeled hit loss and not-modeled hit inclusion for three timing windows, -25 to 100 ns, -25 to 150 ns and -25 to 200 ns respectively. For the timing window of -25 to 100 ns the loss of modeled PMT reflections is roughly 0.25% of the total number of hits and has a radial dependence of roughly 0.3%. For the -25 to 150 ns timing window, the modeled hit loss is negligible and the not-modeled hit inclusion although roughly 0.5% is flat as a function of radius within 0.15%. Lastly, the widest timing window of -25 to 200 ns also has negligible modeled hit loss as well as a small amount of not-modeled hit inclusion that is flat as a function of radius. This window, of course does include the most noise hits. Since the modeled hit loss and not-modeled hit inclusion is tolerable and covers the range of the maximum path length, the timing window of -25 to 150 ns is chosen. The optimal FTK timing window with RSP's prompt timing window is shown in Figure A.11.

The number of noise hits in an event is determined from the PMT noise rate, measured using PGT with the ANXX cuts applied[7]. The mean number of noise hits in an event is given by

$$n_{exp}^{noise} = R_{pmt}\Delta T N_{online} \tag{A.31}$$

[7]Noise rate is loaded from KRLPN_PMT_QC

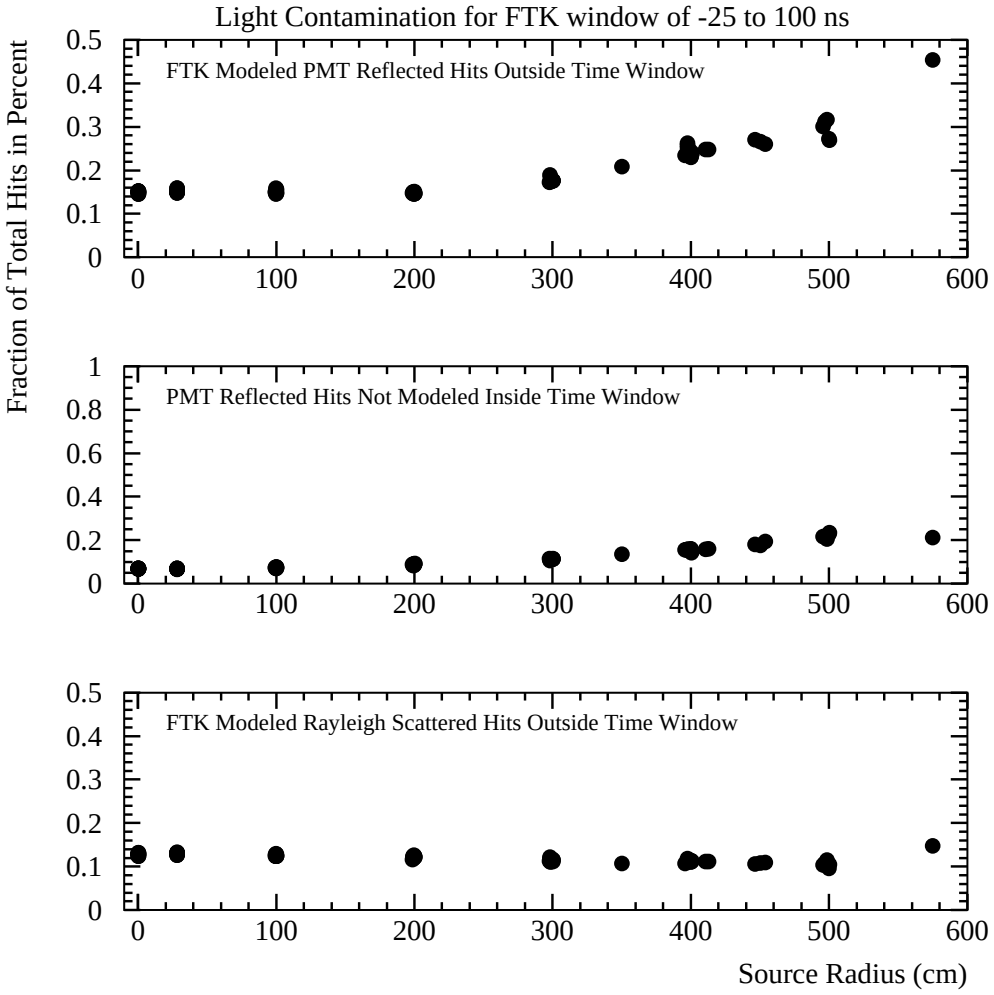

Fig. A.8: Measurement of the modeled hit loss removed by FTK's timing window (Top plot: PMT reflections, Bottom plot: Rayleigh Scattering) and not-modeled hit inclusion (Middle plot: Multiple PMT reflections) using ^{16}N MC as a function of source radius. The timing window is -25 to 100 ns.

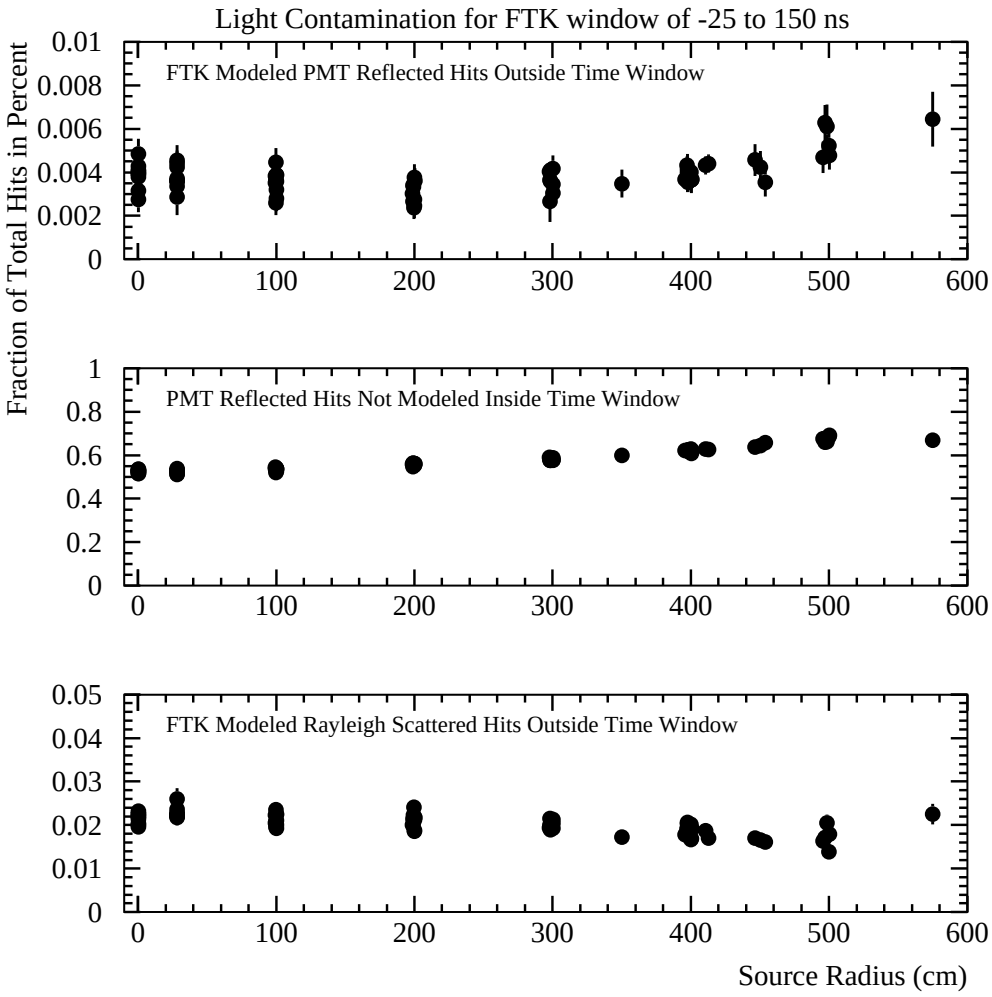

Fig. A.9: Measurement of the modeled hit loss removed by FTK's timing window (Top plot: PMT reflections, Bottom plot: Rayleigh Scattering) and not-modeled hit inclusion (Middle plot: Multiple PMT reflections) using ^{16}N MC as a function of source radius. The timing window is -25 to 150 ns.

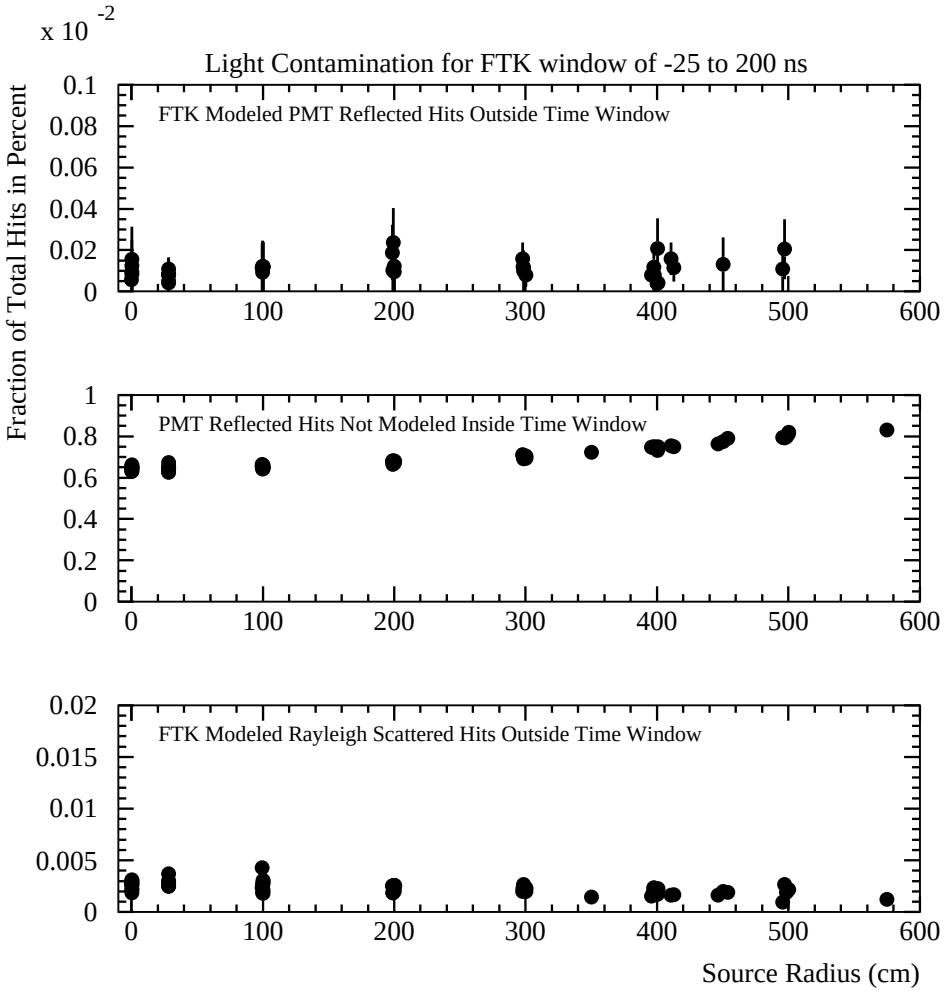

Fig. A.10: Measurement of the modeled hit loss removed by FTK's timing window (Top plot: PMT reflections, Bottom plot: Rayleigh Scattering) and not-modeled hit inclusion (Middle plot: Multiple PMT reflections) using ^{16}N MC as a function of source radius. The timing window is -25 to 200 ns.

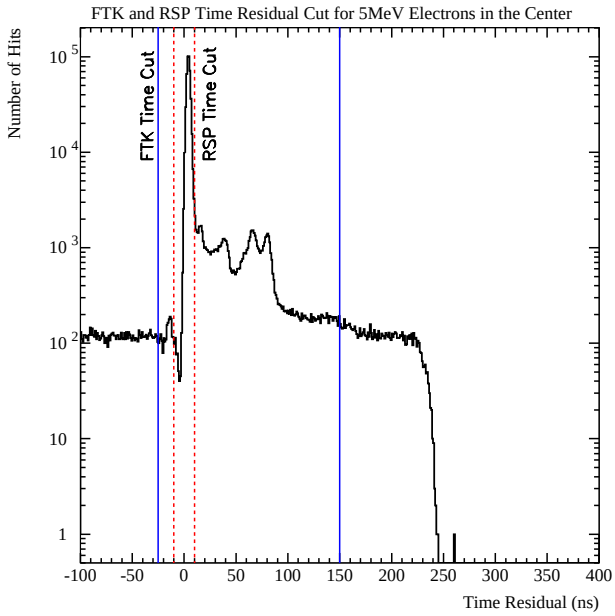

Fig. A.11: PMT time residuals for 5MeV mono-energetic electron MC. The FTK timing cut of $-25 < t < 150$ns and the RSP prompt timing cut ($-10 < t < 10$ns) are also shown.

where R_{pmt} is the PMT noise rate in Hz, ΔT is the length of the event timing window in seconds and N_{online} is the number of tubes online.

A.5 Optimizing the Scattering and AV Reflection Calculations

In the photon bomb technique used to calculate the number of scattered and AV reflected hits, throwing more photons gives a better estimate of the scattering and AV reflection probabilities (Equations 5.25 and A.17) at the expense of CPU time. As demonstrated in Figure A.12, the distribution of probabilities is significantly broadened with smaller photon statistics.

To optimize the number of photons necessary in the scattering and AV reflection bombs, we define the criteria that the number of photons in a bomb can not affect the energy resolution for 5 MeV electrons by more than 0.1%. To calculate this, 5 MeV electrons isotropically distributed in the D_2O were generated with different photon statistics in the scattering and AV reflection bombs. The photon statistics for the scattering and AV reflection bombs were varied separately, but the first and second boundary AV bombs always had the same statistics. The energy resolution for each bomb trial was determined using a simple Gaussian fit.

As seen in Figure A.13, the energy resolution is rather insensitive to the number of photons in the bomb calculations. This is not wholly surprising as the number of Rayleigh scattered and AV reflected hits account for a small fraction of the total light in an event. Fitting the energy resolution as a function of photon statistics to a functional form, the resolution is broadened by 0.1% with 250 and 90 photons for the scattering and AV reflection bombs, respectively. Taking a conservative approach, the bomb statistics is 1000 photons for the scattering calculation and 500 photons for the AV reflection calculation. The PMT reflection calculation also uses a photon bomb, but since this calculation is run only once during initialization 20,000 photons for each wavelength is thrown.

A.5.1 Late Light Time Residual Maximum Likelihood Fit

To tune the amount of late light in the MC, a maximum likelihood fit is used to fit the time residual distribution of ^{16}N data and MC. Section 5.5.1 gives an overview of tuning the late light in the MC, whereas this section discusses the details of the fit.

To determine the PMT reflectivity scale factor, N_p from Equation 5.55, nine time

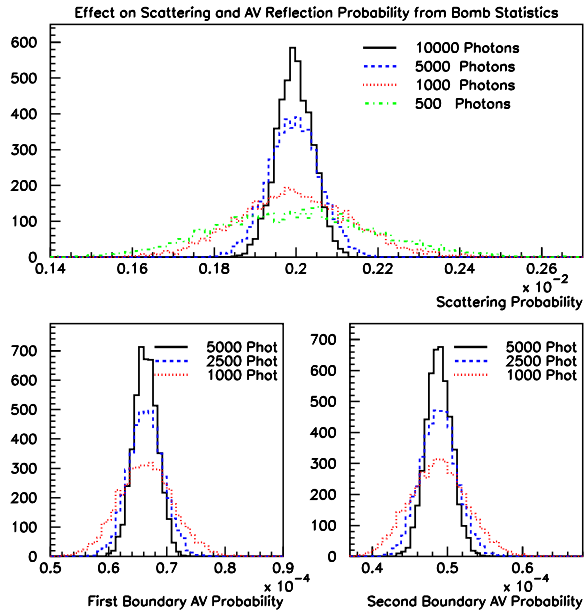

Fig. A.12: MC measured scattering and AV reflection hit probabilities for 5 MeV electrons in the center using different number of photons in the bomb calculation. The top figure is the scattering probability, the bottom figures are the AV reflection probabilities off the first and section AV boundary.

residual PDFs built from ^{16}N MC is fit to ^{16}N data using a maximum likelihood technique. The MC PDFs, representing all possible paths of light in the detector are a direct light PDF (P_d), Rayleigh scattered light PDF (P_r), AV reflected light PDF (P_a), 4 PMT reflected light PDFs (zero (P_{r0}), one (P_{r1}), two (P_{r2}), and three or more (P_{r3}) reflections from the concentrator), other reflected light PDF (P_o) and a noise PDF (P_n). In the most general form of the fit, there are four free parameters, a collection efficiency (N_c), Rayleigh scattering normalization (N_r), AV reflection normalization (N_a) and PMT reflection normalization (N_p). With the exception of the noise PDF, all PDFs are scaled by the collection efficiency factor. The scattered light PDF is scaled by N_r with an additional constraint added such that the total area between the direct light PDF and the Rayleigh scattering PDF is conserved.

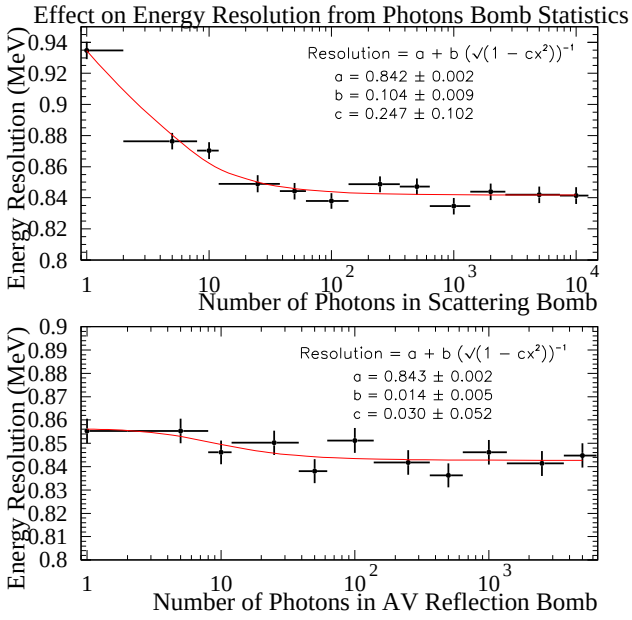

Fig. A.13: Energy resolution of 5 MeV electrons distributed isotropically in the D_2O for different photon statistics in the scattering and AV bombs.

This area conservation is necessary since increasing the Rayleigh scattering decreases the number of direct photons. Similarly, the AV reflected light PDF is scaled by N_a with the same constraint that the sum of the areas of the direct light PDF and this PDF must remain constant. The sum of the MC PDFs can be expressed as

$$\begin{aligned} P_t(N_c, N_r, N_a, N_p) &= N_c A_c P_d + N_c N_r P_r + N_c N_a P_a + \\ & N_c \sum_{\theta} (s(\theta, N_p) P_{r1}(\theta) + s(\theta, N_p)^2 P_{r2}(\theta) + s(\theta, N_p)^3 P_{r3}(\theta)) + \\ & N_c (P_o + P_{r0}) + P_n \end{aligned}$$

where θ is the angle of incidence of the photon with respect to the PMT normal,

$s(\theta, N_p)$ is the concentrator reflectivity scale factor defined in Equation 5.57, and A_c is a conservation term. A_c is defined so that the total area in the direct light, Rayleigh scattered light and AV reflected light PDFs is constant and is given by

$$A_c = 1 + \frac{(1 - N_r)A_r}{A_d} + \frac{(1 - N_a)A_a}{A_d} \tag{A.32}$$

A_d, A_r and A_a are the areas of the direct light, Rayleigh scattered light and AV reflected light PDFs respectively.

In practice it is not possible to fit for N_a. The AV reflected light significantly overlaps with the 35° PMT reflected peak. Since the 35° PMT reflection peak in the MC is shifted late in time with respect to the data (see Figure 5.18), the AV reflections are made unnaturally large in the likelihood fit in order to compensate for this difference in the time residual shape. To ensure that the AV reflections are not too wrong, they can be disentangled from the 35° reflection using the time residual distribution of hits in the opposite direction from the electron direction as seen in Figure A.14. In this region, only the 180° reflections and AV reflections are significant. The AV reflections (peaked around 45 ns) are in good agreement between ^{16}N data and MC.

To reduce the likelihood fit's sensitivity to differences in the time residual shape between data and MC, the fit is done with only two time residual bins, the direct window defined from -25 to 50 ns and the late window defined from 50 to 100 ns. For further simplicity the Rayleigh scattering normalization is also fixed. Doing a global fit with ^{16}N runs inside 250 cm where the separation between the PMT reflections and the direct light is the greatest, the PMT reflection normalization, N_p is 1.083 for the D_2O phase. In the salt phase, the concentrator reflectivity and the PMT angular

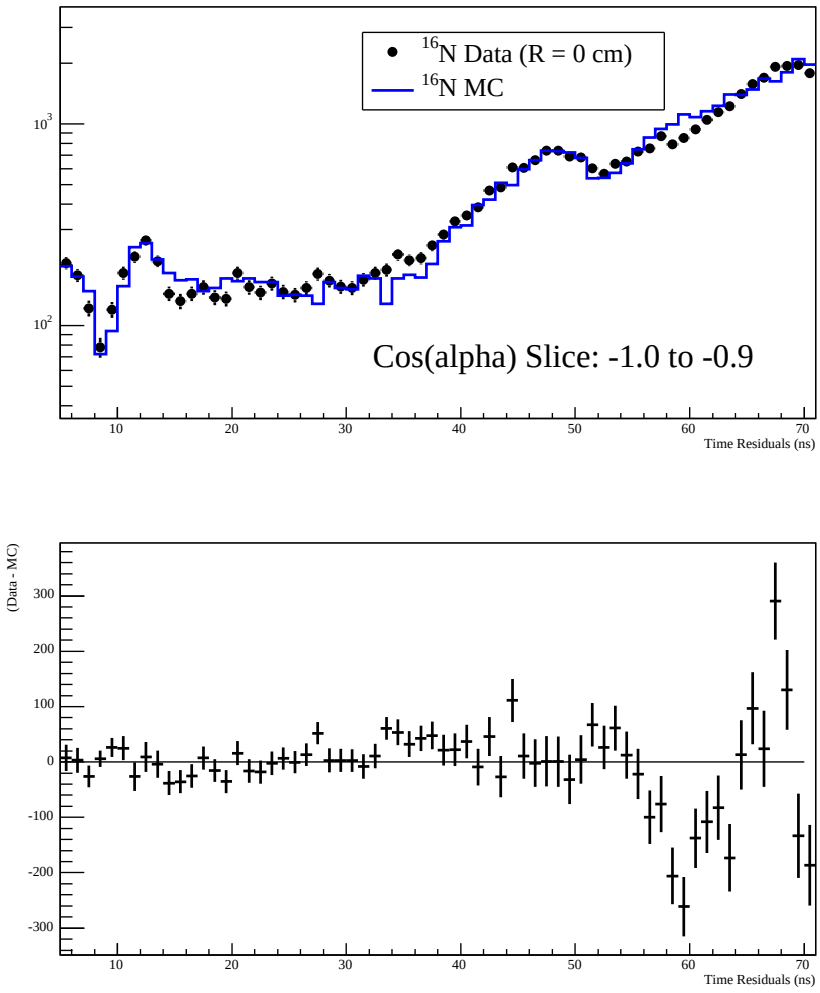

Fig. A.14: Top Figure: Time residual distribution for ^{16}N data and MC at the center with $-1.0 < \cos\alpha < -0.9$ for each hit PMT where α is the angle between the photon direction and the reconstructed electron direction. Bottom Figure: Difference between data and MC. For both data and MC, only events with a reconstructed position $>$ 50cm from the source and the angle between the reconstructed direction and the direction from the source to the reconstructed position is less 25° than are selected.

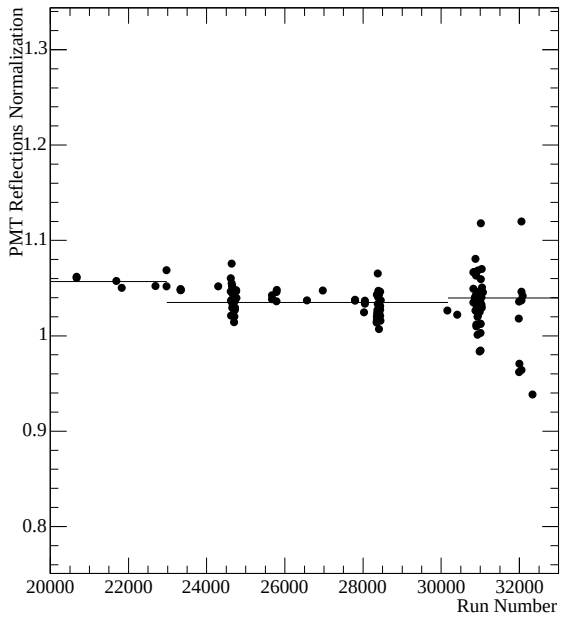

Fig. A.15: N_p for ^{16}N runs in the salt phase as a function of run number. The volume weighted fit result for each time period is indicated by the solid lines.

response as measured using the laserball changed slightly over time. To best model the concentrator reflectivity over the entire salt phase, the fit for N_p was done in three different time periods corresponding to the laserball measurements that showed changes in the angular response. The extracted values of N_p for each of these time periods is shown in Figure A.15.

A.6 Finding a Common Collection Efficiency for FTK and RSP

After successfully tuning the late light in the MC (see Section 5.5), the collection efficiency determined using FTK's timing window and RSP's timing window differs by approximately 0.4%. This remaining difference is due to mis-modeling of the PMT

transit timing distribution in the MC. As indicated in Figure A.16, the number of PMT hits in the first and second late pulses is larger in the ^{16}N data compared to the MC. The first and second late pulses are features of the PMTs but are still hits detecting direct photons. Since RSP's prompt time window cuts the late pulse hits, there is a resulting efficiency factor in RSP which FTK is insensitive to by including all direct hits. To determine this prompt window efficiency factor, a sample of direct hits, free from contamination from PMT reflections (which are also mis-modeled in the MC) is obtained by requiring that a PMT hit must be in the Cherenkov cone ($0.7 < \cos\alpha < 0.8$ where α is the angle between the photon direction and the reconstructed electron direction). To select well reconstructed events, it is also required that the reconstructed γ position is more than 50 cm from the source and the angle between the directional vector from the source position to the reconstructed position and the reconstructed electron direction are collinear within 20°. Applying these selection criteria, the agreement in the PMT timing distribution between data and MC is quite impressive but the late pulses are still underestimated in the MC (Figure A.17).

With the above cuts applied, the prompt window efficiency factor is estimated from the difference between data and MC in the ratio of the prompt peak area (-10 to 10 ns) and the late pulse area (10 to 45 ns). This difference is scaled by the prompt to late ratio of all hits to find the final efficiency factor as expressed below,

$$F_{NWin} = \frac{R'_d - R'_m}{R'_d} R_d \tag{A.33}$$

where F_{NWin} is the prompt window efficiency factor, R'_d is the prompt peak to late pulse ratio with the $\cos\alpha$ cut applied for ^{16}N data, R'_m is the same ratio for ^{16}N

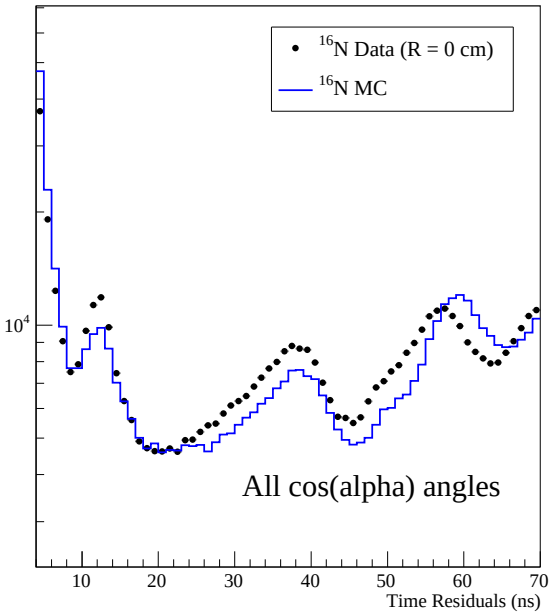

Fig. A.16: Time residual distribution for ^{16}N data and MC at the center, focusing on the late pulse region.

MC and R_d is the prompt peak to late pulse ratio including all hits for ^{16}N data. The prompt window efficiency factor for the three different $\cos\alpha$ slices as plotted in Figure A.18 is consistent for all three slices and approximately 0.4%. To achieve a common RSP and FTK collection efficiency, F_{NWin} is applied to the number of hits in RSP's timing window in the MC only.

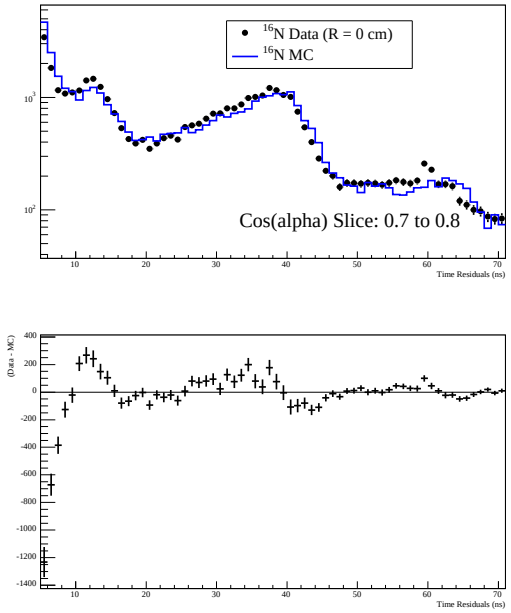

Fig. A.17: Top Figure: Time residual distribution for ^{16}N data and MC at the center with $0.7 < \cos\alpha < 0.8$ for each hit PMT. AV and PMT reflections are largely eliminated by this cut. Bottom Figure: Difference between data and MC.

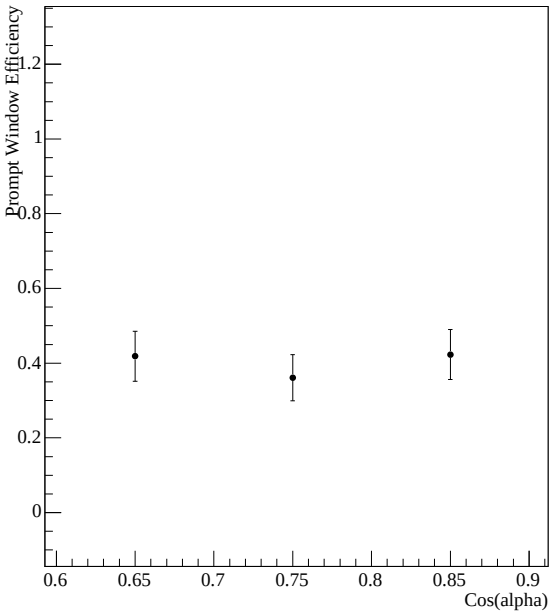

Fig. A.18: Prompt window efficiency factor for the three direct light $\cos\alpha$ bins.

Appendix B

Summary of the DAMN Cuts and Run Selection Criteria

The following appendix summarizes the DAMN cuts used to remove instrumental events in the detector (see Chapter 7), including a detailed discussion of the AMB DAMN cut. A brief overview of the run selection criteria is given here as well.

B.1 The DAMN Cuts

- **Burst Cuts**
  - **Retrigger:** Tags events that are within 5 microseconds of a previous event. This is designed to tag events following large events such as muon events where large amounts of Cherenkov light can be produced, causing multiple triggers. This tag has the negative side effect of tagging some Michel electrons from muon decays.

- N_{Hit} **Burst:** If six events with an N_{Hit} greater than 40 occur within a time window of four seconds, all events in that dead time are tagged. Used to tag flat TAC events which generally occur in bursts.

- **Charge Based Cuts**

  - **AMB:** Tags events that have an ESumHi integral and/or peak value that is more than 3.7 sigma away from the mean. See Section B.2 for more detail. Events with large integral and peak values tend to be flashers, while events with low integral and peak values tend to be electrical pick-up events.

  - **ESum:** Tags events with only the ESumHi and ESumLo trigger bits are set. Events triggering only the ESum trigger have high charge but a small number of hits, which is a signature of flasher events.

  - **QCluster:** Tags events with a high charge or negative railed (charge is larger than the dynamic range of the integrator) charge tube that has at least 3 or more tubes clustered nearby. Tags flasher events which have a high charge tube surrounded by a cluster of cross talk tubes.

  - **QvT:** Tags events where the highest charge tube has a pedestal subtracted QHL (QLL) greater than 1000 (80) counts above the average QHL (QLL) of the event. Additionally the highest charge tube must be between 60 to 250ns before the median tube time in the event. Used to tag flasher events which have a high charge tube.

- **Q/N_{Hit} :** Tags events where the average total charge per number of hit tubes is less than 0.25 photo-electrons after the largest 10% of the charges are removed. Used to tag electrical pick-up events where the total charge is very small for the number of hits that have fired.

- **Geometry Based Cuts**

  - **Flasher Geometry Cut (FGC):** Tags events where the average position of a cluster of tubes is greater than 12m from the average tube position of the event. A cluster is defined as 4 out of 8 channels hit in electronics space or 4 tubes hit within 1m in detector space. Used to tag flashers by searching for a ring of light opposite a tight cluster of tubes.

  - **Crate Isotropy:** Tags events where more than 70% of tubes in the event were hit in a single crate and 80% of the channels hit in the crate occur on two adjacent cards. Used to tag electronic pick-up events which generally occur in a single crate. The PMTs connected to a single crate are arranged in strips in the PSUP so that light from Cherenkov events will illuminate tubes in more than one crate and not be tagged by this cut.

- **Junk Cuts**

  - **Junk:** Removes orphans (PMT hits that failed to be included in the proper event when written to disk) and events that contain the same PMT more than once. Used to remove events where the event information has been corrupted. These types of events contribute a very small fraction of all events. Orphaned tubes account for a miniscule fraction of hit PMTs

and are accounted for when the collection efficiency in the MC is tuned to match the ^{16}N data.

- **Muon Follower Cuts**
  - **Muon Follower Short:** Tags all events that occur within 20s of a muon. Used to remove spallation events produced as the muon passes through the detector.
  - **Missed Muon Follower Short:** Tags all events that occur within 250ms of an event with a $N_{\text{Hit}} \geq 150$. Used to cut spallation events produced by atmospheric neutrino interactions in the detector, where there is no muon tag associated with the event.
- **Timing Based Cuts**
  - **Fitterless Time Spread (FTS):** Tags events where the median time spread between two tubes that are less than 3m apart is greater than 6.8ns. Used to tag flasher events using hit geometry, independent of information about the flashing tube.
  - **In-Time Channel (ITC):** Tags events where 40% or greater of hit tubes are outside of a 93ns 'in-time' window. Used to tag flat TAC events where the times of the hits PMTs are uniform in time.
- **Veto Tube Cuts**
  - **Neck:** Tags events where both Neck tubes have fired or one neck tube has fired but has a high charge and is early in time. Used to veto downward going events that appear to originate in the neck.

– **Owl:** Tags events where three or more Owl and Butts[1] tubes fire. Used to veto muon events which produce light in the outer H_2O volume.

– **OwlEHi:** Tags events with an OwlEHi trigger. Used to veto muon events which have produced light in the outer H_2O volume.

B.2 The Analog Measurement Board

In addition to its distinct topology, a flasher event also has a distinctive ESumHi analog signal as most of the charge in the event comes from a single tube. In order to save information about the analog sum that could later be used to tag flasher events, the analog measurement board (AMB) was designed to calculate the derivative, integral and peak of the ESumHi raw signal (see Section 2.2). The peak and integral values of the ESumHi raw trigger sum have proved extremely useful in removing instrumental backgrounds. The derivate of the ESumHi signal is not used due to timing problems in the AMB (Section B.2.3).

B.2.1 Calibration of the AMB Cut

For flasher events, the integral and peak values are very large relative to the values expected for signal events with the same number of hits. In contrast, pick-up events tend to have a low overall charge but are high in $N_{\rm Hit}$, this results in a very small integral or peak to $N_{\rm Hit}$ ratio.

To design an effective AMB DAMN cut, the integral and peak electronic pedestal values must first be established. To accomplish this calibration, the integral and peak

[1]Berkeley Underwater Tube Testing (BUTT) tubes consists of 22 outward looking tubes in the light water that can be 'easily' removed and are used to test how tubes age in the SNO environment.

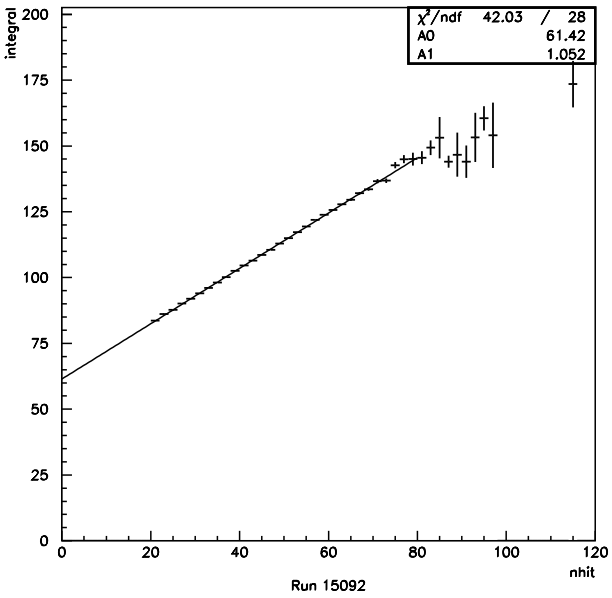

Fig. B.1: AMB integral value as a function of N_{Hit} for ^{16}N data. The fit line is extrapolated to zero to find the pedestal value.

values are determined as a function of N_{Hit} using data from the tagged ^{16}N source. Since the relationship between the integral (peak) value and N_{Hit} is linear, a straight line can be fit to the data and extrapolated to zero to find the pedestal value. An example of such a fit can be seen in Figures B.1 and B.2. Once the pedestal values are established, the ratio of the pedestal subtracted integral (peak) to N_{Hit} is constant as a function of N_{Hit}, with a RMS that goes as $\frac{1}{N_{\mathrm{Hit}}}$ (Figures B.3 and B.4).

Using ^{16}N to establish the 1σ RMS values as a function of N_{Hit}, AMB values which are more than 3.7σ from the pedestal value are tagged. The cut limits plotted with the ^{16}N data are shown in Figures B.3 and B.4. As seen in Figure B.5, the AMB cut is effective at removing flasher and pick-up events with minimal loss of non-instrumental events. The AMB cut eliminates $\sim$ 95% of flasher events while cutting only $\sim 0.2\%$ of ^{16}N data.

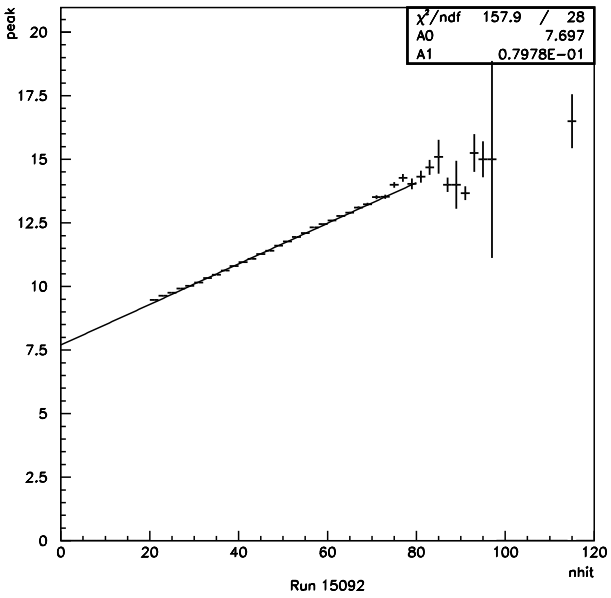

Fig. B.2: AMB peak value as a function of N_{Hit} for ^{16}N data. The fit line is extrapolated to zero to find the pedestal value.

As the AMB cut is based upon the integral and peak pedestal values, it is essential to measure the stability of these parameters over time. Measuring the pedestal values using ^{16}N data taken over the duration of the salt phase indicated that the integral pedestal was stable to 1.2%. The peak value was also stable except for a sudden jump in the pedestal value near the end of the salt phase (Table B.1). As the ^{16}N source is only taken once every few weeks, a daily measure of the time stability can be done with PGT data using events with $N_{\mathrm{Hit}} = 0$. PGT is a pulsed trigger which fires the detector every 5 Hz and is ideal for this measurement since it will trigger the detector even if no tubes have fired. Figure B.6 shows that the pedestal values for the integral and peak are stable over the D_2O phase, except for the large jump in the AMB peak value from 7.65 to 8.90 ADC counts on May 31, 2001. This change took place when there was loss of power to the timing rack where the AMB is housed and is attributed

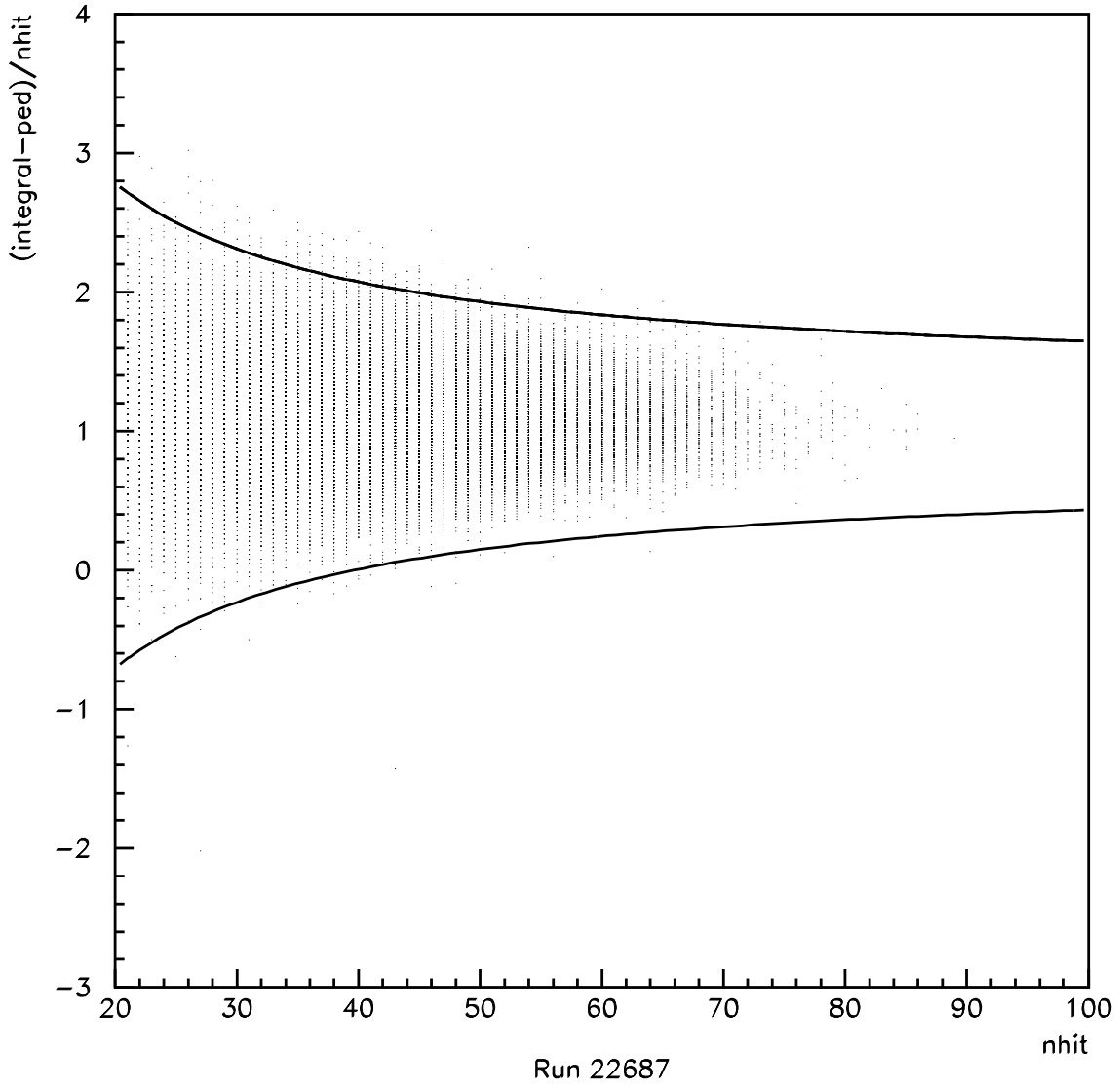

Fig. B.3: Pedestal subtracted Integral/$N_{\rm Hit}$ vs $N_{\rm Hit}$ for ^{16}N data. The lines shown are the $\pm 3.7\sigma$ cut values. Only 0.2% of ^{16}N data is removed by this cut.

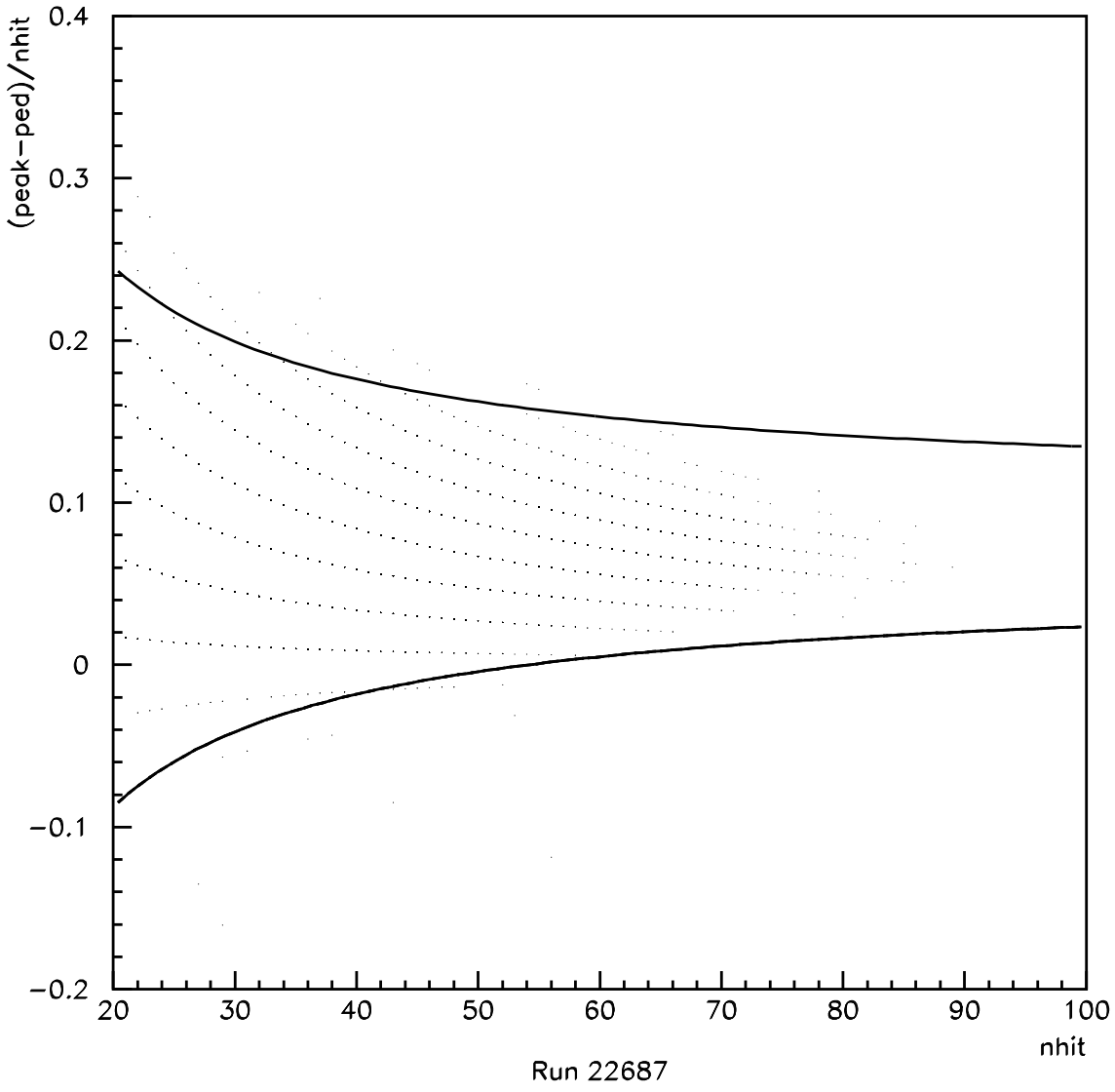

Fig. B.4: Pedestal subtracted Peak/$N_{\rm Hit}$ vs $N_{\rm Hit}$ for ^{16}N data. The lines shown are the $\pm 3.7\sigma$ cut values. Only 0.2% of ^{16}N data is removed by this cut.

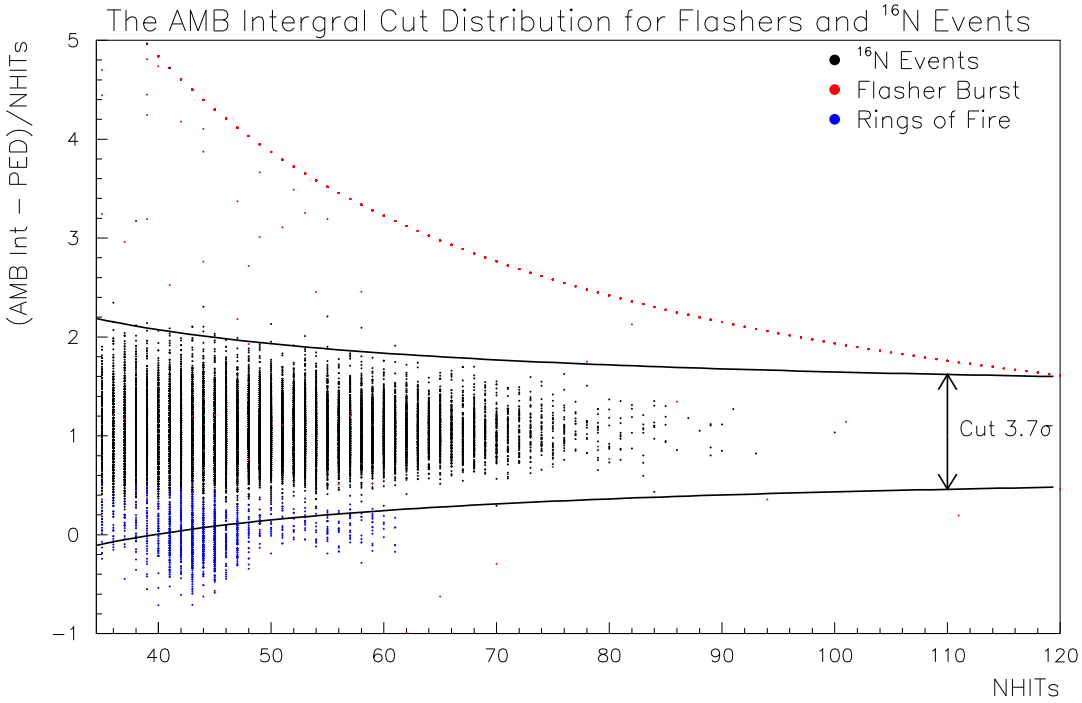

Fig. B.5: AMB integral value as a function of N_{Hit} for ^{16}N data, flashers and pick-up events (rings of fire). Taken from [75]

Category	Run Number	Integral Ped	Peak Ped	Comments
^{16}N	21690	62.14 ± 0.14	8.88 ± 0.01	Center, EXT3 masked in
^{16}N	22686	62.60 ± 0.15	8.90 ± 0.01	Center, EXT3 masked in
^{16}N	22687	62.60 ± 0.13	8.96 ± 0.01	Center
^{16}N	22693	62.50 ± 0.13	9.09 ± 0.01	z = 250
^{16}N	22695	62.63 ± 0.13	9.22 ± 0.01	z = 450
^{16}N	22698	62.60 ± 0.15	9.30 ± 0.01	z = -550
^{16}N	22974	62.17 ± 0.13	9.07 ± 0.01	In center

Table B.1: AMB pedestal values determined by ^{16}N runs in the salt phase.

to a change in the resistance of one of the AMB components. As the peak pedestal value continues to be stable after the jump, the AMB cut was re-calibrated after this date to account for the new pedestal value for the peak.

B.2.2 AMB Cut Acceptance After Large N_{Hit} Events

After events which deposit large amounts of charge, the ESumHi signal has a decay time to return to baseline, resulting in a smaller AMB cut acceptance on decay electrons following muon events [89]. For analyses involving time coincidences (such as anti-neutrino searches), measuring the duration of the ESumHi decay time is important. To measure the AMB cut acceptance after large N_{Hit} events, the laserball was deployed with a high light intensity so that the ESumHi signal was saturated. This laserball intensity covers muon energy depositions up to 2 GeV. The external ASYNC trigger (see Section 2.2) was delayed by different intervals after the laserball firing to measure the AMB integral, peak and derivative baselines[2]. As seen in Figure B.7,

[2]See July 22, 2002 shift report for more details on the laserball settings.

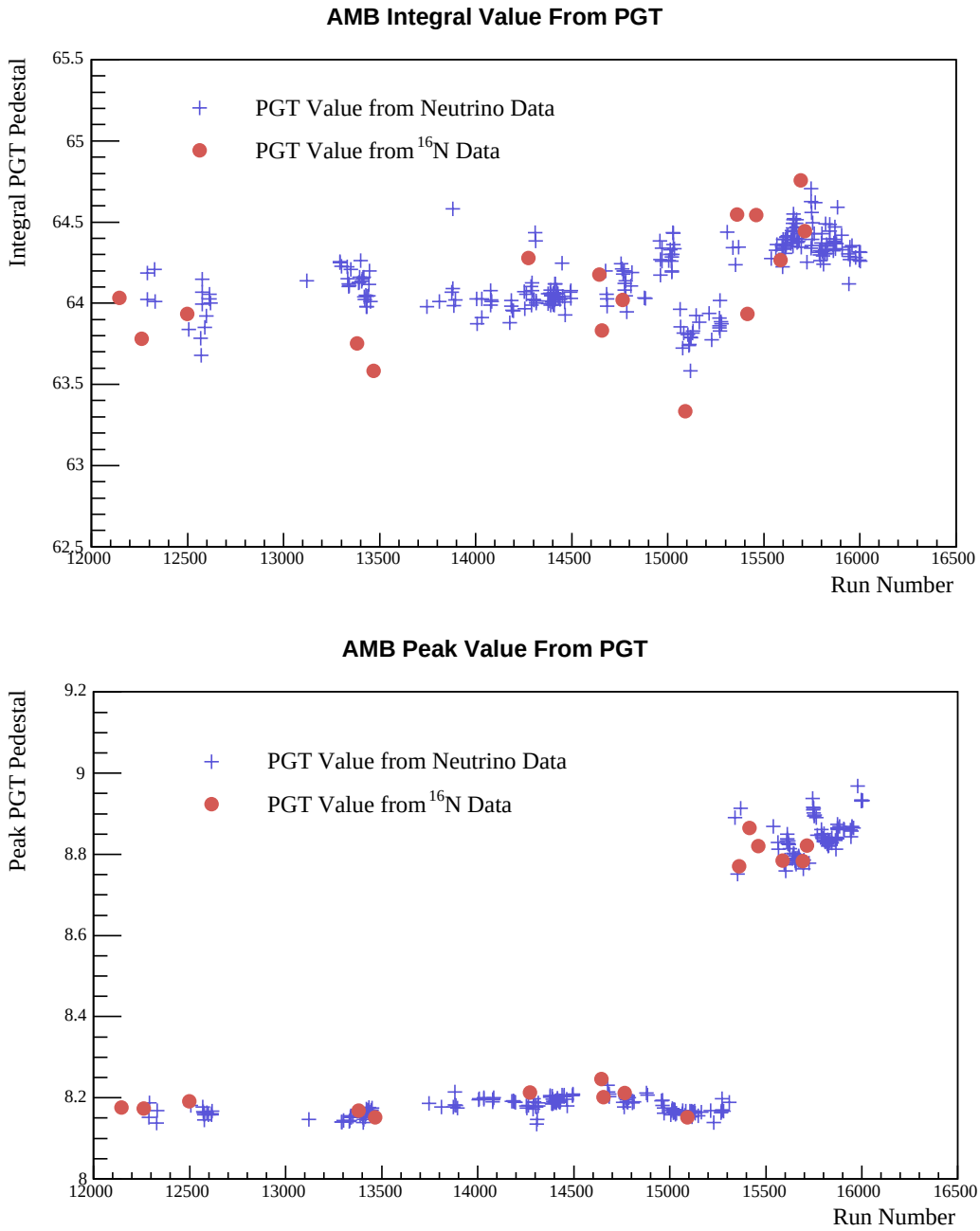

Fig. B.6: AMB integral (top figure) and peak (bottom figure) values for PGT events with an $N_{\mathrm{Hit}} = 0$.

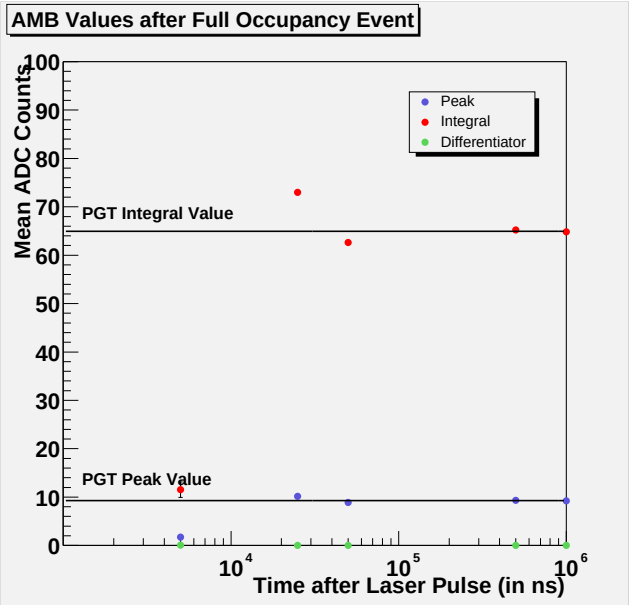

Fig. B.7: AMB integral, peak, and derivative values following a laserball event with very high intensity. Also shown are the AMB integral and peak pedestal values (solid lines).

the AMB returns to its baseline after $50\mu s$ or conservatively 0.5 ms. Note that the errors on the AMB values are shown but are too small to be seen.

B.2.3 The Differentiator

While the AMB integral and peak are effective at removing flasher and pick-up events, the derivative value is not used in the DAMN cut because the derivative values in the ^{16}N data tend to cluster in two groups when only one group is expected. This bimodal nature of the AMB derivate makes using it to tag flashers and pick-up impossible. For a long while, the cause of the bimodal distribution was thought to be a stuck bit in the derivative ADC, but a bit-by-bit investigation of the data showed this was not the problem.

Upon further investigation, the bimodal nature of the derivative was discovered to be the result of the board design. As discussed above, the digitization of the derivative is derived from the raw trigger and the timing of the digitization signal is set so that signal is digitized when the ESumHi pulse crossed the DAQ trigger threshold. If the raw trigger is produced from another MTC/A, other than the ESumHi, the relative timing between the rise of ESumHi analog signal and the raw trigger is shifted as can be seen in Figures B.8 and B.9. Specifically, if an event triggers both the ESumHi and N100, the N100 tends to trigger the detector earlier, therefore whether the event was triggered by the ESumHi or N100 affects where the derivative of the raw ESumHi is taken. The integral and peak are not sensitive to this timing difference since their values are taken over a 200 ns integration period. Fixing this timing issue would require a redesign of the board. Since the integral and peak have shown to be highly effective at removing instrumental events, the derivative will remain wasted information in the data stream.

B.2.4 Modification to the AMB

1. Pin 20 of U27 connected to TP41 (pin 7 of U23)
2. TP37 connected to TP42
3. Pin 2 of U23 lifted off pad
4. TP40 connected to Pin 2 of U23 with 100 ohm resistor
5. Pin 6 of U23 connected to Pin 2 of U23 with 100 ohm resistor
6. Run wire from TP43 (through TP33) to Pin 2 of U15

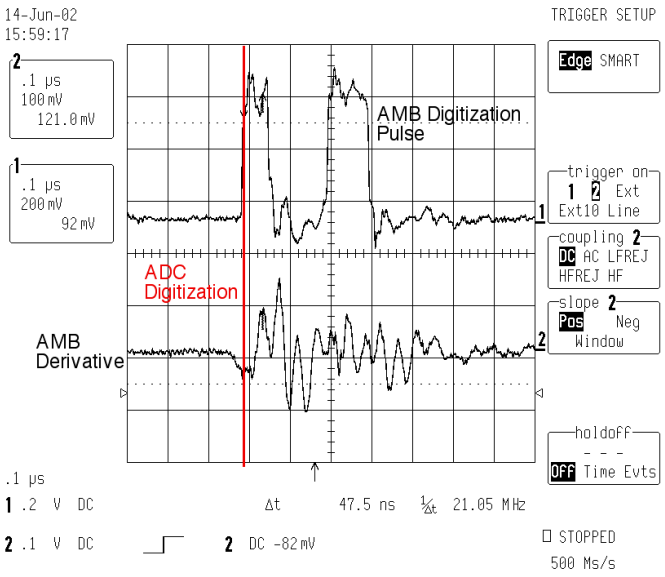

Fig. B.8: AMB derivative digitization with a N100 generated raw trigger. The top pulse is the digitization signal, the bottom pulse is the ESumHi derivative. The red line indicates the ADC digitization and it is arriving too early.

7. Run wire from Pin 10 of U27 (gnd pin) to TP34, wrap wire with above line

8. Pin 2 of U9 lifted off pad

9. Removed R8

10. Pin 3 of Q6 and Q10 lifted, connect to R57

11. Pin 3 of Q8 and Q11 lifted, connect to R59

12. Lift pins 14 and 17 of U5 off pad, connect together

13. Connect Pin 15 of U5 to R4

14. Connect TP9 to TP45

15. Connect TP8 to TP46

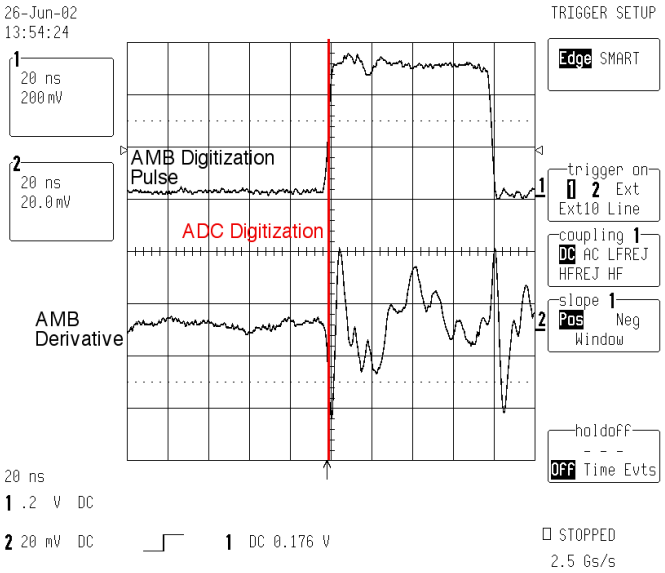

Fig. B.9: AMB derivative digitization with an ESumHi generated raw trigger. The top pulse is the digitization signal, the bottom pulse is the ESumHi derivative. The digitization signal is in-time with the ESumHi derivative. The red line indicates the ADC digitization.

16. Remove R32, R33, R37 and R42

17. Connect TP5 to R33

18. Connect C3 to R3 with 1500 ohm resistor

19. Connect Pins 1 and 15 of U12 to ground

20. Attach BNC connector next to SMB connectors

21. Route 'Sum-in' signal to BNC connector

22. Wrap ground wire with sum-in signal line, ground to BNC connector

23. Connected sum-in signal (wrapped with ground line) to TP40 (Pin 2 of U23)

24. Ground ground line wrapped with sum-in signal to TP39

B.3 Run Selection Criteria

The following criteria must be met for a run to be selected to be used in solar neutrino analysis

- The detector is running with neutrino settings.
- The bubblers are filled and off and no sample line assays are being performed.
- There must be no disruptive activity on deck.
- The temperature on deck must be less than 20.5°.
- Compensation coils must all be on.
- The run must be longer than 30 minutes. This is to ensure that the SPS checks are accurate.
- The fractional dead time due to the burst cuts must be less than 0.2.
- No sources can be deployed and the gate value must be closed
- All crates must have low and high voltage and the triggers enabled. Throughout the run, all crates must have normal occupancy.
- The inward neck tubes (13/15/1 and 13/15/2) must be operational.
- No more than 1% of channels can have sync clear errors.
- The detector event rate must not be greater than 60Hz for longer than 20% of the run's duration.

Appendix C

External Cherenkov Background Estimates Using a Maximum Likelihood Fit

Although the radioassays provide measurements of the amount of ^{214}Bi and ^{208}Tl in the light water (see Section 7.5), they do not measure of activity from the acrylic vessel or the PMT glass. Additionally the assays do not run continuously and therefore do not sample the entire data taking period. To provide constraints on the number of external background events from the acrylic, light water and PMTs inside the signal region, the neutrino data outside the fiducial volume is fit to source data to model the distribution of radioactivity in each region. Having obtained the amount of radioactivity outside the fiducial volume, the source data is used to determine the number of events inside the signal region. This technique, originally developed by Vadim Rusu, has been very successful at measuring the external background rates.

To measure the radioactivity outside the D_2O volume, the radial distributions

of radioactivity in the AV, light water and PMTs are modeled using ^{238}U and ^{232}Th sources deployed near (or in) these regions (see Section C.1 for further details). These distributions are insensitive to ^{238}U and ^{232}Th differences and provide the greatest separation between the three regions.

Having obtained the radial distributions for events in the AV, light water and PMT glass, these distributions are fit to the neutrino data using a maximum likelihood fit in the region of $1.1 < \rho < 2.5$. For the SNO publication on the salt phase data set [19], the fit was done at a lower energy threshold of 4.5 MeV compared to the analysis energy threshold of 5.5 MeV. At higher energy thresholds, the statistics in the radial distributions are too small to obtain a good fit. The radioactivity for each region extracted from the fit at lower energies is scaled to obtain the number of background events in the signal region at 5.5 MeV.

C.1 Building the Background Radial Distributions

To model the external Cherenkov backgrounds, radial distributions for radioactivity in the AV, H_2O and PMTs regions are built from ^{238}U and ^{232}Th source data. Using source data for these distributions has the advantage of reducing this analysis' reliance on the MC, which is less well understood for events outside the D_2O volume. The disadvantage is of having a non-pure sample of radioactivity as the ^{238}U and ^{232}Th sources are not tagged. Although the sources are hot enough as to overwhelm all other activity in the detector, some event selection criteria are still required.

For all the source and the neutrino data, events are required to have ITR > 0.55 and $0.7 < \theta_{ij} < 1.65$. The standard DAMN cuts[1] with the exception of the $N_{\rm Hit}$ burst

[1]retrigger, QVT, QNhit, crate isotropy, AMB, FTS, Owl, junk, neck, Esum, QCluster, ITC,

cut for the source data were applied. The neutrino data also has an additional energy cut of $E < 20$ MeV.

C.1.1 The Acrylic Vessel Background Radial Distribution

To determine the radial distribution for the external background events in the AV, an uncanned[2] ^{232}Th source deployed at 595 cm^3 is used. The ^{232}Th daughter, ^{208}Tl produces a β with a 1.8 MeV endpoint energy but also 2.614 MeV γ. The γ can photo-disintegrate a deuteron, resulting in a free neutron. As the source is deployed in the heavy water, the events from neutron captures are non-negligible. To account for these neutrons, the radial distribution of neutrons produced from the source is modeled using MC[4] and subtracted off the source's radial distribution. The correct number of neutron events produced from the source is obtained by normalizing the number of MC neutron events with a total energy between 6.5 to 8.0 MeV to the number of source events in the same energy region (Figure C.1). In this energy region the events from the source are completely dominated by photo-disintegration neutrons.

In addition to photo-disintegration neutrons, solar neutrino interactions are also a background to the source data. To account for these events, a radial distribution of quiet, no source data[5] is created, scaled to match the live time of the source and then subtracted from the radial distribution of the source. The quiet data has the

FGC, OwlE, muon follower short, and missed muon follower short

[2]The source is not encased in plastic which would prevent the β from producing light in the detector

[3]Runs 25773 and 25779 were used

[4]To obtain high statistic neutron MC, the autosno module MC_Th_U_Source is used

[5]The runlist for the quiet runs is salt_h2o_spike_quiet_p0.runlist in the official run selection runlist directory

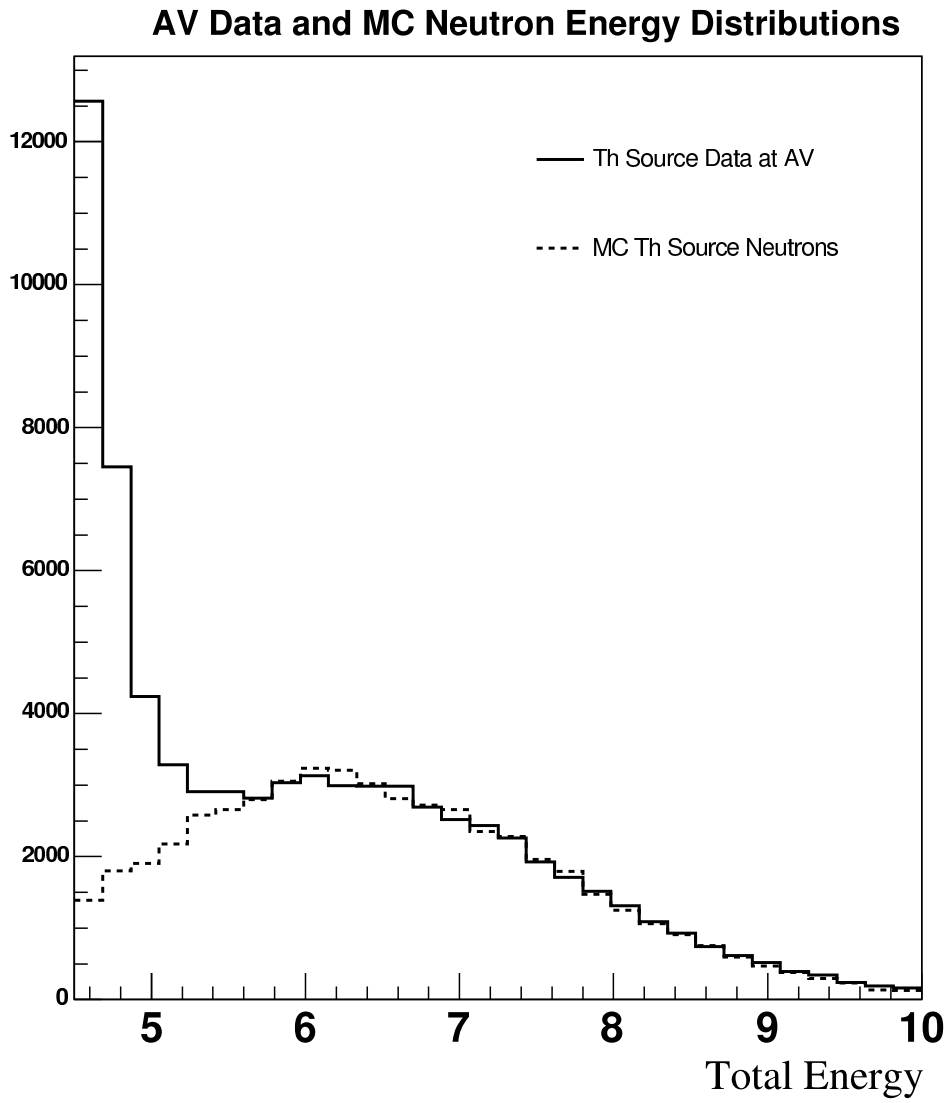

Fig. C.1: Energy distribution for events from the ^{232}Th source and photo-disintegration neutron MC. The neutron distribution has been normalized to the number of events in the source data with a total energy between 6.5 MeV to 8.0 MeV.

same selection cuts applied as the neutrino data.

The left plot in Figure C.2 shows the AV radial distribution before removing the photo-disintegration neutrons and the neutrino background events with the MC neutron radial distribution shown. The majority of events reconstructing away from the AV into the heavy water are neutrons. After removing the neutrons most events reconstruct very near the AV (right hand figure).

C.1.2 The H_2O Background Radial Distribution

The radial distribution for ^{214}Bi and ^{208}Tl decays in the light water was generated using an injection of ^{222}Rn into the light water. This planned spike consisted of two injections with roughly 4.92 days of total live time[6]. Unlike the AV ^{232}Th source, the ^{222}Rn spike is part of the ^{238}U chain and serves as a nice cross check for differences in the radial distribution between ^{238}U and ^{232}Th. In addition to the selection cuts discussed in Section C.1, an energy cut of $E < 20$ MeV is also applied to the spike data.

The decay of ^{214}Bi in the ^{238}U chain produces a γ with enough energy to photo-disintegrate a neutron in less than 1% of the decays. Therefore, removing neutron events from the H_2O radial distribution is not necessary. Accounting for neutrino signal events is still necessary and done in the same way as discussed with the AV source.

[6]Runs used listed in salt_h2o_spike_p0.runlist which is found in the official run selection directory

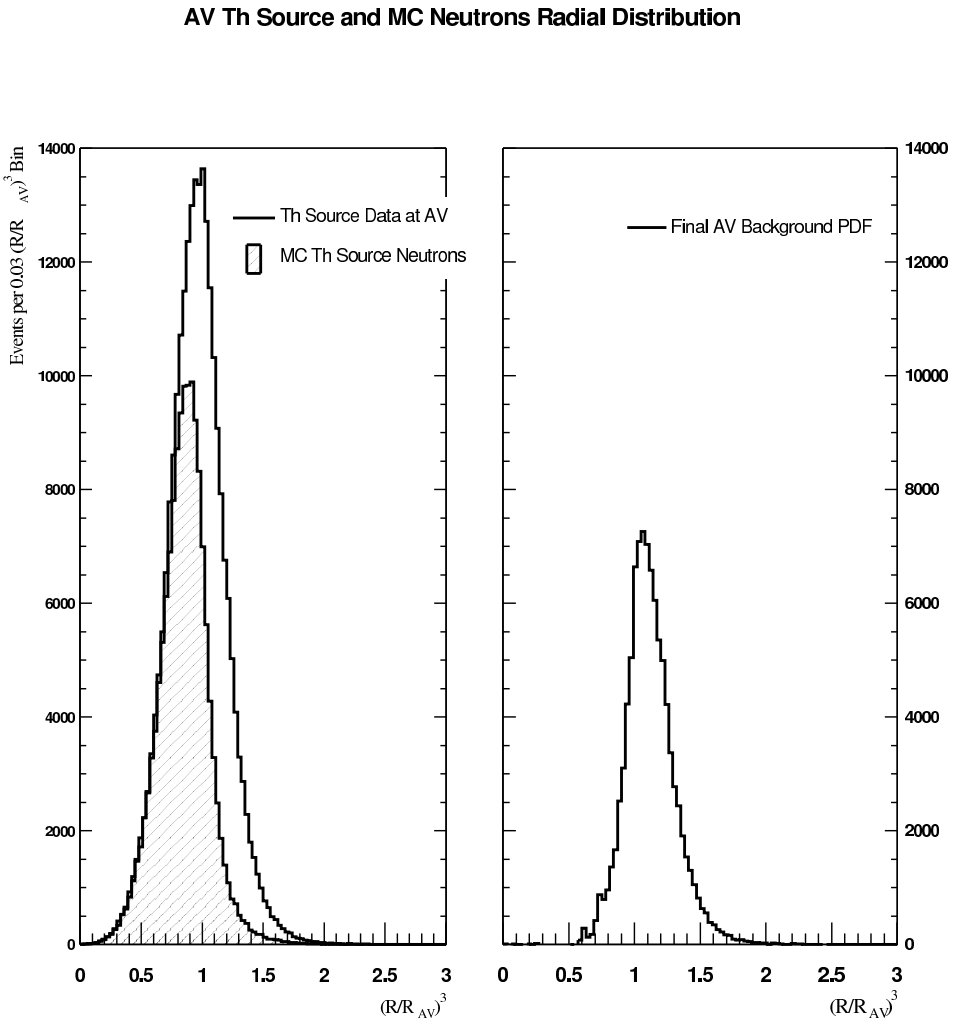

Fig. C.2: On the left is the raw radial distribution for the Th source at the AV plotted with the radial distribution of photo-disintegration neutron MC. On the right is the neutron subtracted AV radial distribution.

C.1.3 The PMT Background Radial Distribution

To model radioactivity from decays in the PMT glass, a very hot ^{232}Th source deployed near the PSUP[7] is used. Although there are a significant number of energetic γ's from the source, these γ's rarely reach the heavy water to be able to photodisintegrate neutrons. The neutrino signal radial distribution is accounted for using the same method as with the AV and H_2O radial distributions. In addition to the standard selection cuts for this analysis, the PMT source requires an energy cut of $E < 8.5$ MeV to remove pathological events that are produced from the source.

Although the PMT source was deployed very near the PSUP and PMTs, it does not completely represent radioactive decays in the PMT glass. Although deployed very close to the PMTs, the source is not located right at the PMT glass and there is some uncertainty in the exact location of the source. As a result the radial distribution of the PMT source does not match the neutrino data as can be seen in Figure C.3. After fitting the source radial distributions to the neutrino data, the PMT radial distribution and the neutrino data do not agree well at $\rho > 2.2$. At this high radius, PMT radioactivity dominates and the H_2O activity can be ignored, therefore good agreement between just the PMT radial distribution and the neutrino data is expected. To achieve a reasonable fit, the PMT radial distribution is shifted outwards by 20 cm to better represent the neutrino data.

[7]Runs 29687, 29688 and 29689 were used

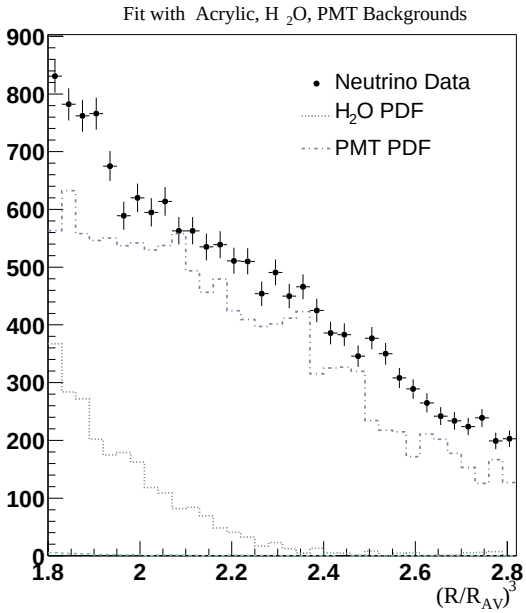

Fig. C.3: Comparison of the PMT radial distribution to the neutrino data at high radius. The PMT radial distribution, normalized based on the maximum likelihood fit does not agree with the neutrino data.

C.2 Fitting for the Number of External Cherenkov Events

Using the radial distributions discussed in the previous section and an energy threshold of 4.5 MeV, the maximum likelihood fit to the neutrino data yields normalization ratios of 0.0256, 1.44, and 1.87 for the AV, H_2O, and PMT regions respectively. These fit results are shown in Figure C.4. The radial distributions provide excellent agreement to the neutrino data. To obtain the number of background events inside the fiducial volume for the energy thresholds of 5.0 and 5.5 MeV, these normalization ratios are used to scale the number of events in the source radial distributions inside 550 cm, which are listed in Table C.1. Including only statistical uncertainties, the

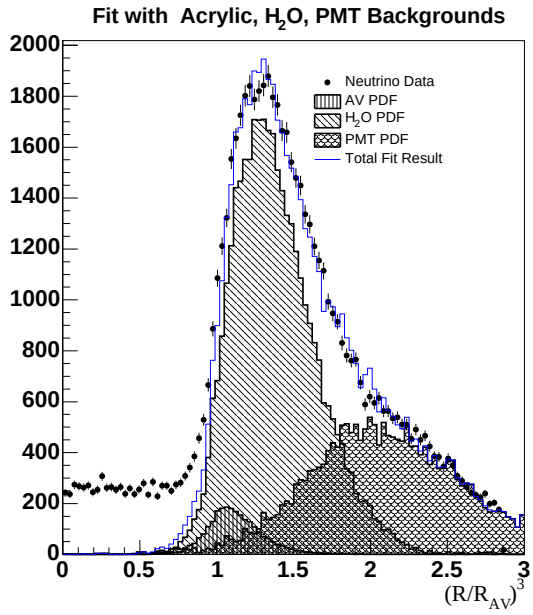

Fig. C.4: Results of the maximum likelihood fit to neutrino data at 4.5 MeV with the radial distributions built from source data shown.

number of background events in the signal region for the salt phase data set are given in Table C.2. Table C.3 lists the results for energy thresholds of 4.5, 5.0 and 5.5 MeV where the maximum likelihood fit has been done separately to neutrino data taken during the day and neutrino data taken during the night.

Since the number of background events in the fiducial volume above an energy of 5.5 MeV is small and consistent with zero, Feldman-Cousins confidence intervals

Threshold(MeV)	AV	H_2O	PMT
4.5	2170 ± 224	104 ± 15	24 ± 8
5.0	172 ± 204	12 ± 11	2 ± 6
5.5	83 ± 183	-9 ± 9	1 ± 5

Table C.1: The number of events inside 550 cm obtained from the AV, H_2O and PMT radial distributions. The radial distributions are normalized by the live time of the source.

Threshold(MeV)	AV	H_2O	PMT
5.0	4 ± 5	17 ± 16	4 ± 11
5.5	2 ± 5	-13 ± 13	2 ± 9

Table C.2: The number of background events inside the fiducial volume expected for the salt phase data set. Two different energy thresholds are listed.

Threshold(MeV)	AV	H_2O	PMT
4.5 Day	29 ± 3	69 ± 10	20 ± 6
4.5 Night	26 ± 3	81 ± 12	25 ± 8
5.0 Day	2 ± 3	8 ± 7	2 ± 5
5.0 Night	2 ± 2	9 ± 9	2 ± 6
5.5 Day	1 ± 2	-6 ± 6	1 ± 4
5.5 Night	1 ± 2	-7 ± 7	1 ± 5

Table C.3: The number of background events inside the fiducial volume expected for the diurnal salt phase data set. Two different energy thresholds are listed.

are used for the H_2O and PMT regions to obtain lower and upper bounds. The number of measured events is the raw number of source events in the signal window (Table C.1) and the number of background events is the number of expected neutrino background events taken from the quiet data (see Section C.1). Once the confidence limits are calculated, the limits are scaled by the normalization ratios obtained from the maximum likelihood fit. For the H_2O source, the upper limit is 3 events and 11 events for the PMT source. For both regions, the lower limit is zero events.

For the AV region, Gaussian statistics were used to calculate the one sigma limits since the number of events from the AV source is too large to use Feldman-Cousins limits. From Table C.2, the number of AV events in the fiducial volume for 5.5 MeV is 2 ± 5. Since a negative number is unphysical, the upper bound is taken to be the Gaussian one sigma upper limit of 7 events and the lower bound is zero events. The lower and upper limits for the three regions are summarized in Table C.4. The limits

Threshold(MeV)	AV (Lower:Upper)	H_2O (Lower:Upper)	PMT (Lower:Upper)
5.5	0:7	0:3	0:11

Table C.4: Lower and upper limits for the AV, H_2O and PMT sources.

were calculated using statistical uncertainties only as the systematic uncertainties are negligible in comparison (see Section C.3).

Adding the limits on the number of AV, H_2O and PMT events directly results an overestimate of the total number of external Cherenkov background events in the signal region. Instead the upper limits were assumed to be the one sigma limits of Poisson distributions. Combining these three Poisson distributions results in a mean of 14.64 events with a sigma of 3.84 events. Using a Gaussian distribution for the AV region and Poisson distribution for the H_2O and PMT regions yields similar results. The one sigma bounds of 18.48 events as the upper limit and zero events as the lower limit was used as the total number of external Cherenkov events in the signal region. Using the same method for the diurnal data sets, the limits are zero to 7.6 events for the day and 8.4 events for the night.

C.3 Evaluating Systematic Uncertainties

Although this analysis minimizes reliance on the MC (see Section C), several systematic uncertainties due to the sources need to be evaluated. All of the following uncertainties were calculated using an energy threshold of 4.5 MeV and the fractional uncertainty is assumed to be the same at higher thresholds. The uncertainties are summarized in Table C.5 and the maximum likelihood fit including systematic

uncertainties is shown in Figure C.7.

C.3.1 Z-asymmetry

A disadvantage with using source data in building the radial distributions is the limited number of locations where the source can be deployed. Discussed in Chapter 6, the detector has a strong asymmetry in energy response in the z-plane. To evaluate effects from this asymmetry, encapsulated ^{232}Th sources deployed in the lower and upper regions were used to measure differences in the radial distributions [90]. The z-asymmetry uncertainty is 3% on the number of external Cherenkov events in the signal region.

C.3.2 Time Variations

Since the source radial distributions are fit to the neutrino data, variations in the amount of radioactivity over time is naturally accounted for but time dependent changes in the leakage fraction needs to be evaluated. The leakage fraction is the ratio of the number of external background events inside the signal region to the total number of external background events inside the maximum likelihood fit region. The source data used to generate the radial distributions cannot be used to determine time dependences since the sources were deployed only once during the salt phase. Instead the neutrino data is used to evaluate any time dependent changes in the leakage fraction.

To use the neutrino data to study changes in the leakage fraction, a reconstruction ratio is defined which represents the ratio of external background events inside the signal region to the number of background events outside the fiducial volume. To se-

lect events inside the signal region as possible external Cherenkov background events, the event must be traveling outward (external backgrounds which mis-reconstruct inside the D_2O tend to have an outward direction). Similarly, to select possible H_2O background events, the event must also be traveling outward but with a reconstructed position in the light water. PMT backgrounds are selected by choosing events that reconstruct near the PMTs and are traveling inward towards the PMTs (PMT events tend to reconstruct with an inward direction). The reconstruction ratio for H_2O backgrounds is expressed as

$$\frac{\text{Number of Events with } R < 550\text{cm, } 4.0 < E < 4.5 \text{ and } \vec{u}\cdot\vec{r} > 0.75}{\text{Number of Events with } 650 < R < 750\text{cm, } 4.0 < E < 4.5 \text{ and } \vec{u}\cdot\vec{r} > 0.50}$$

Similarly for the PMT background events, the reconstruction ratio is defined as

$$\frac{\text{Number of Events with } R < 550\text{cm, } 4.0 < E < 4.5 \text{ and } \vec{u}\cdot\vec{r} > 0.75}{\text{Number of Events with } 720 < R < 850\text{cm, } 4.0 < E < 4.5 \text{ and } \vec{u}\cdot\vec{r} < -0.50}$$

where $\vec{u}\cdot\vec{r}$ is the dot product between the event direction and position vectors. Using these reconstruction ratios to determine any time variations in the leakage fraction has several drawbacks. First, this ratio is non-intuitive since an increase in radioactivity in the light water or the PMTs results in a decrease of these ratios. Second, as seen in the above equations, changes in the heavy water radioactivity or light water radioactivity also affect the reconstruction ratio. It is impossible to decouple changes in the radioactivity with changes in the leakage fraction.

Figures C.5 and C.6 plots the reconstruction ratios as a function of Julian date

since the start of the salt phase data set, where the solid red line indicates the end of the publication [65] data set. In the light water there appears to be a decrease in the reconstruction ratio around a day of 650. The PMT ratio also appears to have some fluctuations over time, but there are no strong trends.

Several studies measuring light water radioactivity over time [91,92] indicate there is an increase in the H_2O activity at approximately the same time that the light water reconstruction ratio begins to decrease in Figure C.5. It is likely that the decrease in the reconstruction ratio is from increases in light water radioactivity, not changes in the leakage fraction. For evaluation of this systematic uncertainty, the conservative approach is to assume all changes in the reconstruction ratio are due to changes in the leakage fraction was taken and this approach is taken here. Although this overestimates the time variation uncertainty, it is a small effect overall. To calculate the uncertainty, the average deviation of the reconstruction ratio was found using a bin size of 39 Julian days. The time dependent uncertainty in the leakage fraction is 14% for the AV and H_2O and 23% for the PMT radial distributions.

C.3.3 ^{238}U and ^{232}Th Differences

To investigate differences in the radial distributions between the ^{238}U and ^{232}Th chains, the H_2O radial distribution is generated using the ^{232}Th source instead of the ^{222}Rn spike. To build the radial distribution using the ^{232}Th source, sources at different radii are volume weighted to obtain a smooth radial distribution throughout the H_2O volume. Details of the volume weighting are discussed in [90]. Using the ^{232}Th H_2O radial distribution in the maximum likelihood fit results in a difference of 57% in the number of events in the signal region.

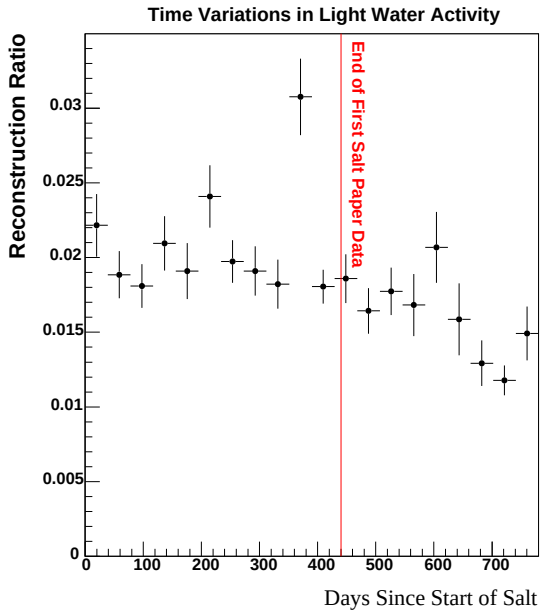

Fig. C.5: Time variation of H_2O events in the neutrino data. The reconstruction ratio is explained in the text.

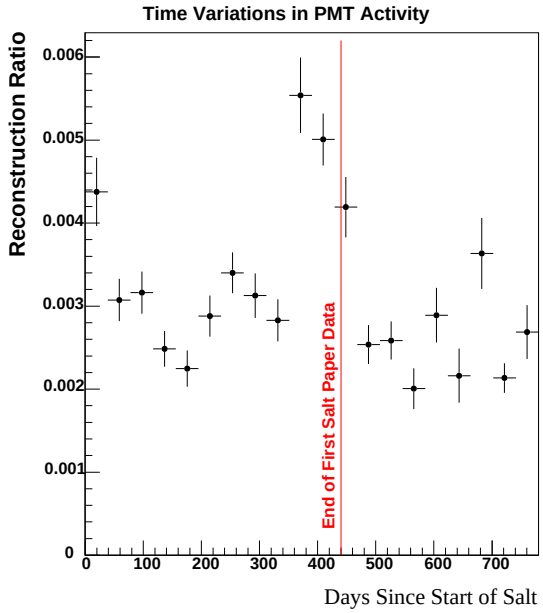

Fig. C.6: Time variation of PMT events in the neutrino data. The reconstruction ratio is explained in the text.

Using the ^{232}Th source for the H_2O radial distribution estimates ^{238}U and ^{232}Th differences in the H_2O distribution, but not the AV. (The PMT radial distribution is not considered here since PMT events which reconstruct inside the D_2O volume are so mis-reconstructed that ^{238}U and ^{232}Th differences are indistinguishable). Another method of estimating the ^{238}U and ^{232}Th differences for the AV and H_2O backgrounds is to compare ^{238}U and ^{232}Th source data deployed at specific points. For the H_2O backgrounds, sources at R = 620cm[8] were used. Sources at large radii were not considered because the ^{238}U source is too weak. As with the AV radial distribution, MC was used to subtract the photo-disintegration neutrons events from the radial distribution. For both the ^{238}U and ^{232}Th sources, the number of source events inside R = 550cm with E > 4.5MeV was calculated and normalized by the number of source events with the same energy threshold within a 30cm shell around the source position. For the ^{238}U source which has low statistics, the Feldman-Cousins method was used to determine the lower and upper limits for the number of source events inside the signal region. The difference in the leakage fraction between ^{238}U and ^{232}Th is 50% for the upper ^{238}U bound.

The same technique can be used to estimate the ^{238}U and ^{232}Th difference for the AV source. Using the ^{238}U source deployed very near the AV[9] to calculate the fractional number of events in the signal region, the difference relative to the ^{232}Th source at the same position is 87%. This systematic uncertainty is large due to poor statistics of the ^{238}U source.

[8] ^{238}U source run was 24242 and ^{232}Th source run was 24187

[9] The canned ^{238}U run 27916 was used

C.3.4 Neutron Energy Scale and Resolution

While this analysis tries to avoid the use of MC, it was necessary to use it to model the radial distribution of the photo-disintegration neutrons produced during the AV ^{232}Th source run. Fortunately, the AV backgrounds account for a small percentage of the overall number of external Cherenkov background events; large uncertainties associated with this radial distribution have a relatively small effect on the fit results.

To estimate the uncertainties from the MC neutron energy scale and resolution, the neutron energy distribution for both the AV ^{232}Th data and the MC neutrons is fit to a Gaussian over the energy range of 5.5 and 9.0 MeV. The difference between the data and MC is +0.5% for the energy mean and 2.0% for the energy resolution. Shifting the energy mean in the MC by 0.5% and repeating the fit results in a 10% difference in the number of background events inside the signal region. Smearing the MC energy resolution by 2.0%, results in a 2.0% difference in the number of background events. Adding the two uncertainties in quadrature results in a 10% overall systematic uncertainty due to energy scale and resolution differences between data and MC.

C.3.5 Radioactivity Volume Distribution

For the AV and PMT radial distributions the sources are point sources used to model radioactivity that is distributed throughout either the acrylic or glass. Additionally the H_2O spike data, although distributed throughout the light water volume, still does not have the same volume distribution as the radioactivity in the neutrino data. To evaluate the systematic uncertainties due to the volume distribution of radioactivity from the source, the H_2O and PMT radial distributions are shifted by 2% both inward

Systematic type	AV(%)	H_2O (%)	PMT(%)
z-asymmetry	3	3	3
Time Variations	14	14	23
U/Th Differences	87	50	-
Neutron subtr.	10	-	-
Volume Distribution	-	50	53
Total	89	72	58

Table C.5: Summary of systematic uncertainties for measurement of the number of external Cherenkov background events.

and outward. The maximum likelihood fit is repeated with the shifted distributions and the difference in the number of background events inside the signal region is taken as the systematic uncertainty. Shifting the radial distribution 2% outward results in a 50% change in the number of background events for the H_2O backgrounds and a 53% change for the PMT backgrounds. Shifting by 2% inward results in a 75% change for the H_2O backgrounds and a 100% change for the PMT backgrounds. As discussed in Section C.1.3, shifting the radial distributions inward results in very poor fits, therefore a symmetric uncertainty of 50% and 53% respectively for the H_2O and PMT radial distributions is assumed.

C.4 Summary

This appendix details a method of constraining the external Cherenkov background events by fitting the expected radial distributions of the AV, H_2O and PMT backgrounds to the neutrino data outside the fiducial volume. Unlike the radioassays this method can determine the radioactivity in the AV and PMTs and time variations in the background rates.

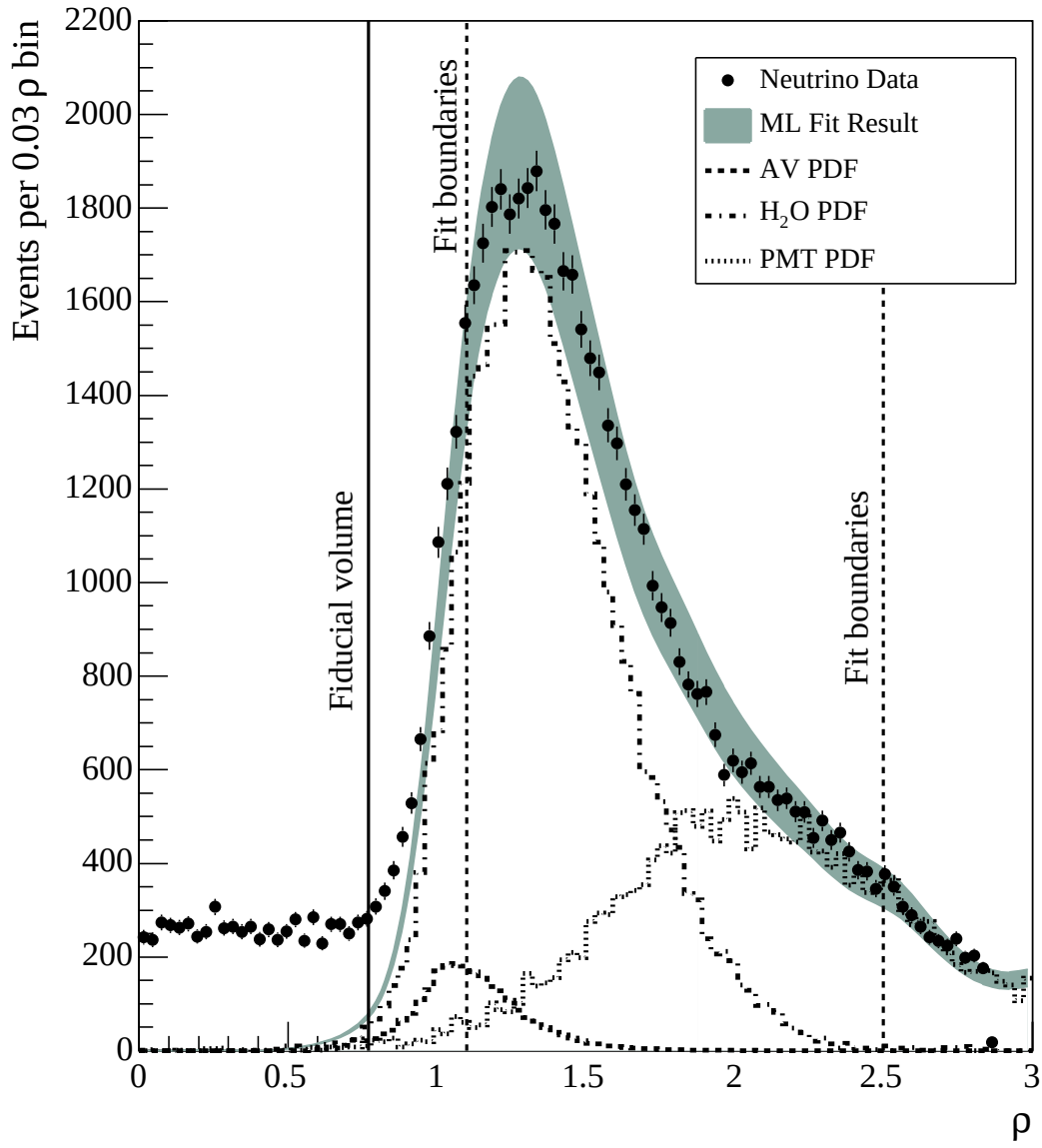

Fig. C.7: Results of the maximum likelihood fit to the neutrino data. The width of the bands on the fit results represents the size of the uncertainties. Both statistical and systematic uncertainties are included. The energy threshold of the fit is 4.5 MeV.

Appendix D

Observable Uncertainties and Corrections

The following appendix details the calculation of the β_{14} and energy non-linearity systematic uncertainties. These uncertainties are applied to the signal extraction as outlined in Chapter 9. The corrections to the cut acceptances for the DAMN and HLCs are also listed here.

D.1 β_{14} Uncertainties

To evaluate the systematic uncertainties in the β_{14} observable, the method developed in [74] is applied. For electrons and neutrons the β_{14} distribution can be well parameterized by a Gaussian to determine the mean and width. To estimate any data and MC differences in both the mean and width, ^{16}N is used at points through the D_2O volume. Since β_{14} mean and width change as a function of energy, ^{16}N events are selected using within an energy range of 4.5 to 6.0 MeV. Other selection criteria of

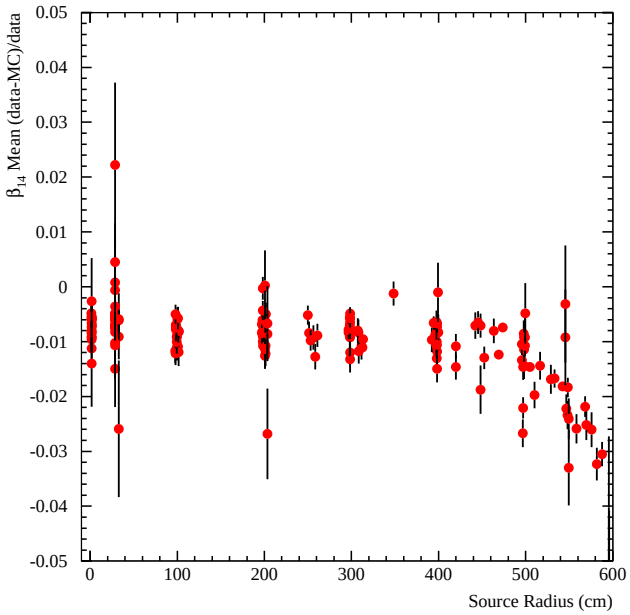

Fig. D.1: Difference in the β_{14} mean as a function of source position for ^{16}N in the D_2O phase.

ITR$>$ 0.55 and $z_{pos} <$ 300cm are also applied.

For ^{16}N in the D_2O phase, the difference in the mean and width as a function of source radius is shown in Figures D.1 and D.2. Similarly, the difference in the β_{14} mean and width between ^{16}N data and MC for the salt phases is shown in Figures D.3 and D.4 respectively. The volume-weighted difference in the mean and width for each phase are listed in Table 9.3.

D.2 Energy Non-Linearity Uncertainty

To calculate data and MC differences in energy scale as a function of energy, the ^{8}Li source which is a multi-energetic electron source is used. Using ^{8}Li deployed at the center, the energy distributions for data and MC are fit using the most probable

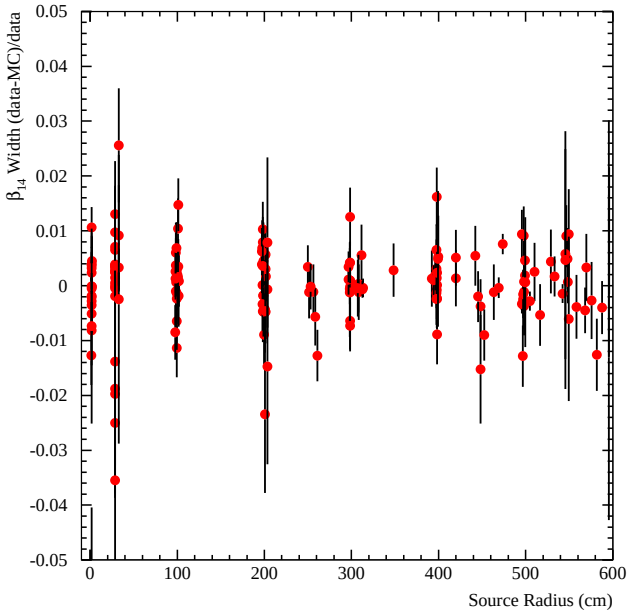

Fig. D.2: Difference in the β_{14} width as a function of source position for ^{16}N in the D_2O phase.

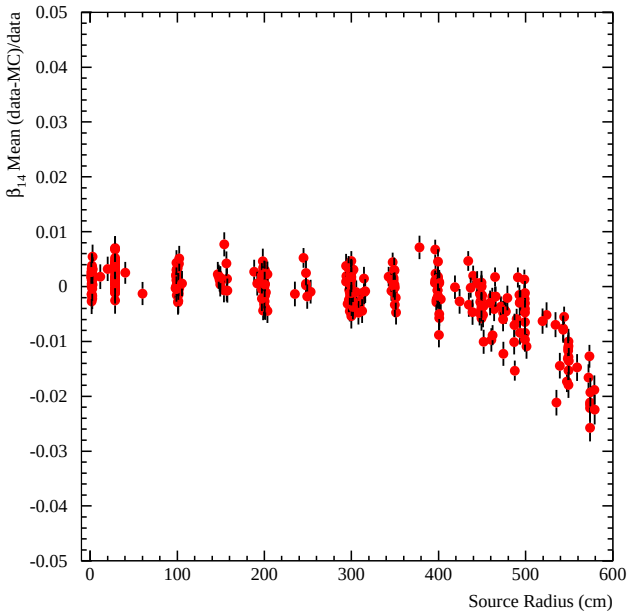

Fig. D.3: Difference in the β_{14} mean as a function of source position for ^{16}N in the salt phase.

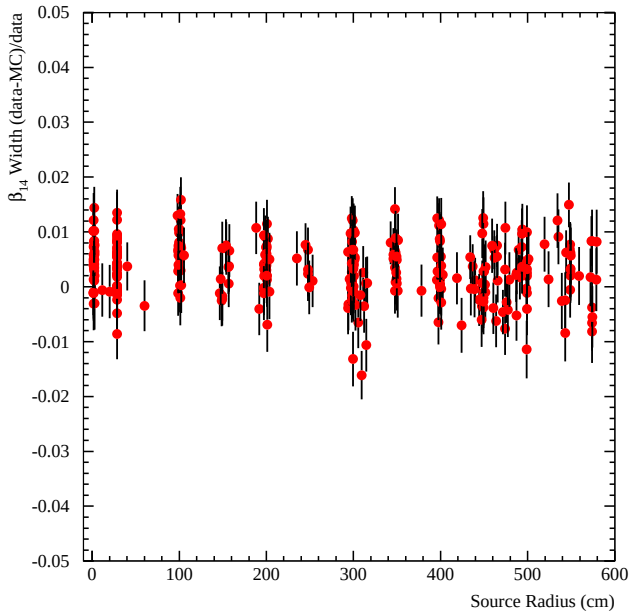

Fig. D.4: Difference in the β_{14} width as a function of source position for ^{16}N in the salt phase.

electron energy fit (see Chapter 6). The result for the fit to ^{8}Li data in the salt phase can be seen in Figure D.5.

To account for energy dependent changes in the energy scale, an additional parameter is added to the most probable electron energy fit expressed in Equation 6.1. The scale parameter p_3 is modified to be an energy dependent scale factor $p_3 + p_3' E$ where E is the event energy. The energy-dependent scale factor is compared between data and MC as shown in Figure D.6. For the D_2O phase, there is a difference in the energy scale of roughly 1% at 10 MeV compared to 5 MeV. In the salt phase, there is no significant energy non-linearity. In the application of systematic uncertainties, the energy non-linearity determined from the D_2O phase is conservatively applied to

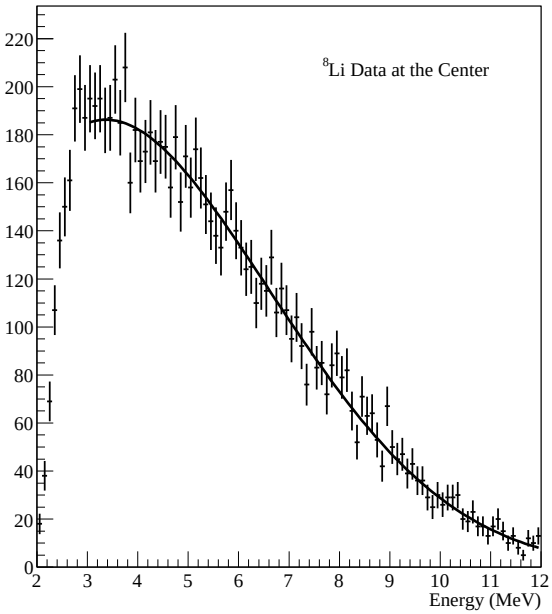

Fig. D.5: Energy distribution for ^{8}Li data at the center. The fit curve is the most probable electron energy fit.

both phases. This uncertainties (δ_e) is parameterized as

$$\delta_e = \frac{a_1 + a_2 E}{a_3 + a_4 E} \tag{D.1}$$

where the values of a_i are listed in Table D.1.

Parameter	Value
a_1	1.1424
a_2	2.2904
a_3	1.1225
a_4	2.1908

Table D.1: Parameter values used for the energy non-linearity systematic uncertainty.

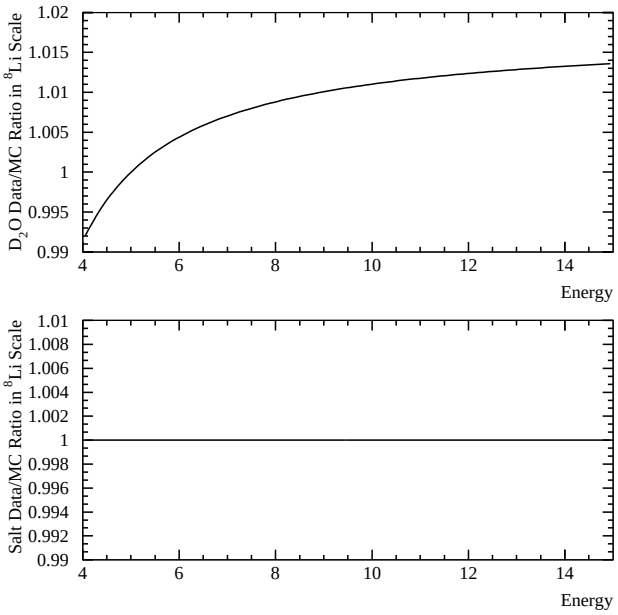

Fig. D.6: Difference between data and MC energy scale as a function of energy for ^{8}Li deployed at the center for the D_2O phase (top figure) and salt phase (bottom figure).

D.3 CC, ES and NC Cut Acceptance

Table D.2 lists the cut acceptance correction factor to the extracted fluxes. This factor accounts for cut acceptance differences in the DAMN and HLC between data and MC. The table lists the correction factor for CC, ES and NC events as a function of energy. For the background PDFs, the CC values were applied for Cherenkov events and the NC values were applied for the photo-disintegration neutron events.

Min. Energy	Max. Energy	CC	ES	NC
3.5	4.4	0.011762	0.023804	0.008118
4.4	4.6	0.010589	0.021584	0.008118
4.6	4.8	0.010600	0.021282	0.008118
4.8	5.0	0.009744	0.019671	0.008118
5.0	5.2	0.008278	0.016564	0.008118
5.2	5.4	0.007917	0.014761	0.008118
5.4	5.6	0.007735	0.013126	0.008118
5.6	5.8	0.008794	0.015355	0.008118
5.8	6.0	0.008451	0.013489	0.008118
6.0	6.2	0.008216	0.012119	0.008118
6.2	6.4	0.008118	0.010701	0.008118
6.4	6.6	0.007541	0.009722	0.008118
6.6	6.8	0.007596	0.009538	0.008118
6.8	7.0	0.008770	0.010789	0.008118
7.0	7.2	0.009147	0.010088	0.008118
7.2	7.4	0.009334	0.010541	0.008118
7.4	7.6	0.010373	0.011000	0.008118
7.6	7.8	0.013177	0.014431	0.008118
7.8	8.0	0.013292	0.014178	0.008118
8.0	8.2	0.011801	0.012082	0.008118
8.2	8.4	0.012660	0.012850	0.008118
8.4	8.6	0.012662	0.012728	0.008118
8.6	8.8	0.013087	0.013631	0.008118
8.8	9.0	0.013211	0.013449	0.008118
9.0	9.2	0.020134	0.021797	0.008118
9.2	9.4	0.020643	0.020927	0.008118
9.4	9.6	0.013594	0.013744	0.008118
9.6	20.0	0.016086	0.017022	0.008118

Table D.2: Cut acceptance correction values accounting for differences in cut acceptance between data and MC.

Bibliography

[1] Y. Fukuda *et al.*, Phys. Rev. Let. **81**(8), 1562 (1998).

[2] Q. R. Ahmad *et al.* (SNO), Phys. Rev. Let. **89**, 011301 (2002).

[3] Y. Fukuda *et al.*, Phys. Rev. Let. **82**(12), 2430 (1999).

[4] B. T. Cleveland, T. Daily, J. Raymond Davis, J. R. Distel, K. Lande, C. Lee, P. S. Wildenhain, and J. Ullman, Astrophysical Journal **496**, 505 (1998).

[5] J. N. Abdurashitov *et al.* (SAGE), Nucl. Phys. Proc. Suppl. **118**, 39 (2003).

[6] W. Hampel *et al.*, Physics Letters B (447), 127 (1998).

[7] M. Altmann *et al.*, Physics Letters B (490), 16 (2000).

[8] E. Aliu *et al.* (K2K), Phys. Rev. Lett. **94**, 081802 (2005).

[9] D. G. Michael *et al.* (MINOS) (2006), `hep-ex/0607088`.

[10] K. Eguchi *et al.* (Kamland), Phys. Rev. Let. **90**, 021802 (2003).

[11] W. Pauli, *In a letter to the physical institute of the federal institute of technology in zurich*, Physics Today (1978).

[12] C. Cowan, F. Reines, F. Harrison, H. Kruse, and A. McGuire, Science **124** (1956).

[13] S. Weinberg, Phys. Rev. Let. **19**, 1264 (1967).

[14] S. L. Glashow, Nucl. Phys. **22**, 579 (1961).

[15] A. Salam, in *Elementary Particle Theory, Relativistic Groups and Analyticity* (1969), pp. 367–377.

[16] S. L. Glashow, J. Iliopoulos, and L. Maiani, Phys. Rev. D **2**, 1285 (1970).

[17] M. Apollonio *et al.* (CHOOZ), Phys. Lett. **B466**, 415:430 (1999).

[18] Y. Ashie *et al.* (Super-Kamiokande), Phys. Rev. **D71**, 112005 (2005).

[19] B. Aharmin *et al.* (SNO), Phys. Rev. C **72**, 055502 (2005).

[20] J. N. Bahcall, A. M. Serenelli, and S. Basu (2005), `astro-ph/0511337`.

[21] J. Bahcall, *Neutrino Astrophysics* (Cambridge University Press, Cambridge, 1989).

[22] J. N. Bahcall, A. M. Serenelli, and S. Basu, Astrophys. J. **621**, L85 (2005).

[23] Y. Fukuda *et al.*, Phys. Rev. Let. **77**(9), 1683 (1996).

[24] L. Wolfenstein, Physical Review **17**(9), 2369 (1977).

[25] S. P. Mikheev and A. Y. Smirnov, Soviet Journal Nuclear Physics **42**(6), 913 (1985).

[26] J. Hosaka *et al.* (Super-Kamkiokande), Phys. Rev. **D73**, 112001 (2006).

[27] H. H. Chen, Phys. Rev. Let. **55**(14), 1534 (1985).

[28] Q. R. Ahmad *et al.* (SNO), Phys. Rev. Let. **89**, 011302 (2002).

[29] T. Araki *et al.* (KamLAND), Phys. Rev. Lett. **94**, 081801 (2005).

[30] J. N. Bahcall, P. I. Krastev, and A. Y. Smirnov, JHEP **05**, 015 (2001).

[31] O. G. Miranda, M. A. Tortola, and J. W. F. Valle (2004), `hep-ph/0406280`.

[32] A. Friedland, C. Lunardini, and C. Pena-Garay, Phys. Lett. **B594**, 347 (2004).

[33] R. Fardon, A. E. Nelson, and N. Weiner, JCAP **0410**, 005 (2004).

[34] M. Cirelli, M. C. Gonzalez-Garcia, and C. Pena-Garay, Nucl. Phys. **B719**, 219 (2005).

[35] V. Barger, P. Huber, and D. Marfatia, Phys. Rev. Lett. **95**, 211802 (2005).

[36] J. Boger *et al.*, Nuclear Instruments and Methods **A449**, 172 (2000).

[37] P. Wittich, *First Measurement of the Flux of Solar Neutrinos from the Sun at the Sudbury Neutrino Observatory*, Ph.D. thesis, University of Pennsylvania (2000).

[38] M. S. Neubauer, *Evidence for Electron Neutrino Flavor Change through Measurement of the* ^{8}B *Solar Neutrino Flux at the Sudbury Neutrino Observatory*, Ph.D. thesis, University of Pennsylvania, Penn (2001).

[39] J. R. Klein, M. S. Neubauer, R. Van Berg, and F. M. Newcomer, *The SNO trigger system*, SNO technical report SNO-STR-97-036, University of Pennsylvania (1997).

[40] The SNO Collaboration, *The SNOMAN User's Manual*, version 5.02 ed.

[41] S. Biller *et al.*, *SNO Electronic Calibration Constants*, Tech. Rep., SNO Collaboration (2001).

[42] J. Cameron *et al.*, *The Gain and the Pain: A Study of Detector Response and Instrumental Backgrounds After the High Voltage Raise*, SNO technical report SNO-STR-99-039, University of Pennsylvania, Oxford University, TRIUMF, and Queens Universty (1999).

[43] R. J. Ford, *Calibration of SNO for the detection of* ^{8}B *neutrinos*, Ph.D. thesis, Queen's University, Kingston, Ontario (1998).

[44] M. R. Dragowsky *et al.*, Nuclear Instruments and Methods **A481**, 284 (2002).

[45] N. Tagg *et al.*, Nuclear Instruments and Methods **A489**, 92 (2002).

[46] A. W. P. Poon *et al.*, Nuclear Instruments and Methods **A452**, 15 (2002).

[47] S. Brice *et al.*, *First Generation Acrylic Encapsulated U/Th Sources*, SNO Technical Report SNO-STR-99-023, LANL, LBNL, Queens University (2000).

[48] R. Lange, *Rn Spike Procedure*, Tech. Rep., Subdury Neutrino Observatory (2005).

[49] CERN Program Library Long Write Up Q100, *Zebra Q100/Q101* (1995).

[50] D. Cowen, G. Jonkmans, R. Komar, C. Okada, and R. Tafirout, *The SNO Database: SNODB v3.06.05*, Penn, Neuchatel, UBC, LBNL, Laurentian (1998).

[51] CERN Program Library Long Writeup Q180, *HEPDB Database Management Reference Manual.*

[52] CERN Program Library Long Writeup Q121, *Physics Analysis Workstation - User's guide.*

[53] *ROOT - An Object-Oriented Data Analysis Framework*, see http://root.cern.ch/.

[54] W. R. Nelson, H. Hirayama, and D. W. Rogers, *The EGS4 code system*, Stanford Linear Accelerator Center (1985).

[55] M. D. Lay, *Creation and Detection of Cerenkov light in the Sudbury Neutrino Observatory*, Ph.D. thesis, University of Oxford (1994).

[56] M. Thorman, *Not Yet Submitted*, Ph.D. thesis, University of Oxford.

[57] Radiation Shielding Information Center, Los Alamos National Laboratory, *MCNP4A, A Monte Carlo N-Particle Transport Code System* (1993).

[58] G. Orebi-Gann, *PMT Angular Response*, Tech. Rep., Oxford University (2005).

[59] J. Klein, *Realistically Simulated Charge Spectrum for SNO and the Prediction of Tube-by-tube Efficiencies*, Tech. Rep., University of Pennsylvania (2005).

[60] J. Klein, *Simulating Threshold and Gain Dependent Channel Efficiencies and the Solution to the Multi-pe Efficiency Problem*, Tech. Rep., University of Pennsylvania (2005).

[61] J. Farine *et al.* (Low Energy Background Working Group), *Low Energy Backgrounds during the Salt Phase of SNO*, SNO Internal Report, SNO (2003).

[62] T. C. Andersen *et al.* (SNO), Nucl. Instrum. Meth. **A501**, 386 (2003).

[63] T. C. Andersen *et al.* (SNO), Nucl. Instrum. Meth. **A501**, 399 (2003).

[64] Q. R. Ahmad *et al.* (SNO), Phys. Rev. Let. **87**, 071301 (2001).

[65] S. N. Ahmed *et al.* (SNO), Phys. Rev. Let. **92**, 181301 (2004).

[66] M. G. Boulay, *Direct Evidence for Weak Flavor Mixing with the Sudbury Neutrino Observatory*, Ph.D. thesis, Queen's University (2001).

[67] C. Tunnel and S. Seibert, *Measuring the Trigger Efficiency in the NCD-Phase and the All-Phase Implications*, Tech. Rep., University of Texas at Austin (2006).

[68] J. R. Wilson, *A Measurement of the* ^{8}B *Solar Neutrino Energy Spectrum at the Sudbury Neutrino Observatory*, Ph.D. thesis, Jesus College, Oxford University, Oxford (2004).

[69] O. Simard, Personal Communication.

[70] J. Klein, *Tuning the High Level Cuts for LETA*, Tech. Rep., University of Texas, Austin (2006).

[71] N. Barros, *Preliminary Optics Fits with Two Angular Responses*, Tech. Rep., Laboratorio de Instrumentacao e Fisica Experimental de Particulas, Lisboa, Portugal (2006).

[72] A. Anthony, *QSLH Correction*, Tech. Rep., University of Texas, Austin (2004).

[73] S. Seibert, Personal Communication.

[74] J. A. Dunmore, *The Separation of CC and NC Events in the Sudbury Neutrino Observatory*, Ph.D. thesis, Hertford College, Oxford University, Oxford (2004).

[75] N. K. McCauley, *Producing a Background Free Data Set for Meausurment of the Charge Current Flux and Day-Night Asymmetry at the Sudbury Neutrino Observatory*, Ph.D. thesis, The Queen's College, Oxford University, Oxford (2001).

[76] V. Rusu, *A Study of Contamination in SNO data using the Bifurcated Analysis Technique*, Tech. Rep., University of Pennsylvania (2000).

[77] N. McCauley *et al.* (Salt Data Cleaning Working Group), *Updates to Data Cleaning for the Salt Phase*, SNO Internal Report, SNO (2003).

[78] G. Cowan, *Statistical Data Analysis* (Oxford University Press, 1998).

[79] CERN Program Library Long Writeup D506, *MINUIT, Function minimization and error analysis.*

[80] K. Miknaitis and A. Hallin, ^{16}N *Z-scan studies in salt and vertex shift systematics*, SNO Internal Report, SNO (2003).

[81] K. Graham, *Salt Data Reconstruction Analysis*, SNO Internal Report, SNO (2003).

[82] G. Orebi-Gann, *Reconstruction Numbers for* D_2O, Tech. Rep., Oxford University (2006).

[83] C. Sims, *Background Determination in the Salt Phase of the Sudbury Neutrino Observatory Experiment*, Ph.D. thesis, Worcester College, Oxford University, Oxford (2005).

[84] J. N. Bahcall, M. Pinsonneault, and S. Basu, Astrophys. J. **555**, 990 (2001).

[85] G. Orebi-Gann, *Sacrifice Plots*, Tech. Rep., Oxford University (2006).

[86] W.-M. Yao *et al.*, Journal of Physics G **33**, 1+ (2006), URL `http://pdg.lbl.gov`.

[87] B. A. Moffat, *The Optical Calibration of the Sudbury Neutrino Observatory*, Ph.D. thesis, Queen's University, Kingston, Canada (2001).

[88] A. Hallin, Personal Communication.

[89] C. Okada, *AMB Cut Efficiency and Anti-Neutrinos*, Tech. Rep., Lawrence Berkeley National Laboratoy (2002).

[90] V. L. Rusu, *Measurement of the Total* ^{8}B *Solar Neutrino Flux at the Sudbury Neutrino Observatory*, Ph.D. thesis, University of Pennsylvania (2003).

[91] A. Poon, *Event Rate in the* H_2O *in-situ Monitoring Window*, Tech. Rep., Lawrence Berkeley National Laboratory (2004).

[92] A. Poon, *Run Rejection Due to Background*, Tech. Rep., Lawrence Berkeley National Laboratory (2004).